University of Liege – Faculty of Applied Sciences

Department of Architectural, Geological, Environmental and Civil Engineering – GeMMe research group

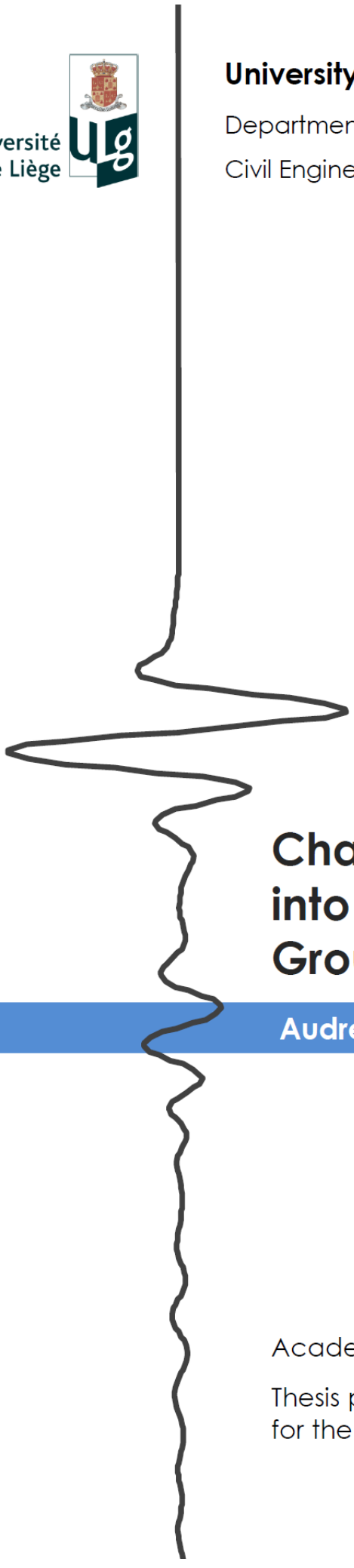

Characterization of thin layers into concrete with Ground Penetrating Radar

Audrey Van der Wielen

Academic Year 2013-2014

Thesis presented in fulfillment of the requirements for the degree of PhD in Engineering Sciences

Research institute

Research Group GeMMe
Department ArGEnCo
Faculty of Applied Sciences
University of Liege, Belgium

Thesis committee

Prof. Luc Courard	Université de Liège	*Advisor*
Prof. Frédéric Nguyen	Université de Liège	*Co-advisor*
Prof. Eric Pirard	Université de Liège	*President*
Prof. Jean-Paul Balayssac	INSA Toulouse	
Prof. Andrzej Garbacz	Politechnika Warszawska	
Prof. Jan van der Kruk	Forschungszentrum Jülich	
Prof. André Plumier	Université de Liège	

Funding

This research has been supported by the F.R.S.-FNRS research fellow grant FC 84664.

Copyright

Citation:
Van der Wielen, A. (2014). Detection and characterization of thin layers into concrete with Ground Penetrating Radar. PhD Thesis, University of Liège, Belgium, pp. XXX.

Abstract

The Ground Penetrating Radar (GPR) is a nondestructive technique increasingly used for the inspection of concrete structures. The method is well suited to study multilayer media, because only a part of the incident energy is reflected at each interface. But the quantitative determination of the thickness and properties of thin embedded layer remains an application under development, in particular when the tests are performed with contact antennas of high frequency. The aim of this work is to contribute to the development of a fast method for the thin layers determination, based on measurements performed with commercial antennas, by proposing an analytical estimation of the reflection coefficient.

As a first step, the equations allowing to estimate the reflection coefficient on a simple interface were developed, taking into account the wave spherical reflection in the near field and the lateral wave propagation. Similarly, for thin layers, equations taking into account the multiple reflections on the interfaces can be developed with different approaches. On the basis of the comparison of these equations with simulations of wave propagation, a hybrid model was defined: it allows approaching the reflection coefficient by the most adapted method depending on the thickness and the permittivity of the thin layer.

This model was then compared to reflection coefficients obtained by FDTD numerical simulations and laboratory tests. The reflection coefficients were obtained by comparing each measurement to a measurement performed on a metallic sheet embedded at the same depth. The tests were conducted on concrete slabs containing air layers of variable dimensions. Exploiting the spectral analysis of the laboratory tests performed with a single antenna, the use of the model allowed determining the permittivity of the layers and their thickness with respective errors of 0% and 20%. When tests with two antennas (CMPs) were performed, the precision was inferior because additional phenomena appear, including different waves propagating at the surface.

Therefore, the proposed method can be applied directly in some precise cases (when a reference measurement on a metallic sheet can be performed), but could be extended to numerous other situations by means of the quantification of the surface phenomena. In this case, it could be applied unaltered, possibly completed by an inversion program, or used as a first step of a more sophisticated method (modelling or full waveform inversion), in order to reduce the space of parameters to investigate.

Résumé

Le Ground Penetrating Radar (GPR) est une technique d'inspection non destructive de plus en plus utilisée pour inspecter les structures en béton. La méthode est bien adaptée pour étudier des milieux présentant plusieurs couches, car seule une partie de l'énergie incidente est réfléchie à chaque interface. Mais la détermination quantitative de l'épaisseur et des propriétés des couches minces enfouies reste une application en cours de développement, notamment lorsque les essais sont pratiqués avec des antennes de contact à hautes fréquences. L'objectif de ce travail consiste à contribuer au développement d'une méthode rapide de détermination de couches minces sur base de mesures réalisées avec des antennes commerciale, en proposant une estimation analytique du coefficient de réflexion.

Les équations permettant d'estimer le coefficient de réflexion sur une interface simple ont été développées dans un premier temps, en tenant compte de la réflexion sphérique des ondes en champ proche et de la propagation de l'onde latérale. De même, pour les couches minces, des équations prenant en compte les multiples réflexions sur les interfaces peuvent être développées de différentes façons. Sur base de la comparaison de ces équations avec des simulations de propagation d'onde, un modèle hybride a été défini : il permet d'approcher le coefficient de réflexion par la méthode la plus adaptée en fonction de l'épaisseur et de la permittivité de la couche mince.

Ce modèle a ensuite été comparé à des coefficients de réflexion obtenus par des simulations numériques en FDTD et des essais de laboratoire. Les coefficients de réflexion sont obtenus en comparant chaque mesure à une mesure effectuée sur une feuille métallique enfouie à la même profondeur. Les essais ont été menés sur des dalles de béton contenant des couches d'air d'épaisseur variable. Sur base de l'analyse spectrale des essais de laboratoire réalisés avec une seule antenne, l'utilisation du modèle a permis de déterminer la permittivité des couches et leur épaisseur avec une erreur respective de 0% et 20%. Lorsque des tests à deux antennes (CMPs) sont effectués, la précision est inférieure car des phénomènes additionnels apparaissent, dont différentes ondes se propageant à la surface.

La méthode proposée peut donc être appliquée directement dans certains cas précis (lorsqu'une mesure sur une feuille métallique peut être effectuée en comparaison), mais pourrait être étendue à de nombreux autres cas moyennant la quantification des phénomènes de surface. Elle pourrait alors être appliquée telle quelle, éventuellement complétée par un programme d'inversion, ou alors utilisée préalablement à une méthode plus lourde (modélisation ou inversion d'onde complète), afin de réduire l'espace des paramètres à considérer.

Acknowledgements

First and foremost, I would like to thank my advisors, Luc Courard and Frederic Nguyen, who offered me to work on this project in the first place and supported me during the whole PhD work. They gave me inspired advices and laboratory support and their detailed proofreading of the manuscript helped me to improve the text and structure the chapters. During the last four years, they offered me a total freedom to lead my research, but also involved me into different research, teaching and vulgarization activities. They also encouraged me to take part to various formations and conferences. I am also thankful to the FNRS, for allowing me a research fellow grant, and the ULg for providing an additional funding for the two last months.

I am also grateful to every person who has given a few minutes or hours to discuss with me, giving advices allowing to guide my research. Hoping not to forget anyone, I can cite Pierre Gilles and Eric Dondonné, Pierre Tihon, Jonathan Pisane, Jan Van der Kruk, Jamal Rhazi and Bilal Filali, Christophe Geuzaine and Véronique Beauvois and Vlatislav Cerveny. I also think of the members of my thesis committee, Andrzej Garbacz and André Plumier.

The experimental part of this thesis would not have been possible without the support of our laboratory team, and especially Amaury. I would also like to thank Lucien Dormal, from the company Ronveaux SA, and Adam Bundhoo , from the company Colas Belgium. The first one provided me with great quality self-compacting concrete slabs for my laboratory tests, and the second one covered my substrate slabs with the optimal asphalt overlay to lead my tests.

I would also like to express my deepest gratitude to Carmen Andrade, who welcomed me in the institute Eduardo Torroja in Madrid to carry on my research and the redaction of the thesis. Thanks also to all my colleagues there, who made this stay such a great memory for me.

Finally, I would like to thank all the people who have simply supported me during the last four years. I am thankful to my direct colleagues, and especially Astrid, Arnaud, Frederic and Sophie. I also would like to thank the girls of the Wednesday noon running: Julie, Ingrid, Fred and Martine. I may never have started without you! I also wish to say a special thanks to my parents and brother, for their continuously moral and occasionally logistical support.

Last but not least, I would like to express my deepest gratitude to the one who was my boyfriend at the beginning of this project, and successively became my fiancé and my husband. François, thank you for your technical help and detailed proofreading, but also for your infinite patience and your indefectible moral support. I don't think I could have done it without you by my side.

Table of contents

Introduction

The maintenance and replacement of the road infrastructures is currently a major concern for the industrialized countries. Indeed, the majority of the road networks were developed in the post-war reconstruction of the years 1945-1985. After this period, the economic crises led numerous governments to reduce the infrastructure maintenance budget to a minimum. As a result, many industrialized countries have now to deal with an ageing network of roads and bridges and colossal investments will be needed in the next years, just to maintain the current infrastructures. The OECD estimates the worldwide investments requirement for the road infrastructures to more than 110 billion of US dollars per year [1].

The issue of infrastructure underfunding is particularly acute when it concerns the bridges maintenance, because aging structures are susceptible to get altered with time and insufficient maintenance is then directly linked to safety concerns. Even if unpredicted bridge collapses are relatively rare, a lack of maintenance often leads to bridges closures or load restrictions, with high traffic and economic consequences. For this reason, many countries are developing bridge maintenance and control programs [2, 3].

In the particular case of Wallonia (Belgium), a total of more than 3500 bridges over highways, roads and waterways, are handled by the local administration [4]. In 2007, the average age of those bridges was estimated to 40 years old [5]. And in only four years, the number of bridges classified as to be repaired, in medium or short term, had increased by 28% [6]. The cost for the inspection, maintenance and repair of all the bridges is important: in 2009, the yearly cost rose up to more than 30 million €, only for Wallonia [4].

The causes of concrete bridge degradation are the constant rise of the traffic charges and the physical-chemical concrete degradation [6]. The increase of the traffic charges is due to the augmentation of the number of vehicles, but also to the growth of the heavy goods vehicles charges. In the period 1985-2005, the annual traffic expansion on Walloon highways has been estimated to 3.9%. On the period 1990-2006, the freight traffic in tons-km has raised up to 90% [7].

The physical-chemical degradations of concrete can be caused by different mechanisms: steel corrosion, concrete freeze sensitivity or alkali-aggregate reactions [6]. Those pathologies can be accelerated by the infiltration of water or chlorides arising from the de-icing salts. If several pathologies are combined in the same structure, they can cause irreparable damage leading to the demolition of the bridge. This happened for relatively recent structures: 30 years old bridges have been destroyed after being submitted to concrete degradation [8].

Figure 1 : Bridge deck suffering from concrete pathologies [9].

In order to prevent such extreme cases, every bridge has to be carefully monitored. A specific inspection (type A), visual and systematic, is planned at least every 3 years, depending on the bridge vulnerability [5]. If any sign of disorder is detected, a detailed inspection (type B) will be considered. During detailed inspections, every useful device can be used to determine the nature and extent of the problem [10].

To precisely characterize the structure geometry and its constitutive materials, cores can be drilled from the edifice. But the results are only representative from a small area and the multiplication of core samplings can cause damages to the edifice [11]. In order to limit to a minimum the number of destructive tests, non-destructive techniques (NDT) of investigation, generally based on methods used in geophysics prospection, have been developed in the last decades [12]. They do not impair the function of the structure and permit regular testing at the same location to evaluate changes in properties with time. They can be calibrated on a small number of destructive tests and give a complete overview of the structure state [13].

Among all the non-destructive techniques, this thesis focuses on the ground penetrating radar (GPR), with the objective to develop a methodology to determine quantitatively the properties of a structure containing a thin layer, using a commercial antenna. Using analytical developments and the analysis of the antennas properties, we developed a methodology of data acquisition and

analysis allowing (under a few conditions) the determination of the layer thickness and permittivity.

The body of the text will be divided into five different chapters. The first one will present the general context of the detection of thin layers with the ground penetrating radar, as well as a review of the literature on the subject.

In the second chapter, we will establish the theoretical bases of the thesis. The physical principles governing the Ground Penetrating Radar waves propagation will be detailed, with a special emphasis on the equations describing the waves reflection in the specific case of an embedded thin layer. Finally, the principles of the finite difference time domain (FDTD) method will be summarized. This numerical simulation method will be used throughout this thesis to simulate the wave propagation.

The third chapter will focus on the studies performed on the antenna to characterize the signal and to optimize the acquisition. After a presentation of the materials and methods used throughout the work, different preliminary tests will be performed to characterize the antenna and define good practice rules for the signal acquisition. Finally, different determination methods for the properties of the surface material will be compared.

Using the theoretical principles detailed in Chapter 2 and the acquisition principles determined in Chapter 3, the two final chapters will tackle the issue of the GPR detection and characterization of thin layers embedded into concrete. In Chapter 4, an analytical estimation of the reflection coefficient will be determined on the basis of the observation of the results of numerical simulations. The feasibility of using those equation to determine thin layers from surface measurements will be tested numerically and experimentally.

The fifth and last chapter is dedicated to the characterization of thin layers by comparing the reflection coefficient extracted from experimental measurements or numerical simulations to its analytical expressions. In the first section of the chapter, only the peak-to-peak amplitude will be extracted from the radargrams and compared to the analytical curves. In the second section, the same radargrams will be exploited to determine the layers properties using a spectral analysis of the reflection coefficient. The last section of the chapter will be dedicated to the layer determination using CMP measurements.

Chapter 1: General context

In this first chapter, we will briefly present the different concrete degradation mechanisms that can lead to the apparition of structural damages (§ 1.1). The second section of the chapter (§ 1.2) will focus on the different non-destructive techniques that can be used for bridges inspection, with a special focus on the Ground Penetrating Radar and its testing capabilities. Finally, in § 1.3, a review of the literature for the specific case of the layer detection with GPR will be presented.

1.1 Pathologies of concrete structures

Concrete structures can be damaged by different deterioration processes. According to the European standard EN 1504-9, the identification of the cause or the causes of defects should be the first step of a complete structure assessment before a concrete repair [14]. It is Indeed generally impossible to evaluate the necessity to repair a structure or to choose a repair method without a complete identification of the origin of degradations and a setting up of protection strategies [15].

One of the most important causes of degradation for prestressed and reinforced bridges is the rebars corrosion [8]. The corrosion of the rebars generates a loss in the reinforcement resistance, but the main danger lies in the expansive nature of the phenomenon, which will generate cracks and delaminations in the surrounding concrete.

The concrete itself can also be damaged due to diverse degradation mechanisms that will ultimately lead to its disintegration. The concrete pathologies are generally accelerated by climatic and exposure conditions. In

concrete bridge decks, the most significant disintegration processes linked to environmental conditions are [12]:

- disintegration due to freeze-thaw cycles;
- alkali-aggregates reactions;
- sulphate reactions.

A more complex degradation process, named concrete decay may be also observed in some cases. This is caused by the combination of several simple degradation processes; it has been observed on numerous concrete bridge decks, generating important delaminations and disintegration [8].

It is important to note that for all the pre-cited degradation mechanisms, water is an essential factor for the development of degradations. Indeed, it is estimated that 99% of the degradation mechanisms require the presence of water (in a liquid state) for developing [8]. In the particular case of bridge decks in cold temperate climate areas, chloride contamination due to the use of road salt is considered likely to be the most serious cause of deterioration [8, 12, 16, 17]. It means that the first cause of concrete degradation is indirectly the presence of defects in the waterproofing system [18].

But materials degradation is not the only cause of structures pathologies: the problems can also be caused by a lack of chemical or thermal compatibility between healthy materials, causing the apparition of delaminations.

The mechanisms of the different pathologies will be detailed in the next paragraphs.

1.1.1 Steel reinforcement corrosion

Corrosion is an electrochemical process involving an anode, a cathode and an electrolyte. In reinforced concrete, steel rebars can provide both anode and cathode, and moist concrete matrix forms an acceptable electrolyte. In the anodic zone, iron atoms dissolve into the interstitial solution as ions Fe^{2+}. This causes a local diminution of the section of the rebar. In the same zone, the electrical equilibrium requires the release of electrons:

$$Fe \leftrightarrow Fe^{2+} + 2\,e^{-} \tag{1}$$

These electrons travel in the electrolyte as an electrical current and they are consumed in the reduction reaction with Fe atoms at the cathode. This reaction results in the precipitation of $Fe(OH)_2$ and in an increase in metal volume (up to 800%). The phenomenon is described in Figure 2 [8, 15].

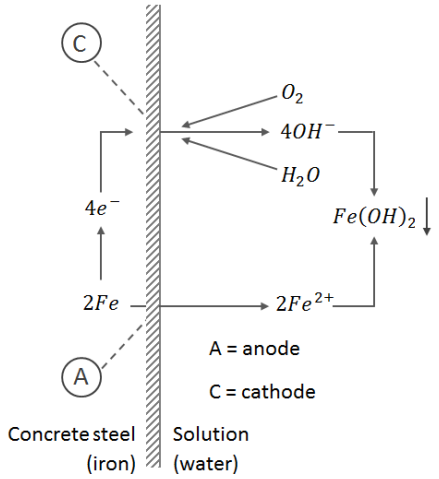

Figure 2 : Corrosion mechanism (after [8]).

Concrete is a high alkalinity material, in which a passivating film appears around reinforcing steel bars, protecting them from corrosion. To observe corrosion in reinforcing bars, three different factors must be present simultaneously:

- an electrolyte with a high ionic conductibility;
- oxygen in the cathode zone;
- disruption of the passivating film by chlorides attack or carbonation.

If a passivating film appears around steel rebars into healthy concrete, it is due to its high pH, situated around 12.5. A phenomenon susceptible to decrease this pH is carbonation: the CO_2 naturally contained into the atmosphere dissolves into the interstitial water of the concrete at the surface of the structure and reacts with the lime contained into the concrete. The simplified reaction mechanism is:

$$Ca(OH)_2 + CO_2 \rightarrow CaCO_3 + H_2O \quad (2)$$

The dissolution of CO_2 creates a decrease of pH to about 9. This is not damageable for the concrete itself but, at this pH, the passivating film is disrupted and steel corrosion can take place. For this reason, concrete carbonation is a very common cause of bridge degradation. An easy mean to reduce carbonation damages is to ensure the respect of concrete cover for the bottom surface of the slab, directly in contact with air [8].

Another cause of passivating film disruption can be a chloride attack, which can permit corrosion of the steel bars even in a non-carbonated concrete. For this reason, de-icing salts (NaCl or $CaCl_2$) can play a crucial role in the corrosion process [15]. The chloride act as a catalyser of the reaction, generating a very fast and local pitting corrosion (Figure 3) [8].

Figure 3 : Rebars corroded by a chloride contamination [9].

In addition to the spoiling of the rebars themselves, with a diminution in their effective section, corrosion also damages surrounding concrete because of the volume change of corroded steel in the cathode zone. In function of the corrosion level of the rebar, concrete tensile strength and quality of the concrete-rebar bond, this can lead to cracking, spalling and, in drastic cases, concrete delaminations [12, 15, 19].

1.1.2 Pathologies leading to concrete disintegration

The disintegration of concrete can be the consequence of different deterioration mechanisms. Indeed, it can be induced by the physical stresses generated by freeze-thaw cycles as well as by chemical reaction such as the alkali-aggregate reactions or the sulphate reactions.

1.1.2.1 Freeze-thaw cycles

Freeze-thaw cycles may damage concrete if it is too porous and is able to absorb water. Indeed, concrete interstitial water will expand into pores close to the surface when transformed into ice and cause microcracking and localized stress in concrete matrix. A concrete submitted to a high number of freeze-thaw cycles can lose its whole cohesion.

A solution to avoid this problem is to use concrete with entrained air: this creates air bubbles inside concrete, in which water coming from the capillaries will have the possibility to expand without causing any damage [20]. Unfortunately, the presence of the bubbles also causes a strength decrease, seldom compatible with the resistance requirements for bridges [9].

Another solution to limit the damages due to freeze-thaw cycles is to use a concrete with a low water to cement ratio (inferior to 0.5); those high-strength concretes will indeed present a higher traction strength and lower porosity dimensions [8].

1.1.2.2 Alkali-aggregates reactions

Alkali-aggregates reactions can occur when specific aggregates containing reactive forms of silica react with potassium, sodium and calcium hydroxide from cement paste or from de-icing salts. The reaction produces a gel that takes place around the aggregates. When submitted to moisture, this gel expands, creating microcracks in the surrounding concrete, that becomes less and less impermeable and allows an increasing quantity of water to reach the aggregates [15, 21].

1.1.2.3 Sulphate reactions

This category regroups all reactions implying sulphate ions (SO_4^{2-}). These ions react with the cement compounds, resulting in the possible formation of two products: the ettringite and the thaumasite. The ettringite formation is a highly expansive phenomenon, which will cause cracking of the concrete. The thaumasite is not expansive, but it is formed to the detriment of tobermorite, which is the highest resistant cement paste compound. This results in concrete disaggregation [8].

As sources of sulphates, we can mention maritime environment, specific ground water, products storage, organic matter in decomposition and atmospheric pollution. Anyway, in some cases, the presence of sulphate reaction was observed without the presence of any of those factors, the sulphates coming then from the cement paste itself [18].

1.1.3 Concrete decay

This complex form of concrete degradation was first observed and named in 1985. Ever since, more than 70 cases have been diagnosed in Wallonia. It occurs in both reinforced and prestressed bridges, mostly in beam-type structures [9]. The concrete decay is a complex process, involving several simple pathologies: freeze-thaw cycles, alkali-aggregates reactions and chloride attacks… [9, 18]. In some situations, the decay of decks slabs can ultimately lead to their perforation (Figure 4 (a)) [8].

The phenomenon generally develops as a top-down process and creates two main types of degradation [8]:

- concrete disintegration at the upper surface of the slab, at the interface slab/preslab or at the bottom surface of the deck: only the granular framework is remaining.

- concrete delamination: the concrete degrades into a few millimetres thick leaves, essentially at the upper surface of the slab, creating horizontal cracks (Figure 4 (b)).

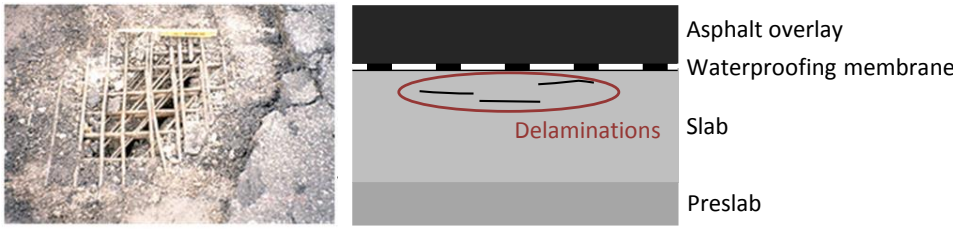

Figure 4 : Damages due to concrete decay [18, 22]
(a) Slab perforation (b) Delaminations location.

1.1.4 Degradations due to materials incompatibility or non-adhesive interfaces

Structural problems can be due to material degradation, but also to incompatibilities between different materials. This is true in new structures compounded of different materials in contact, but it is also a key factor in structural repair. The incompatibility can be chemical, thermal or mechanical (mainly due to a lack of surface preparation).

When two materials in contact are chemically incompatibles, this will induce a lack of adherence that will ultimately lead to the apparition of delaminations at the interface.

Thermal incompatibility happens when the dilatation coefficients of the materials are too different. This causes the apparition of high shearing stress at the interface when the structure is submitted to temperature variations [12].

The debonding of an interface can also be due to an improper surface preparation, causing a lack of mechanical strength at the interface. The surface preparation (for example sandblasting) should ensure a sufficient roughness to obtain a good interlocking without creating microcracks. Coupled with an adequate bonding agent, it insures a good transmission of the mechanical stresses between the materials and prevents the apparition of debonding [23, 24].

1.2 Non-destructive methods in civil engineering

When disorders are detected during the visual inspection of a bridge, specific detailed inspections are decided. During those inspections, the objective is to determine whether the structure is still suitable for its designed use: defects are detected and quantified so that maintenance and repair works can be planned. During those inspections, non-destructive techniques are more and more used as a complement to the destructive tests, allowing inspection of larger areas and reduction of the number of destructive core samples. [25].

In addition to the detection of defects, non-destructive testing can also be used on healthy structures, in order to estimate or check the building characteristics. This can be part of an assessment to evaluate the residual strength of an old structure, but can also be applied on new (or recently repaired) structures, in order to assess the respect of initial specifications of the client [11].

Two different objectives are often distinguished for non-destructive techniques: the material assessment and the structure geometry determination. Material assessment methods aim at determining the quality of concrete, the water content or the corrosion situation of the rebars, while the purpose of geometry determination methods is to determine the dimensions of the reinforced concrete structures.

Some methods are uniquely dedicated to the material characterization. An example is the Schmidt (or rebound) hammer, a spring loaded hammer used for estimating the compressive strength of surface concrete using the rebound height after striking the concrete surface [26, 27]. But many methods can be used for both the material and the geometrical characterization. Examples are the radar and gamma rays, whose propagations are linked to the concrete water content, or the ultrasounds, whose speed is related to the concrete compressive strength.

In this section, common non-destructive techniques used in the inspection and the characterization of concrete structures are presented, with a particular focus on the methods used for the geometry determination. The methods can be classified in two categories, depending on whether the measurement is based on electromagnetic (§ 1.2.1) or compressive (§ 1.2.2) waves. Finally, § 1.2.3 will detail the main applications of the Ground Penetrating Radar for the inspection of civil engineering structures.

1.2.1 Electromagnetic methods

Depending on their frequency, electromagnetic waves present totally different physical behaviour. For this reason, they are usually classified in different wave types: radio waves, infrareds, X-rays,… An overview of the approximate frequency range of all the waves types is displayed in Figure 5.

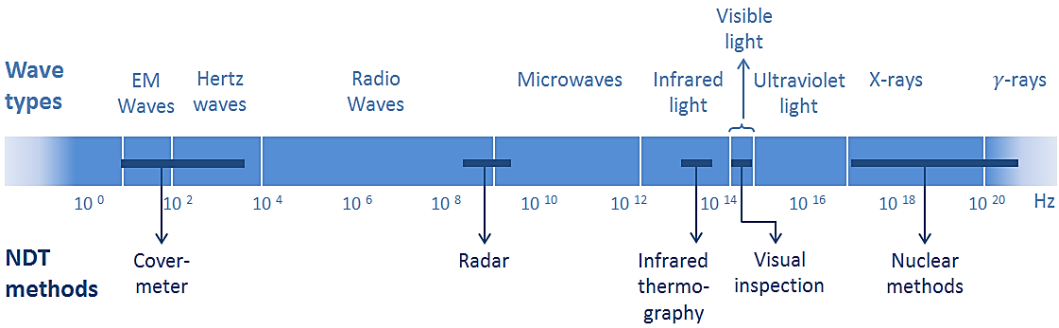

Figure 5 : Non-destructive techniques in the electromagnetic spectrum (after [26, 28]).

Many electromagnetic frequencies can be used in non-destructive testing (Figure 5). The most common methods (visual inspection, infrared thermography, ground penetrating radar, cover-meter and nuclear methods) are described in the following paragraphs. To this list, we could also add the microwaves non-destructive testing, which can be used for the evaluation of the moisture content [25].

1.2.1.1 Visual inspection

Any investigation campaign on a structure starts with a visual inspection. It can be considered as an electromagnetic method as the visible light and the colours correspond to a specific frequency range in the electromagnetic spectrum.

Visible indicators of problems are for example surface degradation, water leakage, movements or metal corrosion [15]. A relationship has been established between degradation of the slab near-to-surface layer of the and stains on the inferior surface, after a high number of cores drilling into damaged decks in Wallonia [8]: if visual inspection reveals signs of concrete distress, further investigation is necessary.

1.2.1.2 Infrared thermography

Infrared thermography is an electromagnetic method, whose useful wavelengths ($1\ \mu m - 100\ \mu m$) are intermediate between the visible spectrum and the radar spectrum [29]. Every surface emits an infrared radiation, whose amplitude will depend on the material, the surface condition, the observation angle, the distance and the temperature [30].

If all parameters are constant, the infrared thermography show local temperature variations, which can be due to the presence of voids beside the surface. Indeed, the thin air layer in the void acts as an insulator from the deeper concrete, and the delaminated surface will then warm up or cool down more quickly than the rest of the structure.

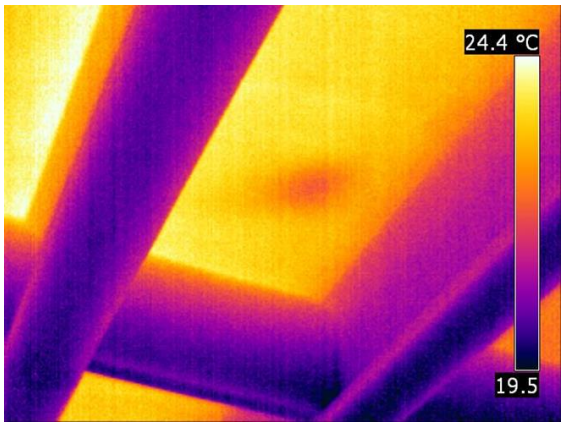

Figure 6 : Infrared detection of a defect in a concrete bridge deck [31].

With infrared thermography, large areas can be tested simultaneously. However, to be used successfully, it requires an external thermic solicitation (for example the sunrise or the sunset), and variations in the surface (if the whole bridge is delaminated, no defect will be detected. This method is particularly well adapted to detect adhesion defects after placing the waterproofing membrane and concrete delaminations [30, 32]. It will give a good estimation of the delaminations extent, but does not give indications about their depth [32].

1.2.1.3 Ground penetrating radar

The Ground Penetrating radar is an electromagnetic non-destructive method, using the frequency range 0.5-2.6 GHz for concrete testing. It is based on the reflection of short electromagnetic pulses on the interfaces inside the structure. Two main types of GPR antennas are distinguished: the contact antennas, maximizing the power of the transmitted waves, and the non-contact (horn) antennas, allowing fast material testing. The different uses of GPR in non-destructive inspection of concrete structures will be detailed in § 1.2.3.

1.2.1.4 Cover meter

The cover meter uses very low frequency electromagnetic waves (~ 0.05 - 5 kHz), using either eddy current effects or magnetic induction effects [33]. The probe creates a magnetic field, which will be affected in the presence of metallic reinforcement. Using this field variation, the device detects the rebars, but also determines their depth if their diameter is known (and vice-versa) [26]. The cover and the size of the rebars can also be simultaneously estimated using an adequate acquisition procedure. In combination with the GPR, the cover meter allows a very good determination of two layers of reinforcement [25].

1.2.1.5 Corrosion measurement

Different methods can be used to estimate the corrosion of the reinforcing rebars. Most of them use direct or low-frequency alternative electric current.

Zones of possible reinforcement corrosion can be detected by the half-cell potential mapping method, measuring the potential difference between the surface concrete and a reference electrode [26]. To obtain a quantitative estimation of the instantaneous corrosion rate, the linear polarization resistance (LPR) method can be used. In this technique, the corrosion equilibrium is disturbed by a counter electrode around the half-cell, insuring a homogeneous current distribution along the reinforcement in the inspected zone. Among numerous limitations [19], the main drawback of both methods is the fact that they need a connection to the reinforcement steel, which may require a localized drilling into concrete [34, 35].

1.2.1.6 Nuclear methods

The nuclear methods use the very high frequency X-rays and gamma rays. X-rays are produced by a specific electric device, while gamma rays are produced by a pellet of radioactive element. Their use in non-destructive testing mainly relies on the fact that their amplitude is highly attenuated in dense materials [26].

A first method to exploit the characteristics of nuclear rays is the radiography, high-scale equivalent to the medical examination technique. A photographic film is placed on the opposite side of the structure and allows a visualization of the denser zones (rebars) or voids [25, 26].

Radiometry uses the gamma rays. Unlike in radiography, the ray amplitudes variation are measured by a probe: the radiometer. This method can be used in transmission mode as the radiography, but also in backscatter mode, when only one side of the structure is accessible [27].

Those methods are complicated to apply, because of the heavy administrative procedure linked to the nuclear risk. X-rays are intrinsically less dangerous than gamma-rays and they also have the advantage to be produced by a generator that can be turned off and not by a permanently radioactive material. The x-rays main disadvantage is the low portability of the equipment [11, 26].

1.2.2 Methods based on sound waves

Sound waves, also called elastic or acoustic waves, need a medium to propagate. As shown in Figure 7, only a limited range of frequencies are actually audible to humans.

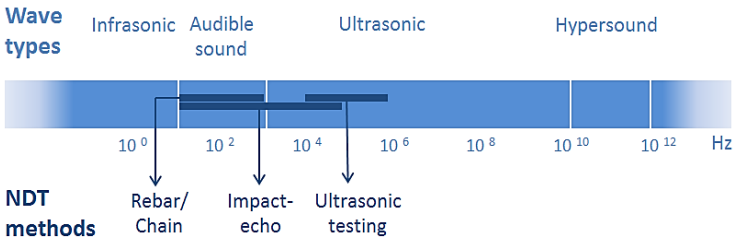

Figure 7 : Non-destructive techniques based on sound waves (after [26, 28, 36]).

In Figure 7, the frequency range of the most common non-destructive sound methods for concrete are represented. Unlike the electromagnetic methods, the frequencies excited by the different methods are not very different. The main difference lays in the method selected for the wave emission.

Two different types of sound waves are distinguished: the P-wave, or compressional wave, and the S-wave, or shear wave. The shear wave is also called the secondary wave, because its propagation speed is lower. Surface waves have specific (Rayleigh and Love) propagation modes [28, 37].

1.2.2.1 Metal rebar and chain dragging tests

Those methods are straightforward tests allowing detecting the presence and the extent of a delamination. The metal rebar test consists in hitting the concrete slab with a metal rebar. If the slab is delaminated, the shock will create a hollow sound, easily distinguishable from the sound obtained on an intact slab. If the concrete is covered by an overlay, it has to be exposed before the test. In some countries, the metal rebar is replaced by a heavy metal chain dragged on the exposed concrete in order to produce the hollow sound. With this alternative method, greater areas can be tested within a short time [30].

1.2.2.2 Impact echo

In the impact-echo method, the sound waves are generated by a steel sphere impact at the surface of the concrete and have a frequency inferior to 80 kHz. Wavelengths typically range from 5 cm to 2 m, which is sufficient to avoid detection of the natural heterogeneities of concrete. Waves reflect on interfaces between materials of different acoustic properties. Those interfaces are typically situated between concrete and air, concrete and water or concrete and steel. The acoustic properties of two different concretes are generally too slight to be detected; it means that the main applications are to detect voids and cracks or steel rebars inside concrete. [38].

The measured signal is transformed into the frequency domain through a fast Fourier transform (Figure 8). The resonance peak can be related to the reflection depth.

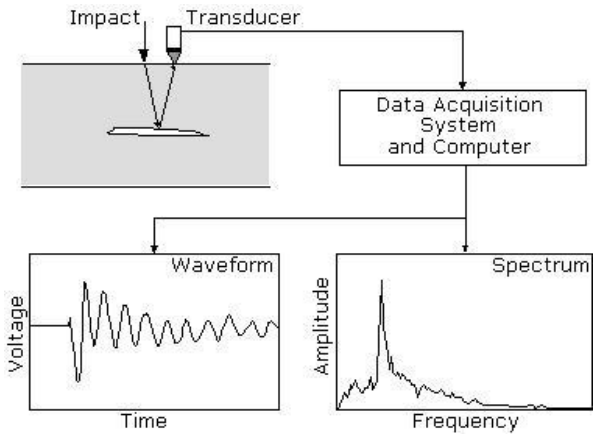

Figure 8 : Impact-Echo principle [36].

1.2.2.3 Ultrasonic testing

Different methods using ultrasonic waves for non-destructive testing have been developed. Two of them are more widespread: ultrasonic pulse echo (UPE) and ultrasonic pulse velocity (UPV) [11]. In both cases, the ultrasonic wave is emitted and measured by transducers transforming electrical energy into mechanical energy and vice-versa. The contact between the transducer and the concrete

surface has to be excellent. For this reason, the method will require a proper surface preparation and/or the use of a coupling agent.

In ultrasonic pulse echo method, the transducer emits a short pulse of ultrasonic wave. The wave propagates into the material and reflects on boundaries separating materials with different densities and elastic properties. The reflection time is estimated and the distance to the reflecting interface is calculated if the compressional wave speed is known [26, 28]. The method is particularly efficient to detect delaminations, discontinuities and small cracks, to detect compaction faults inside post-tensioning tendons or for measuring slab thickness [25, 27].

In the ultrasonic pulse velocity (UPV) method, the receiving transducer is coupled to the specimen at a known distance, so that the propagation speed can be deduced from the time interval between the transmission and reception of a pulse can. This speed can be correlated to the concrete quality and strength [26].

1.2.3 Ground penetrating radar inspection of structures

Ground Penetrating Radar (GPR), is a non-destructive evaluation technique used in soil, sediment and rock prospection since the sixties. It is frequently used for ice studies, archaeological or geophysical research and, since the eighties, it has been increasingly used in concrete elements characterization. Initial civil engineering applications included condition assessment of highway pavements and their foundations, with applications to structural concrete focussing on bridge decks inspection [39].

GPR is now recognized as a useful tool in concrete structures characterization. The widespread applications generally focus on the geometrical characterization of the structures: thickness [40], detection of defects such as delaminations or cracks, localization of reinforcing bars. Recent works also showed that radar could be used for the characterization of the material itself, which opens new application fields: detection of humid and salt-contaminated zones [41] or measurement of the water content [39, 42, 43]. In both geometry and material characterization, the qualitative detection of variations into the structure is of current application, while the quantitative estimation of properties is still subject of researches to improve the methods accuracy and robustness.

In this section, representative examples of studies focusing on the current main uses of GPR are detailed: rebars detection, layers thickness estimation and humid zones detection. The particular case of layer thickness determination will be detailed in § 1.3.

1.2.3.1 Detection of rebars

The detection of rebars with ground penetrating radar is relatively straightforward for the first layer of rebars. By a combination of GPR and cover meter, layers of reinforcement can even be differentiated [25]. From GPR measurement, the

distance between rebars can be precisely determined. The rebar depth can be estimated as well, but the precision is lower due to possible heterogeneities in the material or surface effects. The diameter of the rebars can be estimated as well, but it requires a sophisticated analysis (for example an artificial neuronal network) and the precision remains lower [44]. A better solution for diameter estimation is to use a cover meter in combination with the radar.

As an illustration of the possibilities of detection of rebars with GPR, Figure 10 displays a profile that we measured on a prestressed box girder concrete bridge (Figure 9 (a)) in Kirchberg, Luxembourg, in June 2010. The objective of the test was to determine the position and quantity of reinforcement and prestressing cables in the bottom part of the bridge. The profile measurement was facilitated by the fact that the space under the bridge had been partially backfilled in prevision to the upcoming bridge demolition (Figure 9 (b)). The profiles were performed close to the zone where the bridge would be cut (represented by the red paint line in Figure 9 (c)). The resulting profiles are displayed in Figure 10.

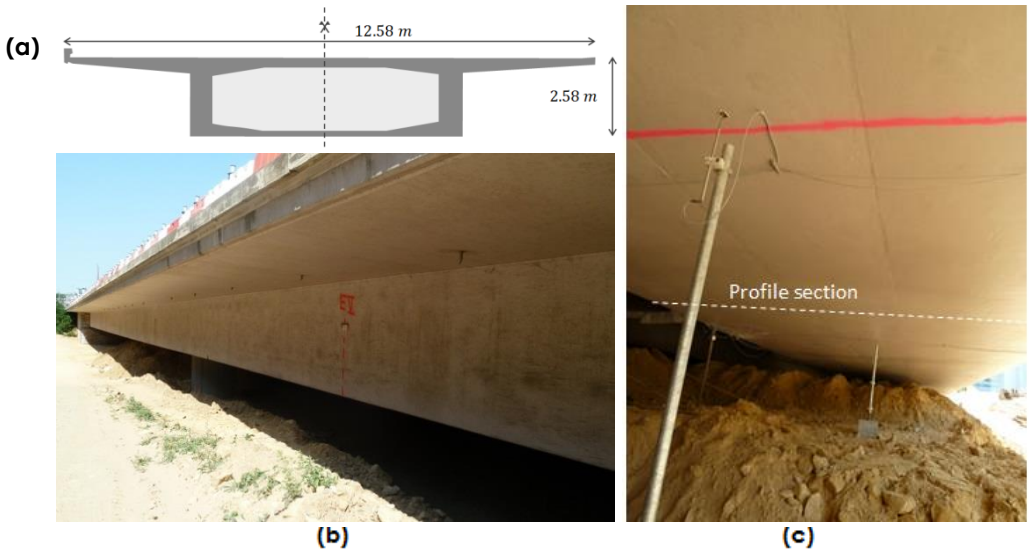

Figure 9 : Tested bridge (a) section;
(b) lateral view; (c) deck bottom view, with the profile line.

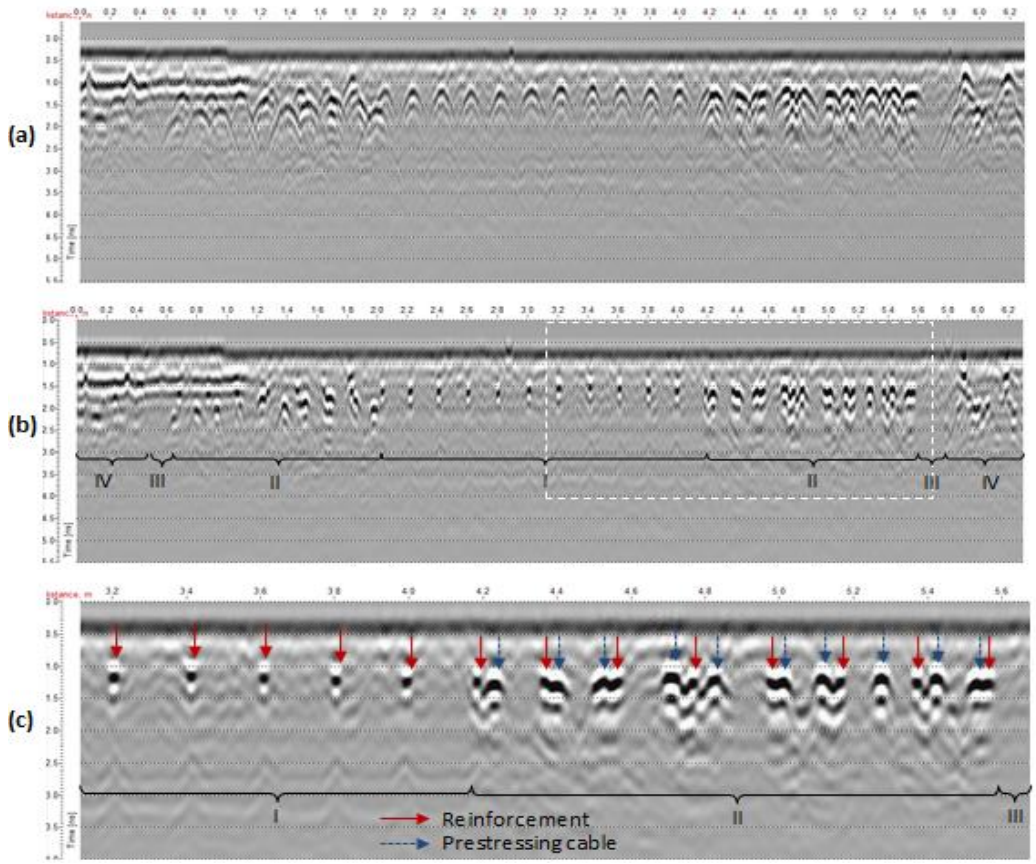

Figure 10 : Profile measured on the bottom of a prestressed bridge. (a) Raw measurement; (b) after signal treatment (migration), detection of different rebars zones; (c) zoom on the limit between zones I and II and differentiation of the two types of reinforcement.

In Figure 10 (a), the raw signal measured by the radar is represented. The same profile, after signal treatment (time zero adjustment and migration F-K), is displayed in Figure 10 (b) and Figure 10 (c), in which a part of the radargram is enlarged. After this signal treatment, the prestressing cables are distinguishable from the reinforcing bars because their reflection keeps a curvature: their diameter is too important to appear as punctual.

This distinction can be observed in the zones situated in the centre of the deck (Zones I and II), hyperbolas corresponding to reinforcing bars are visible every 20 cm, at a depth of about 6 cm. In Zone II (1-2.5 m from the centre), prestressing cables are detected as well. They are situated a little deeper than the reinforcing rebars (at about 8 cm), with more important depth variations. We evaluated their number to 10 on each side of the bridge.

1.2.3.2 GPR thickness determination

The ground penetrating radar is one of the most popular methods for the thickness determination of structure elements, and in particular to estimate the thickness of road asphalt overlays [30].

Many papers tackle this problem [40, 45-47]. The method adopted by most authors consists in measuring in the radargram the time of the reflection on the different interfaces (Figure 11 (a)). To transform this information on depth estimation, an estimation of the wave speed is needed. The wave speed mainly depends on the dielectric permittivity (see § 2.1.2), which can be evaluated on the basis the amplitude reflected on the different interfaces. The GPR antennas generally used for those tests are air-launched horn antennas, which can be mounted on cars for automatic measurements at a relatively high speed (up to 100 km/h) [46].

In Figure 11 (b), Hugenschmidt [45] compares the asphalt thickness estimated by GPR with a 1.2 GHz contact antenna to the actual thickness, measured during pavement removal operations. He showed that the error was small (inferior to 11 mm for the tested structures). The validity of the all-GPR measurements for asphalt thickness estimation was also confirmed by Loizos [47].

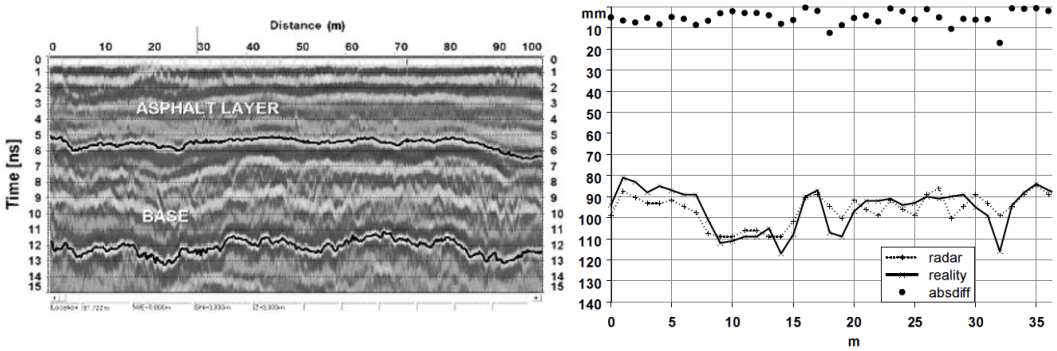

Figure 11 : (a) Example of road survey displaying the interfaces between the different layers [47]. (b) Comparison of the asphalt thickness estimated by GPR measurements to the real one [45].

1.2.3.3 Detection of humid zones

A good example of the possibilities opened by GPR utilization on concrete structures is given by Perez-Gracia [48] for the inspection of the reinforced concrete base of a block of flats. The slabs of the underground parking of the buildings showed evidence of moisture and numerous cracks were visible at the surface. Forty different GPR profiles were recorded in the building.

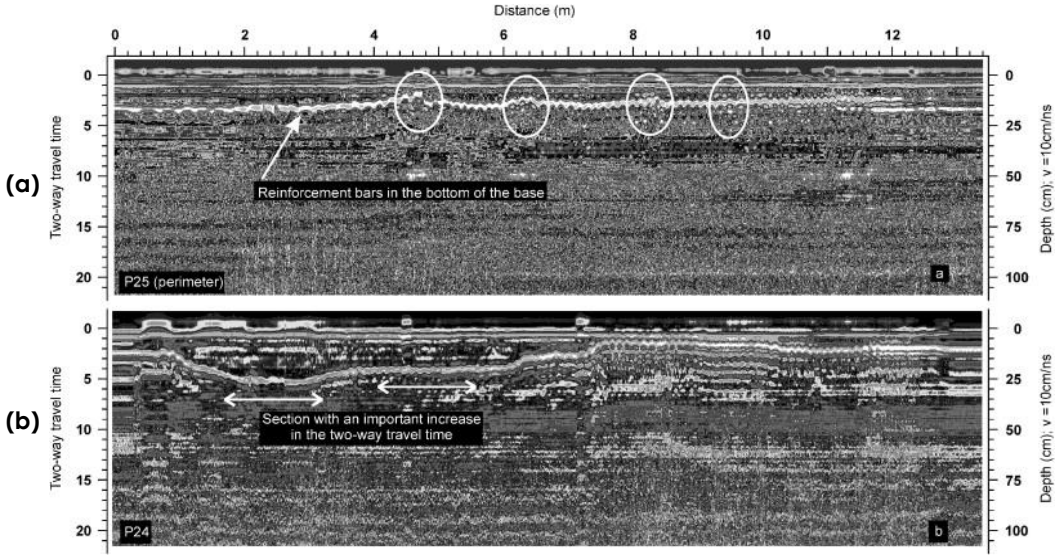

Figure 12 : Profiles showing evidence of (a) cracks and (b) humid zones [48].

On each profile, the reinforcement bars situated at the bottom of the slabs were clearly visible. Faults and cracks appeared as local changes of the time associated to the rebars, indicated by white circles on profile P25 (Figure 12 (a)). The humidity causes a decrease of the concrete speed and thus increases the two-way travel time. This is clearly visible on the scan P24 (Figure 12 (b)).

With those radar results, it was possible to create maps of the cracks (indicated by black points on Figure 13 (a)). If some of the detected cracks correspond to visible cracks on the surface (reported as grey lines), a majority of them weren't visible. A map of the humid zones was also drawn (Figure 13 (b)) and the presence of a shallow water table, probably responsible for the humidity problems, was also revealed.

(a)

(b)

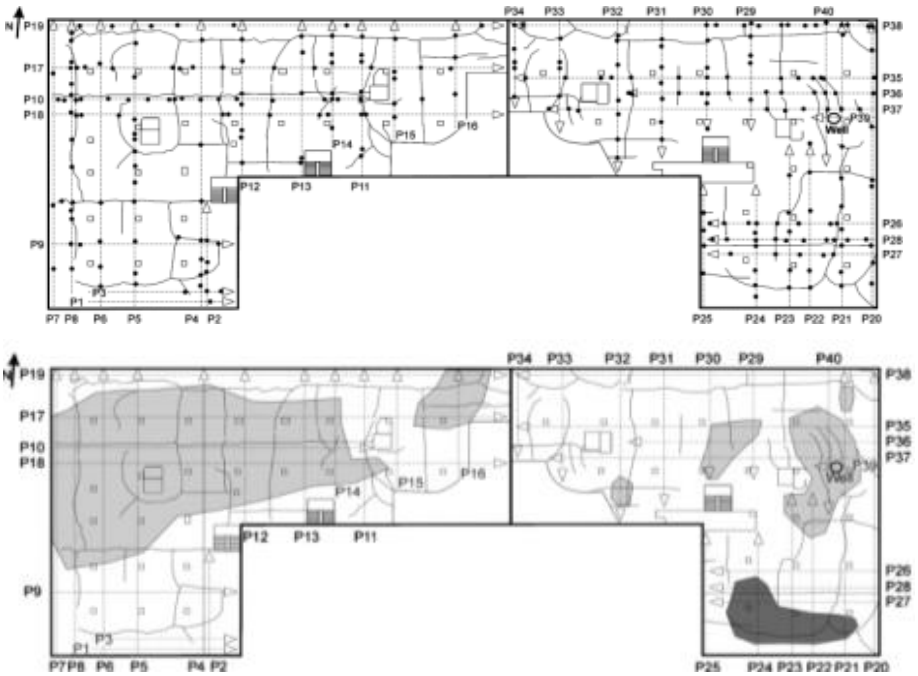

Figure 13 : Maps of (a) points with evidence of cracks (b) humid zones [48].

In addition, this GPR inspection of the slabs permitted to detect variations in the slab thickness. To distinguish them from the wet zones, the authors used the different frequency content of the radargrams.

1.3 GPR detection of thin layers

Among all the non-destructive methods, the Ground Penetrating Radar is well adapted to inspect multilayer structures because only a percentage (about 50%) of the energy is reflected at every interface. An inspection can thus reveal the thickness and electromagnetic properties of two layers or more, if the conditions are favourable [40], as shown in §1.2.3.2. This is not possible with other non-destructive techniques such as impact-echo or ultrasonic testing, because they use stress waves which have an air-concrete reflection coefficient almost equal to 100%.

But when the considered layer is thin, the radar waves reflections on both interfaces of the thin layer generate a complex global reflection which can be hard to recognize and interpret for the radar user. In this situation, the layer is detected but a deeper analysis of the signal is required for a quantitative estimation of its properties. Different researches are currently led to achieve this goal, and the objective of this thesis is to contribute to the development of a fast method for the thin layers characterization.

The first part of this section (§ 1.3.1) will describe different situations in which thin layers are present in civil structures. In the second part (§ 1.3.2) we will present a

brief literature review for the different methods allowing to determine thin layers into concrete with GPR.

1.3.1 Thin layers in civil engineering structures

In many structures, features presenting a small thickness to surface ratio are relatively common. Almost every soil or wall in recent commercial, residential or industrial building is constituted of multiple layers of different materials: concrete, bricks, wood, plaster, insulation material, waterproofing membrane, air… Each one of the different layers is selected to bring to the element the required properties in resistance, but also insulation, waterproofness and appearance.

The layered structures are also widespread in civil engineering structures, and especially in the roads and bridges design [49]. Concrete bridge decks are typically compounded of a concrete slab (sometimes casted on concrete pre-slabs), covered by an asphalt overlay. Between those layers, all modern bridges include a waterproofing layer, to prevent the (de-icing salts contaminated) water penetration into the concrete. In Wallonia, the waterproofing layer can consist of casted asphalt (for a thickness of 15 mm), bituminous sheets or resin [30] (Figure 14).

(a) **(b)** **(c)**

Figure 14 : Different types of waterproofing layers used on the bridges in Wallonia : (a) Casted asphalt; (b) Bituminous sheet and (c) resin [30].

The waterproofing layer, presenting usually a thickness inferior to 5 mm, is a vital element for the durability of the bridge. Indeed, all the concrete degradation mechanisms (freeze-thaw cycles, corrosion, alkali-aggregate reactions, …) require the presence of water to develop [12, 18, 50]. Detecting problems in the waterproofing membrane can thus help to prevent many degradation mechanisms.

If the defects into the membrane may be difficult to detect due to their small lateral extension, the presence of a problem may still be detected using the difference of properties of the concrete under the membrane. Indeed, a wet zone in the underlying concrete will have a larger extension, especially after a rain event.

At another scale, thin layers into concrete can be caused by some degradation mechanisms, and especially the concrete decay (§ 1.1.3). Indeed, one of the consequences of this pathology is the apparition of concrete delaminations at the upper surface of the slab: the concrete degrades into a few millimetres thick leaves, creating horizontal cracks [8]. The horizontal delaminations caused by concrete decay can be considered as well as very thin layers appearing in the structure. Their thickness is usually very low (<1 mm), but can sometimes rise up to a few millimetres, as can be observed in Figure 15.

(a) (b)

Figure 15 : (a) Concrete core drilled from a bridge deck; (b) View from the surface of the corresponding hole (Photo P. Gilles (SPW)).

After raining events, those delaminations are usually preferential paths of water penetration into the concrete, creating horizontal wet zones that can be sometimes more easily detected with radar.

1.3.2 Thin layers resolution with GPR

In order to illustrate the difficulty of thin layer detection with GPR, the measurements performed on three samples representing a road structure are displayed in Figure 16. For each sample, the bottom material is a concrete slab, with a thickness of 10 cm, and the surface material is a 7 cm asphalt overlay. In the first case, the materials are directly in contact. In the second case they are separated by a 4.5 mm waterproofing bituminous layer. In the last sample, a local defect (air void with a thickness of 3.9 mm) was created at the concrete surface before laying the bitumen, to simulate the presence of a delamination.

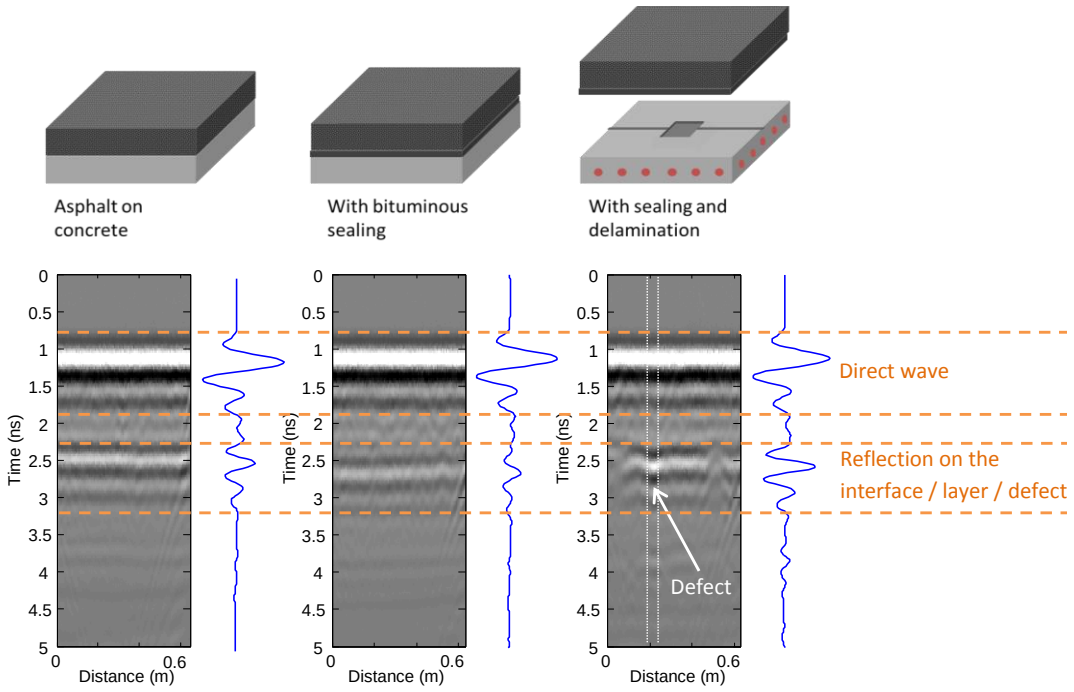

Figure 16 : Example of GPR measurements performed on layered samples, with the presence of different thin layers.

In Figure 16, it is visible that the reflection with and without the bituminous layer are different, but the presence of the bituminous layer could not be deduced from the signal without a deeper analysis than a visual inspection. The presence of the defect under the sealing layer is visible, thanks to a brutal change of the reflected amplitude. Nevertheless a further analysis would be required to characterize the nature and thickness of the defect.

The exact equation for a reflection from a single embedded layer and considering simple harmonic waves was reported by Rayleigh [51]. The extension of this theory to seismic wavelets was then proposed by Widess [52], who set the limit of thin layers to $\lambda/8$ and observed linearity between the layer thickness and the reflected amplitude.

To detect and determine thin layers with ground penetrating radars, or more generally to try determining a layered medium, different approaches have been considered in the literature:

- Ray-tracing method;
- Inversion of the reflection spectral content;
- Full waveform inversion.

Each one of these methods has been used and improved by different authors and given successful results under specific conditions. They will be briefly introduced in the next sections.

1.3.2.1 Ray-tracing method

The ray-tracing method is based on the analysis of the reflection time and amplitude. It approximates the wave propagation to a propagation as geometrical optical rays. This method allows to estimate the propagation time into the medium and to use the physical laws ruling optical reflection and refraction (for example Fresnel reflection coefficients of Snell's refraction law). The ray-based method is only valid for low-conductivity, non-magnetic materials and does not take into account the wave phenomena as diffraction or polarization [53].

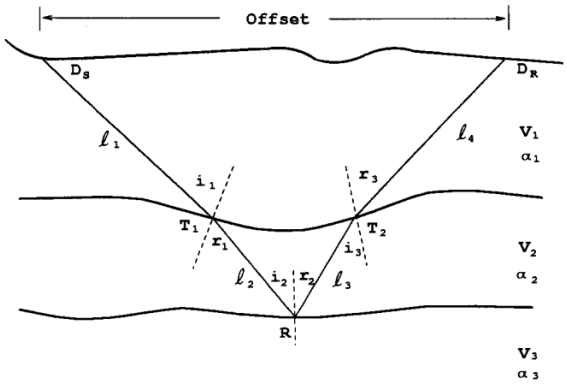

Figure 17 : Typical ray path in a three layers medium [53].

This is the most direct way to analyze the radargrams registered with GPR. The time, and possibly the amplitude, of the reflections measured in the radargram are evaluated and are directly used to determine the thickness and permittivity of the different layers. A good example is given by Al-Qadi [40], who applied this method to the determination of a road structure.

If thin layers are involved, the different reflection events overlap in the radargram and this method cannot be directly used. But the interferences generated by the thin layers can be taken into account by specific equations [54]. This requires the presence of the thin layer to be suspected by the user (for example through core drilling) before analyzing the signal.

Ray-based methods are often derived from seismic techniques. Indeed, the acoustic waves propagate as rays and most acquisition procedures can be adapted for radar inspection. This is the case of the profile measurements, in which the underground is measured by moving the antennas along the surface, but also of common mid points (CMP) measurements, performed by moving away the two antennas. This method allows obtaining a range of offsets and incident angles.

1.3.2.2 Inversion of the reflection spectral content

This method studies the reflection of GPR waves on thin layers, and in particular the variations of the amplitude and phase versus offset (APVO) curves. The high dependence of the reflection coefficient on the layer properties and thickness

can lead to the determination of those properties on the basis of measurements with a variable offset.

The extension of this method, initially developed for seismic data, was initially suggested by Bradford and Deeds [55], who used the amplitude versus offset (AVO) curves to detect pollutant plumes over water table. Other authors suggested to exploit all the frequency range of the radar wavelet, for a single reflection. They determined thin-bed fractures using the amplitude versus frequency [56] or the amplitude and phase versus frequency [57] curves. They also introduced the frequency dependence of the material properties through a Jonscher formulation (see Appendix 2). Deparis [58, 59] successfully combined both approaches, inverting the APVO curves for different frequencies in order to characterize thin fractures in limestone formations.

1.3.2.3 Full waveform inversion

One of the most recent and promising method for the determination of thin layers with GPR is the full waveform inversion (FWI). With this method, the forward model aims at fitting the whole GPR waveform, and not only a single parameter such as the amplitude of a reflection event. It has been used successfully to determine the properties of layered soils and concrete slabs [60, 61].

This method requires an excellent knowledge of the incident signal emitted by the radar. For this reason, its first developments included the use of horn, off-ground antennas, for which the near-field effects can be neglected. The antenna has to be calibrated over a metallic plane [60]. To avoid the computation of the signal Fourier transforms, the measurements can be performed using a succession of continuous sine wave of various frequencies.

Recently, the FWI has been applied to the determination of concrete structures. Patriarca [62] used the FWI to estimate the dielectric parameters of concrete slabs and their thickness. He managed to simulate the full waveform response of a crack into concrete and to determine the depth and aperture of a crack whose filling properties were known. In [61], Kalogeropoulos used a bistatic horn antennas to estimate the chlorides and moisture contents in concrete slabs.

Bush [63] tackled the problem of the FWI with on-ground antennas, for geologic applications. The coupling of the antennas with the surface highly influences the incident wavelet. For this reason, the inversion process includes an explicit optimization of the effective source wavelet.

The issue of near-field, on-ground radar was also tackled by Lambot [64], who modeled radar antennas using an equivalent set of infinitesimal electric dipoles. After a complex calibration of the antennas over a metallic plate, the inversion of results registered by on-ground antennas revealed to be possible. Nevertheless, the concordance between real and modeled results are less satisfactory than with sine signals and horn antennas.

Chapter 2: Ground Penetrating Radar theory

In the first chapter, different current uses of ground penetrating radar (GPR) were presented, as well as the different methods used to determine thin layers thickness. In this second chapter, the theoretical principles related to this work are presented. In the first section (§ 2.1), we present the global wave propagation theory. In the second one (§ 2.2), the equations of the reflection coefficient of thin layers are developed. Those equations will be used in Chapter 5 to estimate the layer thickness from experimental and numerical tests. Finally, in § 2.3, the principles of the finite difference time domain (FDTD) are presented. This numerical method will be used all along the thesis to perform simulations.

2.1 Physical properties of radar waves

The GPR principle is to create, with an emitter antenna, very short pulses of electromagnetic waves which propagate through the medium in all directions (or in the half-space downward only, if the antenna is shielded). They reflect on the interfaces between materials of different electromagnetic properties. At the surface, a receiver antenna measures the amplitude of the signal over time (Figure 1). Each measurement made by the receiving antenna is called a sample. The set of all the samples collected at the same point is called a trace or a scan in which both the direct wave and the waves reflected on the different interfaces can be observed.

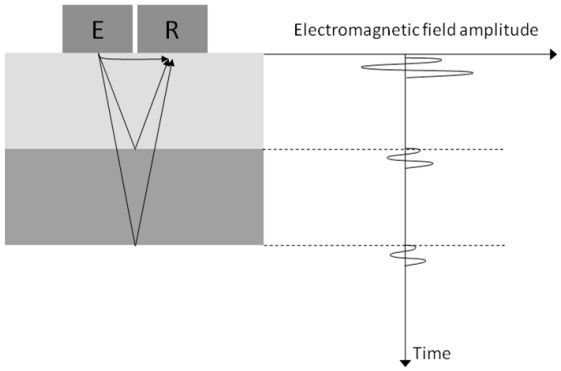

Figure 18: Simplified GPR trace measured on a two-layer structure.

In electromagnetic spectrum, radar frequencies range from 100 MHz to 100 GHz. For geological applications, in which penetration depth has to be quite important, frequencies of antennas are generally inferior to 500 MHz. For civil engineering applications, useful central frequencies can rise up to 2.6 GHz [44, 65].

2.1.1 Propagation of electromagnetic waves

GPR waves are electromagnetic waves, whose behaviour can be described using two different sets of relationships: Maxwell's equations and the constitutive equations. Only Maxwell's equations are exact: the constitutive equations are only accurate for isotropic linear materials. Nevertheless, they can be used as good approximations to solve Maxwell's equations [66].

2.1.1.1 Maxwell's equations

The four Maxwell's equations describe the relationships linking the different fields and properties in a dielectric environment submitted to a magnetic field.

$$\nabla \times \vec{E} = -\frac{\partial \vec{B}}{\partial t} \tag{3}$$

$$\nabla \times \vec{H} = \vec{j} + \frac{\partial \vec{D}}{\partial t} \tag{4}$$

$$\nabla \cdot \vec{D} = \rho \tag{5}$$

$$\nabla \cdot \vec{B} = 0 \tag{6}$$

In those equations,

- $\vec{E}$ is the electric field strength vector (V/m);
- $\vec{B}$ is the magnetic flux density vector;

- $\vec{H}$ is the magnetic field vector (A/m);
- $\vec{J}$ is the electric current density vector (A/m²);
- $\vec{D}$ is the electric displacement vector (C/m²);
- ρ is the electric charge density (C/m²);
- t is the time (s).

The first equation (3) is Faraday's law and expresses that a varying magnetic field generates a closed loop electric field. The second equation (4) reflects Ampere's law and describes that an electric current gives rise to a magnetic field. The third equation (5) expresses that any electric displacement $\vec{D}$ starts or ends on an electric charge, which means that any electric field should terminate on a charge or form closed loops. The last equation (6) expresses the fact that magnetic charges do not exist: all the flux loops are closed [67].

2.1.1.2 Description of the constitutive equations

In addition to Maxell's equations, the physical properties of the materials and the electromagnetic field are also related by three constitutive equations:

$$\vec{J} = \sigma . \vec{E} \tag{7}$$

$$\vec{D} = \varepsilon . \vec{E} \tag{8}$$

$$\vec{B} = \mu . \vec{H} \tag{9}$$

Where:

- σ is the electric conductivity (S/m)
- ε is the dielectric permittivity (F/m)
- μ is the magnetic permeability (H/m)

In equations (7), (8) and (9), σ, ε and μ are scalars only if the material is homogeneous, linear, isotropic, time-invariant, nondispersive and nonmagnetic. Otherwise, they should be expressed as complex functions of the vector position (if the material is not isotropic and homogeneous) and of the frequency if the material is dispersive. This will be the case for many applications in radar (see § 2.1.6).

Equation (7) describes how free charges flow to form a current when an electric field is present. In concrete, electric conductivity is linked to the number, the charge and the speed of ionic particles moving under the electric field action and to the concrete porous structure characteristics.

Equation (8) describes how constrained charges are displaced in response to an electric field. This movement creates a dielectric displacement current.

The last constitutive equation (9), describes the magnetic field influence on intrinsic atomic and molecular magnetic moments. Concrete being a non-magnetic material, μ is equal to μ_0, void permeability [54].

In dispersive materials, the conductivity and permittivity are complex values and depend on the frequency (f).

$$\sigma(\omega) = \sigma'(\omega) + i\sigma''(\omega) \tag{10}$$

$$\varepsilon(\omega) = \varepsilon'(\omega) - i\varepsilon''(\omega) \tag{11}$$

Where:

- $\omega = 2\pi f$ (12)

- $i^2 = -1$ (13)

In the radar frequency range, it is impossible to experimentally distinguish the contribution of electric conductivity from that of dielectric permittivity in the total current density. Therefore, effective parameters σ_e and ε_e are defined to take into account both effects [44]:

$$\varepsilon_e = (\varepsilon_e' - i\varepsilon_e'') = \left(\varepsilon' + \frac{\sigma''}{\omega}\right) - i\left(\varepsilon'' + \frac{\sigma'}{\omega}\right) \tag{14}$$

$$\sigma_e = (\sigma_e' + i\sigma_e'') = (\sigma' + \omega\varepsilon'') + i(\sigma'' + \omega\varepsilon') \tag{15}$$

Generally speaking, σ and ε are tensors and can be non linear. Indeed, they can be dependent on electric field magnitude and direction. Anyway, for GPR applications, those parameters are generally treated as field independent scalar quantities [54]. Experimental works proved that this assumption is close to reality when high frequencies are employed [68].

Consequently, in (7), total current density $\vec{j}$ generated by the application of the electric field $\vec{E}$ can be expressed as a function of effective conductivity or effective permittivity:

$$\vec{j} = \sigma_e\vec{E} = i\omega\varepsilon_e\vec{E} \tag{16}$$

Permittivity is usually expressed as a relative value, when divided by ε_0 (void permittivity):

$$\varepsilon_r = \frac{\varepsilon_e}{\varepsilon_0} = \varepsilon_r' - i\varepsilon_r'' \tag{17}$$

The imaginary part of relative permittivity, ε_r'', represents energy losses by absorption, resulting from combined effects of σ' and ε''. The real part ε_r' represents the material capacity to accumulate electric energy by electric polarization. It is usually defined as the concrete dielectric constant. In radar frequency range, the polarization can be induced by different mechanisms [69]:

- electronic polarization due to the distortion of the electronic cortege of an atom with respect to its nucleus;
- ionic polarization due to the relative motion of anions and cations within a crystalline structure;
- dipole polarization, linked to water molecules in concrete constituting permanent dipoles;
- interfacial polarization, linked to charge accumulation at solid-liquid interfaces.

The first two phenomena are applicable to all solids. In case of concrete, they dominate in the absence of dipole particles i.e. in dry conditions. In presence of water, dipole polarization, which is related to water content, has the greatest importance and electronic and ionic polarization can be neglected. The dominating influence of water content on relative permittivity was experimentally confirmed by Soustos [68].

Interfacial polarization is linked to the ionic concentration in interstitial solution but is characterized by very low relaxation frequencies (1-100 KHz). At radar frequencies, it does not have time to settle and does not contribute to the total permittivity, even if it has a great influence on conductivity [69].

2.1.2 Speed of electromagnetic waves

By introducing the constitutive equations (7), (8) and (9) into Maxwell's equations (3) and (4), it is possible to obtain a differential equation describing the spatial/temporal variations of the electric field [54]:

$$\vec{\nabla} \times \vec{\nabla} \times \vec{E} + \mu\sigma\frac{\partial \vec{E}}{\partial t} + \mu\varepsilon\frac{\partial^2 \vec{E}}{\partial t^2} = 0 \tag{18}$$

The electric field $\vec{E}$ can be expressed as a function of the time:

$$\vec{E} = f(\vec{r} \cdot \vec{k}, t)\hat{u} \tag{19}$$

In (19), $\vec{k}$ is the propagation direction, $\vec{r}$ is the spacial position, t is the time and $\hat{u}$ is an orthogonal vector. The respective positions of the different vectors are represented in Figure 19.

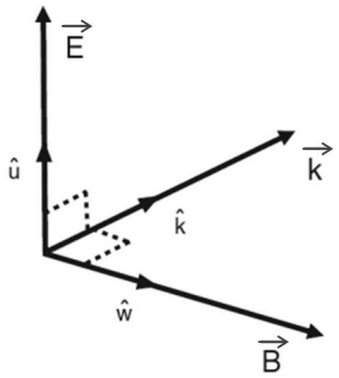

Figure 19 : The electric field, $\vec{E}$, magnetic field, $\vec{B}$ and the propagation direction, $\vec{k}$ are orthogonal. $\hat{u}$,$\hat{w}$ and $\hat{\vec{k}}$ are orthogonal unit vectors [70].

If we introduce $\beta = \vec{r} \cdot \vec{k}$, the scalar distance in the direction that the field varies, (19) becomes:

$$\vec{E} = f(\beta, t)\hat{u} \tag{20}$$

In (20), β is the scalar distance in the field variation direction and $\hat{u}$ is an orthogonal vector. Introducing (20) into equation (18) leads to a differential equation of the second order [54]:

$$\frac{\partial^2}{\partial \beta^2} f(\beta, t) - \mu\sigma \frac{\partial}{\partial t} f(\beta, t) - \mu\varepsilon \frac{\partial^2}{\partial t^2} f(\beta, t) \equiv 0 \tag{21}$$

This equation can be simplified if the propagation medium can be considered as a low loss environment, in which the attenuation losses can be neglected. The criterion for a low loss environment, with ω the angular velocity (12), is [71]:

$$\frac{\sigma}{\varepsilon\omega} \ll 1 \tag{22}$$

Concrete, in radar frequency range, can often be considered as a low loss medium [54]. Under this low loss condition, the differential equation (21) can be solved [54] and we have:

$$v = \frac{1}{\sqrt{\varepsilon\mu}} \tag{23}$$

If we are considering a non-magnetic material, $\mu = \mu_0$ and $\varepsilon = \varepsilon_r \varepsilon_0$. Even reinforced concrete can be considered as non-magnetic because the waves only travel into the concrete, the rebars being perfect reflectors. By introducing the speed of light

$$c = \frac{1}{\sqrt{\varepsilon_0 \mu_0}} = 0.3\ m/ns \tag{24}$$

and neglecting the effects of the imaginary part of the effective dielectric permittivity ε_r'', which is possible because concrete is a low-loss medium, the wave velocity can be finally approximated as:

$$v = \frac{c}{\sqrt{\varepsilon_r'}} \tag{25}$$

Table 1 gives typical values of relative permittivity, conductivity and velocity for common geological materials and the different materials that will be encountered during this thesis.

Table 1 : Typical relative permittivity, electrical conductivity and velocity for common soil, rocks and building materials [13, 54, 68, 72-74].

Material	ε_r'	σ (mS/m)	v (m/ns)
Air	1	0	0.30
Distilled water	80	0.01	0.033
Fresh water	80	0.5	0.033
Sea water	80	3000	0.01
Dry sand	3-5	0.01	0.15
Saturated sand	20-30	1-10	0.06
Limestone	4-16	0.5-2	0.075-0.15
Silts	5-30	1-100	0.05-0.13
Clays	5-40	2-1000	0.05-0.13
Granite	4-7	0.01-1	0.11-0.15
Concrete	4-10	1-100	0.09-0.15
Polystyrene	2.6	$<10^{-10}$	0.19
Polyethylene	2.3	$<10^{-10}$	0.20
Bitumen	2.6 – 2.8	$<10^{-10}$	0.179-0.186

For concrete, the main factors influencing the dielectric permittivity are its water content and the frequency. This was proven by Soustos et al. [68], who performed tests by direct measurement on concrete with a coaxial transmission line. They

showed that the influence of frequency is weak for high frequencies, while the concrete conductivity increases linearly with frequency (Figure 20).

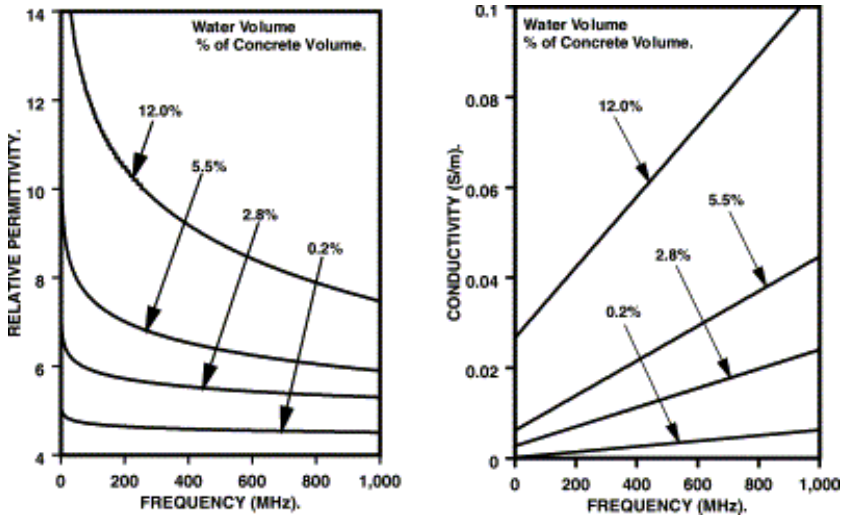

Figure 20 : Typical variations of permittivity and conductivity with frequency and moisture content [68].

They also proved that cement type and concrete strength had a minor influence on the dielectric properties of concrete, especially with regard to its relative permittivity. The main influent factor turned out to be the water content of the samples, whose influence on permittivity can be considered as linear (Figure 21).

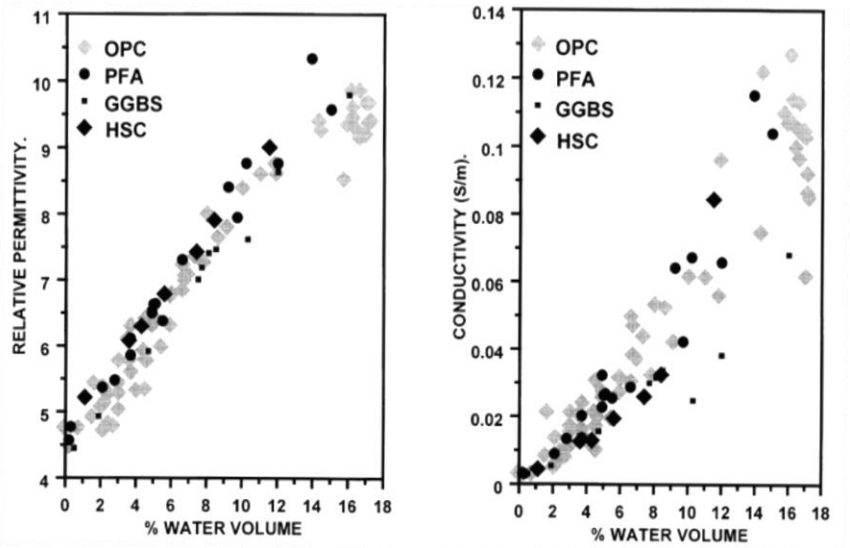

Figure 21 : Influence of water content on dielectric properties [68].

2.1.3 Ground Penetrating Radar acquisition methods

When inspecting the ground or a structure with GPR, different acquisition methods are distinguished, depending on the antennas configuration. A first distinction is made between the transmission mode, in which the waves travel

directly from one antenna to the other through the structure, and the reflection mode, using the reflection inside the material to transmit the waves from one antenna to the other one. The transmission mode requires that both sides of the structure are accessible, which is seldom the case in reality. For this reason, the reflection mode is far more widespread, and transmission modes will not be considered in this work.

In the reflection mode, two different configurations are frequently used. In the first one, the profile scanning, the transmitter and the receiver are moved together along the surface. This enables to obtain a direct representation of the subsurface. The second acquisition mode is the common mid point (CMP). It uses varying distance between the antennas. With this method, a single point of the structure is tested, to evaluate the speed of the waves or to detect a local reflector.

These two acquisition methods (Profiles scanning and CMP measurements) will be briefly presented in § 2.1.3.1 and § 2.1.3.2. Finally, in § 2.1.3.3, we will describe how the relative position of the antennas determines the propagation mode of the waves (transverse electric or magnetic).

2.1.3.1 Profile scanning

In this radar auscultation method, the transmitter and the receiver are moved together along a defined line of the structure surface. The user selects the spatial interval separating all the traces recordings. All the scans taken together and represented as a function of their position constitute a profile (Figure 22). This is the most common radar auscultation method, and is also referred to as common offset test (the offset is the distance between the transmitter and the receiver).

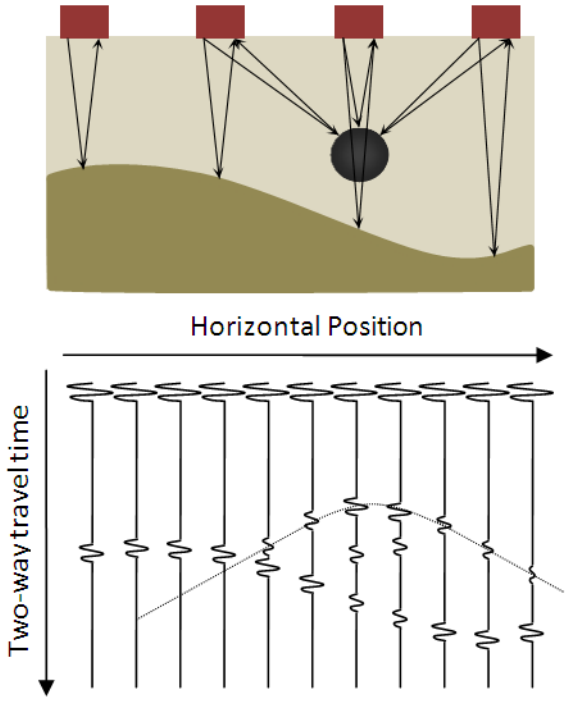

Figure 22 : Profile acquisition principle.

In a profile, many quantitative properties of the inspected structure or ground can be directly observed. Indeed, the interfaces are directly observable. The local features, however, appear in the radargram as hyperbolas, because they are already visible before being just over the features, and are still visible further. The shape of hyperbolas can help determining the dielectric properties of the material (§ 3.3.1.3).

If the antennas offset is known, the depth of the reflection z can be deduced from the two-way travel time t displayed on the radargram:

$$z = \frac{\sqrt{t^2 v^2 - x^2}}{2} \tag{26}$$

If the antennas offset x is small by comparison to the depth of the target z, this equation becomes simply:

$$z = \frac{t\,v}{2} \tag{27}$$

2.1.3.2 Common mid point (CMP) measurement

The other mode of acquisition is the CMP, in which the reflection point remains constant and the offset is gradually increased (Figure 23).

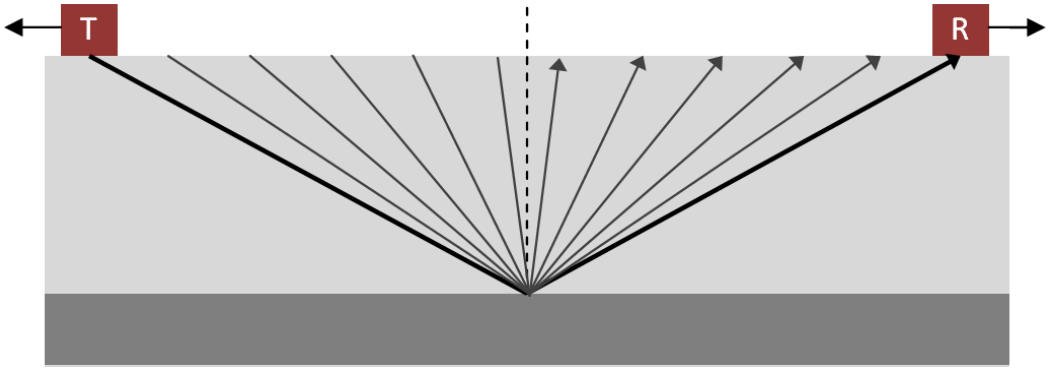

Figure 23 : CMP acquisition principle.

Figure 24 (a) represents a CMP radargram obtained by 2D FDTD simulations performed with GprMax [75]. In this radargram, we can recognize characteristic waves, corresponding to different paths between the antennas (Figure 24 (b)).

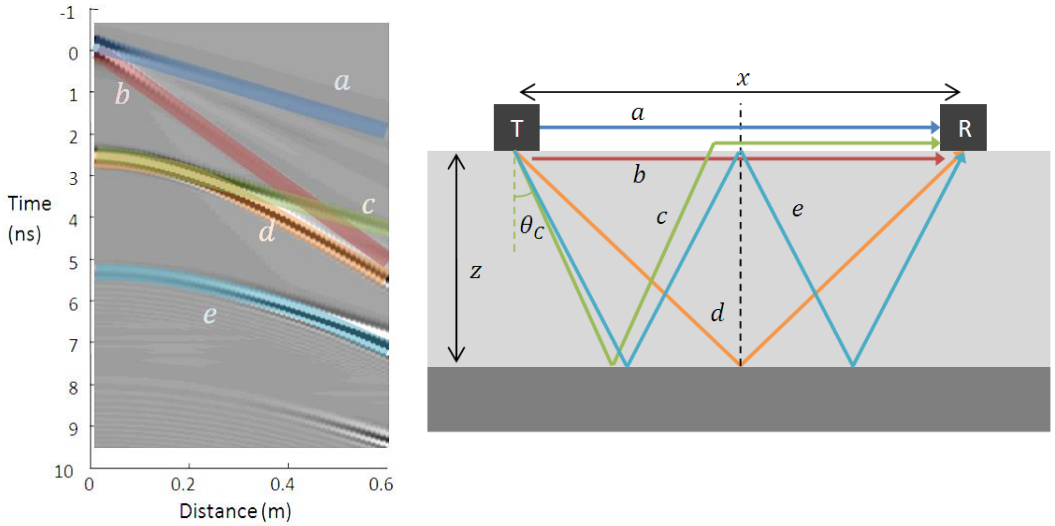

Figure 24 : Typical radargram obtained with CMP.

In Figure 24, wave a is the direct wave in the air. Its speed is known and equal to the speed of light $c = 30\ cm/ns$. It is supposed to cross the origin of axes, thus it can help to find the emission time t_0 if the initial offset is known. The time of reception of this wave is:

$$t_a = t_0 + \frac{x}{c} \tag{28}$$

Wave b is the direct wave into the ground. It gives directly the speed v of the radar waves into the material. Its time of reception is

$$t_b = t_0 + \frac{x}{v} \tag{29}$$

Another highly visible curve in CMP radargrams is the critically refracted wave c. This wave actually travels in the air, which explains its final slope equal to 30

cm/ns, after a reflection with the critical angle inside the material, which gives the waves crossing the surface an horizontal inclination. The equations of the recording times of all the curves appearing in Figure 24 are developed in Appendix 1.

2.1.3.3 Antennas orientation: transverse electric and magnetic modes

In most radar tests, both for profiles and CMP acquisitions, the GPR antennas are parallel and oriented perpendicular to the investigation direction. The acquisition is then in the transverse electric (TE) mode (Figure 25), which means that the electric field is polarized perpendicularly to the propagation plane [55]. This is always the case when using a single shielded antenna, because the receiver and emitter antennas are parallel into the box (see Figure 45).

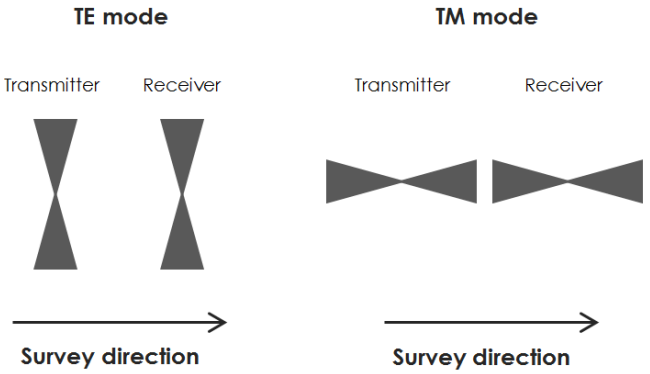

Figure 25 : TE and TM configurations for bistatic antennas.

In the opposite configuration, transverse magnetic (TM) mode (Figure 25), it is the magnetic field that is polarized perpendicular to the propagation plane. This mode is less used because less energy is radiated, but it can be useful in some configurations to use both modes in order to maximize the information measured from the surface [55].

Some properties, as the antenna radiation pattern or the reflection coefficient, are highly dependent on the considered mode [54, 55]. The case of the reflection coefficient in the TM mode will be treated in Appendix 3. Nevertheless, in the experimental and numerical tests presented in this thesis, we uniquely used the TE mode. Adding the analysis of TM waves in the same configuration is an avenue that might be worth exploring in order to improve the results.

2.1.4 Attenuation, scattering and dispersion

Different phenomena decrease the amplitude of the radar wave during its propagation.

- The ohmic attenuation, caused by the conductivity of the material;
- The scattering attenuation, caused by heterogeneities into the medium;

- The dispersion, caused by the variability of the dielectric properties of the concrete with frequency;

- The geometric spreading, caused by the geometric expansion of the wave energy into the space.

2.1.4.1 Ohmic attenuation

The ohmic, or intrinsic, attenuation is caused by the electric losses into the material. The attenuation factor α describes this diminution in function of the covered distance x.

If the incident wave is a plane sinusoid travelling in the x direction, equation (18) can be solved, and the value of the electric field is given by:

$$E(x,t) = E_0\, e^{-\alpha x} e^{i\omega\left(t-\frac{x}{v}\right)} \tag{30}$$

In this equation, E_0 is the initial electromagnetic field strength and ω is the angular frequency. The wave speed v and the attenuation factor α depend on the dielectric properties of the concrete, as well as on the angular frequency (31) [54, 71, 76].

$$\alpha = \omega\left\{\left(\frac{\mu\varepsilon}{2}\right)\left[\left(1+\frac{\sigma^2}{\omega^2\varepsilon^2}\right)^{\frac{1}{2}}-1\right]\right\}^{1/2} \tag{31}$$

$$v = \omega\left\{\left(\frac{2\varepsilon}{\mu\sigma^2}\right)\left[\left(1+\frac{\sigma^2}{\omega^2\varepsilon^2}\right)^{\frac{1}{2}}-1\right]\right\}^{1/2} \tag{32}$$

The two parameters are linked by the relationship:

$$v = \frac{2\alpha}{\mu\sigma} \tag{33}$$

Two simplifying assumptions are currently made to estimate v and α. The first one is that the inspected material is non-magnetic, which yields $\mu = \mu_0$, where $\mu_0 = 4 * 10^{-7} H/m$ is the magnetic susceptibility of free space. The second assumption consists in considering that we are in low loss conditions (equation (22)). With these two assumptions, (31) and (32) can be estimated by:

$$v = \frac{1}{\sqrt{\varepsilon\mu_0}} \tag{34}$$

$$\alpha = \frac{\sigma}{2}\sqrt{\frac{\mu_0}{\varepsilon}} = \frac{\mu_0\sigma v}{2} \tag{35}$$

Equation (34) is then identical to (25), which was obtained directly from Maxwell equations.

2.1.4.2 Scattering attenuation

The wave scattering attenuation is due to the heterogeneities in the material. When the size of heterogeneities is small regarding the wavelength, they will not be visible in the GPR scan. This is normally the case of the aggregates into concrete, because the wavelength λ is given by the equation

$$\lambda = \frac{v}{f} \tag{36}$$

Using the expression (25) for the speed v, (36) becomes:

$$\lambda = \frac{c}{f\sqrt{\varepsilon_r'}} \tag{37}$$

The case in which the aggregates are the most susceptible to be detected is for high frequencies and low permittivity. If $f = 3\,GHz$ and $\varepsilon_r' = 4$, we find $\lambda = 5\,cm$, which is a dimension superior the size of aggregates in classical concrete.

But each small interface still reflects a small amount of energy in all directions, and if heterogeneities are numerous in the material, all these small losses will considerably decrease the amplitude finally reflected to the radar.

The scattering attenuation is, as the ohmic one, an exponential phenomenon:

$$E_x = E_0\, e^{-\alpha_{scattering} x} \tag{38}$$

The scattering attenuation coefficient $\alpha_{scattering}$ is proportional to the number of scatterers, as well as to the "scattering area". When the size of the particles is not negligible regarding the wavelength, this scattering area is described by the Mie scattering theory and is frequency dependant. When the size of the particles is very small, the scattering area can be estimated by Rayleigh scattering cross section A, which can be estimated by [76]:

$$A = C r^6 f^4 \tag{39}$$

In (39), C is a constant, r is the radius of the heterogeneity and f is the frequency. The scattering attenuation is thus highly frequency dependent. For a 2.3 GHz GPR test on a concrete presenting an aggregate radius of 2 cm, the order of magnitude of the scattering attenuation coefficient could be about 0.5 m^{-1}, which can be superior to the ohmic attenuation for dry concrete.

2.1.4.3 Dispersion

Most commercial GPR antennas emit short wavelets, for which the signal is composed of a range of frequencies, distributed around a nominal value. But many properties of the materials, and in particular the attenuation, are frequency dependent (see §§ 2.1.4.2 and 2.1.6).

During the wavelet propagation, the higher frequencies will thus be submitted to a higher attenuation than the lower frequencies, while the differences in permittivity will create a difference in the speed at which travel the different frequency components. This will result in a change in the wavelet shape and amplitude [77].

Correcting the dispersion is particularly important in a lossy medium, when using wavelet or deconvolution analyses, which suppose a constant wavelet shape. The frequency analysis, using a Fourier transform, allows to consider each frequency component independently and thus to take into account the frequency dependant wave dispersion.

2.1.4.4 Geometric spreading

During the propagation of the radar wave in a medium without attenuation, its total power is supposed to remain constant. As the wave spreads spherically away from the antenna, the power density decreases proportionally to the sphere surface. This phenomenon will be described in more details in the chapter dedicated to the study of the direct wave (§ 3.2.4).

2.1.5 Impedance and admittance

The impedance of a plane electromagnetic wave is defined as the ratio between the amplitudes of the magnetic and electric fields [54].

$$\bar{Z} = \frac{|\bar{E}|}{|\bar{H}|} \tag{40}$$

The third constitutive equation (9) allows evaluating the magnetic field as a function of the magnetic flux density vector $\bar{B}$:

$$|\bar{H}| = \left|\frac{\bar{B}}{\mu}\right| \tag{41}$$

If we introduce the time definition of the electric field (19) into the first Maxwell's law (3), we find:

$$\frac{\partial B}{\partial t} = -k \times \hat{U}\, \frac{\partial f}{\partial \beta} = -k \times \hat{U}\, \frac{\partial f}{\partial t}\frac{\partial t}{\partial \beta} \tag{42}$$

But $\beta = \vec{r} \cdot \vec{k}$ is the distance covered by the wave in its propagation direction. Its derivative by respect to the time $\partial\beta/\partial t$ is then simply the wave speed v. We find thus:

$$\frac{\partial}{\partial t}\left(B + \frac{(k \times \hat{u})f}{v}\right) = 0 \tag{43}$$

$$B = -\frac{(k \times \hat{u})f}{v} = \frac{(\hat{u} \times k)f}{v} \tag{44}$$

Finally, we find, for a medium in which conductivity is negligible (lossless):

$$Z = \frac{f}{f/\mu v} = \mu v = \sqrt{\frac{\mu}{\varepsilon}} = \frac{1}{c\sqrt{\varepsilon_r}} \tag{45}$$

In the particular case of a plane transverse electromagnetic wave travelling through a homogeneous medium, the wave impedance is equal to the medium intrinsic impedance, defined as the complex ratio between the applied voltage and measured current. This electric impedance is the AC (alternative current) equivalent of the DC (direct current) resistance and is expressed in ohms.

The admittance is defined as the inverse of the impedance. It is thus given by:

$$Y = \frac{1}{Z} = \sqrt{\frac{\varepsilon}{\mu}} = c\sqrt{\varepsilon_r} \tag{46}$$

2.1.6 Frequency dependence of the GPR properties

As seen in § 2.1.4.1, the speed and attenuation of the GPR waves in a given material are not constant, but tend to increase with frequency. At low frequencies, the GPR waves diffuse into the material and do not reach a wave behaviour until a transition frequency f_t (47), at which both the speed and the attenuation tend to stabilize. The low frequency diffusion is used in EM induction techniques.

$$f_t = \frac{\sigma}{2\pi\varepsilon} \tag{47}$$

For the frequencies superior to f_t, the speed and attenuation in most materials experience a stabilization zone, called the GPR plateau, in which the properties can be considered as stable, even if they increase slightly.

For higher frequencies (from 500-1000 MHz, depending on the water content), the properties, especially the attenuation, increase again, because of two different phenomena:

- the water approaches its relaxation frequency, which means that its permittivity begins to decrease and its conductivity to increase. Physically, when the frequency reaches a few GHz, the water molecule dipole moment can no longer track the applied electric field. The water molecule dipole alignment is not synchronized anymore with the external exciting field, which causes energy dissipation in the material. Microwave ovens use this phenomenon to heat water-containing food;

- as explained in § 2.1.4.2, the scattering attenuation is highly dependent on the wave frequency. Its contribution to the wave attenuation becomes then important.

In Figure 26, Annan [54] represented the evolution of the velocity and the attenuation in a geologic material versus the exciting frequency, as a function of the water content. The velocity remains relatively constant until about 4 GHz, but the attenuation is submitted to a high increase, even for permittivities inferior to 1 GHz.

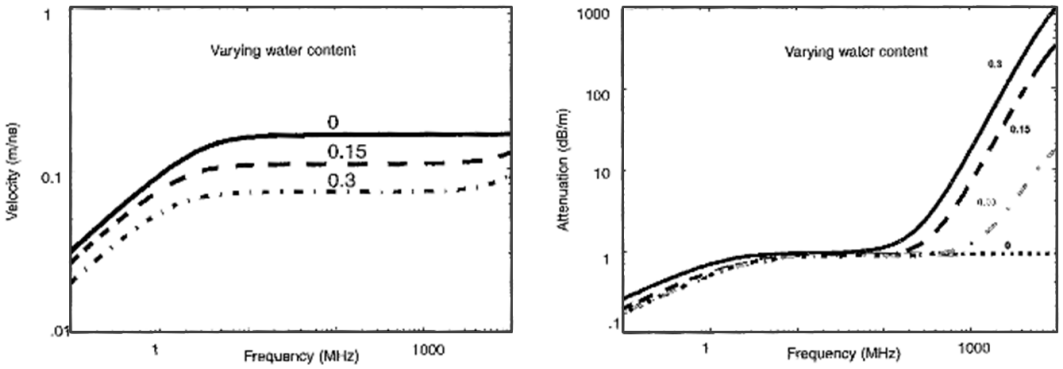

Figure 26 : Frequency dependence of the velocity and attenuation in geological materials, depending on the water content [54].

Different mathematical models have been elaborated to take into account the frequency dependence of the dielectric permittivity. Three of them (Debye, Cole-Cole and Jonscher models) are detailed in Appendix 2.

2.1.7 Reflection coefficient

The GPR waves are reflected when they meet an interface in the underground or into the structure, revealing the presence of this material change and allowing the estimation of its depth. But if the user is interested in determining the material properties of the buried medium, he has to study in details the amplitude (and possibly the phase) of the reflected wavelet. Those parameters can be related to the material properties (and especially to the permittivity) thanks to the reflection coefficient theory.

The reflection coefficient, R, is equal to the proportion of the incident wave amplitude I that will be reflected at the interface, producing a reflected wave of amplitude RI (Figure 27). If a phase change occurs at the interface, the reflection

coefficient can have an imaginary part. Anyway, no energy can be created from a reflection, so the reflection coefficient always lies inside the unit circle [78].

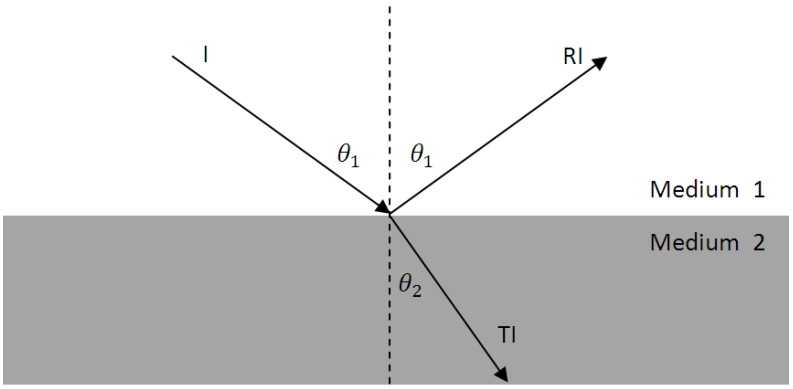

Figure 27 : Geometry of a wave reflection on an interface.

Because the global energy is preserved at the interface, the transmission coefficient T is deduced from the reflection coefficient [76].

$$T_{TE} I = I + R_{TE} I$$
$$T_{TE} = 1 + R_{TE} \quad (48)$$

This equation is only valid in the transverse electric mode (TE). The transmission coefficient can be situated outside of the unit circle [78].

The reflection coefficient depends on the contrast in dielectric properties between the two mediums, but also on the incidence angle of the wave. For example, a wave perpendicular to an interface will penetrate much better into the second medium than a raking wave, that will almost totally be reflected. Generally speaking, in terms of impedance, the Fresnel reflection coefficient in the transverse electric (TE) mode is given by

$$R_{TE} = \frac{Y_1 \cos\theta_1 - Y_2 \cos\theta_2}{Y_1 \cos\theta_1 + Y_2 \cos\theta_2} \quad (49)$$

In this equations, Y_1 and Y_2 are the respective admittances of the two layers (see § 2.1.5) and θ_1 and θ_2 are the respective inclinations of the wave. This transverse electric equation applies to the electric field in the transverse electric plane (which corresponds to the plane perpendicular to the antenna if the emitting antenna is a dipole,). For transverse magnetic equations and reflection coefficients for the magnetic field, see in Appendix 3.

If the medium is lossless, this equation can be expressed in function of the dielectric permittivities of the media ε_{r1} and ε_{r2}, using (46):

$$R_{TE} = \frac{\sqrt{\varepsilon_{r1}}\cos\theta_1 - \sqrt{\varepsilon_{r2}}\cos\theta_2}{\sqrt{\varepsilon_{r1}}\cos\theta_1 + \sqrt{\varepsilon_{r2}}\cos\theta_2} \tag{50}$$

Figure 28 depicts the reflection coefficient for different permittivity contrasts and incident angles, with ε'_{r1} and ε'_{r2} the relative dielectric permittivities of the mediums 1 and 2 in Figure 27. When the second layer has a higher dielectric permittivity than the first one, the reflection coefficient increases smoothly towards one when the angle increases. When the second layer has a lower dielectric permittivity than the first one (dashed lines), the amplitude of the reflection coefficient is the same at vertical incidence, but it increases very fast to one. The limit angle from which the reflection is total is called the critical angle.

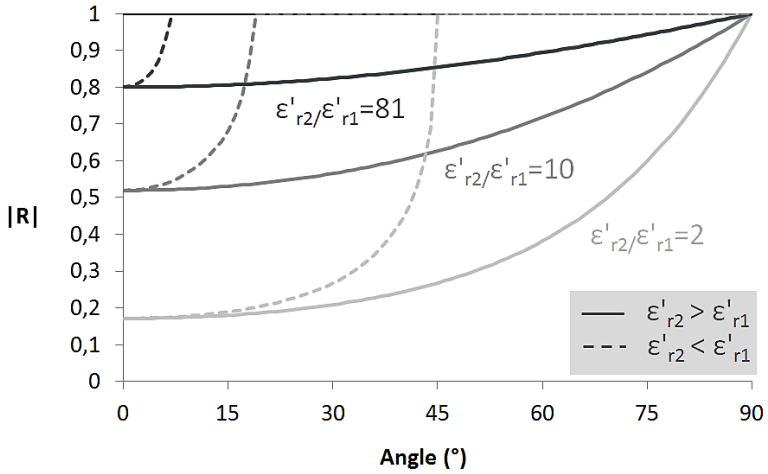

Figure 28 : Description of the Fresnel reflection coefficients (see Figure 27) The dashed lines represent the case of inverse permittivity ratios.

If the incident wave is perpendicular to the interface ($\theta_1 = \theta_2 = 0$), the reflection coefficient simply becomes:

$$R_{TE,\perp} = \frac{\sqrt{\varepsilon_{r1}} - \sqrt{\varepsilon_{r2}}}{\sqrt{\varepsilon_{r1}} + \sqrt{\varepsilon_{r2}}} \tag{51}$$

The definition (50) of the reflection coefficients is referring to the incident and transmitted angles θ_1 and θ_2. However, those angles are not independent but are linked by Snell's law, which expresses the conservation of energy at the interface of two materials. This law, valid in numerous domains in wave physics, can be written (for lossless media):

$$\frac{1}{v_1}\sin\theta_1 = \frac{1}{v_2}\sin\theta_2 \tag{52}$$

Using this relationship, θ_2 can be expressed in function of θ_1 in (50). Moreover, if we consider a low loss medium, the velocity ratio can be expressed in function of the permittivities ratios (25).

$$\begin{aligned}\cos\theta_2 &= \cos\left(\arcsin\left(\frac{v_2}{v_1}\sin\theta_1\right)\right)\\ &= \sqrt{1-\left(\frac{v_2}{v_1}\sin\theta_1\right)^2}\\ &= \sqrt{1-\frac{\varepsilon_{r1}}{\varepsilon_{r2}}\sin^2\theta_1}\end{aligned} \tag{53}$$

Equation (50) becomes:

$$\begin{aligned}R_{TE} &= \frac{\cos\theta_1 - \frac{\sqrt{\varepsilon'_{r2}}}{\sqrt{\varepsilon'_{r1}}}\cos\theta_2}{\cos\theta_1 + \frac{\sqrt{\varepsilon'_{r2}}}{\sqrt{\varepsilon'_{r1}}}\cos\theta_2}\\ &= \frac{\cos\theta_1 - \sqrt{\frac{\varepsilon'_{r2}}{\varepsilon'_{r1}} - \sin^2\theta_1}}{\cos\theta_1 + \sqrt{\frac{\varepsilon'_{r2}}{\varepsilon'_{r1}} - \sin^2\theta_1}}\end{aligned} \tag{54}$$

The reflection coefficient can be negative if material 2 has a higher relative permittivity than material 1 (Figure 27), which is the case for embedded metallic rebars for example, whose dielectric permittivity approaches the infinity. At an interface between air and concrete, the reflection coefficient is about 50%, which means that GPR waves are able to penetrate beyond such interfaces and detect deeper features in the material.

In the expression of Fresnel reflection coefficient (54), the term under the square root will be negative if the deeper material has a lower permittivity than the surface one and if $\theta_1 > \theta_{cr}$. We have then:

$$\frac{\varepsilon'_{r2}}{\varepsilon'_{r1}} < sin^2\,\theta_1 \tag{55}$$

The reflection coefficient becomes imaginary, with unit amplitude and non-zero phase. The theoretical reflection phase for a reflection with ε'_{r1} = 7.7 and ε'_{r2} = 1 is displayed in Figure 29 (a). The resulting effect on the reflected wave can be observed in Figure 29 (b), displaying the radargram of a synthetic CMP with the same parameters. We observe that the phase change is visible in the graph. Indeed, for the low angles, the main peak in the reflection seems to be a black peak, surrounded by two white peaks. At large angles, the main peak is a white peak, surrounded by two important white peaks. The phase change is then almost equal to 180°.

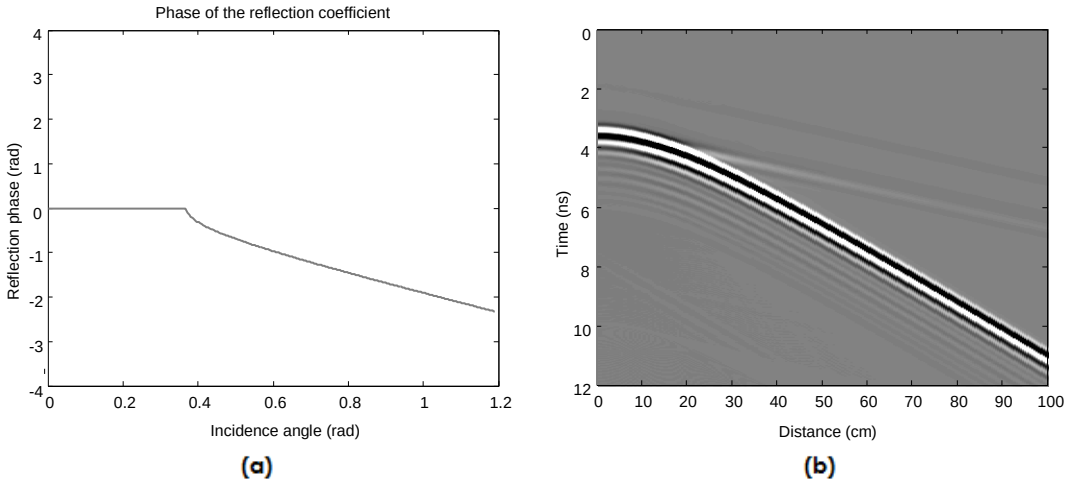

Figure 29 : Angle-dependant reflection phase change for $\varepsilon'_{r1} = 7.7$ and $\varepsilon'_{r2} = 1$. (a) Theoretical reflection phase change. (b) Resulting effect on the measured wavelet.

2.1.7.1 Evanescent wave

When a total reflection occurs, the amplitude and the phase of the transmission coefficient are not equal to zero. No power is transmitted to the second medium but a field is generated along the interface. This powerless field is the evanescent field. It is represented in Figure 30.

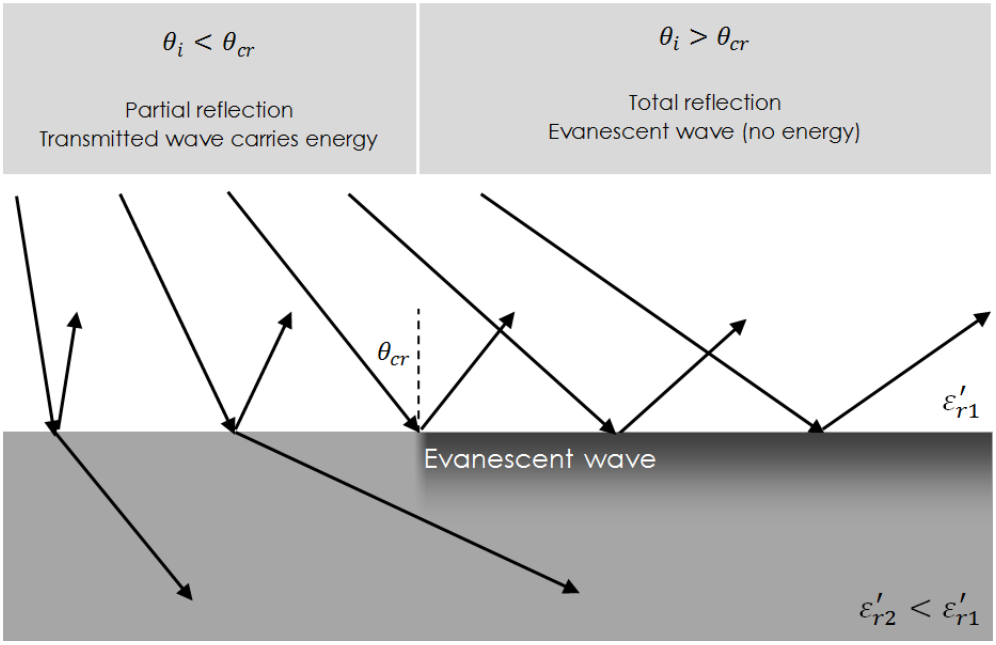

Figure 30 : The evanescent wave appears when the incident angle θ_i is superior to the critical angle.

The transmitted wave is the evanescent wave, traveling along the interface at the horizontal speed [79]:

$$v_{h,\,envanescent} = \frac{v_1}{sin\,\theta_1} \tag{56}$$

Its amplitude decays exponentially from the interface, with the amplitude decaying as [78, 79]:

$$E_{evanescent,\,z} = A_0\, e^{i\omega \frac{sin^2\,\theta_1}{v_1^2} x}\, e^{-\omega z \left(\frac{sin^2\,\theta_1}{v_1^2} - \frac{1}{v_2^2}\right)^{-\frac{1}{2}}}\, e^{-\omega t} \tag{57}$$

In (57), ω is the pulsation and z is the distance from the interface in the direction of medium 2. The wave decays thus rapidly in the z direction, especially for large incident angles. But the evanescent wave cannot be neglected in all cases. Indeed, if a second interface is present close to the first one (in the zone where the evanescent wave amplitude is not negligible), the wave can be transmitted and reflected by this second interface and becomes a propagative wave again [80].

The general equations describing the transmission coefficient ((48)-(54)) can be applied without modification to estimate the evanescent wave [81]. For post-critical reflection, the expression under the square root in (54) is negative, and the reflection and transmission coefficient are thus imaginary numbers. Their amplitudes are respectively equal to $|R|$=1 and $|T| = 0$, but their phase is not equal to zero. The wave propagates into the second medium with an imaginary angle of energy transfer which can be calculated using Snell's equation (52):

$$\theta_{trans} = asin\left(\frac{v_2}{v_1} sin\,\theta_1\right) \tag{58}$$

2.1.7.2 Reflection of spherical waves

The Fresnel reflection coefficients described in § 2.1.7 are rigorously valid only for plane waves, i.e. waves whose propagation fronts are planes. In reality, the waves emitted by radar antennas always present spherical wave fronts, and can only be considered as plane waves at an infinite distance of the antenna. This is rarely the case for high frequency ground penetrating radars, designed to visualize low-depth features into structures.

When the incident wave is spherical and not plane, the Fresnel reflection coefficient can be used as an approximation, but it is not exact anymore [82, 83]. The actual reflection coefficient presents a deviation which can be considerable in the neighborhood of the source, if the dielectric parameters of the materials are very similar or in the vicinity of the critical angle [82]. The apparent reflection coefficient will then be frequency dependent. As a corollary, the approximation (54) is very good when the second material has a significantly lower speed than the surface material.

If the incident angle θ_1 is close to the critical angle θ_{cr} (Figure 31), a correction can be applied to the Fresnel reflection coefficient to take into account the spherical reflection.

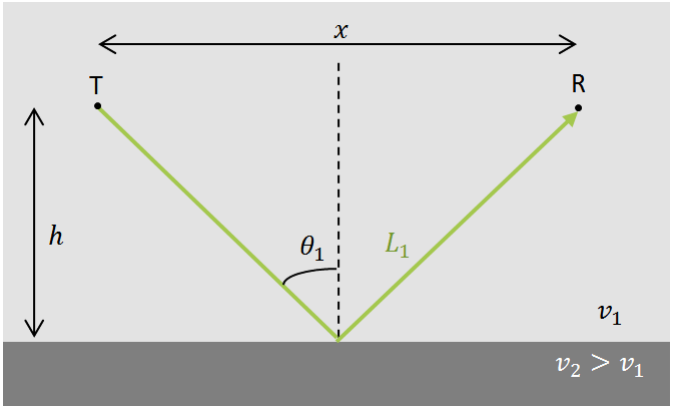

Figure 31 : Reflection of a spherical wave on an interface.

If we note $n = \frac{\sqrt{\varepsilon' r2}}{\sqrt{\varepsilon' r1}} = \sin\theta_{cr}$ the refraction index, Fresnel reflection coefficient (54) can be rewritten:

$$R_0 = \frac{\sqrt{1-\sin^2\theta_1} - \sqrt{\mathrm{n}^2-\sin^2\theta_1}}{\sqrt{1-\sin^2\theta_1} + \sqrt{\mathrm{n}^2-\sin^2\theta_1}} \tag{59}$$

This reflection coefficient can be expressed as the sum of two functions R_1 and R_2:

$$R_0 = R_1 + R_2(1-\sin^2\theta_1)(\mathrm{n}^2-\sin^2\theta_1) \tag{60}$$

With

$$R_1 = \frac{(1-\sin^2\theta_1) + (\mathrm{n}^2-\sin^2\theta_1)}{(1-\sin^2\theta_1) - (\mathrm{n}^2-\sin^2\theta_1)} \tag{61}$$

$$R_2 = \frac{-2}{(1-\sin^2\theta_1) - (\mathrm{n}^2-\sin^2\theta_1)} \tag{62}$$

The reflected wave under and beyond the reflection coefficient can then be expressed in function of those two functions [82]:

$$R_{12,\mathrm{spherical}} = R_1 + R_2\sqrt{1-\sin^2\theta_1}\sqrt{\mathrm{n}^2-\sin^2\theta_1}\,\mu(\beta) \tag{63}$$

In (63), the function $\mu(\beta)$ accounts for the discrepancies between $R_{spherical}$ and R_0, and is equal to 1 when the incident angle is different from the critical angle. Its analytical expression encloses a complex integral which can be solved

numerically. It depends on β, a function related to the dielectric properties and to the geometry of the reflection (Figure 31).

$$\mu(\beta) = \frac{1}{\sqrt{\pi}} \frac{\int_{-\infty}^{\infty} e^{-\varphi^2} \sqrt{\varphi - \beta\, e^{\frac{i\pi}{4}}}\, d\varphi}{\sqrt{\beta\, e^{\frac{i\pi}{4}}}} \tag{64}$$

With

$$\beta = \sqrt{\frac{k_1 x}{2 \sin^3 \theta_1}} \left(\sqrt{1 - \mathrm{n}^2} - \sqrt{1 - \sin^2 \theta_1} \right) \tag{65}$$

The spherical reflection coefficient amplitude and phase obtained by (63) are represented in Figure 32 for an air-concrete (ε'_{r1} = 7.7) reflection. It is compared to the reflection coefficient obtained by the plane waves approximation (50).

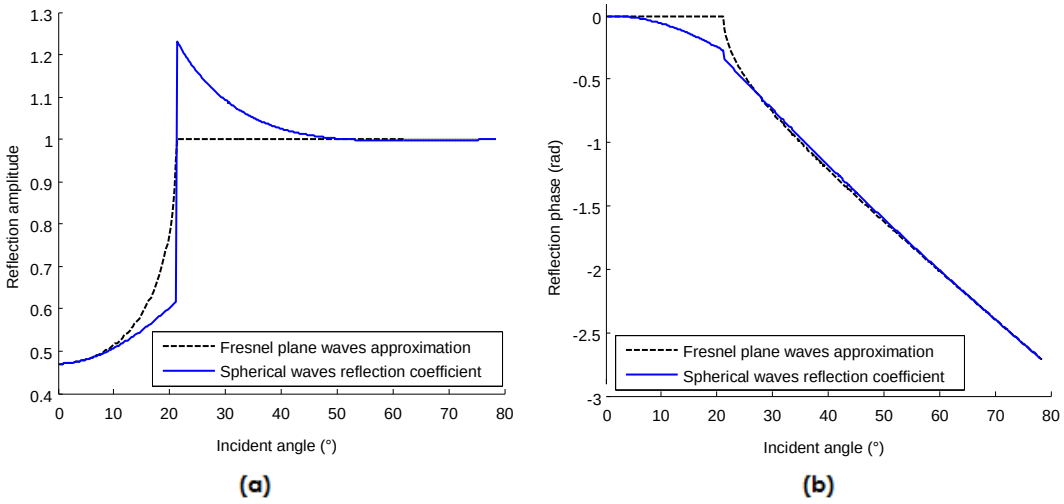

Figure 32 : Amplitude (a) and phase (b) of the spherical reflection coefficient, comparison with the plane wave approximation.

The reflection coefficient at the critical angle can be estimated through the formula [82]:

$$R_{\theta_{cr}} = 1 - \frac{1.644\sqrt{n}}{\left(2k_1 h\sqrt{1-n^2}\right)^{1/4}} e^{\frac{i\pi}{8}} \tag{66}$$

We remark a brutal leap in the reflection coefficient amplitude at the critical angle. In reality, this leap is never observed because the critical angle is also the point of apparition of the lateral wave, which will interact with the reflected waves for the larger angles. The reflection coefficient that will be observed in reality is generated by the combination of both waves. Its equation will be developed in the next paragraph.

2.1.7.3 Interaction with the lateral wave

When an incident wave impacts the interface with the critical angle, a lateral wave, also called critically refracted wave, is produced and travels along the interface. With spherical waves, this always happens when the incident angle θ_1 is superior or equal to the critical angle, as the waves are emitted from the radar in all directions (Figure 33).

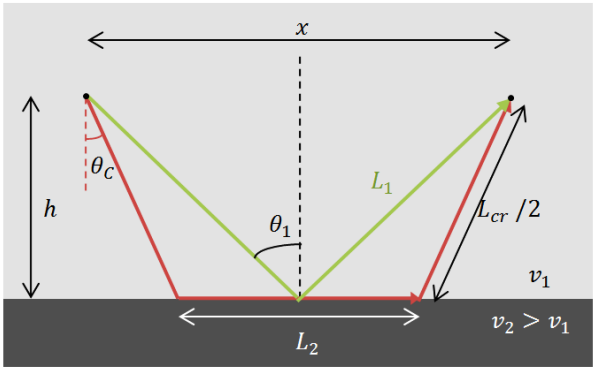

Figure 33 : Representation of the ray propagation of a lateral wave.

For incident angles superior to the critical angle, the electrical field amplitude of the lateral wave is equal to [82, 83]:

$$E_{lat} = \frac{2in}{k_1(n^2-1)\sqrt{x}\,{L_2}^{3/2}}\, e^{i(k_1 L_{cr}+k_2 L_2)}\, F(\eta) \tag{67}$$

In (67), k_j is the propagation constant of the material:

$$k_j = \left(\frac{\omega}{v_j} + i\alpha_j\right) \tag{68}$$

The wave is then traveling along the interface, with a speed equal to the speed in the second medium, and is attenuated proportionally to the distance in the second medium exponent 3/2.

The function $F(\eta)$ in (67) accounts for the wave specific behavior close to the critical angle. Indeed, without this correction function, the critical wave amplitude would be equal to infinity at the critical angle. The parameter η is defined by:

$$\eta = \sqrt{2k_1 L_1}\; sin\frac{\theta_1 - \theta_{cr}}{2} \tag{69}$$

In (69), L_1 is the distance that would be covered by a wave simply reflected on the interface (Figure 33). The function $F(\eta)$ is defined by an integral in the complex plane [82].

$$F(\eta) = \frac{\left(2\eta e^{\frac{i\pi}{4}}\right)^{3/2}}{\Gamma(3/2)} \int_0^{\infty} e^{-\varphi^2 - \sqrt{2}\eta(1+i)\varphi} \sqrt{\varphi}\, d\varphi \tag{70}$$

This integral does not have any analytical solution, even if it can be approached for specific values by asymptotic expansions [83]. Nevertheless, it can be evaluated numerically for all values, and is represented in Figure 34.

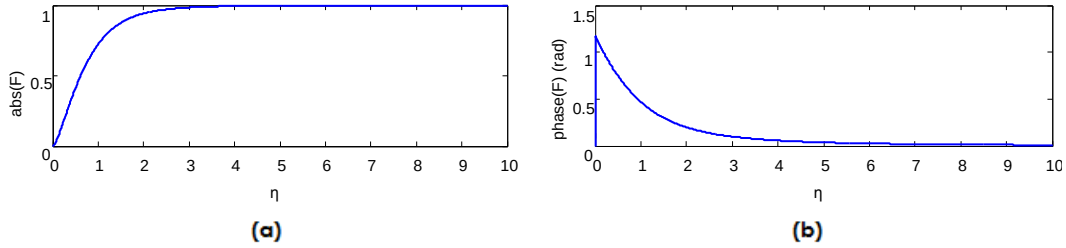

Figure 34 : (a) Amplitude and (b) phase of the function $F(\eta)$.

When $\eta \to 0$, the function $F(\eta)$ approaches zero; but it does not mean that the amplitude of the refracted wave is equal to zero. Indeed, the parameter ${L_2}^{3/2}$ in (67) decreases faster than $F(\eta)$.

As the lateral wave is not reflected, we have to define a pseudo-reflection coefficient that could be added to the reflection coefficient on the interface (63) to obtain the global reflection coefficient. It is obtained by multiplying the lateral wave amplitude by the inverse of the reflected wave propagation term $e^{i\,k_1 L_1}/L_1$.

$$R_{lateral} = E_{lat} \frac{L_1}{e^{i\,k_1 L_1}} \tag{71}$$

We obtain then the apparent reflection coefficient for the spherical waves [82]:

$$\begin{aligned} R_{global} &= R_{lateral} + R_{spherical} \\ &= \frac{2in}{k_1(n^2-1)\sqrt{x}\,{L_2}^{3/2}}\, e^{i(k_1 L_{cr} + k_2 L_2)}\, F(\eta) \frac{L_1}{e^{i\,k_1 L_1}} \\ &\quad + R_1 + R_2 \sqrt{1 - sin^2\,\theta_1} \sqrt{n^2 - sin^2\,\theta_1}\, \mu(\beta) \end{aligned} \tag{72}$$

The formulas (63)-(72) are based on the exact solution approximated by high-frequency asymptotic methods. Those approximations are totally valid when the source-interface distance is sufficiently important, when the propagation constant k_1 is high and for interfaces with a low velocity contrast. In the configurations and distances used in this thesis, these equations can thus not be considered as exact. According to the Červený, it could probably be possible to derive similar formulas that would remain valid in this case through the use of a different dimensionless parameter (Vlatislav Červený, personal communication, July 30, 2013).

Nevertheless, these curves still constitute a far better approximation of the real values than the Fresnel approximation. This can be observed in Figure 35, in which the angle-dependent amplitude and phase of the global reflection coefficients obtained with this formula are compared to values derived from 3D numerical modeling results. In the considered configuration, $\varepsilon'_{r_1} = 7.7$, $\varepsilon'_{r_2} = 1$ and $h = 10\,cm$, and incident frequencies range from 2.5 to 3.5 GHz.

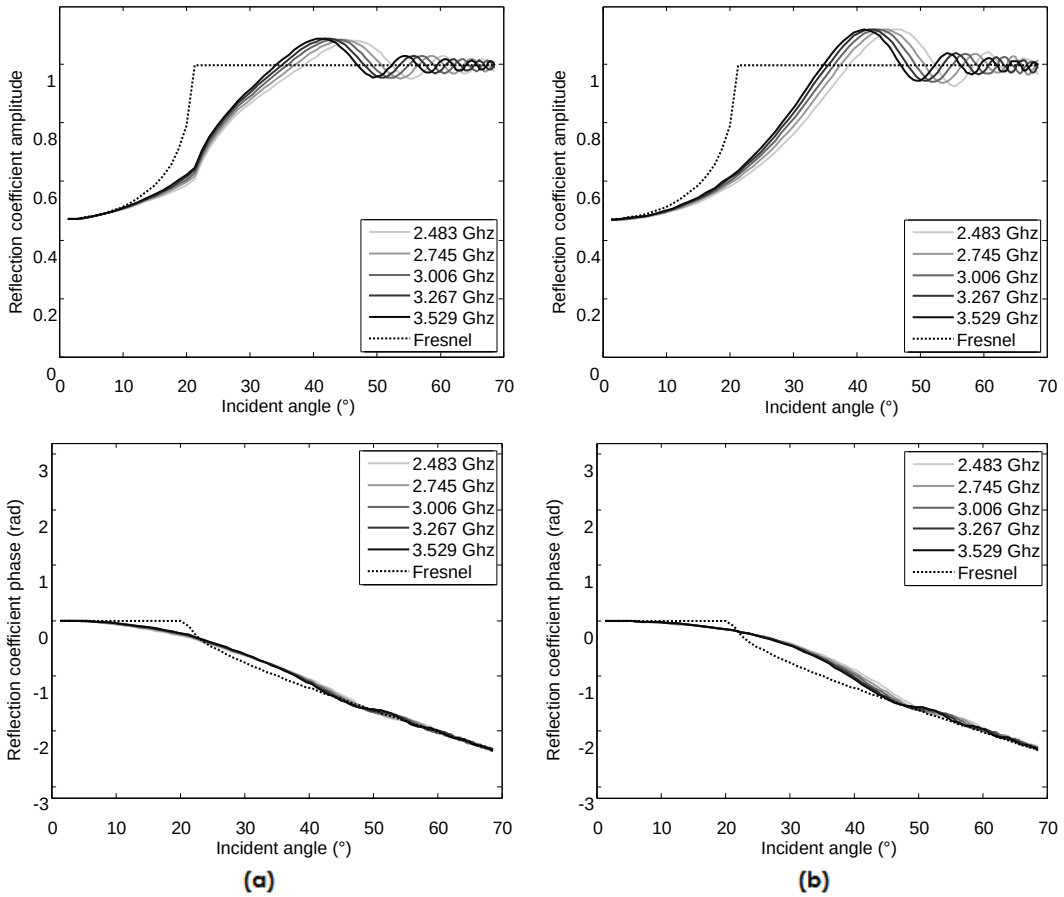

Figure 35 : Amplitude and phase of the global reflection coefficients with $\varepsilon'_{r_1} = 7.7$, $\varepsilon'_{r_2} = 1$ and $h = 10\,cm$: (a) obtained with the spherical waves formulas; (b) obtained through the analysis of 3D numerical simulations.

The reflection coefficient differs very much from the Fresnel predictions in the vicinity of the critical angle and presents oscillations due to the interaction with the lateral wave. The concordance with numerical results is relatively good. In particular, the position of the amplitude maxima is well predicted. The difference of peak amplitude between 3D simulations and spherical waves equations is less than 3% at 3 GHz, while it is more than 10% between the simulations and the plane wave formulation. At the critical angle, the difference if considering the plane wave formulation rises above 50%. This illustrates the importance to consider the spherical waves formulations instead of the classical Fresnel plane waves expressions to evaluate the reflection coefficient when considering low-depth targets.

The extension of these formulas to a two dimensional case is given in Appendix 4.

2.1.8 Resolution

The resolution in GPR testing is the minimum distance between two reflectors for which the two events will be distinguishable in the radargram. The estimation of the resolution will be dependent on the alignment direction (horizontal or vertical).

2.1.8.1 Vertical resolution

The vertical resolution of the radar, also called longitudinal, range or depth resolution, depends mainly on the length of the emitted pulse, which is inversely related to the frequency bandwidth of the wave.

Two successive reflections will appear as distinguishable events if the reflected pulses are clearly separable on the radargram. Two different methods are applied to determine the vertical resolution. The simplest one [48] suggests to choose the wavelength λ as the vertical resolution. A more complicated method [54] proposes to use the width of the pulse at half amplitude W (Figure 36). According to the authors, the peaks should be distinguishable if the time separation between the pulses is higher than $W/2$. The vertical resolution Δr is then the distance covered by the wave during a time equal to $W/4$. The vertical resolution is then equal to:

$$\Delta r = \frac{Wv}{4} \tag{73}$$

Theoretically, Δr is thus independent of the reflection depth. Anyway, in practice, the resolution will decrease at larger distances, due to pulse dispersion and attenuation [54].

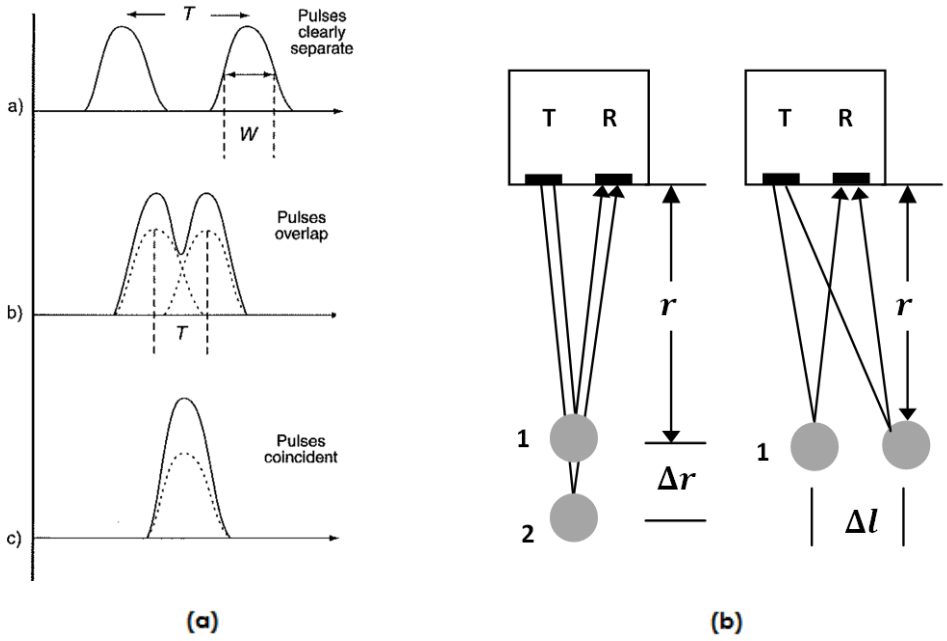

Figure 36 : Peak separation in the radargram (a); range and lateral resolution (b) [54].

2.1.8.2 Horizontal resolution

Horizontal (or lateral) resolution can be determined in the same way as vertical resolution, by considering that the minimum time difference between the two wave arrivals is equal to $W/2$. If the lateral offset is small compared to the depth of the targets d, we obtain [54]:

$$\Delta l = \sqrt{\frac{vdW}{2}} \tag{74}$$

In this equation, we can see that the lateral resolution depends on the depth of the target: the larger the depth, the lower the lateral precision.

Another approach is consists in considering the horizontal resolution equal to the first Fresnel zone radius for signals related to the center frequency f_c. First Fresnel zone is the finite-sized footprint of the wave, travelling in a cone of radiation, on any interface (Figure 37). If a feature has a smaller dimension than this first Fresnel zone, it will not be pictured [65].

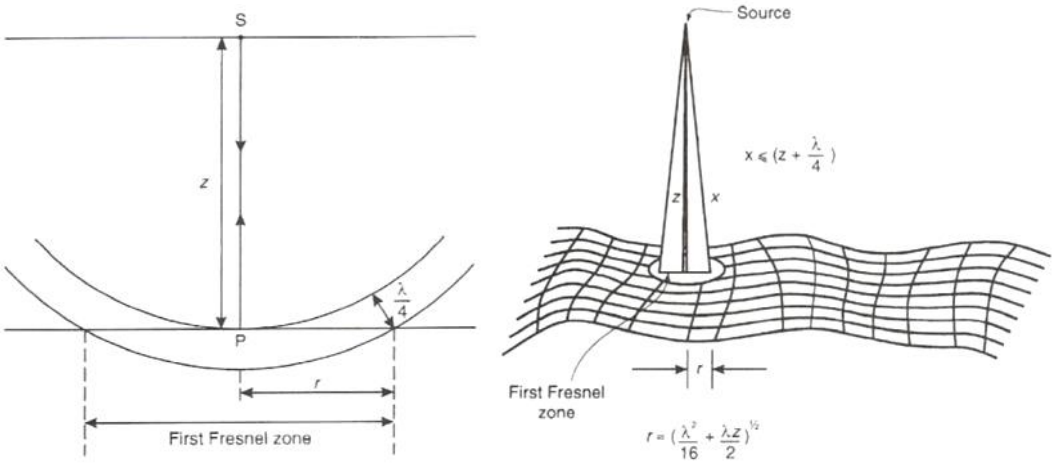

Figure 37 : First Fresnel zone [65].

From Figure 37, we have:

$$\Delta l = \sqrt{\frac{\lambda_c^2}{16} + \frac{\lambda_c d}{2}} \tag{75}$$

Where λ_c is the wavelength associated with the center frequency of the antenna. If λ_c is small in comparison to the depth, we obtain:

$$\Delta l = \sqrt{\frac{d\lambda_c}{2}} \tag{76}$$

This equation is identical to (74) if we use the relationship between the pulse width and the center frequency:

$$W = \frac{1}{f_c} = \frac{\lambda_c}{v} \tag{77}$$

The two expressions of horizontal resolutions described in equations (75) and (76) were compared to experimental data obtained on concrete samples by Perez-Gracia & al. [84]. They also compared the results to other equations, expressing the First Fresnel zone as an ellipse or including the attenuation coefficient. The results obtained with the equations previously described give a good estimation of the minimum distance to detect two targets with no or small interferences. Anyway, it is possible to detect the presence of two different targets for a shorter distance, which is better described by elliptical first Fresnel zone equations.

2.2 Thin layers analysis

When a layer is inspected with GPR, if its thickness is superior to the vertical resolution (§ 2.1.8.1), it can be estimated from the time interval between the reflections on the two interface limiting the layer. For thinner layers, such an analysis is not possible because the pulses overlap in the radargram. Moreover, the radar incident waves (I) undergo multiple reflections on the two limit interfaces, which generates constructive and destructive interferences. This is visible in Figure 38, in which the radar traces obtained numerically on thin layers of different thicknesses are represented.

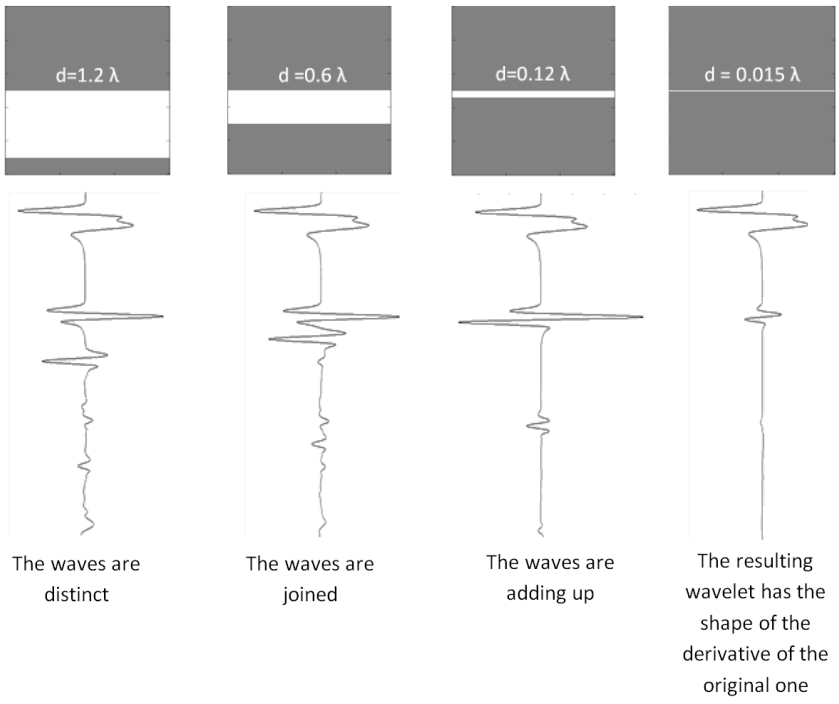

Figure 38 : Description of the reflection interferences caused by a thin layer.

But if the user knows that he is inspecting a thin layer (because he knows the inner composition of the structure, or after core drilling), further information can be extracted from the radargram through the use of more sophisticated methods than a simple radargram visual inspection. Those methods range from a simple peak-to-peak amplitude evaluation of the reflection [85], which can be sufficient if the layer material is known, to a full waveform inversion, which gives very good and accurate results [64, 86] but requires a detailed analysis of the radiating antenna (see § 1.3.2).

In this section, we describe how a ray-based approximation can be used to estimate the global reflection amplitude of the thin layer by considering the incident signal as a sum of plane sine waves [54, 83]. Two different approximations will be proposed to take into account the inclination of the incident waves. In Chapter 4 and Chapter 5, these approximations will be used to estimate the layers properties from numerical and measurements.

2.2.1 Thin layers detection with a vertical incidence

The global reflection coefficient R_{121} reflected from a thin layer of medium 2 embedded into a matrix of medium 1 can be estimated by the sum of the reflection coefficient of all successive reflections from the layer (Figure 39).

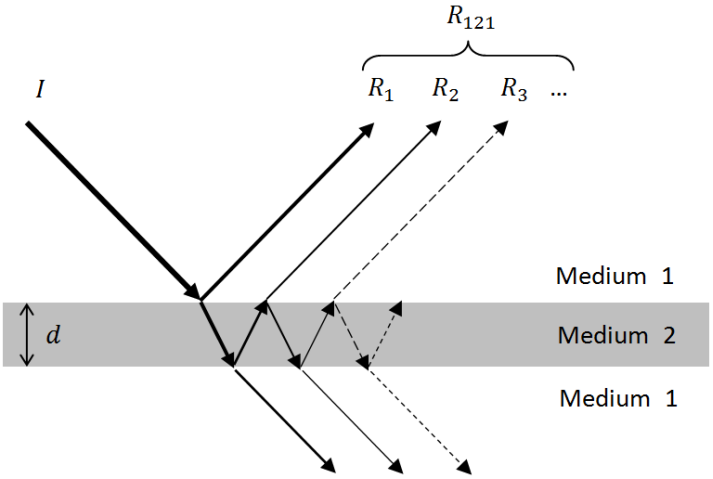

Figure 39 : Multiple reflections in a thin layer.

For an incident plane wave, the different reflection amplitudes can be estimated as functions of the different Fresnel transmission and reflection coefficients of the two interfaces R_{12}, R_{21}, T_{12} and T_{21}(see § 2.1.7). We assume a medium without attenuation.

$$\begin{aligned} R_{121} &= R_1 + R_2 + R_3 + \cdots \\ &= R_{12} + T_{12}T_{21}R_{21}\beta + T_{12}T_{21}R_{21}^3\beta^2 + \cdots \\ &= R_{12} + \frac{T_{12}T_{21}}{R_{21}}\sum_{n=1}^{\infty}(R_{21}^2\beta)^n \end{aligned} \tag{78}$$

In (78), β is the temporal delay (or phase change) undergone by the signal while a back-and-forth into the layer. If $|R_{21}^2\beta|<1$, which is always the case if the reflection is not total, the geometric series formula can be used. The reflection coefficient becomes then:

$$R_{121} = R_{12} + \frac{T_{12}T_{21}R_{21}\beta}{1 - R_{21}^2\beta} \tag{79}$$

All the reflection and transmissions can be expressed as a function of R_{12}.

$$\begin{gathered} R_{21} = -R_{12} \\ T_{12} = 1 + R_{12} = 1 - R_{21} = 2 - T_{21} \end{gathered} \tag{80}$$

Equation (79) becomes:

$$R_{121} = R_{12}\,\frac{1 - \beta}{1 - R_{12}^2\beta} \tag{81}$$

If the signal is a sine wave, we can evaluate the phase change β:

$$\beta = e^{i4\pi\frac{d}{\lambda_2}} \tag{82}$$

The theoretical complex reflection coefficient is then given by (83):

$$R_{121}\left(\frac{d}{\lambda}, R_{12}\right) = R_{12}\frac{1 - e^{\frac{i4\pi d}{\lambda_2}}}{1 - R_{12}^2 e^{\frac{i4\pi d}{\lambda_2}}} \tag{83}$$

In (83), d is the thickness of the layer and λ_2 is the wavelength into the thin layer. This exact equation for a reflection from a single embedded layer, considering plane harmonic (sinusoidal) waves for a lossless layer, was reported by Rayleigh. If one is only interested in the amplitude of the reflection, it is also given by the relationship (84) [51, 52]:

$$|R_{121}| = |R_{12}|\frac{\left(1 + \sqrt{\frac{\varepsilon'_{r1}}{\varepsilon'_{r2}}}\right)^2}{\sqrt{\left(2\sqrt{\frac{\varepsilon'_{r1}}{\varepsilon'_{r2}}}\cot\left(2\pi\frac{d}{\lambda_2}\right)\right)^2 + \left(1 + \frac{\varepsilon'_{r1}}{\varepsilon'_{r2}}\right)^2}} \tag{84}$$

The evolution of $|R_{121}|$ with the ratio of the layer thickness to the wavelength in the thin layer is drawn in Figure 40.

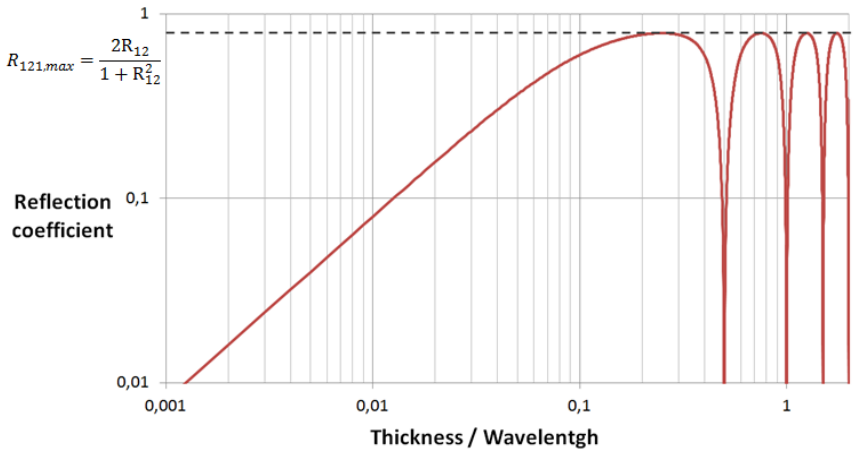

Figure 40 : Reflection coefficient for an air thin layer into concrete.

The first maximum occurs when the layer thickness is equal to a quarter of the wavelength in the layer (λ), and has then a periodicity of $\lambda/2$. At the different maxima, the reflection occurring on the thin layer has a greater reflection coefficient $R_{121,max}$ than a reflection that would occur on a simple interface (R_{12}). This amplitude is given by (85):

$$R_{121,max} = \frac{2R_{12}}{1+R_{12}^2} \tag{85}$$

When the thickness of the layer can be considered as low compared to the wavelength (ratio up to 0.09), the reflection coefficient is directly proportional to the layer thickness [52, 54]. It can then be estimated by the following linear approximation (84) [6]:

$$R_{121} \cong 4\pi \frac{R_{12}}{1-R_{12}^2}\frac{d}{\lambda} \tag{86}$$

When the thickness d is small compared to the wavelength in the layer λ, β can be approximated by the two first terms of its Taylor series:

$$\beta = e^{i4\pi\frac{d}{\lambda_2}} \cong 1 + i4\pi\frac{d}{\lambda_2} \tag{87}$$

The expression (81) of R becomes:

$$R_{121} = R_{12}\frac{-i4\pi\frac{d}{\lambda_2}}{1-R_{12}^2-R_{12}^2 i4\pi\frac{d}{\lambda_2}} \tag{88}$$

If we are considering a thin layer, $\ll \lambda_2$; it means that the term $R_{12}^2 i4\pi\frac{d}{\lambda_2}$ can be neglected by respect to the other terms. Equation (88) becomes:

$$R_{121} = -4\pi i \frac{R_{12}}{1-R_{12}^2}\frac{d}{\lambda_2} = \left(\frac{-R_{12}}{1-R_{12}^2}\frac{2d}{v_2}\right)\omega i \quad (89)$$

In (89), the wavelength has been expressed as a function of the speed, considering $\lambda = v/f = v2\pi/\omega$.

If the thickness can be considered as small for all the wavelengths contained in the signal, (89) can be solved to express the transient response $R(\omega)$ of the thin layer as a function of the solicitation $S(\omega)$ [54]:

$$R(\omega) = RS(\omega) = \left(\frac{-R_{12}}{1-R_{12}^2}\frac{2d}{v_2}\right)\omega i S(\omega) = i\omega C S(\omega) \quad (90)$$

By using a Fourier transform, we can obtain the response in the temporal domain:

$$r(t) = C\frac{d}{dt}s(t) \quad (91)$$

In the temporal domain, the shape of the reflected signal will thus be identical to the derivative of the signal, multiplied by a constant linearly dependent on the thickness of the layer [54]. This derivation of the initial wavelet had already been described by Widess [52]. It is visible in Figure 38: the reflection on the thinner layer $(d/\lambda = 0.015)$ has the shape of the derivative of the reflection on the thicker layer $(d/\lambda = 1.2)$.

If the intrinsic attenuation into the layer cannot be neglected $(\alpha \neq 0)$, a similar development can be made and (81) becomes:

$$R_{121} = R_{12}\frac{1-\beta e^{-2d\alpha}}{1-R_{12}^2\beta e^{-2d\alpha}} \quad (92)$$

The geometric attenuation into the layer cannot be taken into account into the geometric series formula and will thus be neglected. This approximation is valid as long as the layer is sufficiently thin.

If the incident wave is spherical and the source is too close to the interface for the plane wave approximation to be valid, equations of § 2.1.7.2 can be used as well in (78), but this has to be done numerically as they do not have analytical solutions.

2.2.2 Thin layers detection with an oblique incidence

In this section, we develop analytical formulations to take into account the angle influence in the thin layer reflection coefficient. Two different approaches are considered: the approximation to a geometric series and the sum truncation. In

§ 4.1.2, those methods will be compared to numerical results in order to determine the limitations of the methods to approach the real propagation behaviour.

Most GPR tests are in fact performed with an oblique incidence. This is always the case in CMP tests, in which the incident angle varies all along the measurement. But the angle of incidence may also not be negligible when a profile is performed. This is especially the case for high frequency radar with limited (< 30 cm) penetration depth. The small distance between the antennas (equal to a couple of centimetres) may not be negligible regarding the target depth.

The variation of the angle influences the reflection coefficients (§ 2.1.7), but it also has an influence on the time shift generated by the reflection in the layer. Each multiple has a different path into the layer, but also into the matrix, which modifies the attenuation.

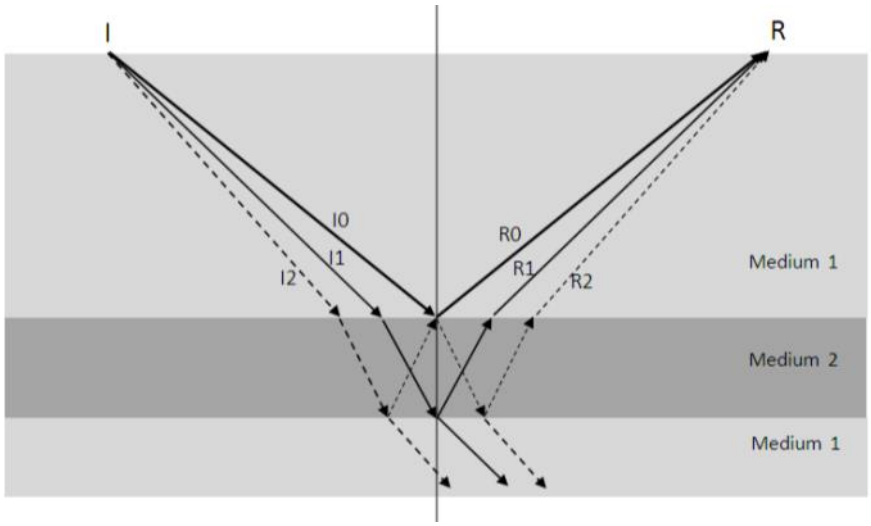

Figure 41 : Multiple reflections in a thin layer.

As in the case of a vertical incidence, the reflected amplitude can be evaluated as the sum of all the different multiples.

$$
\begin{aligned}
R_{121} &= R_0 + R_1 + R_2 + \cdots \\
&= R_{12}(\theta_0) + T_{12}(\theta_1)T_{21}(\theta_{12})R_{21}(\theta_1)\beta_1 \frac{e^{-\alpha_l \Delta x_{l,1}}\, e^{+\alpha_m \Delta x_{m,1}}}{\frac{x_{tot,1}}{x_{tot,0}}} \\
&+ T_{12}(\theta_2)T_{21}(\theta_2)R_{21}^3(\theta_2)\beta_2 \frac{e^{-\alpha_l \Delta x_{l,n}}\, e^{+\alpha_m \Delta x_{m,n}}}{\frac{x_{tot,2}}{x_0}} + \cdots \\
&= R_{12}(\theta_0) \\
&+ \sum_{n=1}^{\infty} T_{12}(\theta_n)T_{21}(\theta_n)\big(R_{21}(\theta_n)\big)^{2n-1}\beta_n \frac{e^{-\alpha_l \Delta x_{l,n}}\, e^{+\alpha_m \Delta x_{m,n}}}{\frac{x_{tot,n}}{x_{tot,0}}} \\
&= R_{12}(\theta_0) - \sum_{n=1}^{\infty} \frac{1 - R_{12}^2(\theta_n)}{R_{12}(\theta_n)} R_{12}^{2n}(\theta_n)\beta_n \frac{e^{-\alpha_l \Delta x_{l,n}}\, e^{+\alpha_m \Delta x_{m,n}}}{\frac{x_{tot,n}}{x_{tot,0}}}
\end{aligned}
\tag{93}
$$

In (93), β_n is the phase change of the n^{th} signal compared with the first simple reflection R_0; α is the attenuation coefficient into the layer and $\Delta x_{l,n}$, $\Delta x_{m,n}$ and $x_{tot,n}$ are respectively the path of the wave into the layer, the variation of the path into the matrix and the total distance for the n^{th} multiple.

In contrast to the vertical case, the different terms cannot be directly summed up using the geometric series formula. Indeed, the reflection coefficients and the different phase changes vary from one multiple to another due to the angle variation. Two approaches can be considered to overpass this problem. The first one (section 2.2.2.1) consists in assimilating the wave to a plane wave. With this approximation , the geometric series formula can be used to transform the series (93) into an analytical expression. In the second method (section 2.2.2.2), the n first terms of the series are calculated, and the terms of higher order are neglected. Both methods will be compared in § 2.2.2.3, before being confronted to numerical results in § 4.1.2.

2.2.2.1 Approximation to plane waves

If the incident wave is a plane wave, all reflection angles will be identical, as well as the reflection coefficients.

$$
\begin{aligned}
\theta_n &\cong \theta_0 \\
R_{12}(\theta_n) &\cong R_{12}(\theta_0)
\end{aligned}
\tag{94}
$$

The phase shift undergone for each back and forward in the layer will be identical. The simple reflection and the first multiple are represented in Figure 42.

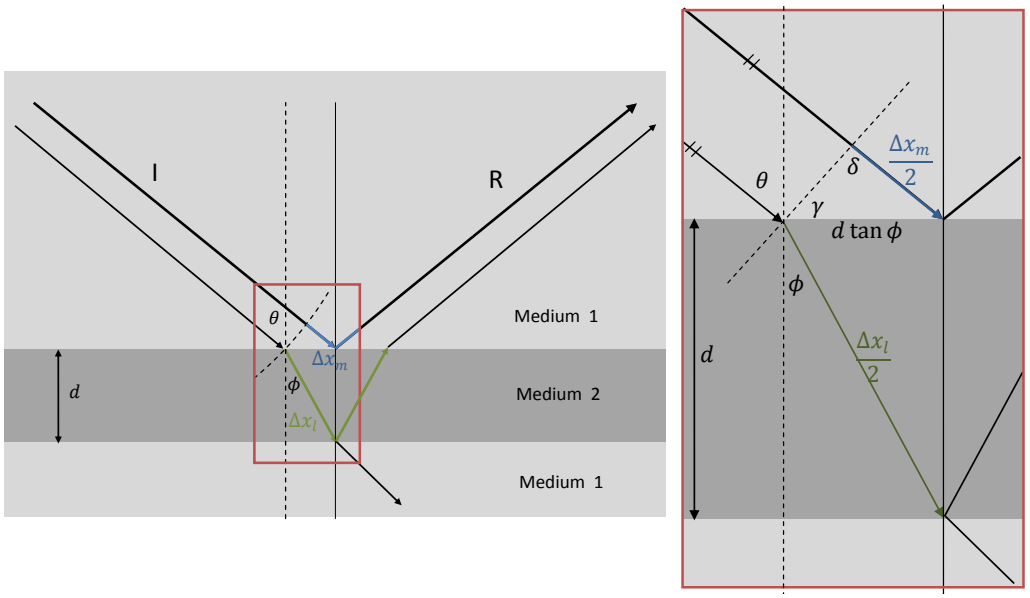

Figure 42 : Geometric detail of the first reflection of a plane wave on a thin layer and its first multiple.

The time delay between the two arrivals is equal to the difference between the travel time into the layer $2\Delta x_l$ and the difference of length of the rays into the matrix $2\Delta x_m$. We have then, using Snell's relationship (52) between the incident and transmitted angles:

$$\begin{aligned}\Delta t_1 &= \frac{\Delta x_l}{v_2} - \frac{\Delta x_m}{v_1} \\ &= \frac{2d}{v_2 \cos\phi} - \frac{2d \tan\phi \sin\theta}{v_1} \\ &= \frac{2d}{v_2 cos\,\phi} - \frac{\frac{2d \tan\phi\, v_1}{v_2 \sin\phi}}{v_1} \\ &= \frac{2d}{v_2 cos\,\phi}(1 - sin^2\,\phi) \\ &= \frac{2d \cos\phi}{v_2}\end{aligned} \tag{95}$$

For a sine wave, the phase change for each back and forward into the layer is then equal to:

$$\begin{aligned}\beta_1 &= e^{i\omega\Delta t_1} \\ &= e^{i4\pi\frac{d\,cos\,\phi}{\lambda_2}}\end{aligned} \tag{96}$$

As all the waves are parallel, the time delay is proportional to the number of multiples. For a sine wave, the phase change can then be generalized:

$$\begin{aligned}\beta_n &= \beta_1^n \\ &= e^{i4\pi n\frac{d\cos\phi}{\lambda_2}}\end{aligned} \tag{97}$$

The intrinsic attenuation depends on the distance variations, which are proportional to the distance variation in the first multiple:

$$\Delta x_{l,n} = \frac{2dn}{\cos\phi_n} = \frac{2dn}{\sqrt{1-\frac{v_2^2}{v_1^2}\sin^2\theta_0}} = n\Delta x_{l,1} \tag{98}$$

$$\Delta x_{m,n} = -2dn\tan\phi_n\sin\theta_n = -2dn\frac{\frac{v_2}{v_1}\sin^2\theta}{\sqrt{1-\frac{v_2^2}{v_1^2}\sin^2\theta_0}} = n\Delta x_{m,1} \tag{99}$$

The geometric attenuation depends on the quotient $\frac{x_{tot,n}}{x_{tot,0}}$, which cannot be expressed as a power of n. Nevertheless, if the layer is very thin respect to its depth, i.e.:

$$d \ll h \tag{100}$$

We can consider that we have

$$\frac{x_{tot,n}}{x_{tot,0}} \cong 1 \tag{101}$$

Using the relationships (97)-(99), as well as the approximation (101), equation (93) can be solved with the geometric series formula if $|R_{12}^2(\theta_0)\beta_1 e^{-\alpha_l\Delta x_{l,1}+\alpha_m\Delta x_{m,1}}|<1$ (which is always the case except in case of total reflection). The reflection coefficient becomes then, if the geometric attenuation into the layer is negligible:

$$\begin{aligned}&R_{121} \\ &\approx R_{12}(\theta_0) - \sum_{n=1}^{\infty}\frac{1-R_{12}^2(\theta_0)}{R_{12}(\theta_0)}\left(R_{12}^2(\theta_0)\beta_1\right)^n e^{n\left(-\alpha_l\Delta x_{l,1}+\alpha_m\Delta x_{m,1}\right)} \\ &\approx R_{12}(\theta_0) - \frac{1-R_{12}^2(\theta_0)}{R_{12}(\theta_0)}\sum_{n=1}^{\infty}\left(R_{12}^2(\theta_0)\beta_1 e^{-\alpha_l\Delta x_{l,1}+\alpha_m\Delta x_{m,1}}\right)^n \\ &\approx R_{12}(\theta_0) - \frac{R_{12}(\theta_0)\beta_1 e^{-\alpha_l\Delta x_{l,1}+\alpha_m\Delta x_{m,1}}\left(1-R_{12}^2(\theta_0)\right)}{1-R_{12}^2(\theta_0)\beta_1 e^{-\alpha_l\Delta x_{l,1}+\alpha_m\Delta x_{m,1}}} \\ &\approx R_{12}(\theta_0)\frac{1-\beta_1 e^{-\alpha_l\Delta x_{l,1}+\alpha_m\Delta x_{m,1}}}{1-R_{12}^2(\theta_0)\beta_1 e^{-\alpha_l\Delta x_{l,1}+\alpha_m\Delta x_{m,1}}}\end{aligned} \tag{102}$$

This reflection coefficient estimation is almost exact for a plane wave, as only the geometric attenuation is not taken into account.

If the incident wave is not a plane wave but a cylindrical or spherical wave (Figure 41), equation (102) can be used to estimate the layer reflection coefficient (78). The incident angles of all multiples are then identified to the angle of the simple reflections.

$$\theta_n \cong \theta_0 \tag{103}$$

This approximation is valid for thin layers when $\varepsilon_{r2} > \varepsilon_{r1}$ (Figure 41) or when $\varepsilon_{r2} < \varepsilon_{r1}$ if the incident angle is inferior to the critical angle. When $\theta_0 > \theta_{cr}$ (Figure 43), this approximation gets very far from the ray theory, as all the ray paths have a theoretical incident angle inferior to the critical angle (and can then be largely inferior to θ_0)

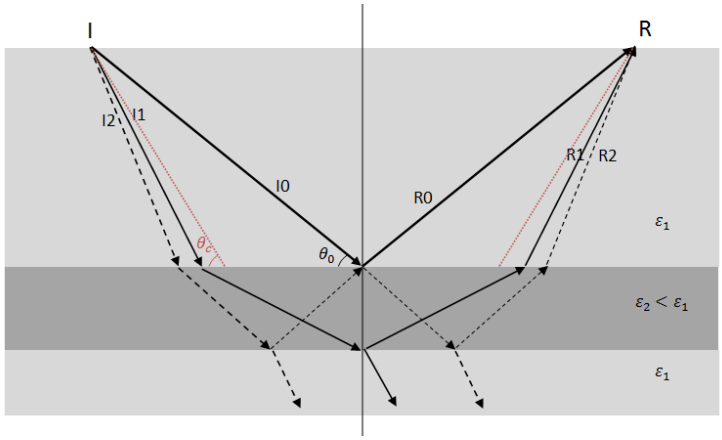

Figure 43 : Thin layer reflection of a spherical wave for incident angle superior to the critical angle.

The approximation calculates all the transmitted waves as if they had the incidence angle θ_0. When $\theta_0 > \theta_{cr}$, the transmitted wave is an evanescent wave (see § 2.1.7.1) and the transmission angle is imaginary. Anyway, this evanescent angle generates a reflection on the second interface and a reflected wave will be calculated anyway.

2.2.2.2 Exact evaluation of the first multiples

An alternative for estimating the reflection coefficient is the estimation of the exact value of the first terms of equation (93). The reflection angles θ_n are determined utilizing the fact that the total horizontal path must be in every case equal to the distance between the antennas, and that the angles into the matrix and into the layer are linked by Snell's law (52). The path lengths into the matrix p_m and into the layer p_l are determined from these angles.

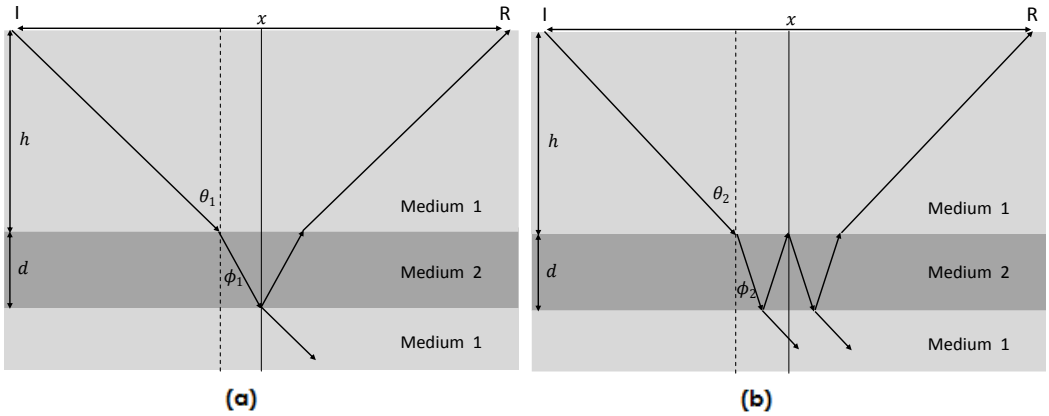

Figure 44 : First (a) and second (b) multiple of the reflection event.

For the simple reflection on the first interface, the angle and the path lengths are directly determined.

$$\begin{cases} \theta_0 = atan\left(\frac{x}{2h}\right) \\ p_{m,0} = \sqrt{h^2 + \frac{x^2}{4}} \\ p_{l,0} = 0 \end{cases} \quad (104)$$

For the n^{th} multiple with reflections into the thin layers, these equations become:

$$\begin{cases} \frac{x}{2} = h\,tan\,\theta_n + nd\,tan\left(asin\left(\frac{v_2}{v_1}sin\,\theta_n\right)\right) \\ p_{m,n} = \frac{nh}{cos\,\theta_n} \\ p_{l,n} = \frac{2nd}{\sqrt{1 - \frac{v_2^2}{v_1^2}sin^2\,\theta_n}} \end{cases} \quad (105)$$

Equations (105) cannot be solved directly for θ_n. One solution is to transform it into a even polynomial equation of the 8th degree. Among the eight solutions of this equation, θ_n is the only positive real value inferior to θ_{cr}.

Once the angles are determined, the reflection coefficients for simple interfaces $R_{12}(\theta_n)$ can be determined using formula (54). The global reflection coefficient for the n^{th} multiple (which does not account for the phase of the reflection) is then equal to:

$$R_{Ampl,121,n} = -\left(1 - R_{12}^2(\theta_n)\right) * R_{12}^{2n-1}(\theta_n) \quad (106)$$

From the values of the distances into the matrix and into the layer $p_{m,n}$ and $p_{l,n}$, we can determine the geometric attenuation $G_n$of each multiple compared to

the geometric attenuation of the simple reflection, as well as the intrinsic attenuation O_n.

$$\frac{A_n}{A_1} \propto G_n = \begin{cases} \frac{x_1}{x_n}, & in\ 3D \\ \frac{\sqrt{x_1}}{\sqrt{x_n}}, & in\ 2D \end{cases} \quad (107)$$

$$\frac{A_n}{A_1} \propto O_n = e^{p_{m,n}\alpha_m + p_{l,n}\alpha_l} \quad (108)$$

In addition to the attenuation, a phase change p_n is affecting each multiple as well. For a sine wave, this phase change is equal to:

$$P_n = \frac{e^{i2\pi f t_{tot,n}}}{e^{i2\pi f t_{tot,0}}} \quad (109)$$

Where

$$t_{tot,n} = \frac{p_{m,n}}{v_m} + \frac{p_{l,n}}{v_l} \quad (110)$$

The global reflection coefficient for each multiple is then given by

$$R_{121,n} = R_{Ampl,121,n}\, G_n\, O_n\, P_n \quad (111)$$

And the general reflection coefficient can be estimated by

$$|R_{121}| = \left| \sum_{n=0}^{\infty} R_{121,n} \right| \cong \left| \sum_{n=0}^{n_k} R_{121,n} \right| \quad (112)$$

Where n_k is the finite number of multiples that will be studied.

2.2.2.3 Comparison of the two methods

The two methods presented in the previous chapters present different equations to represent the same phenomenon. They results from different approximations and are not expected to be valid in every situation. A comparison of the reflection coefficients calculated by these methods to values obtained from numerical simulation will be presented in § 4.1.2. But different observations can already be made from the equations.

The two methods only give similar results when the incident angle is much inferior to the critical angle. For larger angles, both methods calculate the same first reflection on the layer (R_0) but estimate very different incident angles, and thus very different reflection coefficients, for the other reflections.

On one hand, the first terms approximation (§ 2.2.2.2) calculates exactly the angle of incidence of each multiple in order to respect the refraction laws (104). On the other hand, the plane wave approximation (§ 2.2.2.1) approximates every incident angle to the incident angle of the first reflection (146). Therefore, the multiples calculated by the methods are very different, and correspond in fact to two different sets of waves travelling in reality. The "multiple reflections" calculated by the plane wave approximation correspond to the evanescent wave and its different reflections into the layer.

Indeed, all the "multiple reflections" are calculated from the first reflection coefficient (see (102)), whose amplitude is equal to 1 for large angles. The transmission coefficient has thus an amplitude equal to zero but a real phase and an imaginary propagation angle, which are the characteristics of the evanescent wave (see § 2.1.7.1). On the other hand, the exact estimation of the first terms does not take into account this evanescent wave, because the multiples are calculated for incident waves under the critical angles (Figure 43). A possibility to improve the first terms estimations method would be to introduce separately the evanescent waves (calculated by equation (57)) into the formulas.

Other phenomena that were not taken into account by neither of the methods are the spherical nature of the waves (§ 2.1.7.2) and the lateral wave propagation (§ 2.1.7.3). The first reflection in both methods could take these phenomena into account using the formula (72).

2.3 *Finite difference modelling of radar waves propagation*

The interpretation of real GPR data can be challenging. Indeed, even for relatively simple geometries, the multiple paths and reflections of the radar waves can result in a relatively complex radargram. Interpretation hypotheses can be checked through laboratory experiments, but these are expensive and time-consuming. In many cases, they are thus advantageously replaced by numerical simulations, which are an easy and fast method to explore different scenarios.

The FDTD (finite differences time domain) method is largely used for GPR simulations. It is an easy, explicit and robust method allowing the use of complex pulses and nonlinear behaviour. Once the code is written, the user can simply generate models by modifying the mesh [87]. Disadvantages are that it can have a high computational cost, especially for 3D refined models, and that curve surfaces can be hard to represent with the square grid. Those problem can be partially solved in some programs allowing to refine the mesh in critical zones [87], but for curve surfaces, the finite elements method can be a preferable alternative [88].

2.3.1 Global principle

The principles of the FDTD algorithm have been published by Yee in 1966 [89]. It uses finite differences to solve Maxwell's equations. It has the particularity to solve alternatively the electric and the magnetic fields. The medium is discretized in cubic cells; the electric field is evaluated in the middle of the faces while the magnetic field is defined on the mesh. With this method, each field unity is surrounded by four components of the other field. The electric and magnetic fields are alternatively calculated, with temporal and spatial steps $\Delta t/2$ and $\Delta x/2$ [87].

2.3.2 Stability

The time step used on the modelling cannot be arbitrarily chosen. As a necessary condition for the stability of the computation, the stability criterion of Courant (Courant, Freidrichs and Lewi [90]) has to be respected by the time step:

$$\Delta t \leq \frac{1}{c\sqrt{\frac{1}{\Delta x^2}+\frac{1}{\Delta y^2}+\frac{1}{\Delta z^2}}} \tag{113}$$

In (113), c is the light speed (maximum speed of electromagnetic waves) and $\Delta z \rightarrow \infty$ if working in two dimensions. This stability criterion expresses that the time step between each amplitude evaluation cannot be superior to the travel time of the waves between two grid points. [87]

2.3.3 Numerical dispersion

An insufficiently refined mesh will induce numerical dispersion and attenuation. For this reason, it is essential to use a sufficiently small spatial step. In two and three dimensions, this dispersion is anisotropic: the oblique waves travel faster than the waves propagating in one of the mesh direction, creating a distortion of the wave front [87].

2.3.4 Limit conditions

One of the main challenges for modelling the propagation of electromagnetic waves is to create permeable boundaries to simulate an open medium. Indeed, if the limits of the computational domain do not correspond to any real interface, the waves should be able to cross them without any reflection on the borders. This could be simply obtained by generating a domain wide enough so that the waves never to reach the borders, but this would be particularly slow and inefficient in terms of computing cost [87].

Different limit solutions have been elaborated to tackle this problem. The oldest one (1981) is Mur's absorbing boundary conditions [91]. This method uses one-way

wave equations allowing the waves to propagate in only one direction. It gives excellent theoretical solutions but numerical dispersion lowers the quality of the results that can be observed in reality.

In 1994, Bérenger [92] introduced the Perfectly matched layers (PML). In opposition to the ABC, they do not let the waves cross the borders, but they are designed to absorb them. The difficulty is to ensure that there will not be any reflection, for any incident angle, at the interface between the propagation medium and this absorbent layer artificially placed all around the domain. For this reason, the PML are constituted of different layers, with a gradation in the electromagnetic properties. The efficiency of PML increases with the number of layers, but a higher number of layers induces a higher computing cost and a smaller effective computing domain. By comparison to the ABC, the PML give better results, but for an increased computing time. Some variants of the PML can also help to improve again their efficiency [87, 93].

In the FDTD program GprMax [75] that will be used in this work, both the ABC and the PML can be implemented. Their efficiency will be compared in § 3.1.4.2.

Chapter 3: Study of the high frequency antennas signal

As explained in Chapter 2, radar waves behaviour can be analytically described in many situations. However, when the complexity of a problem increases, Maxwell equations become impossible to solve analytically. Numerical modelling must be used to solve the wave propagation problem, or analytical solutions must be developed with strong simplifying assumptions, which may not be valid in all cases.

The numerical modelling may predict with a very good precision the radar wave propagation. However, synthetic radargrams will only be comparable to experimental measurements under the condition that the radar waveform is accurately introduced into the program. It is thus important for the radar user to exactly know the features of the wave emitted by his device.

Similarly, analytical equations, such as the reflection coefficient for the thin layers, may only be applied to determine the parameters from real data when all the other phenomena have been taken into account. In particular, the geometric attenuation and the radar radiation pattern of the antennas have to be quantified in order to be integrated into the equations. It is also essential to be aware of the limitations of the selected relationships.

But if a good knowledge of the incident signal may help calibrating the numerical simulations and establishing the limitations of the analytical expression, it can also help to improve the field measurement routine. Indeed, good acquisition parameters and adapted measurement configurations will help to decrease the measurement noise and maximize the useful information into the different signals.

This chapter is divided into three sections. In the first one (§ 3.1), the materials and methods of the experimental and numerical tests performed throughout the

whole thesis are presented. The antennas system is described, as well as the global methodology for estimating the reflection coefficient, the test configurations and the numerical parameters that will be used to perform the simulations.

In the second section (§ 3.2), different properties of the radar signal are studied in detail: the frequency content, the time drift, the signal noise, the geometric attenuation and the radiation pattern.

Finally, in § 3.3, the specific problem of the in-situ determination of the surface concrete permittivity is tackled. Different methods are compared for the determination of the permittivity of a concrete slab, in order to determine an acquisition routine that can be used to optimize the permittivity measurements.

3.1 Materials and methods

This section presents the materials and methods that will be used in this work to determine the reflection coefficient from experimental measurements and numerical simulations.

3.1.1 Instrumentation

Our high frequency system is composed of two 2.3 GHz antennas manufactured by Malå Geoscience. The antennas are shielded to prevent the wave propagation above the antennas. They are connected by coaxial cables to a control unit; this is connected to a laptop for data visualization and storage. They can be equipped with a displacement registration system (wheel). Each antenna encloses two bowtie antennas: a receiver and an emitter. They are positioned 2 mm above the bottom of the shielded box. The geometry of the antennas, deduced from manufacturer information (Christer Renström, personal communication, May 18, 2009), is depicted in Figure 45.

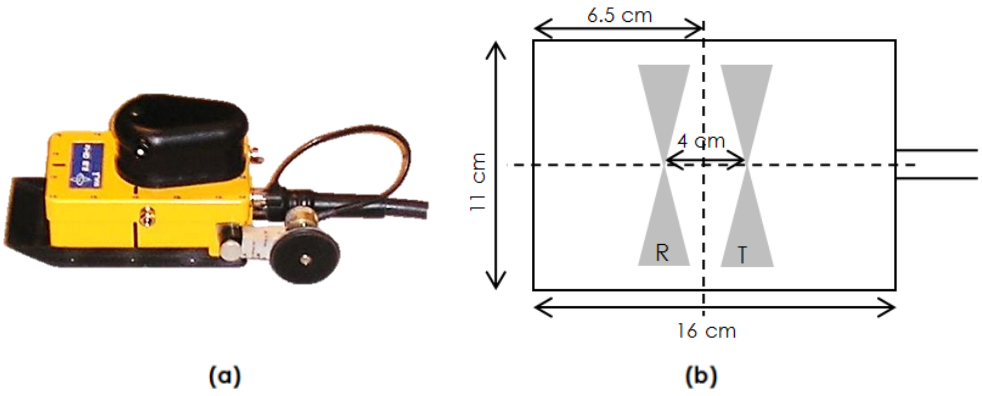

Figure 45: (a) High frequency GPR antenna; (b) antenna geometry.

The high nominal frequency of the antennas (2.3 GHz) maximizes the resolution. According to the manufacturer, their radial resolution is approximately equal to 1.3 cm and their maximum penetration depth equal to 40 cm.

3.1.2 Tests for the determination of the reflection coefficient

In §§ 2.1.7 and 2.2, the analytical expressions for the determination of the reflection coefficient were detailed. To be able to use those expressions to characterize a buried material, it is important to be able to extract the reflection coefficient from the measurements. But when a radar measurement is performed, many other parameters influence the measured signal [55]. Those parameters are listed in Figure 46 for a two layers medium.

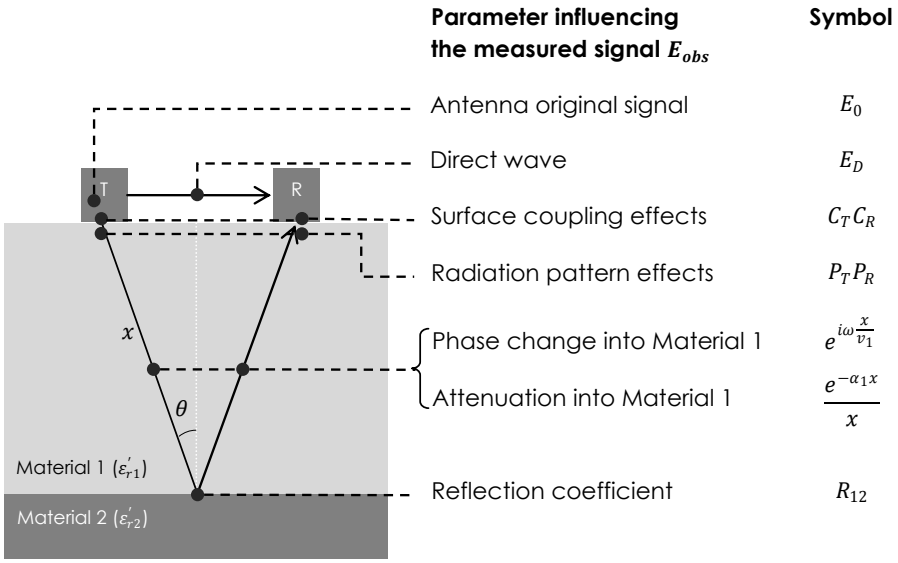

Figure 46 : Parameters influencing the electric field E_{obs} measured over an interface buried in an homogeneous material.

The amplitude of the electric measured field E_{obs} can be written:

$$\begin{aligned} E_{obs} &= E_D + E_{refl,12} \\ &= E_D + E_0 * C_T C_R P_T P_R * e^{i\omega\frac{x}{v_1}} * \frac{e^{-\alpha_1 x}}{x} * R_{12} \end{aligned} \quad (114)$$

In (114), E_0 is the antenna original signal, E_D is the direct signal travelling from the transmitter to the receiver. The coupling effects, C_T and C_R, and the radiation pattern effects, P_T and P_R, are functions of the incident angle θ and of the angular velocity ω. x is the distance covered into material 1, v_1 and α_1 are respectively the speed and the attenuation coefficient in this material and can depend on the angular velocity if the material offers dispersive properties (see § 2.1.6).

3.1.2.1 General method for the extraction of the reflection coefficient

The reflection coefficient R_{12} can only be extracted from a single measurement E_{obs} if all the parameters in (114) are perfectly known, included the exact radiation properties of the antennas. This is the strategy used by the full-waveform inversion, in which the antenna radiation must be measured in order to calibrate the forward equations [64].

If the radiation pattern of the antenna into the material 1 (P_T and P_R) can be estimated (which is the case when all the targets are situated in the far field – see § 3.2.5.1), another strategy is to perform a CMP measurements and to work with the relative amplitudes between two points of different incidences. This method is used in diverse APVO curves inversion techniques for geological applications [55, 58].

The method that will be mainly used in this thesis consists in comparing the amplitude measured on the interface $E_{refl,12}$ (Figure 47 (a)) to the amplitude measured on a perfect reflector placed at the same depth (Figure 47 (b)). As the antennas are placed in the exact same position, all the surface terms and the propagation terms will be exactly the same as for the interface between materials 1 and 2. Only the reflection coefficient R_{12} in (114) will be equal to -1.

$$\begin{aligned} E_{obs,\ PR} &= E_D + E_{refl,PR} \\ &= E_D + E_0 * C_T C_R P_T P_R * e^{i\omega\frac{x}{v_1}} * \frac{e^{-\alpha_1 x}}{x} * -1 \end{aligned} \tag{115}$$

When the incident wave is a pulse and the interface is sufficiently deep, the reflected amplitude E_{Refl} can easily be separated in the global radargram E_{obs} from the direct wave E_D, because they occur at different times (see Figure 24). But in many cases, the determination of the reflected wave amplitude will require the direct wave to be suppressed from the measured signal. This is especially the case when the incident wavelet is a continuous sine or if the interface is situated at a low depth. The direct wave travels partly in air and partly in the material surface: that means that its exact behaviour is highly complicated and poorly described by analytical expressions. The best solution consists in measuring it separately in a zone without target and then suppressing it from all the measured signals (Figure 47 (c)).

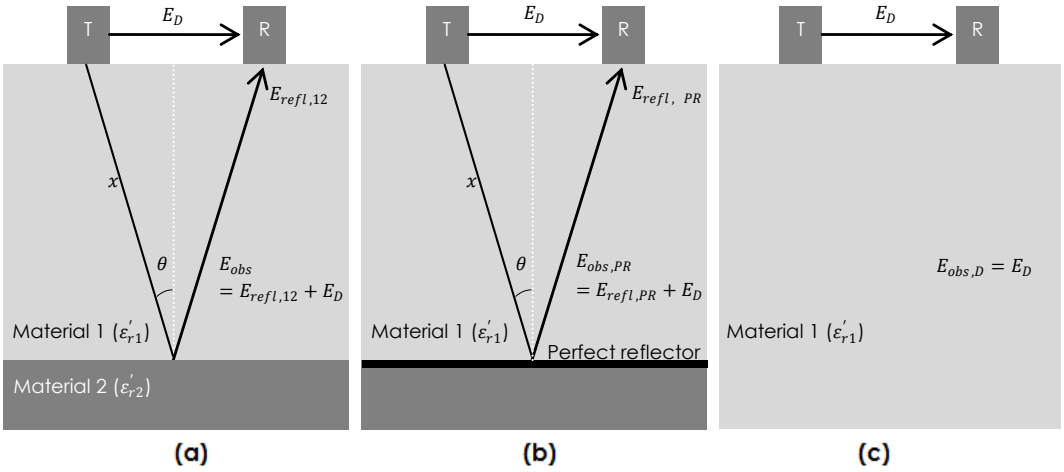

Figure 47 : Comparison of the electromagnetic field amplitude observed (a) after reflection on an unknown interface (E_{obs}); (b) after reflection on a perfect reflector ($E_{obs,PR}$) and (c) when only the direct wave is measured ($E_{obs,D} = E_D$).

The equation allowing to determine the reflection coefficient of the interface R_{12} is then:

$$R_{12} = -\frac{E_{obs} - E_D}{E_{obs,\ PR} - E_D} \tag{116}$$

3.1.2.2 Experimental setup for the determination of the reflection coefficient

In practical terms, the method described in the previous section is straightforward when the material 1 is air: it only requires to immobilize the antenna in front of the surface and to perform measurements with and without placing a thin perfect reflector (as an aluminium foil) on the surface. This method will allow to determine the permittivity of the material (see the application § 5.2.3.3).

When the interface or the thin layer is embedded into another material, the method described in the previous section requires to be able to place a perfect reflector at the investigated depth. For all the laboratory tests performed in this thesis, we used two 10 cm thick concrete slabs. They were cast horizontally with self-compacting concrete so that they have one perfectly smooth and horizontal face (the formed one) while the other one is still relatively smooth, but not so perfectly (it is troweled).

The slabs have sufficient dimensions (50*80 cm and 50*100 cm) to avoid side effects. The 20 cm length difference between the slabs was decided to facilitate the handling of the superior slab. Indeed, two straps could be placed around the slab extremities, so that it could be lifted by a stacker without the need of specific anchorages into the concrete (Figure 48 (a)).

At the interface between the slabs, different situations were created (Figure 48 (b)). To perform tests with an air layer of variable thickness, an air gap was introduced through the use of plastic or wooden spacers of different thicknesses (ranging from 1 to 96 mm). Those spacers were placed between the two casted faces, so that the horizontal thickness variation of the layer was as small as possible.

The direct wave was obtained by performing the measurement without any spacer, on a double slab. The two very smooth formed surfaces were then in contact and we considered that the reflection at the interface (caused by surface imperfections) could be neglected. This direct wave was then subtracted from all the other signals. The measurements on a perfect reflector were performed by placing an aluminium foil between the slabs.

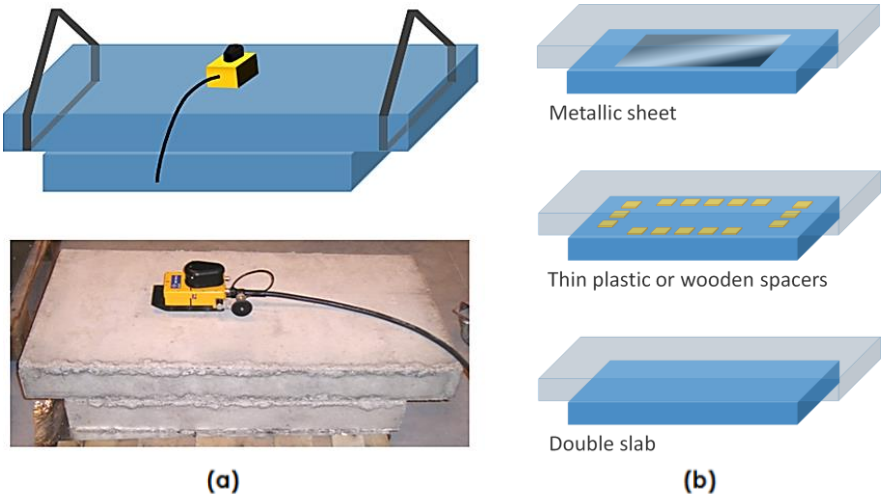

Figure 48 : (a) Experimental setup for the determination of the reflection coefficient. (b) Specific configurations for the measurement of the perfect reflection, the air thin layer and the direct wave.

For specific tests, we also measured the reflection of a slab suspended over the void, to measure the concrete-air reflection coefficient (§ 3.3.2.3), and we placed a bituminous layer between the slabs, to evaluate its permittivity and test another material than air (§ 5.2.3.3).

3.1.2.3 Specific problem of the post-critical incidence

If the incident angle is too large, and especially if it is superior to the critical angle, the method described in § 3.1.2.1 will not be totally valid anymore. Indeed, in addition to the reflected wave, a lateral wave with a critical incidence into the matrix will propagate into the layer (Figure 49, wave c). A similar wave, with a critical incidence as well, will be reflected on the layer or on the metallic reflector, and be refracted at the surface to propagate as a surface wave (wave d). Another one will propagate at the surface before propagating into the matrix and reflecting into the layer (wave e). We believe that it should be possible to develop equations describing the propagation of those waves, just as it was done for the lateral wave propagation in § 2.1.7.3). Nevertheless, their radiation pattern

coefficients $P_T P_R$ in (114) is different than for the reflected wave b because their incident angle is different. If this phenomenon is not taken into account, it will decrease the precision in the reflection coefficient determination.

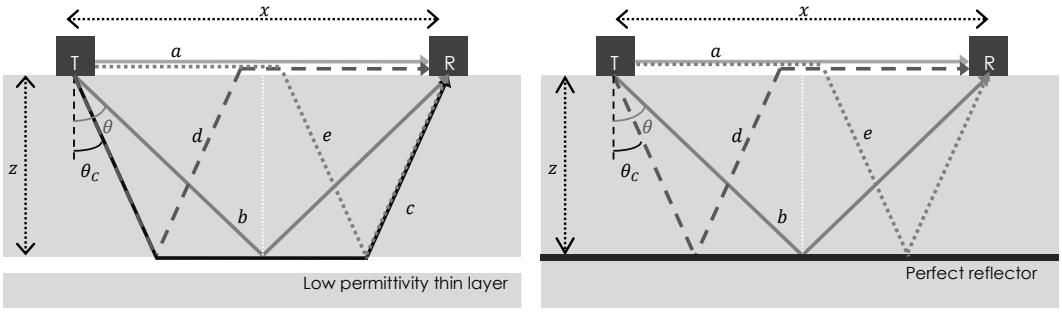

Figure 49 : Waves measured in a GPR reflection test with a post-critical incidence: (a) direct wave, (b) reflected wave, (c) lateral wave and (d) (e) surface-lateral waves.

When performing numerical simulations, this problem can be easily avoided by modelling antennas embedded into concrete (Figure 50). This method will be used in § 4.1 to compare the different analytical expressions for the reflection on thin layers.

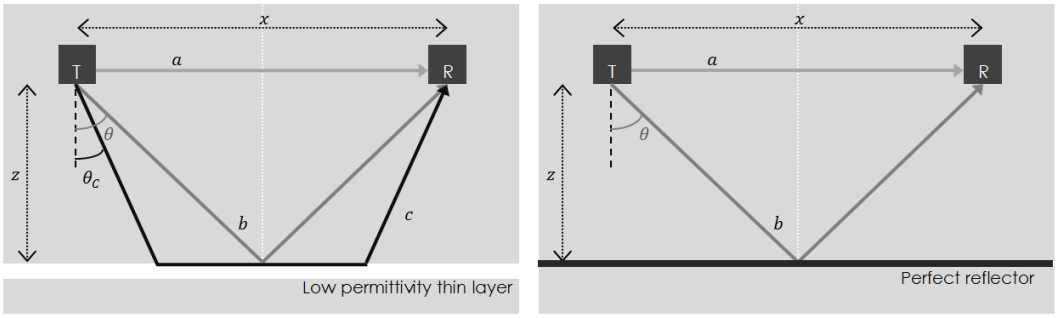

Figure 50 : Waves measured in a GPR reflection test with a post-critical incidence and embedded antennas: (a) direct wave, (b) reflected wave and (c) lateral wave.

Embedding the antennas is obviously not an option in the case of experimental tests. This problem will be discussed in § 4.2.

3.1.3 Tests configurations

In this section, the different acquisition configurations that will be used in this thesis are described. The results of the tests will be described in the next chapters.

3.1.3.1 Static tests

The static tests refer to all tests for which antennas are stationary. Their objective can be to characterize the direct wave or to investigate a structure offering low variations in the lateral directions. The advantage of static tests is that each

measurement can be reproduced several times in order to increase the number of stacks and decrease the noise.

The static tests can be performed with one antenna (monostatic) or two antennas (bistatic). A monostatic measurement can be automatically performed simultaneously to any bistatic measurement. When a static test is performed with two antennas, we always placed the two antennas front faces in contact (see Figure 52 (a)). In this configuration, both emitter-receiver offsets are perfectly known and determined by the antennas geometry (Figure 45 (b)).

We especially distinguish:

- the direct wave in the air: the antennas are lifted in the air in a direction insuring that the wave would not encounter reflectors before several meters. If the test is bistatic, the second antenna is pressed against the first one, recreating in air the initial position of a CMP test (Figure 51 (a)).

- direct wave on the material surface: designates a test in which the antenna is placed on the surface of a material, which is sufficiently thick to observe the propagation between the two antennas without interaction with deeper reflections. In the tests on concrete, the direct wave was often obtained by superposing two smooth slabs. This method is not perfect because the roughness of the slabs is not zero, but it gives a good approximation of the direct waves. The bistatic version of this test corresponds to the first trace of a CMP, but with multiple measurements to decrease the noise through stacking (§ 3.2.3.1).

- surface reflection test (Figure 51 (b)): the radar is placed parallel to the surface at a distance of about 20 to 40 cm (if the sample size is limited, the antenna should not be too far from the surface otherwise the edges would appear in the radargram). A second measurement should be performed from the same distance with a metallic sheet covering the surface. With this method, the reflection coefficient can be directly determined by dividing the reflected amplitudes. The distance from the antenna to the surface does not have to be precisely controlled if the two measurements are performed from the exact same position.

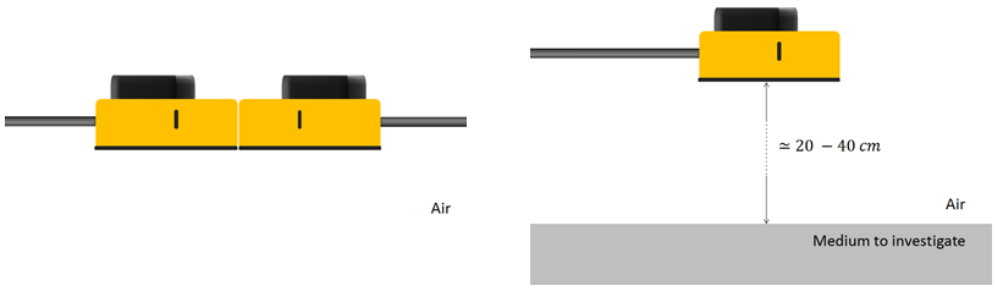

Figure 51 : (a) Antennas configurations for a bistatic measurement of the direct air wave; (b) Configuration for surface reflection measurements.

3.1.3.2 Profile tests

The profiles acquisition is the fastest and most common test configuration used with GPR. It is monostatic and a wheel is used to estimate the antenna displacement. In the framework of this thesis, measurements are performed every 2 to 5 millimetres, depending on the required precision and on the possibility to slow down the acquisition.

3.1.3.3 Common mid-point tests

A regular CMP is performed by moving the two antennas away from a central initial point at the same speed (see Figure 23). In reality, if the test is performed manually without specific equipment, there will always remain speed differences between the two antennas: it will create imprecisions in the radargram. For this reason, if the medium is not too laterally variable, it is often preferable to move only the antenna equipped with a wheel. This is the equivalent of a "walk away" test in seismics. It is not rigorously a Common Mid Point measurement, but the higher precision in the radargram allows a better parameters determination. For this reason, all CMPs in this work are performed with one antenna remaining still. This antenna should be placed sufficiently far from the edges of the structure (at minimum 10 cm from the antenna extremity) in order to avoid complex side reflection in the radargram (Figure 52 (a)).

3.1.3.4 Attenuation tests

To measure the attenuation of the radar wave as a function of the distance of the reflector (see section 3.2.4), the radar is fixed on a rolling trolley (Figure 52 (b)). As the wave speed in air is perfectly known, there is no need to use the measuring wheel and the distance from the reflector can be exactly determined from the time shift in the radargram between the direct wave and the reflection. During the test, the radar is slowly moved away from the object whose reflection is studied.

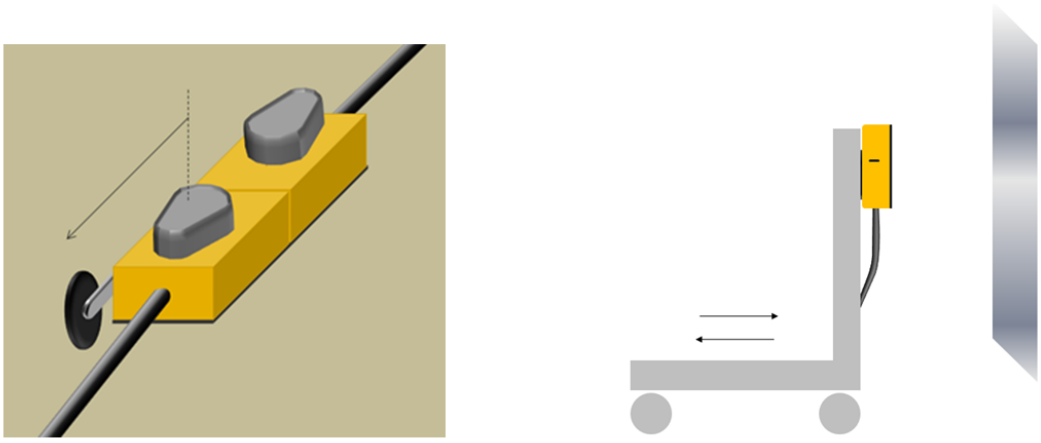

(a) (b)

Figure 52 : (a) Configuration for the measurement of a CMP; (b) Configuration for signal attenuation in air measurements.

3.1.4 Finite differences modelling program

The numerical simulations were performed with the program GprMax (version 2.0), designed by Giannopoulos [75]. In this section, we determine all the numerical parameters that will be used in the simulations throughout this work.

3.1.4.1 Incident signal

In three dimensions, different signal sources are available in GprMax. Among others, the emitted signal can be a hertzian dipole, a plane wave or a line source. In two dimensions, the only possible source is a line source (corresponding to a point in the 2D model). In 2D and 3D, different excitation signals are available, as the sine wave or a Ricker pulse, and the user can also introduce a personalized signal.

We designed an excitation file allowing to obtain a modelled direct wave in air (with the antennas 4 cm spaced) similar to the direct wave measured by our radar. The excitation signal was adapted from the direct wave measured in air with a trial-and-error approach. The initial temporal signal was inverted, resampled, scaled, time-shifted, low-passed and multiplied by an adequate Gaussian curve to obtain the personalized excitation file. As it can be observed in Figure 53, the direct wave in air measured with the antennas and obtained after modelling are similar. This allows a good qualitative visual comparison of the results.

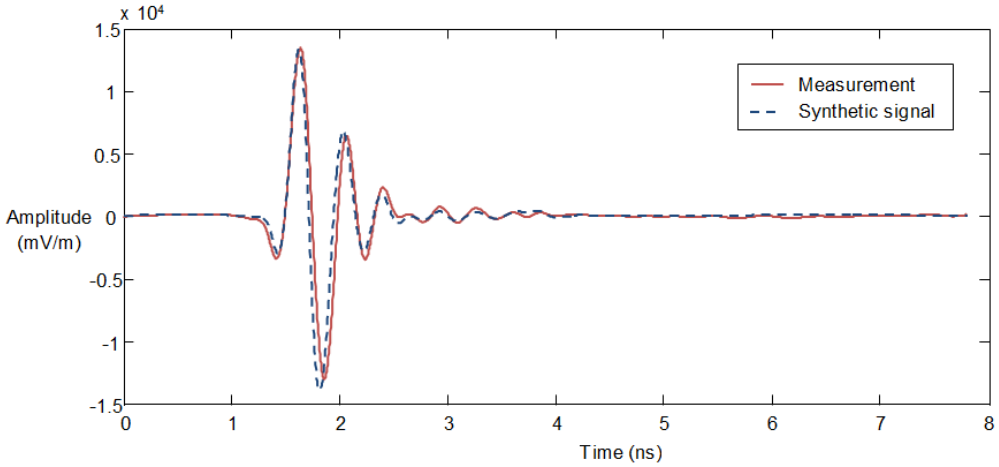

Figure 53 : Comparison of the measured direct wave in air and the modelled direct wave in air obtained with a realistic excitation signal.

3.1.4.2 Boundary conditions

Two different limit conditions are available in GprMax to make the model boundaries permeable to the radar waves: the PML (Perfectly Matched Layers) and the ABC (Absorbing Boundary Conditions) (see § 2.3.4). Both methods were applied to a simple case in order to evaluate their efficiency. We kept the default parameters of the program for these limit conditions. The ABC order is then equal to 3 (the highest) and the PML are constituted of 8 layers.

The model is a profile performed over a thin layer of air embedded into concrete, with an infinite lateral extensions. The modelling properties are described in Table 2, the geometry is detailed in Figure 54 and the radargrams obtained with the two types of boundary conditions are displayed in Figure 55.

Table 2 : Modelling properties for the boundary condition comparison test

Pulse	Ricker
Spatial step	0.125 cm
ABC order	3 (default value)
PML number of layers	8 (default value)

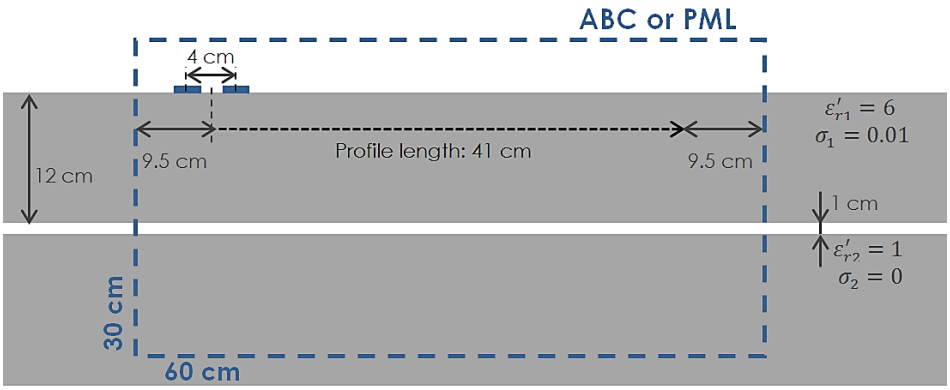

Figure 54 : Geometry of the 2D FDTD simulation performed to compare the ABC and PML boundary conditions.

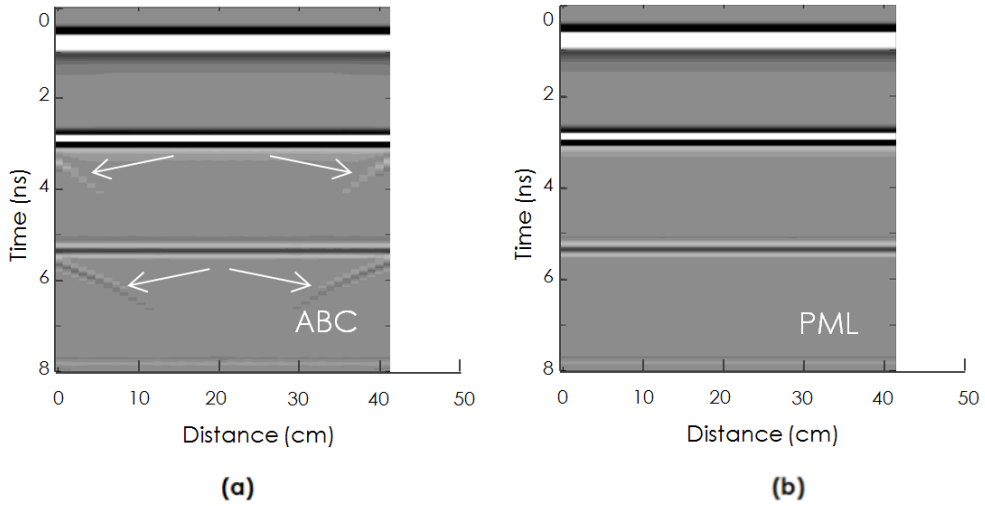

Figure 55 : Profiles measured on a thin layer embedded into concrete (Table 2) with (a) ABC and (b) PML as boundary conditions. The white arrows designate artificial reflections on the model boundaries.

When ABC are used as boundary conditions (Figure 55 (a)), artificial reflections are observable. They are especially visible when the border crosses the thin layer (white arrows). Those artificial reflections have a hyperbolic shape, similar to the reflections that would appear at the boundaries of a slab of limited dimensions.

With the PML (Figure 55 (b)), no reflections are visible in the radargram, because the amplitude of the artificial reflections is three orders of magnitude lower than with ABC. For this reason, we will only use PML in this thesis, despite the fact that they require a larger computation time.

3.1.4.3 Spatial and temporal discretization

If the spatial step selected for a simulation is too large, it is susceptible to decrease the results accuracy. In particular, a large spatial step will increase the numerical dispersion, which will affect the propagation in slanted directions (§ 2.3.3). For this reason, it is important to test a model with a multidirectional propagation to validate the selected spatial step.

To minimize the numerical dispersion, it is suggested [94] (§ 2.3.3) to limit the spatial step as function of the minimum wavelength λ_{min}:

$$\Delta x < \frac{\lambda_{min}}{10} \tag{117}$$

If we perform simulations using the nominal frequency of our antenna, 2.3 GHz, the minimum wavelength (in water) is equal to $\lambda_{min} = 1{,}45\ cm$, so a spatial step of $\Delta x = 1.25\ mm$ should be appropriate.

We tested this step in a simple configuration described in Figure 56 (a), in which the amplitude transmitted horizontally is compared to the amplitude transmitted with a variable angle.

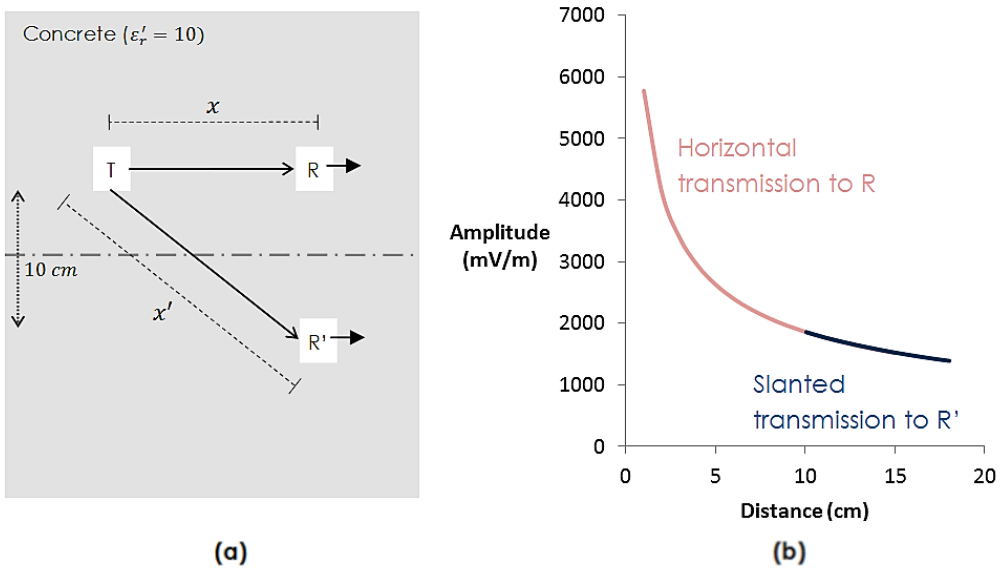

Figure 56 : FDTD simulation for the comparison of horizontal and slanted transmitted amplitude: (a) test configuration and (b) measured amplitude.

The amplitude transmitted with a slanted incidence is slightly higher than with the horizontal incidence, but the difference is really small (less than 1%). For the numerical dispersion concerns, the spatial step $\Delta x = 1.25\ mm$ is then acceptable.

But for this work focused on the reflection coefficient, we also need the simulations to be able to reproduce the wave reflections. To assess that the model is sufficiently refined for this application, we performed the same test comparing the amplitude reflected on a perfect reflector to the amplitude that would be obtained at the same total distance into concrete, without reflection (Figure 57). With this method, the influence of the numerical dispersion of the propagation is suppressed because the wave inclination is the same in both cases.

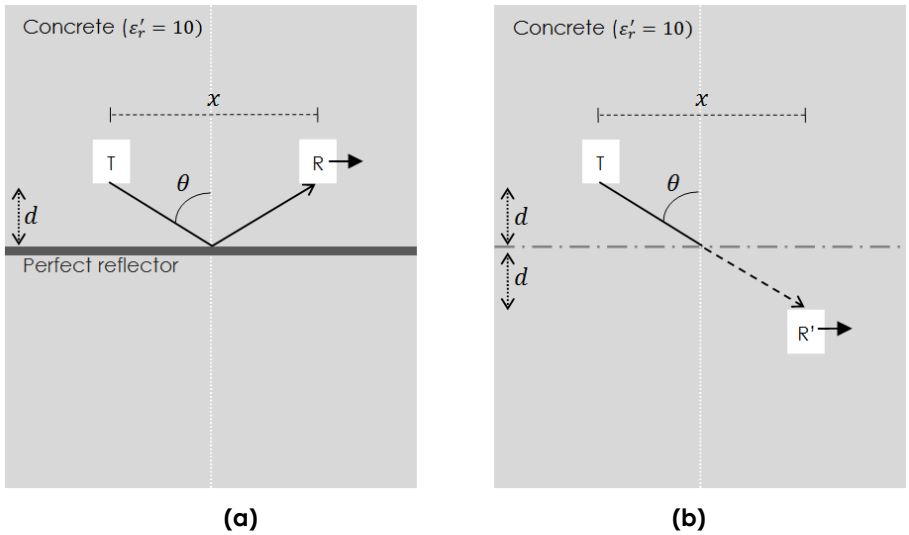

Figure 57 : (a) Configuration of the simulations to estimate the reflection coefficient on a perfect reflector; (b) Comparative simulations carried out to estimate the reference amplitude.

Results are displayed in Figure 58, for the step $\Delta x = 1.25\ mm$ and for a refined step $\Delta x = 0.625\ mm$.

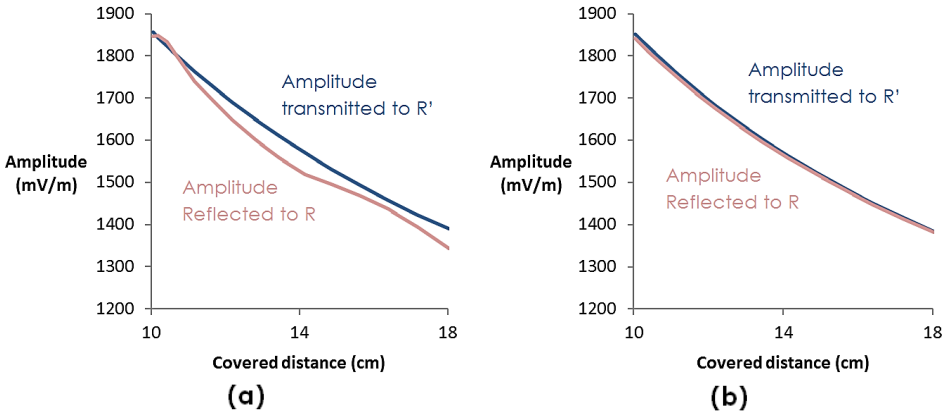

Figure 58 : Comparison of the amplitude reflected on a perfect reflector to the amplitude transmitted at the same distance (a) with a step of 1,25 mm; (b) with a step of 0.625 mm.

We observe that a refined step is necessary to obtain a good precision for the reflection coefficient. With this step, the maximum error is equal to 0.6% and observed for the smallest incident angle (5.7°). We used this refined step $\Delta x = 0.625\ mm$ for all the 2D simulations in the thesis. In three dimensions, the step had sometimes to be increased to 1 mm in order to satisfy the maximum memory allowance criterion necessary to launch simulations.

Using the spatial step selected by the user, the time step is automatically calculated by the program using Courant's number [87] (§ 2.3.2) multiplied by a time stability factor of 0.97.

3.1.4.4 Determination of the reflection coefficient

The reflection coefficient of an interface can be estimated by comparing the amplitude measured over the interface to the amplitude measured on a perfect reflector, from the same position (see § 3.1.2.1). We applied this principle to numerical simulations with embedded antennas (Figure 59).

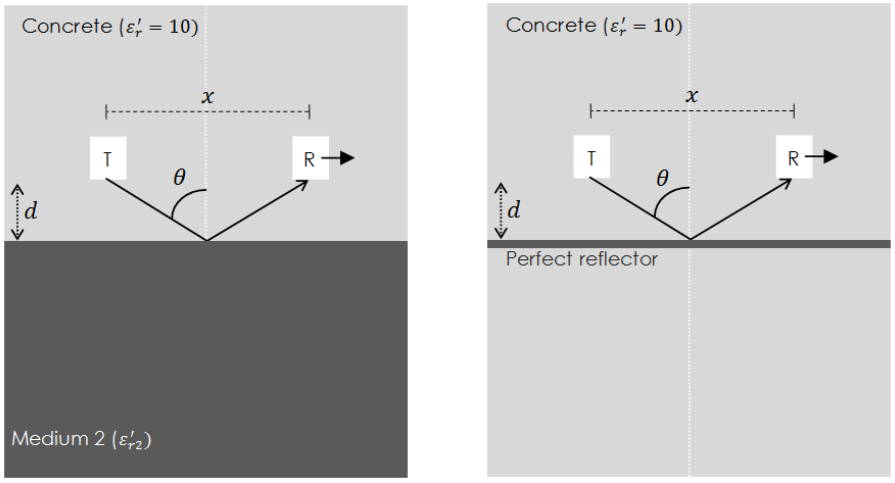

(a) **(b)**

Figure 59 : (a) Configuration of the simulations to estimate the reflection coefficient on interfaces; (b) Comparative simulation carried out to estimate the reference amplitude.

In Figure 60, the evolution of the reflection coefficients with the incident angle θ is traced for embedded materials with different permittivities ε'_{r2}. For each incident angle, the reflected amplitudes measured on those various interfaces are determined using equation (116). The reflection coefficients obtained by this method for a continuous sine wave are compared to the reflection coefficients estimated by the Fresnel equations (49) (which corresponds to a plane wave approximation) and to the coefficients estimated with the equations taking into account the spherical reflection (§ 2.1.7.3).

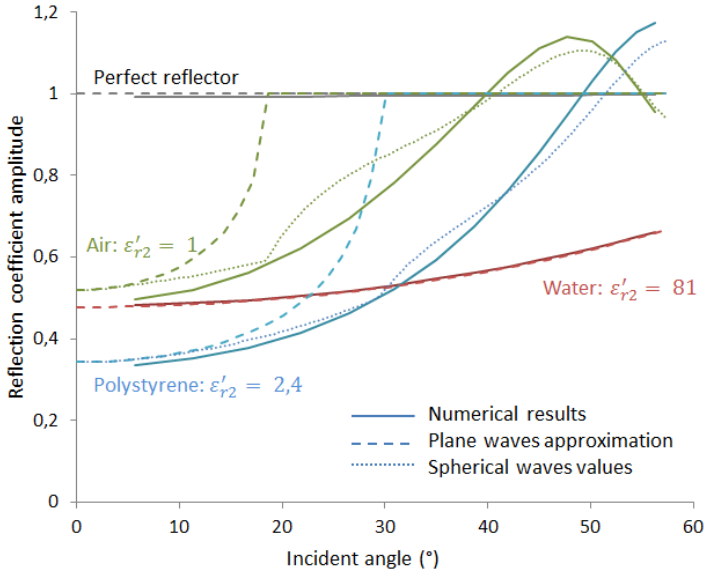

Figure 60 : Numerical estimation of the reflection coefficient on interfaces between concrete ($\varepsilon'_{r1} = 10$) and different materials, and comparison (in dotted lines) with the Fresnel and spherical waves reflection coefficients.

We observe that, for the materials presenting a lower speed than concrete (for example water), the results are very well predicted by both the plane and spherical waves reflection coefficients (which are quasi identical). This is logical, as there is no critical angle when the speed of the deeper material is lower, and no lateral wave either. In this case, the Fresnel equations are totally accurate.

When the lower material has a higher speed than concrete (for example air), we observe a large discrepancy between the plane wave prediction and the numerical reflection coefficients. As the reflection interface is situated at only 5 cm from the source, the wave front curvature is important and the assimilation to a plane wave gives results very far from the reality. In addition, when the incident angle is superior to the critical angle, the lateral wave is transmitted through the second medium (§ 2.1.7.3) and interferes with the reflected wave, creating an apparent reflection coefficient superior to one.

Those phenomena (circular wave front and lateral wave interferences) are taken into account by the equations of the spherical reflection coefficient, which gives a better prediction of the numerical result. The estimation of the reflection coefficient at the critical angle and the prediction of the interference peaks position are fairly good. The method still presents some discrepancies: the peaks amplitude is underestimated and the amplitude for angles just greater than the critical angle is overestimated. This is due to some approximations in the method, which are accentuated by the fact that the distance source-interface is very small (§ 2.1.7.3).

When the incident signal is a pulse and not a sine wave, the same method can be applied to determine the reflection coefficient, using the peak-to-peak amplitude of the reflected wavelet (see § 5.1). The wavelets corresponding to the reflection on the interface and to the critically refracted wave rapidly separate

after the critical angle, and their interaction is limited. The numerical reflection coefficients are compared to the plane waves and spherical waves predictions in Figure 61.

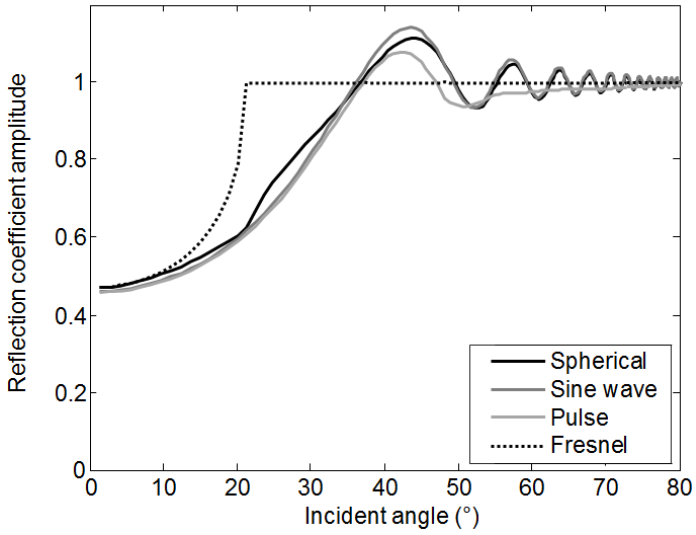

Figure 61 : Reflection coefficient amplitude for a concrete ($\varepsilon'_{r1} = 7.7$)- air interface, measured from a distance of 10 cm. Comparison of the theoretical estimations for plane and spherical waves to numerical results obtained with a realistic pulse and a sine wave.

The replacement of the sine wave by a pulse limits the oscillations to incident angles under 55°. The peak of maximum amplitude is comprised into this zone and is still important even if its amplitude is lower than for the sine wave ($R_{max,pulse} = 1.08$ while $R_{max,sine} = 1.14$). For incident angles larger than 55°, the reflected and refracted waves arrive with a sufficient time interval to stop interacting into the radargram (see Figure 24). The fact that the reflection coefficient with the pulse is not exactly equal to one after wavelet separation is probably due to the change of phase of the reflected wave (Figure 29).

From these observations, we conclude that the plane wave approximation should only be used to approximates angles close to zero if the lower medium has a higher permittivity. For larger angles, the spherical approximation is more appropriate, but the approximation is valid only for limited angles when the incident wave is a pulse.

3.1.4.5 Comparison of the 2D and 3D modelling

Finally, we tested for possible 2D/3D artefacts, by performing identical tests in GprMax 2D and GprMax 3D. The spatial step and model dimension had to be adapted to be run in three dimensions. The modelling parameters are summarized in Table 3, and the modelling results are represented in Figure 62, in which they are compared to the Fresnel equations (49), as well as to the spherical equations (§ 2.1.7.3) and spherical equations adapted in two dimensions (Appendix 4).

Table 3: Modelling parameters for the estimation of 2D/3D artefacts

	2D	3D
Spatial step	1 mm	1 mm
Pulse	Ricker	Ricker
Nominal frequency	2.3 GHz	2.3 GHz
Source type	Line source	Dipole
Model dimensions	0.7 * 0.25 m²	0.7 * 0.25 * 0.1 m²
Approximate computation time	20 s	2h30

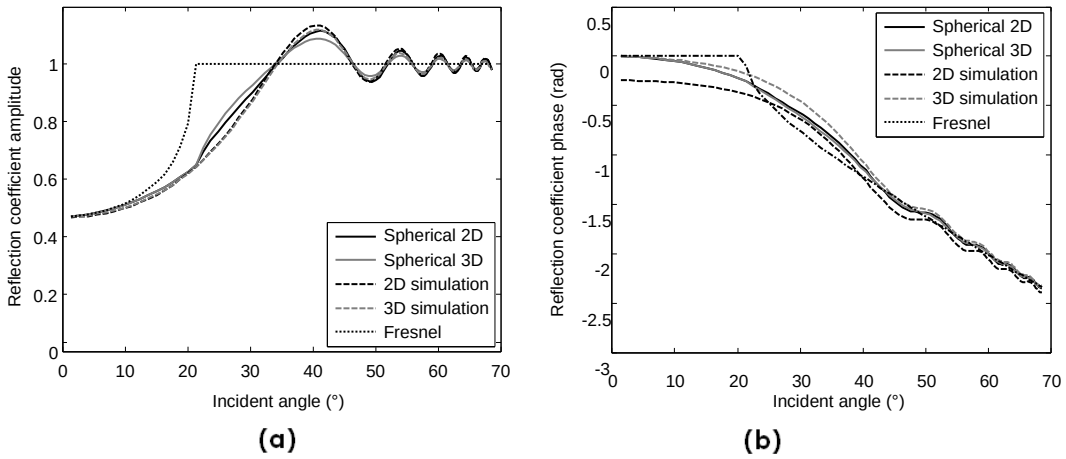

Figure 62 : (a) Amplitude and (b) phase of the reflection coefficients measured through 2D and 3D modelling and estimated with the spherical waves formula.

In the numerical simulations as well as in the spherical equations, the oscillations measured in two dimensions have higher amplitude than in the 3D simulation. In both cases, the equations overestimate slightly the amplitude of the oscillations and present a slope discontinuity at the critical point. The precision of the equations in 2D and 3D seems to be comparable, even if the slope discontinuity is less visible in two dimensions.

Concerning the phase, the reflection coefficients estimated from 3D modelling results tend to underestimate the phase analytical values, while the 2D simulation tends to overestimate them. The phase shift of π at a vertical incidence was well predicted in 3D but not in 2D.

3.1.4.6 Dispersion of the dielectric properties

The program allows using the Debye dispersive law (Appendix 2) for the evolution of the permittivity in the material as a function of the frequency. This function was not used in the framework of this thesis, assuming an invariable dielectric permittivity in the considered frequency range.

3.2 Study of the radar direct wave

The radar direct wave is a complex entity which depends on many parameters. The antenna model, with its specific geometry and nominal frequency is a key factor, but the test conditions (presence of a surface, distance of the target) will influence the measured amplitude. The acquisition parameters selected for the radar (warming up time, automatic stacking) will also have an influence on the measured signal.

It is important to have a good knowledge of the direct wave for two reasons. The first one is to optimize the acquisition parameters, so that the signal is as stable and noise-free as possible. The other reason is to be able to take into account a maximum of parameters when comparing experimental results to numerical or analytical data.

In this section, we performed different tests to characterize the radar direct wave and its interaction with the medium or with a reflector. First, we determined the frequency content of the direct signal. We evaluated its temporal instability and its noise, and the methods to decrease those problems. We also measured the geometric attenuation of the waves as well as the influence of the target shape on the backscattered amplitude. Finally, the radiation pattern of the antenna was measured on sand.

3.2.1 Radar direct air signal

3.2.1.1 Time-domain signal

The direct monostatic wave in the air was measured and traced in the time domain (Figure 63).

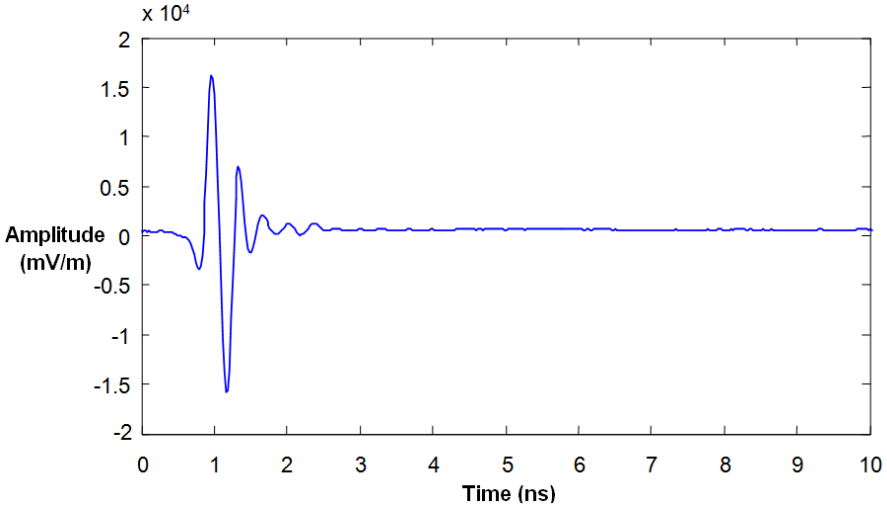

Figure 63 : Radar direct air signal in the time domain.

The direct signal is constituted of different lobes. If only the five first lobes, which present the largest amplitude, are considered, the pulse duration is about 1.2 ns. If we consider the ten first lobes, containing almost all the pulse energy, the pulse duration is about 2.1 ns.

3.2.1.2 Frequency content of the direct air signal

In Figure 64 (a), the frequency content of the signal, obtained through a fast Fourier transform (FFT) is represented. The constant component of the signal, appearing in the frequency spectrum as the amplitude at a null frequency, is important. It can be simply removed from the signal by subtracting its mean value in the time domain. The resulting spectrum is represented in Figure 64 (b).

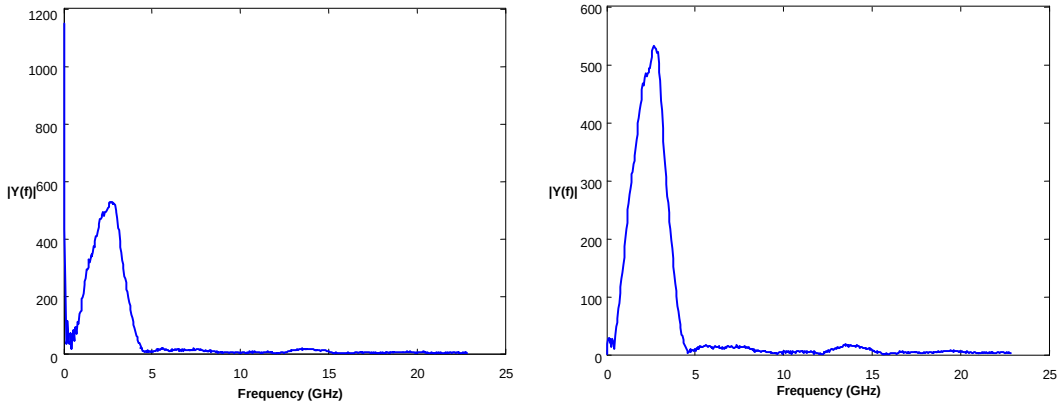

(a) **(b)**

Figure 64 : Amplitude Spectrum of the direct signal in air (a) rough signal; (b) after subtraction of the mean signal value.

The frequencies contained in the signal range from 0.5 to 4.5 GHz, with a maximum occurring at 2.8 GHz. This frequency is higher than the nominal frequency of the antenna (2.3 GHz). This spectrum appeared to be dependent on the antenna and the acquisition conditions (see Figure 69).

3.2.2 Signal time stability

The radar direct wave is often considered as the sum of an invariant signal and some noise, whose amplitude can be reduced through the use of signal treatment procedures. For example, if the noise may be assimilated to white noise, stacking the signal will ensure a reduction of the signal random noise. If the noise is due to strong background reflections, the visibility of local defects can be enhanced by removing the mean trace from the whole profile.

In practice, the signal emitted by commercial antennas is evolving with time, at least during the first minutes after the antenna has been switched on. The operator should then wait during a warming up time before making any measurement. In case no indication is given by the antenna manufacturer, the ASTM standard [95] suggests a heating time of 20 minutes. In this section, we will

observe the signal after ignition, in order to determine if this recommendation is adapted to guarantee a stable signal for our antenna.

3.2.2.1 Description of the signal stability problem

If we trace monostatic air direct wave measurements performed at different times after the antenna has been switched on, we observe that this direct trace highly changes within the first minutes up to one hour after starting up the system. The mean signal amplitude increases, the wave arrives earlier and the wavelet shape changes as well. All those changes weaken the efficiency of all the background removal methods.

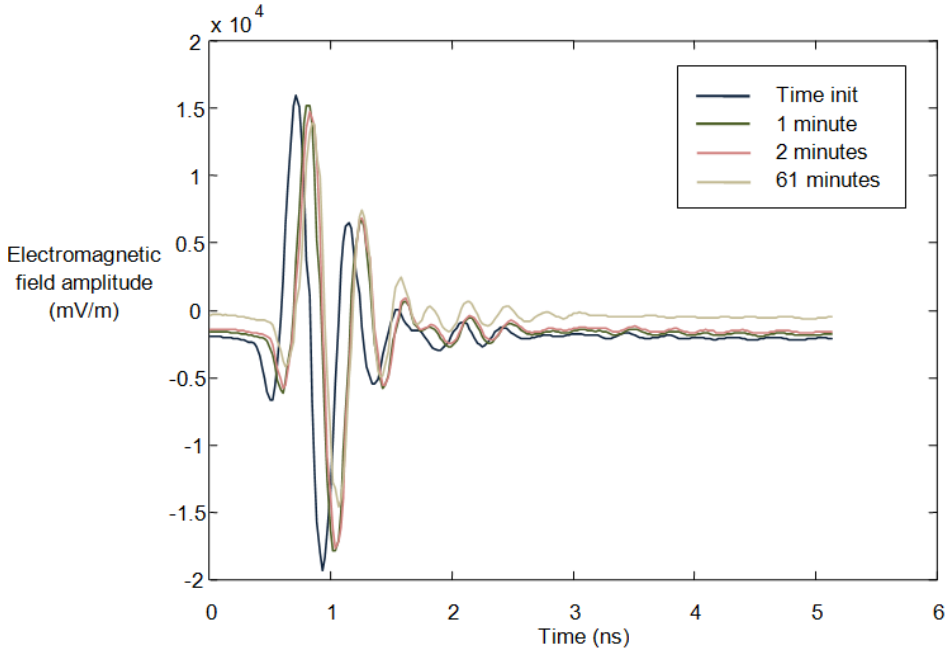

Figure 65 : Evolution with operating time of the direct signal in the air.

Evolution of the mean amplitude

We measured the evolution of the mean amplitude of the wave with time in order to evaluate the time required for the device to warm up.

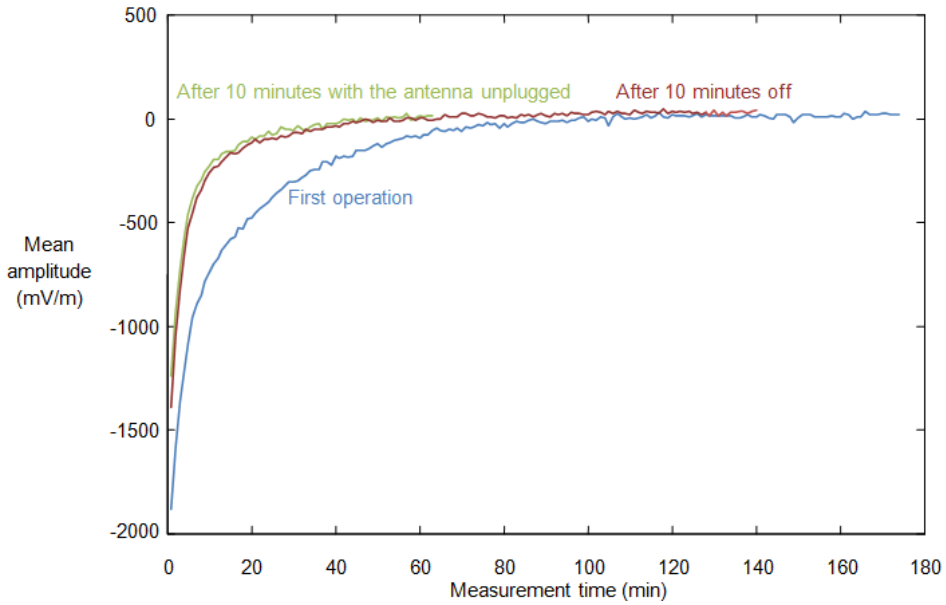

Figure 66 : Evolution of the direct signal mean amplitude in the first minutes after ignition.

The mean signal amplitude mainly changes during the first 60 minutes and can be considered as stabilized after 80 minutes. If the antenna is switched off for a short time after having been completely warmed up, its warming time was highly reduced (about 30 minutes if the antenna has been turned off for 10 minutes). The re-heating time is comparable if only the antenna is unplugged or if the control unit is turned off as well. This confirms that it is the antennas and not the control unit that require to be warmed up.

If the antennas are insufficiently warmed up, the use of signal processing routines, like the mean trace removal, can be compromised, especially for profiles needing a long measurement time. An example of bad imaging resulting from insufficient warm-up is given in Figure 67: it, corresponds to a CMP measured on a concrete slab just a few seconds after the antenna had been switched on. The background colour is visibly changing with time.

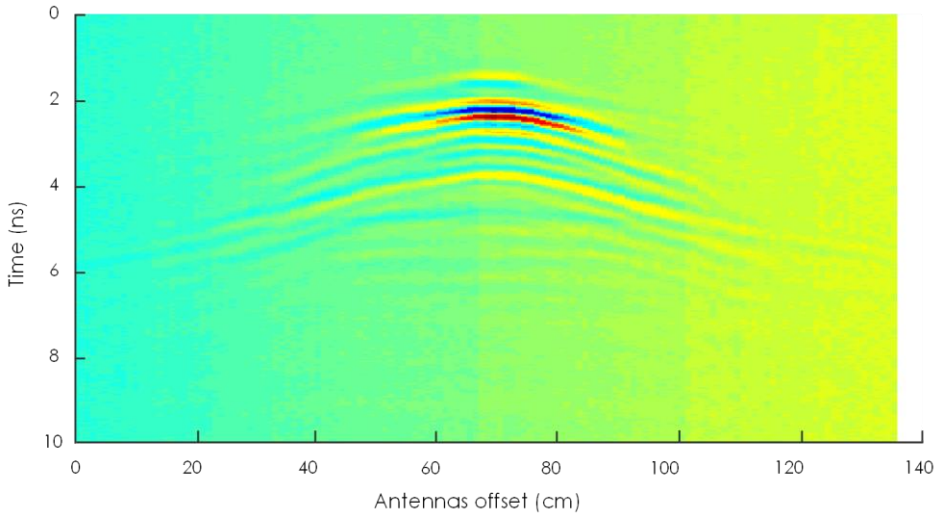

Figure 67 : CMP performed on a concrete slab after insufficient pre-heating time.

The mean signal change can be corrected by removing the mean value of each trace, which is not the case for the other parameters presented hereafter.

Evolution of the time of first arrival

A static surface reflection test was performed with a metallic reflector. The measurement times of the maximum and minimum signal peaks were then evaluated. They are represented in Figure 68.

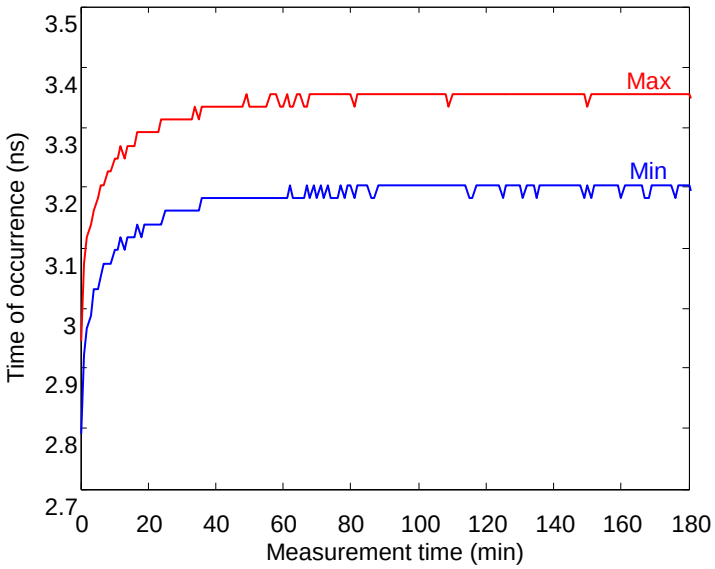

Figure 68 : Time of occurrence of the minimum and the maximum of the reflection.

The time at which the reflection is measured changes up to 0.4 ns while the antenna is warming up. If all reflection times are compared to a same time zero, this could lead to an error in the estimation of the depth of the detected interface. In this case, the error would be of 6 cm in air and about 2 cm in concrete. This error is divided by four if the reference time zero is estimated after 10 minutes of warming up.

Evolution of the frequency content

The amplitude spectra of the traces presented in Figure 65 are represented in Figure 69.

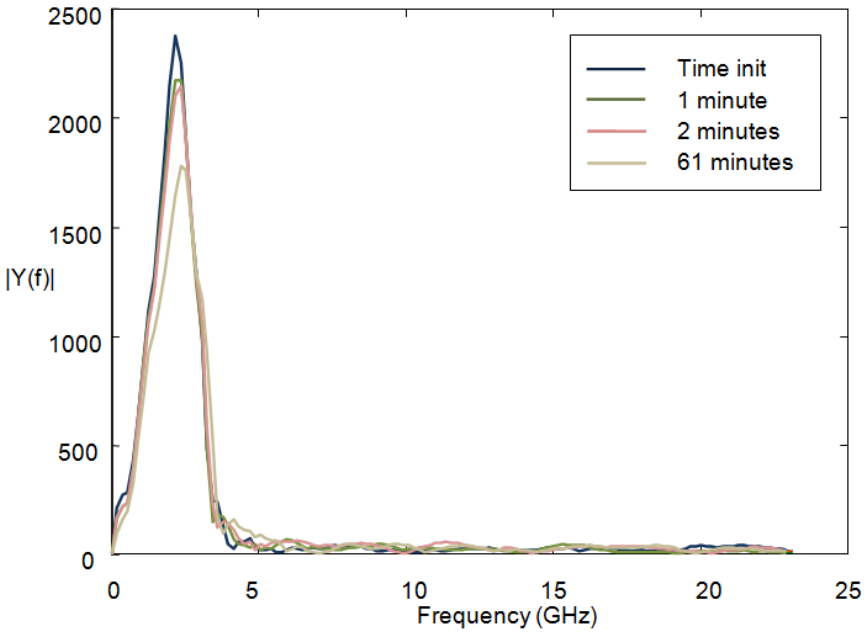

Figure 69 : Direct air waves frequency content evolution with the operating duration.

The amplitude peak decreases with time and the peak maximum seems to be shifted to slightly higher frequencies. If this evolution is present in a radargram, it can induce large errors when calculating amplitude ratios (for example when calculating a reflection coefficient).

Signal performance compliance

Different tests can be performed on the signal in order to insure the signal quality. We evaluated the system performances in different configurations, with a procedure inspired from the ASTM D 6087 – 05 standard, concerning the evaluation of asphalt-covered bridge decks [95]. The details of the tests are given in Appendix 5.

We showed that both the long-time and short-time stability criteria of the standard are not fulfilled by our antenna, even by increasing the stacks number. We conclude that the stability of our antenna signal is poorer that the stability that can be reached with horn antennas (for which the standard was initially written).

3.2.3 Signal noise

The noise in radar measurements is due to many factors. A distinction is often made between the background, or clutter, noise, and the white noise. Daniels [96] defines the clutter as "signals that are unrelated to the target scattering characteristics, but occur in the same sample time window and have similar spectral characteristics to the target wavelet". The clutter, often resulting from the antenna ringing, the non-target echoes or the target multiple echoes [67], should

be repeatable for two identical measurements. This is not the case of the additive white noise.

The additive white noise is due to the imprecision in the signal acquisition by the radar. Sources for this noise can be thermal electronic agitation or errors introduced by the analog to digital signal conversion [67]. Because the causes of this white noise are multiple, it is likely that its distribution function would be close to a Gaussian curve [97]. This is a consequence of the central limit theorem, stating that, under certain (fairly common) conditions, the sum of a large number of random variables, with unknown probability functions, will have an approximately normal distribution. One easy way to estimate the white noise level is to evaluate the standard deviation of the measurement, for each sample.

3.2.3.1 White noise reduction through signal stacking

The white noise can be lowered by using the stacking method, in which several identical measurements are performed at each point and then averaged. The useful signal is supposed to be the same in each signal; it will be visible in the average signal, while the white noise is supposed to be random and its average should then decrease with the number of stacks. This can be explained by the expression of the standard deviation of the sum of two random variables x and y:

$$\sigma_{x\pm y} = \sqrt{\sigma_x^2 + \sigma_y^2 + 2\sigma_x\sigma_y\rho(XY)} \tag{118}$$

Where $\rho(XY)$ is the correlation coefficient of the two variables x and y. If the variables are independent, which is the case for a normally distributed white noise, the correlation coefficient is zero. If, moreover, the standard deviation of the two sets of data x and y is random (which is the case here because we suppose that both data sets were measured in identical conditions and have thus identical properties), (118) becomes:

$$\sigma_{x\pm y} = \sqrt{2\,\sigma_x^2} = \sqrt{2}\,\sigma_x \tag{119}$$

The standard deviation of a signal is proportional to the signal itself. The mean of two signals is thus:

$$\sigma_{\frac{x\pm y}{2}} = \sqrt{2}\,\frac{\sigma_x}{2} = \frac{\sigma_x}{\sqrt{2}} \tag{120}$$

The same analysis can, of course, be performed for more than two signals.

$$\sigma_{n\ stacks} = \frac{\sigma_{initial\ signal}}{\sqrt{n}} \tag{121}$$

To illustrate this stacking property, we can compare the noise measured in static surface reflection measurements in function of the number of signals used in each

stack (Figure 70). The noise is estimated as the standard deviation of the Hilbert envelope of the signal amplitude.

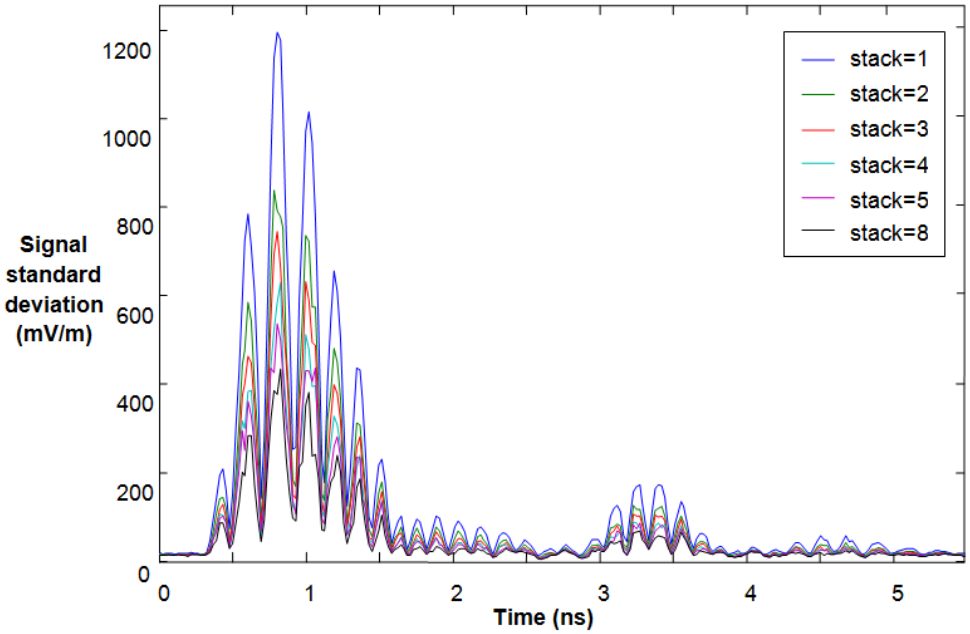

Figure 70 : Decrease of the signal envelope standard deviation due to numerical stacking.

As expected, the noise is reduced when the stacking number increases. The peaks noise amplitude is inversely proportional to the root square of the stacks numbers, as predicted by (121). This observation is not valid anymore for the parts of the signal presenting lower amplitude. For those parts, the noise does not tend to zero when the number of stacks increases. This is due to the fact that the noise, for those samples, is largely due to the time drift of the antenna. The same test realized with a shorter time between measurements should show a clearer tendency to zero.

The same test was performed using the automatic stacking option of our control unit. The results are compared to the post-processing numerical stacking in Figure 71.

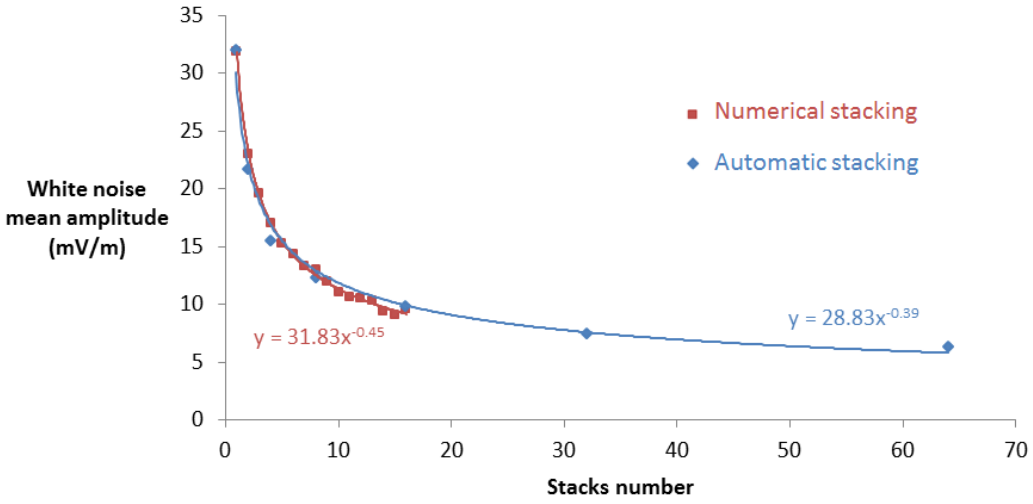

Figure 71 : Comparison of the white noise amplitude decrease obtained by numerical and automatic stackings.

The effect of automatic stacking seems to be similar to that of a numerical stacking. Actually, it is very interesting to use the automatic stacking function because all the measurements are performed in a very short time: this is very important in dynamic measurements, because it ensures that the stacked samples are measured in a quasi-identical position.

In addition to the time duration and the spatial distance between samples measurements, the automatic stack number is one of the factors that will limit the speed of measurement for profiles or CMPs. A stack value higher than 8 generally induces a very slow measurement.

3.2.3.2 Signal-to-noise ratio test

The signal-to-noise ratio was estimated for the direct wave as well as for the first and second reflection on a metallic plate, for seven different automatic stack values (1, 2, 4, 8, 16, 32 and 64). For each stack value, 125 measurements were performed with a time interval of two seconds. All those measurements were performed after a long warming up time of the antenna (more than 4 hours).

To estimate the signal, we calculated the mean signal for each stack value and we measured the peak-to-peak amplitude for each event. The noise is obtained by estimating the standard deviation of each sample and then picking its maximum for each event.

The signal-to-noise ratio was estimated by dividing each signal amplitude by twice the corresponding standard deviation (to correspond to the 62.8% interval of variation).

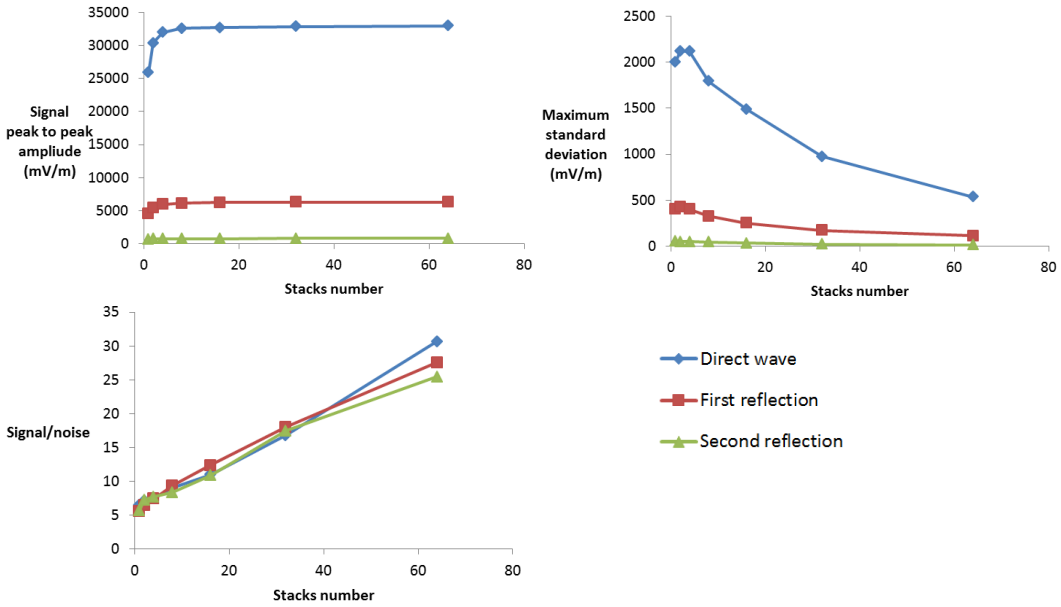

Figure 72 : Signal, standard deviation and signal-to-noise ratio.

We observe that the measured amplitude increases with the number of stacks, especially until 8 stacks, and then tends to stabilize. On the opposite, the measured standard deviation, representing the noise, decreases with the number of stacks, except for a very small number of stacks.

The signal-to-noise ratio seems to be relatively constant for the different parts of the signal and to evolve as an affine relationship of the number of stacks. The initial increase of the noise is indeed compensated by the increase of the signal amplitude. When 64 stacks were used, the signal-to-noise ratio seems to be higher for the direct wave than for the reflection events, but this trend has not been confirmed by other measurements.

3.2.4 Signal geometric attenuation

In addition to the ohmic and scattering attenuation described by Annan [70] (§ 2.1.4), the radar waves also undergo geometric attenuation due to their spreading into space.

Indeed, the wave power is preserved during its propagation. The power density is thus decreasing when the propagation surface increases. In three dimensions, with a spherical propagation, the energy decreases proportionally to the inverse of the squared radius.

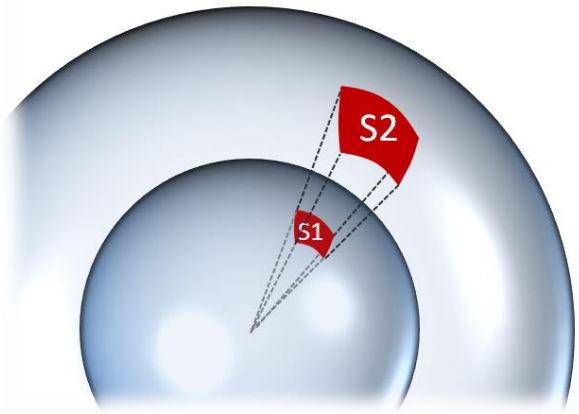

Figure 73 : Spherical spreading of the waves. The power received on the two sphere portions S1 and S2 is equal. The power density decreases thus proportionally to the propagation surface.

For this reason, in 3D propagation, we should observe:

$$P \propto \frac{1}{4\pi R^2} \tag{122}$$

In (122), P is the power density and R is the sphere radius. If the wave is submitted to intrinsic attenuation as well, the power remaining at a distance R from the emitter is given by [98]:

$$P = \xi_{TX}\, G_{TX} \frac{e^{-2\alpha R}}{4\pi R^2} P_{TX} \tag{123}$$

In (123), P_{TX} is the power emitted by the antenna, G_{TX} is the gain of the transmitting antenna and reflects the antenna radiation directivity, ξ_{TX} is the transmitter efficiency, α is the attenuation coefficient in the medium and R is the distance covered by the wave.

The wave amplitude is proportional to the square root of the power. The amplitude will decrease proportionally to the inverse of the radius. [99, 100]

$$\frac{A}{A_0} \propto \frac{e^{-\alpha R}}{R} \tag{124}$$

In two dimensions, the emitter is virtually a line source and the propagation surface is a cylinder, with a surface proportional to the radius. The propagated amplitude will decrease proportionally to the inverse of the radius square root.

$$\frac{A_{2D}}{A_0} \propto \frac{e^{-\alpha R}}{\sqrt{R}} \tag{125}$$

The results simulated in two dimensions should be corrected before comparison to laboratory experiments.

When the wave is reflected on an object, only a portion of the energy is sent back towards the antenna, depending on the target reflection coefficient (that has been studied in § 2.1.7) but also on its geometry. We will consider here simple geometries and perfect reflectors only.

If the reflector is localized and sufficiently far from the antenna, the radar range equation (126) can be applied [98, 101]. The range (R_g) is the target distance from the antenna. The total back and forward path length of the wave is thus approximately equal to 2 R_g if the emitting and receiving antennas are close. This equation considers that the reflector acts like a secondary source, generating a secondary spherical spreading of the wave energy.

$$\frac{P_{RX}}{P_{TX}} = G_{TX} \frac{e^{-4\alpha R_g}}{(4\pi)^2 {R_g}^4} \ \sigma \tag{126}$$

$$\frac{A}{A_0} \propto \frac{e^{-\alpha R}}{R^2} \tag{127}$$

The reflected power depends on the target radar cross section σ. This parameter is linked to the target projected cross section; but it also depends on its reflectivity (its reflection coefficient) and on its directivity (convex shapes will increase the geometric spreading). For most geometries, it is frequency dependant [102]. One exception is the sphere, when its radius is larger than $5\lambda/\pi$, which corresponds to the optical region. In this case, we have:

$$\sigma = \pi r^2 \tag{128}$$

With r the radius of the sphere. When its radius is inferior to $\lambda/2\pi$, the sphere is sufficiently small to be considered as being in the Rayleigh region. Its cross section can be evaluated by the formula [103]:

$$\sigma = \frac{\pi^5 r^6}{\lambda^4} \tag{129}$$

For spheres of intermediate radius (i.e. when $r \cong \lambda$), the scattering behaviour is submitted to Mie resonance and oscillates between $0.26\pi r^2$ and $4\pi r^2$[102]. Anyway, for all spheres, regardless their dimension, the received power P_{rx} remains proportional to the inverse of ${R_g}^4$.

If the reflector is an infinite plane perpendicular to the antenna, the wave is simply reflected symmetrically to the propagation that would have occurred without the presence of the plane reflector. If the antenna is shielded and only emits in one hemisphere, the infinite plane can virtually reflect all the energy; equation (124) can thus be directly used, with considering R as the total roundtrip distance to the plane target. Equation (126) can also be used by considering $\sigma = 4\pi R^2$. Different values have been proposed in [103] for initial spherical waves,

namely $\sigma = \pi R^2$ or $\sigma = \pi \lambda R/2$, when considering the first Fresnel zone of reflection only.

When the wave is reflected on a rebar, the secondary source acts like a line source, presenting cylindrical wave propagation. We should then have:

$$\frac{A}{A_0} \propto \frac{e^{-\alpha R}}{\sqrt{R^3}} \tag{130}$$

These equations are necessary for the inversion of measured amplitudes, in order to recover the parameters of the target. In the two next paragraphs, we tried to develop numerical and experimental tests to check their applicability in the case of shielded radar and targets whose dimensions could not be considered as negligible regarding the wavelength.

3.2.4.1 Estimation of the geometric attenuation in numerical simulations

2D and 3D simulations have been performed with GprMax to assess the influence of the geometric attenuation. It confirmed the equation (125) in two dimensions, and equation (124) in three dimensions, when the measured field has the same polarization as the emitting dipole (Figure 74 (a)). On the opposite, the electric field measured in the other direction (Ex if the dipole is oriented in the y direction), is not equal to zero but very low and the amplitude decreases then proportionally to the inverse of the squared distance (Figure 74 (b)).

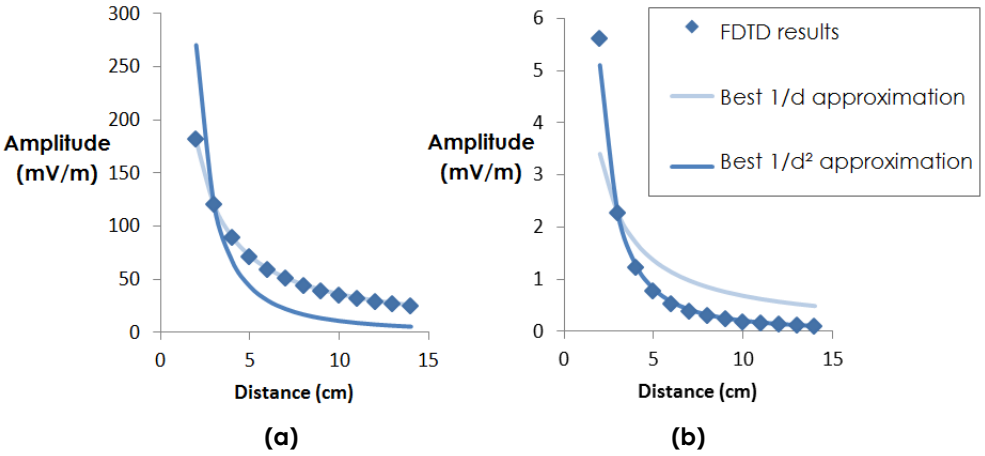

Figure 74 : Geometric attenuation of the (a) Ey and (b) Ex electromagnetic fields in a 3D simulation in which the emitting dipole has a y orientation.

3.2.4.2 Measurement of the geometric attenuation

We performed some laboratory measurements to confront the theoretical relationships to real laboratory conditions. Indeed, different papers [101, 104] have shown that measurements did not perfectly fit the theoretical relationships. One reason for this discrepancy is that, in the range equation, the source is

supposed to be punctual. With a bow-tie antenna, this only can be observed in the far field.

Measurement on a plane reflector

A large plane metallic reflector has been used for testing. The antenna was fixed on a movable support and initially placed close to the surface; it was moved away until reaching a large distance (4.3 m) from the surface and then moved back to its initial position (Figure 52 (b) p 80).

In order to achieve a precise estimation of the distance covered by the wave, it was evaluated from the time interval in the radargram between the measurements of the direct wave and of the reflection, rather than from measurements on the experimental setup. The time at which the direct wave could be observed was supposed to correspond to the time for which the wave has covered the four centimetres separating the two antennas. The speed of the waves in air being equal to 30 cm/ns, the distance estimated by this method, with f_s the sampling frequency, is directly given by (131):

$$distance\ [cm] = \frac{step_{refl} - step_{direct\ wave}}{f_s * 10^{-9}} * 30 + 4 \qquad (131)$$

In Figure 75, the different reflected peak-to-peak amplitudes are plotted as functions of the distance at which they have been observed (for distances above 8 cm).

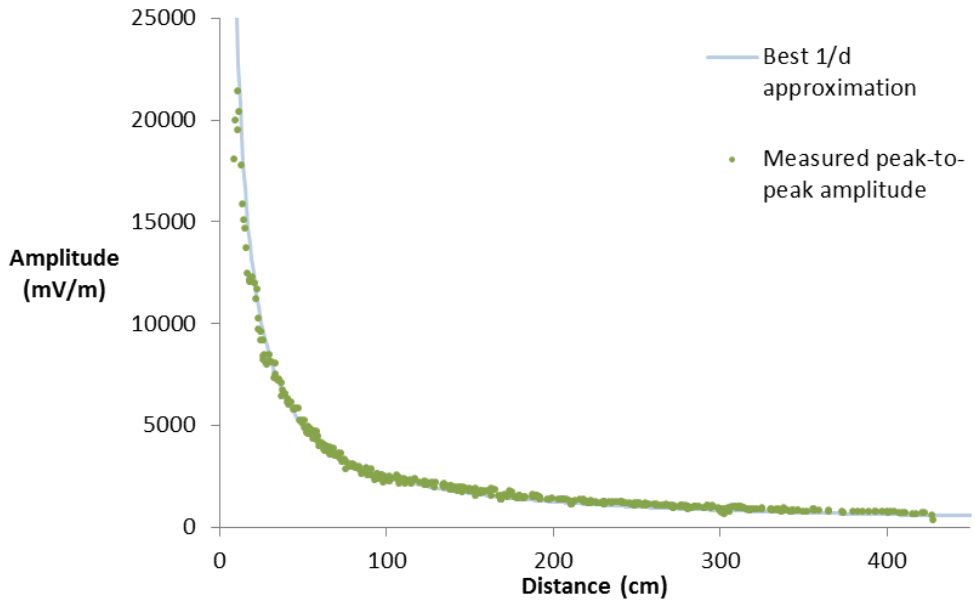

Figure 75 : Geometric attenuation in air.

The correlation with a curve evolving with an inverse distance relationship is very good even in the near-field. Numeric fitting details are given in Table 4. This correlation is even better when only the furthest measurements are considered.

This means that in this case, the theoretical equation with an inverse distance relationship can be used with a very good precision.

Influence of the reflector geometry on the geometric attenuation

As explained in § 3.2.4, the shape of the reflector has a large influence on the backscattered (reflected) amplitude. The projected cross section is important, but also the global shape, influencing the directivity. For GPR concrete inspection, non-planar features are relatively common. The most obvious examples are of course the metallic rebars, constituting cylindrical targets.

In this section, we performed tests on a very long steel rebar. In a first experimental configuration, it was placed parallel to the bowties, which corresponds to the case of a rebar perpendicular to the radar profile direction during a classic concrete inspection. This is the configuration in which the rebars are easily recognized, because they appear as hyperbolas into the radargram. Moreover, as it will be detailed in the chapter 3.2.5.1, it is the configuration in which a metallic rebar is susceptible to receive and reflect the most energy, due to the donut-shaped radiation pattern of the antenna [105].

In a second experimental configuration, the rebar was placed perpendicularly to the bowtie antennas. Due to polarization concerns, this configuration is susceptible to generate a very low reflection, especially if the radius of the rebar is small compared to the wavelength [105]. Finally, we performed the same test on a small steel ball of 22.99 mm diameter.

According to the theoretical considerations described in § 3.2.4, which do not take into account the polarization concerns nor the near-field bowtie specificities, we would expect to have an attenuation proportional to R^{-2} for the steel ball and proportional to $R^{-1.5}$ for the rebars. Detailed results are listed in Table 4, while all the measurements and their best exponent approximations (with the least square criterion) are drawn in Figure 76.

Table 4 : Regression properties for the curves obtained in air for geometric attenuation.

Reflector type	Considered distance	Equation	A	b	R^2	Mean deviation of the prediction
Plane reflector	L > 8 cm	$A\,x^{-b}$	18.29 E+04	-0.9261	0.9906	1.47E+02
		$A\,x^{-1}$	22.51 E+04	-1	0.9809	3.09E+02
	L > 100 cm	$A\,x^{-b}$	19.06 E+04	-0.9332	0.9552	6.66E+01
		$A\,x^{-1}$	26.84 E+04	-1	0.9949	7.82E+01
Bar (parallel)	L > 5 cm	$A\,x^{-b}$	19.30 E+04	-1.3295	0.9797	1.06E+02
		$A\,x^{-3/2}$	30.91 E+04	-3/2	0.9894	1.75E+02
Bar (perpen-dicular)	L > 9 cm	$A\,x^{-b}$	84.86 E+04	-2.0914	0.9775	2.73E+02
		$A\,x^{-3/2}$	20.59 E+04	-3/2	0.9370	6.78E+02
		$A\,x^{-2}$	71.05 E+04	-2	0.9686	3.08E+02
Steel ball	L > 5 cm	$A\,x^{-b}$	6.43 E+04	-1.3496	0.9546	2.00E+02
		$A\,x^{-3/2}$	6.49 E+04	-3/2	0.7966	3.58E+02
		$A\,x^{-2}$	9.40 E+04	-2	0.5274	6.74E+02

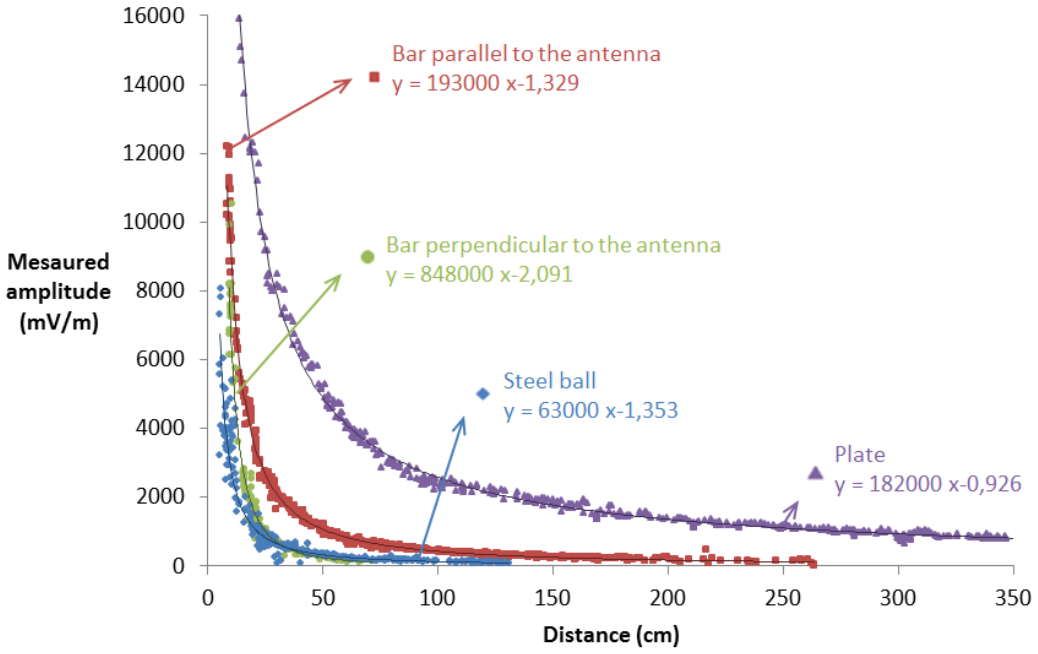

Figure 76 : Attenuation in air of the measured peak-to-peak amplitude as a function of the total distance covered by the wave and comparison with the power curves presenting the best correlation coefficients.

When the rebar is parallel to the antennas, we observe that the best correlation is obtained for an exponent of -1.33, while we would have expected -1.5. Anyway, the correlation coefficient R^2 is not bad at all for -1.5 (0.98); we also observe that the mean deviation of the results is lower. The $Ax^{-1.5}$ seems then perfectly acceptable.

When the rebar is placed perpendicularly to the antennas, the reflection amplitude is, as expected, smaller than for the parallel orientation. For this reason, amplitudes for offsets superior to 75 cm could not be evaluated, because they are inferior to the noise level. The best fit was obtained for an exponent -2.09, smaller than expected -1.5. This could be due to some polarization effects. We have indeed observed in the numerical simulations (§ 3.2.4.1) that the electric field in the direction perpendicular to the main electric field could be decreasing proportionally to the inverse squared distance. This approximation gives an acceptable correlation coefficient R^2=0.969.

In the case of a steel ball, we considered distances up to 130 cm. At small distances from the antenna, the amplitudes are very low, even lower than for the perpendicular rebar. It means that, at larger distances, the measured amplitudes are slightly larger. Indeed, in this case, the best fit for the attenuation factor exponent is obtained for -1.353, while we expected -2 for a local defect. This could be due to some radiation pattern effects, which will be studied in the next paragraph.

3.2.5 Antenna radiation pattern

The radiation pattern describes the influence of the emission direction on the amplitude of the waves emitted by the GPR antenna. In the first part of this section, the different factors influencing the radiation pattern of bowtie antennas are described. In the second part, we intended to measure the radiation pattern of our device when placed on sand.

3.2.5.1 Theoretical considerations

High frequency contact antennas are constituted by two bowtie antennas. Those antennas are similar to dipole antennas and have a comparable donut-shaped radiation pattern, corresponding to a perfect circle in the transverse electric (TE) mode (Figure 77) [54, 104].

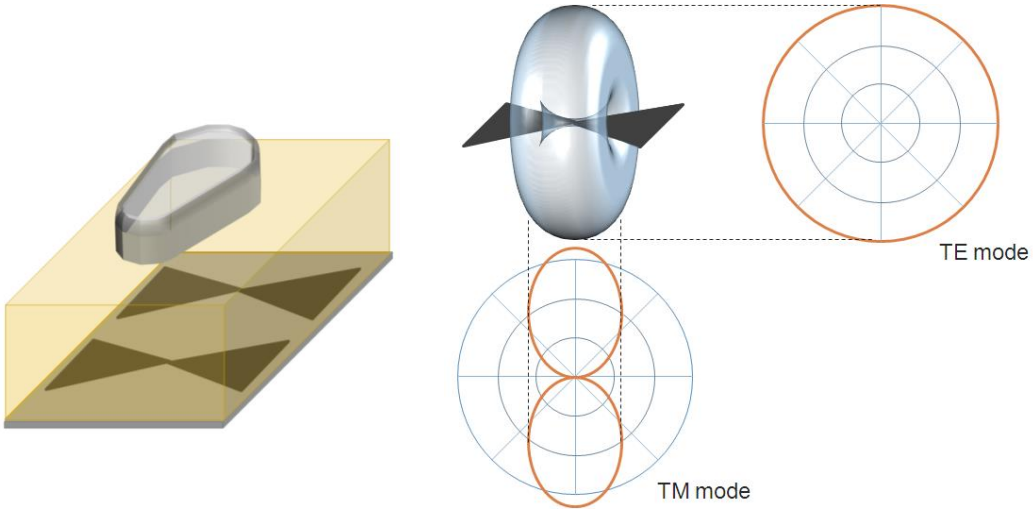

(a) (b)

Figure 77 : (a) Schematic position of the two bowties antennas into the shielding box; (b) radiation pattern of a bowtie antenna [104].

If an emitting dipole antenna is placed close or in contact with the inspected surface, its radiation pattern greatly changes. In the TE mode, a peak of maximum amplitude appears for a wave inclination equal to the critical angle (Figure 78).

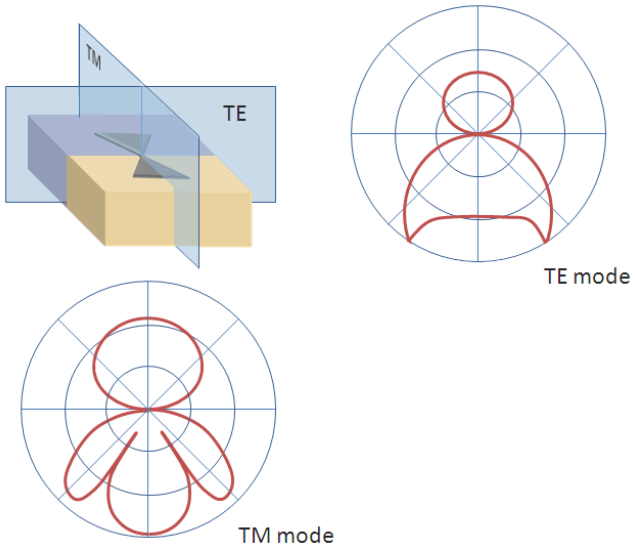

Figure 78 : Radiation pattern of a bowtie antenna when placed against the surface of a different medium [54].

This ground radiation pattern depends on the dielectric permittivity contrast between the two materials, but also on the height of the antenna above the surface. Equations describing those radiation patterns on a surface have been established by different authors [106-108]. Those equations are valid for far-field radiations, i.e. sufficiently far from the antenna to neglect the terms in the Maxwell propagation equation that decay faster than r^{-1}. According to Millard [104], an equation permitting to describe the far field limit distance R_{ff} is:

$$R_{ff} \geq \frac{2L_A^2}{\lambda} + \lambda. \quad (132)$$

In (132), L_A is the characteristic antenna length (i.e. the distance between two opposite apexes of each bowtie) and λ is the wavelength in the medium. In simple terms of wavelengths, authors generally estimate that the far-field limit is between 3λ [104] and 8λ [108], possibly up to 40λ according to some papers [109, 110].

Those distances are seldom reached in the measurements performed with contact high frequency GPR antennas. For this reason, it is difficult to rely on theoretical equations in order to take into account the radiation pattern of the antenna. Another discrepancy between those equations and real antennas is the presence of the metallic shield, which tends to increase the directivity of the antenna and thus to change its radiation pattern [104].

A promising method for radiation pattern determination is the complete modelling of the antenna into a 3D FDTD code [111]. The drawback of this technique is that the inner geometry and composition of the antenna have to be perfectly known.

For a given material, it is also possible to experimentally measure the radiation pattern. This can be performed directly using a second antenna to measure the radiation pattern of the first one or, indirectly, measuring the signal reflected on a metallic target (monostatic method).

3.2.5.2 Experimental measurement of the radiation pattern on sand

We measured the radiation pattern of our antenna by using a small steel ball buried at different depths (from 0 to 20 cm) in a sand box. 70 cm long profiles were performed with 2.3 GHz antenna on the sand surface, just above the ball ((Fig. 7). Those tests were performed on sand rather than concrete because loose materials allow placing the reflector at any depth.

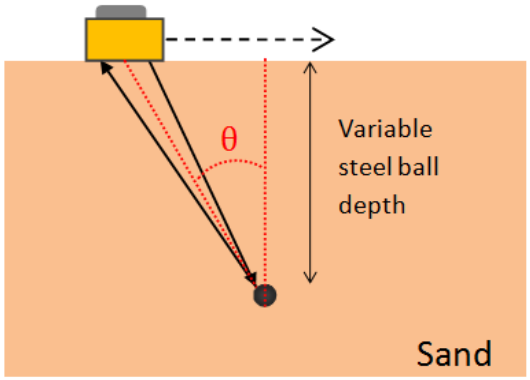

Figure 79 : Schematic principle of the radiation pattern experimental measurement.

From measurements in air on the same steel ball, we estimated the geometric attenuation factor from the steel ball to the distance exponent 1.353 (§3.2.4.2).

The raw results in sand were thus multiplied by this factor; they were also divided by the attenuation factor, estimated from all the measurements performed just above the ball, for the different depths. To lower the noise of the signals, the profiles performed at the same depth (two or three) were averaged, before to be smoothed by a moving average of five elements. Finally, all the amplitudes were normalized to the mean amplitude observed at 0° (Figure 80).

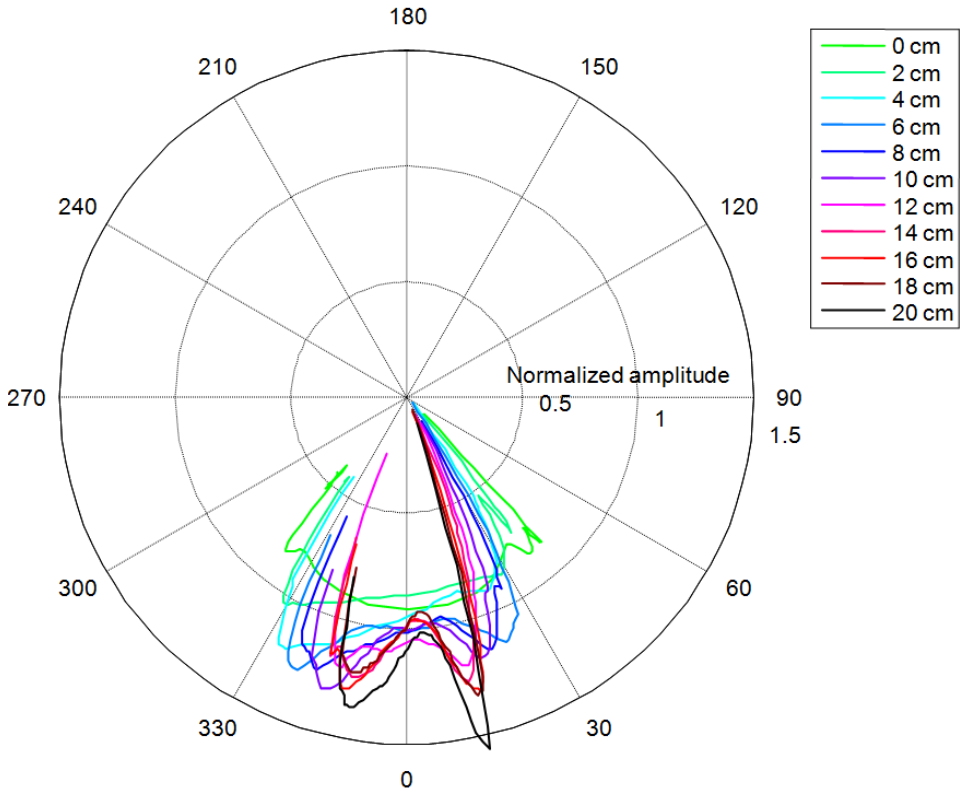

Figure 80 : Dependence of the wave inclination angle on the reflection amplitude. Those results were deduced from monostatic measurements on a ball buried in sand at different depths.

We observe that the radiation pattern is highly dependent on the depth, especially within the first 15 cm, corresponding to about 2λ. Features detected by high frequency GPR are often situated at lower depths.

The radiation pattern is dependent on the antenna model, as well as on the surface condition, on the mode (monostatic or bistatic) and on the ground permittivity [12]. A rigorous analytical expression of the radiation pattern (of P_t and P_r in (114) for example) in the near field should then be a function of all those different parameters. Such an analytical function would be necessary for the parameters determination when no normalization with a reflection on a metallic reflector is possible (see § 3.1.2.1).

3.2.6 Conclusions

From all the observations made in this section, we drew a few conclusions that influenced all the subsequent signal acquisition and treatment (in § 3.3 but also in Chapter 4 and Chapter 5).

During the acquisition, it is important to warm up the antenna during a minimum of 60 minutes before performing any measurement, in order to minimize the time drift effect. For a very good precision, the heating duration should be extended to 80 minutes. Then, the automatic stack function of the radar has the same effect than a post-processing stack and divides the white noise by the square root of the stacks number. For this reason, the automatic stacking number should be kept relatively high (8 is a good compromise between noise reduction and acquisition speed).

As a first step of the data processing, it is always interesting to subtract the mean amplitude of each signal. It will suppress the uninteresting constant component of the frequency spectrum and it will decrease the time drift effect.

We also measured the geometric attenuation undergone by waves reflected on objects with different geometries. The analysis of the amplitude decrease confirmed the dependence in R^{-1} for a large reflection plane. In two dimensions, the dependence is in R^{-2}, so the data should be corrected to fit the real results.

When the waves are reflected on objects that are not planes, their geometric attenuation factor will be affected. For a rebar parallel to the dipole, the expected dependence in $R^{-3/2}$ was observed. When the rebar is perpendicular to the antenna, the expected $R^{-3/2}$ attenuation may underestimate the actual attenuation, which seems closer to R^{-2}. On the other hand, for the steel ball, the expected R^{-2} attenuation could not be observed. The results suggested a weaker attenuation with a $R^{-1.3}$ dependence,

Finally, the analysis of the radiation pattern measured on sand showed its important evolution in the near field. An approximation based on far-field equations will then be insufficient to predict the angle-dependant amplitude. Such prediction should take into account the target distance in addition to the antenna geometry, the surface condition, the mode (monostatic or bistatic) and the ground permittivity. The method developed for extracting the reflection coefficient (§ 3.1.2.1) frees us from the necessity to determine precisely the radiation pattern. But, as it will be demonstrated in § 4.2.3, it will introduce some imprecisions in some configurations. For this reason, the development of a method for the near field radiation pattern estimation is one of the most promising field of research to improve the thin layer characterization technique in the future.

3.3 Determination of concrete electromagnetic parameters with GPR

The accuracy of radar survey results is directly linked to the precision of the electromagnetic parameters of the concrete. Firstly, because in lossless media, the dielectric permittivity is directly linked to the wave speed (25) and is therefore used to estimate the depth of the detected features. Secondly, concrete dielectric permittivity can also be an indicator of the concrete water content, which can be controlled by this method.

Different techniques are especially dedicated to the measurement of the relative permittivity. In laboratory, the measurement can be directly performed by using a coaxial transmission line [68]. On site, TDR (Time Domain Reflectometer) measurements can be performed. The TDR probe consists in long metallic sensors that are embedded into the ground and allow a direct evaluation of the material permittivity. This method is frequently used for loose materials like sand or soil, but, in the case of concrete, the necessity of embedding the sensors into the material is a severe drawback. For this reason, they are seldom used for concrete evaluation, except for big civil works (dams, bridges), which require a high evaluation and maintenance level during their whole lifetime; in this case, the probes are embedded into the fresh concrete. Another disadvantage of the TDR is that every measurement only gives information about a few cm^3 of material. As it is a destructive method in concrete, in may not be sufficient to evaluate a whole structure [112].

As an alternative to these direct methods, the dielectric permittivity can be estimated from measurements performed with the radar. In addition to the fact that they do not require additional equipment than the radar needed for the inspection, these methods also have the advantage to be totally non-invasive, even for concrete inspection. Different techniques are presented in this section, before to be tested on the measurement of a concrete slab permittivity.

3.3.1 Methods description

To estimate the surface concrete permittivity with GPR, specific tests can be performed. With the surface reflection test, the estimation is based on the evaluation of the surface reflection coefficient. When CMPs are measured, the estimation can be based of the direct wave or on the time of arrival of an embedded reflection. If reflectors are present, the estimation can also be derived from the profile measurements. All these methods will be described in the next sections.

3.3.1.1 Surface reflection measurements

This method consists in comparing the surface reflection measured at a distance of a few decimetres to the reflection obtained from the same distance on a

perfect reflector (§ 3.1.3.1). The ratio between those two amplitudes corresponds to the reflection coefficient of the interface between air and the surface concrete.

If we consider that the incident wave is perpendicular to the interface (which is a valid assumption if the antenna is placed sufficiently far from the surface), the reflection coefficient is given by (51), in which material 1 is air and material 2 is the surface concrete. We have thus:

$$R_{\text{surface}} = \frac{1 - \sqrt{\varepsilon_{surface}}}{1 + \sqrt{\varepsilon_{surface}}} \tag{133}$$

$$\varepsilon'_{r,surface} = \left(\frac{1 - R_{\text{surface}}}{1 + R_{\text{surface}}}\right)^2 \tag{134}$$

From (134), the dielectric permittivity of the surface is thus univocally determined by the reflection coefficient measured from the surface.

The drawback of this method is the fact that it only reveals the permittivity of the surface. If a gradient is present into the concrete, the mean permittivity will be different from the surface permittivity, and the depth of the detected features could be misevaluated.

3.3.1.2 Permittivity evaluation from radar direct wave

Dielectric properties of concrete can be evaluated by measurement of the propagation speed of the direct wave in the material. Two different techniques are described by Klysz & al. [113].

The first one is a direct measurement of the propagation speed of the wave maximum energy, estimated from eleven different receiver positions (CMP). This could approach real velocity even if dispersion and attenuation can modify the shape of the wave and thus the velocity measurement.

The second one is based on the spectral analysis of the radar surface wave. The use of a Fourier transform frees calculations from changes in the shape of this wave during its propagation. However, this technique is more complicated and is submitted to more noise because only one pair of receivers can be taken into account after each measurement [114].

It was shown that both methods tended to underestimate the permittivity value for the lowest water content (i.e. for low permittivity values and high wave speed), because it is difficult to separate contributions of direct wave in the material from direct wave in the air.

3.3.1.3 Speed evaluation using a buried reflector

The speed of the wave is directly linked to the dielectric permittivity in the material (25). If the depth of a reflector is known, the speed can easily be determined, as well as the permittivity. If the depth of the reflector is unknown, the permittivity determination using the speed will require the analysis of a measurement containing more information. If a local reflector (as a rebar, for example) has been detected in the radargram, the whole hyperbola reflected from the rebar can be used to estimate the speed. Indeed, the shape and position of the hyperbola permit to univocally determinate the speed in the material. In CMP measurements, the planar reflectors appear as hyperbolas as well. The permittivity and the depth can thus be simultaneously determined from the reflection time.

To use all the information contained into the radargram, the reflection amplitude can be inverted as well. The parameters are adjusted to generate an analytical or modelling solution that would fit the measurements. Ferrieres & Klysz [115] showed that numerical simulation results obtained with a 2D FDTD model could be in good accordance with experimentally measured dielectric properties.

3.3.2 Comparison between indirect methods for the determination of the permittivity of concrete

All the methods listed here are theoretically valid for estimating the concrete permittivity. Nevertheless, some methods are more affected by the noise or by measurement imprecisions. For this reason, we decided to test a smooth concrete slab with different methods in order to determine a measurement and analysis procedure for the future tests. On this test sample, we performed various tests and analysis:

- surface reflection analysis;
- static and dynamic tests reflection analysis, based on reflection time;
- static reflection analysis, based on reflected amplitude.

All tests were performed on the same day and on the same slab. The 10 cm thick slab had been realized by the company Ronveaux with self-compacting concrete in order to present a perfectly smooth, almost bubble free, formed surface and a relatively smooth troweled surface. All measurements were performed with the antenna on the free surface, so that the bottom reflection took place on the smooth casted surface. A second identical slab was used to obtain the direct wave, using the good contact between the formed surfaces. Both slabs had been stored during 4 months in a climate room with HR=60%: we can reasonably assume that there is virtually no humidity gradient.

3.3.2.1 Surface reflection analysis

For this test, we compared the reflection on the concrete to a reflection on an aluminium sheet, after subtraction of the direct wave in air (see § 3.1.3.1). Results are presented in Figure 81 (a).

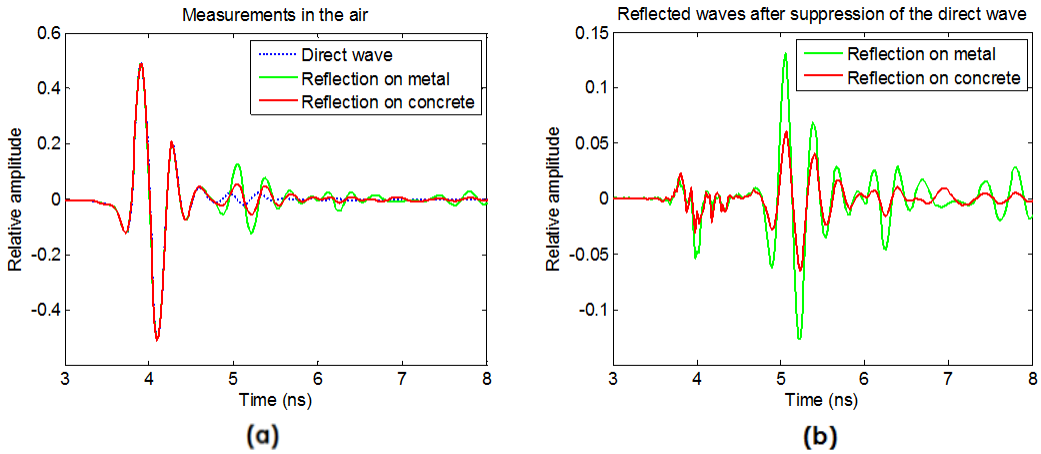

Figure 81 : Determination of the surface reflection coefficient (a) raw measurements; (b) after direct wave suppression.

Because of the relatively long duration of the radar pulse, it is important to subtract the direct wave to obtain a good precision. The reflection is evaluated from the peak-to-peak amplitudes ratio. In this case, we have:

$$R = \frac{A_{concrete}}{A_{metal}} = -0.4878 \tag{135}$$

Using equation (134), we deduce $\varepsilon'_r = 8.437$ and, with (25), $v_1 = 10.328\ cm/ns$.

3.3.2.2 Permittivity determination based on the reflection time

Because the dielectric permittivity is directly linked to the velocity, it can be deduced from the propagation time, if the time zero and the geometry are known. If the geometry is unknown, a dynamic measurement is necessary to determine simultaneously the thickness and the permittivity. The time of observation of every event is the maximum of the Hilbert envelope of the amplitude, so that the measurements are not affected by the phase change.

Time zero determination

In a GPR radargram, only the waves measured by the receiving antenna appear. The exact emission time of the pulse is unknown and has to be determined from the measurements. Any error on the time zero will directly impact on the calculated travel time, so it is important to achieve a good precision in the time zero determination.

The most rigorous method to determine the time zero is to perform a static measurement in air with the same configuration as used on concrete (monostatic or bistatic)(see § 3.1.3.1). In the corresponding profiles, the distances between antennas are known, as well as the wave speed (30 cm/ns). The time zero is then obtained by subtracting the corresponding propagation time from the time of direct wave observation.

$$t_0 = t_{obs} - \frac{d_{antennas}}{30\ cm/ns} \tag{136}$$

If we have measured a direct wave in the air, time zero is 4/30=0.133 ns and 13/30=0.433 ns, respectively, before the recording times of the monostatic and bistatic measurements.

If no record of the direct wave in the air is available, the direct wave on the medium can be used to estimate the time zero. This direct wave is a complex combination of the direct wave in the air, the direct wave in the medium and the wave reflected on the medium surface. For this reason, the peak of maximum energy cannot be directly related to the time zero.

Nevertheless, the time zero can be estimated with a limited error by considering that the maximum energy peak travels at the speed of air. The maximum error committed with this approximation can be calculated for the different antennas distances. If the medium is not water, the theoretical maximum error that could be committed with this method is 0.533 ns (which is the time difference for a wave covering 4 cm at 30 cm/ns and 6 cm/ns, respectively) for a monostatic measurement and 1.73 ns for a bistatic measurement.

We can compare the direct waves and the peaks of maximum energy measured on different media to the peak of maximum energy measured in the air, for the two configurations (Figure 82):

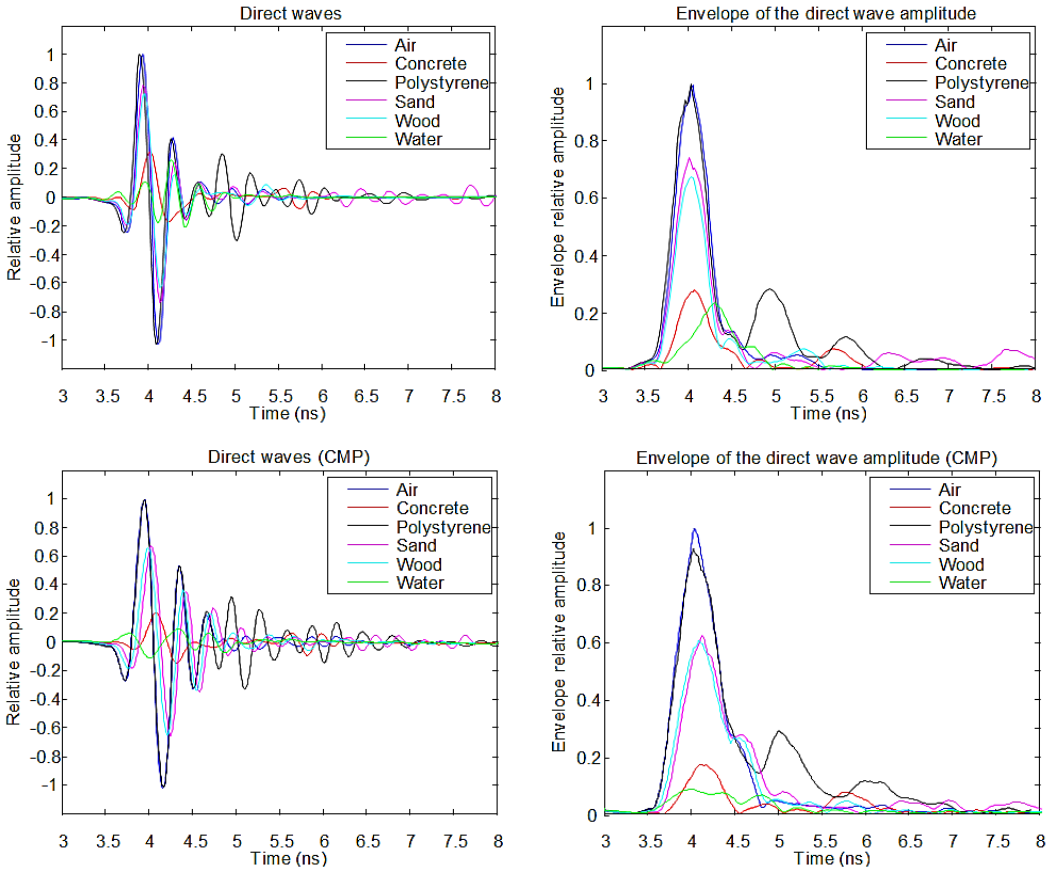

Figure 82 : Comparison of the direct waves (left) and the amplitude envelopes (right) for the direct wave in a monostatic (up) and bistatic (bottom) measurement.

The time shifts observed on these different materials and the corresponding apparent speed for the peak of maximum energy are gathered in Table 5.

Table 5 : Direct wave envelope amplitude peak time shift and corresponding apparent speeds.

Material	Approximate material speed (cm/ns)	Monostatic (antennas distance =4 cm)		Bistatic (antennas distance =13 cm)	
		Delay observed with direct wave in air (ns)	Apparent speed (cm/ns)	Delay observed with direct wave in air (ns)	Apparent speed (cm/ns)
Concrete	10	0.0361	23.608	0.0794	25.35
Polystyrene	25	-0.0216	35.800	-0.0144	31.031
Sand	20	0.0144	27.076	0.0577	26.477
Wood	26	-0.0144	33.632	0.0505	26.869
Water	3.3	0.3103	9.016	-0.0433	33.330

In Table 5, we observe that, as expected, the direct waves travel at an intermediate speed between the material speed and the speed of light. For this reason, the direct waves in these configurations cannot be directly used for the material speed determination.

For monostatic measurements, except in the case of water, the method let us to estimate the time zero with a relatively good precision: the error is inferior to 0.04 ns if we consider that the direct wave always travels at the speed of light. Nevertheless, we observe some negative errors, which are incompatible with the theory and are due to method or measurements imprecisions. For this reason, it still can be useful to systematically measure a direct wave in air to obtain an accurate value for the initial time.

In bistatic measurements, the direct wave energy on water is highly attenuated and no real peak can be observed, inducing corruption of any analysis based on this method. The speed of light can be a satisfactory approximation for most materials, but the error increases with the material impedance and is totally unacceptable when the material contains a high percentage of water. For this reason, it will be very useful to perform a bistatic measurement in air (Figure 51 (a)) in order to obtain a reliable time zero. If a preliminary determination of time zero is not possible, a better option than the approximation with the speed of light could simply be the inclusion of the time zero as a parameter of the curves fitting.

Static measurement

If a ray propagation is considered and x is the distance between the antennas, the speed in the first material v_1 and the thickness h are linked by the relation:

$$v_1 = 2 * \frac{\sqrt{\frac{x^2}{4} + h^2}}{t_{refl}} \tag{137}$$

The dielectric permittivity can be determined using relation (25). If the nominal thickness of the slab $h = 10\ cm$ is introduced into the equation, we find from the monostatic measurement that $\varepsilon'_{r1} = 6.98$ and, with the bistatic measurement, $\varepsilon'_{r1} = 8.32$. The difference between both measurements is relatively important. If we perform the same analysis to the second reflection on the slab bottom in the monostatic measurement, we find $\varepsilon'_{r1} = 7.54$. It seems that the analysis of the first reflection from a monostatic measurement tends to underestimate the concrete permittivity. This could be due to the thin plastic and air layer between the antennas and the concrete surface (of 2 mm), which is susceptible to modify the wave path.

Dynamic measurement

To determine the permittivity of concrete if the geometry is unknown, the best solution is to use a dynamic measurement (CMP). In the radargram, the two first

reflections are automatically detected using the envelope peaks. Depending on the noise, the first 10-15 cm of the CMP test can be selected with this method.

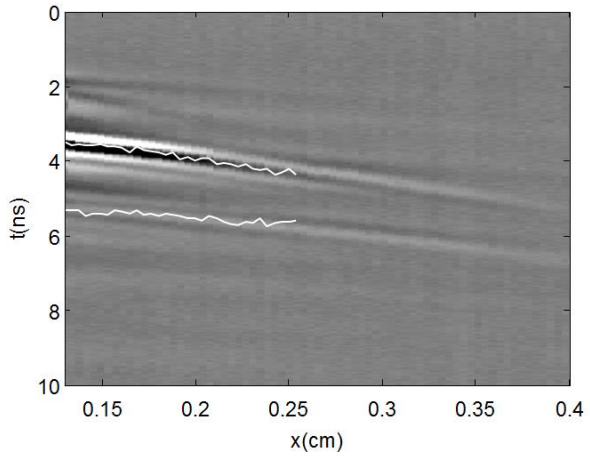

Figure 83 : Automatic detection of the 33 first samples of the first and second reflection of a CMP, based on the maximum of the amplitude envelope.

When the second reflection is too weak to be identified, the analysis should only be based on the first reflection. The parameters are determined by a minimization of the error between the synthetic curve generated for a set of parameters and those automatically detected samples. The inversion can be performed using the thickness as a data, which should improve the results. It can be based on a combination of the samples picked for the first and the second reflection, or it can be based on one reflection only. The results are displayed in Table 6 for a selection of the 33 first samples.

Table 6 : slabs parameters determined from the analysis of the CMP measurements.

	1st reflection	2nd reflection	Both reflections
h=10 cm	$\varepsilon_{r1} = 8.40$	$\varepsilon_{r1} = 8.39$	$\varepsilon_{r1} = 8.40$
h unknown	ε_{r1} =8.83 $h = 9.5\ cm$	$\varepsilon_{r1} = 5.96$ $h = 12.28$	$\varepsilon_{r1} = 8.41$ $h = 9.98\ cm$

When h is known, the analysis is very precise and the results do not depend on the reflection event that is studied. When h is unknown, however, we observe that a study based on both reflections is highly preferable to the analysis of only one reflection, which can give a truncated result. The resulting curves for only the second reflection and for both reflections are displayed in Figure 84.

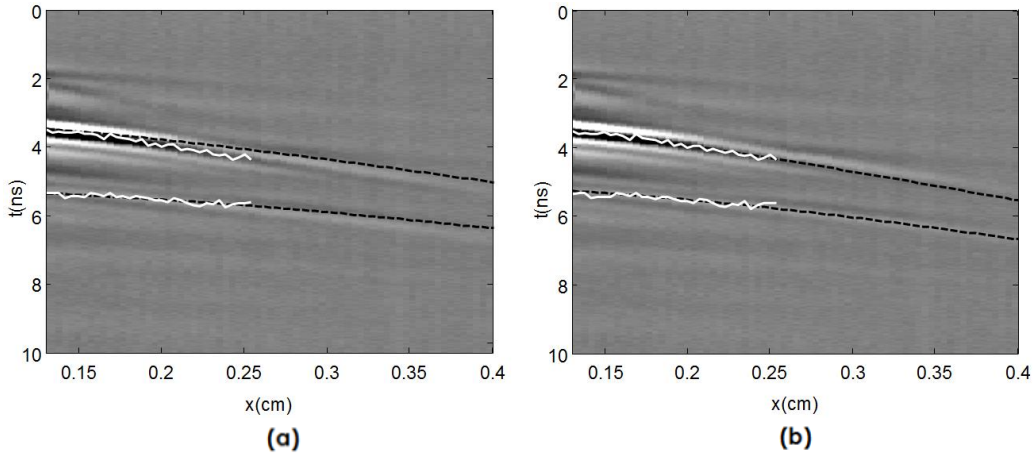

Figure 84 : Best approximation of the CMP reflections (represented by the dashed line) with h unknown (a) based on the second reflection only; (b) based on the two first reflections.

Measurements without preliminary estimation of t_0

We performed the same dynamic measurements using t_0 as an unknown value to determine from the curves shapes, in addition to h and ε'_{r1}. This analysis was performed using the two first reflections.

Table 7 : Parameters ε'_{r1}, h, and t_0 determined from CMP first and second reflection curves.

	Both reflections, t_0 unknown
h=10 cm	$\varepsilon_{r1} = 8.36$ $t_0 = 1.2145\ ns$
h unknown	$\varepsilon_{r1} = 7.73$ $h = 10.31\ cm$ $t_0 = 1.2775\ ns$

The values of t_0 are relatively close to the value estimated from the direct wave in the air: $t_0 = 1.2075$. The results are relatively precise, with a fair estimation of all parameters. In the absence of a measurement of a direct wave (or if the measurement is not precise enough, due to the time shift for example), this method is a good alternative.

3.3.2.3 Permittivity determination based on the reflected amplitude

We performed static measurements from the surface of the concrete slab, which was first hung in the air and then placed on a metallic sheet. As the reflected waves are not totally separated from the direct wave (Figure 85 (a)), the amplitude ratio estimation is more precise after subtraction of the direct wave (Figure 85 (b)).

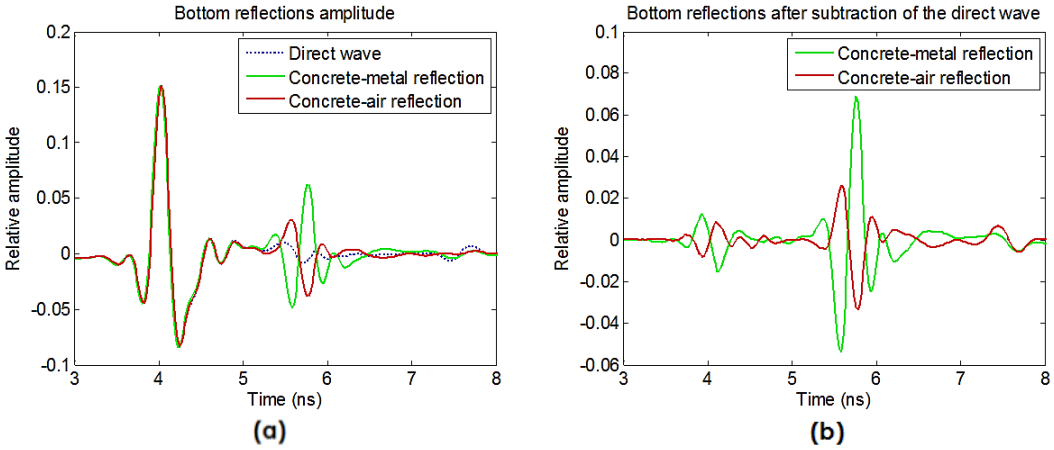

Figure 85 : Determination of the permittivity through bottom reflection amplitude: (a) raw measurements; (b) after direct wave suppression.

In this case, the amplitude ratio gives R=0.4865 (positive because the reflection coefficient of the metallic sheet is -1). To increase the precision, we took into account the inclination for the calculation of the permittivity (equation (54)):

$$\varepsilon'_{r,1} = \frac{1}{\left(\cos\theta * \frac{1 - R_{surface}}{1 + R_{surface}}\right)^2 + sin^2\theta} = 6.53 \qquad (138)$$

This value is very low and can be explained by the imperfection of the direct wave measurement.

The same analysis has been performed with the bistatic measurement; the reflection coefficient was then equal to 1. This implies that the incident angle (33°) is superior to the critical angle, but does not give additional information.

3.3.2.4 Conclusions

From the tests that were carried on in this chapter, we drawn different observations, that we took into account to determine a measurement routine for the parameters determination.

The surface reflection test is a simple method to estimate the material permittivity. It allows repetitive measurements on any surface. The drawbacks of the method are the fact that it requires a suspension frame on site, and that it is only representative of the surface properties.

The time zero has to be estimated in order to determine the time of occurrence of every reflection event into the radargram. It should always be determined from an air measurement (which is quick and easy to perform). If it is not the case, a good alternative for static tests is to suppose that the direct wave measured on the material has the speed of light. This approximation is not valid for bistatic measurements, for which it is better to invert the time zero from the measured curves.

After determining the time zero, the reflection time analysis gives relatively different values for monostatic and dynamic measurements (with an error superior to 20%). In particular, the analysis based on the first reflection of the monostatic measurement seems to lead to an underestimation of the permittivity.

The CMP measurements analysis gives very good results if the thickness is known and the results are the same if the first and/or the second reflection is studied. However, if both h and ε_r' have to be determined, the best results are obtained if both reflections are used. The analysis of the second reflection only should be avoided.

The analysis based on the reflection amplitude rather than on the reflection time revealed to be less reliable, due to the difficulty to suppress a direct wave and the necessity to know the thickness for estimating the incidence angle. As long as other methods are available for the surface parameters estimation, this method will not be used anymore.

On the basis of those results, we determined our procedure for the determination of the surface concrete permittivity. We decided to measure a CMP on concrete and analyse the two first reflections (when the second reflection is sufficiently visible). For the time zero determination, we used as often as possible the bistatic direct wave in air. For the results assessment, we used additional surface reflection tests whenever possible.

Chapter 4: Analysis of the APVO curves reflection coefficient

As seen in § 2.2, thin layers generate reflections whose amplitudes will depend on the dielectric properties of the materials, the incident angle and the thickness-to-wavelength ratio. The amplitude and phase of the reflections may be analytically described through equations (102) and (112). In this chapter, those analytical formulations are confronted to amplitude and phase versus offset (APVO) curves obtained through numerical modelling.

In the first section (§ 4.1), we will determine which one of these methods is the most suitable to approximate the amplitude and phase of the reflection. Different variations of these methods will be tested and compared to amplitude and phase versus offset (APVO) curves determined from FDTD simulations. The method will then be optimized to provide a good analytical prediction of the reflection coefficient for each configuration.

In the second section of this chapter (§ 4.2), these analytical APVO curves of the reflection coefficient will be compared to numerical and experimental curves obtained in realistic conditions. Indeed, the fact that the measurements are performed from the surface will induce additional phenomena that are not taken into account by the equations (see § 3.1.2.3). We will try to evaluate the influence of these phenomena on the curves and the possibility to estimate nevertheless the layer parameters.

4.1 Optimization of the APVO curves analytical formulation

When high frequency GPR tests are performed, the incident angle it frequently too large to be assimilated to zero. This situation occurs when CMP tests are performed (§ 2.1.3.2), but also for many static tests, in which the antennas offset cannot be neglected regarding the target depth.

The CMP measurements contain more information, which is susceptible to allow the determination of a higher number of parameters, or reaching a higher precision in the parameters determination. When CMP tests are performed, we obtain the variations of the amplitude and phase of the measured wave as a function of the offset for each frequency. These variations are referred to as APVO curves (for Amplitude and Phase Versus Offset). If the measurements are corrected for all the other parameters (as described in Figure 50), the APVO curves reflect the variations of the reflection coefficient.

Two methods were described in § 2.2.2 to estimate analytically the reflection coefficient amplitude and phase for a thin layer as a function of the incident angle: the plane wave approximation (equation (102)) and the first terms exact evaluation equation (112).

Those methods, based on a ray propagation of radar waves, only give approximations of the real behaviour, in which intervene other phenomena, such as evanescent waves, spherical reflection of the waves (with the lateral wave) (§ 2.1.7.3) or other nonlinear near-field effect.

In the first section of this chapter, the propagation of the wave when encountering a thin layer will be analysed through forward FDTD modelling, and the corresponding APVO curves will be extracted and analysed.

In the second section, we will compare the APVO curves obtained through numerical modelling to the curves calculated by analytical methods. The two methods presented in § 2.2.2 will be tested, but also derived methods obtained after introduction of specific phenomena which are not taken into account but are not negligible.

In the third section, we will try to improve and combine the analytical methods in order to obtain a hybrid method able to predict the APVO curves in a maximum of cases. This development will finally be extended to fit 3D results.

4.1.1 Observation of wave propagation in 2D FDTD simulations

In order to select the best analytical method to characterize thin layers, we performed FDTD simulations in two dimensions. The aim was twofold: to observe

the wave propagation in order to understand the phenomena that are predominant in the physics of wave propagation and to extract APVO curves that will be used as a reference to evaluate the estimations obtained by the different analytical methods.

To observe the physical behaviour of the wave when reflecting on a thin layer, 2D modelling snapshots of the wave propagation are taken. The simulation describes the reflection of a 2.3 GHz realistic pulse (§ 3.1.4.1) emitted by embedded antennas (Figure 50) into homogeneous concrete ($\varepsilon'_{r1} = 7.7$) over a simple air interface and over air layers of 1, 5 and 10 cm. The snapshots are taken 4 ns after the beginning of the simulation (Figure 86).

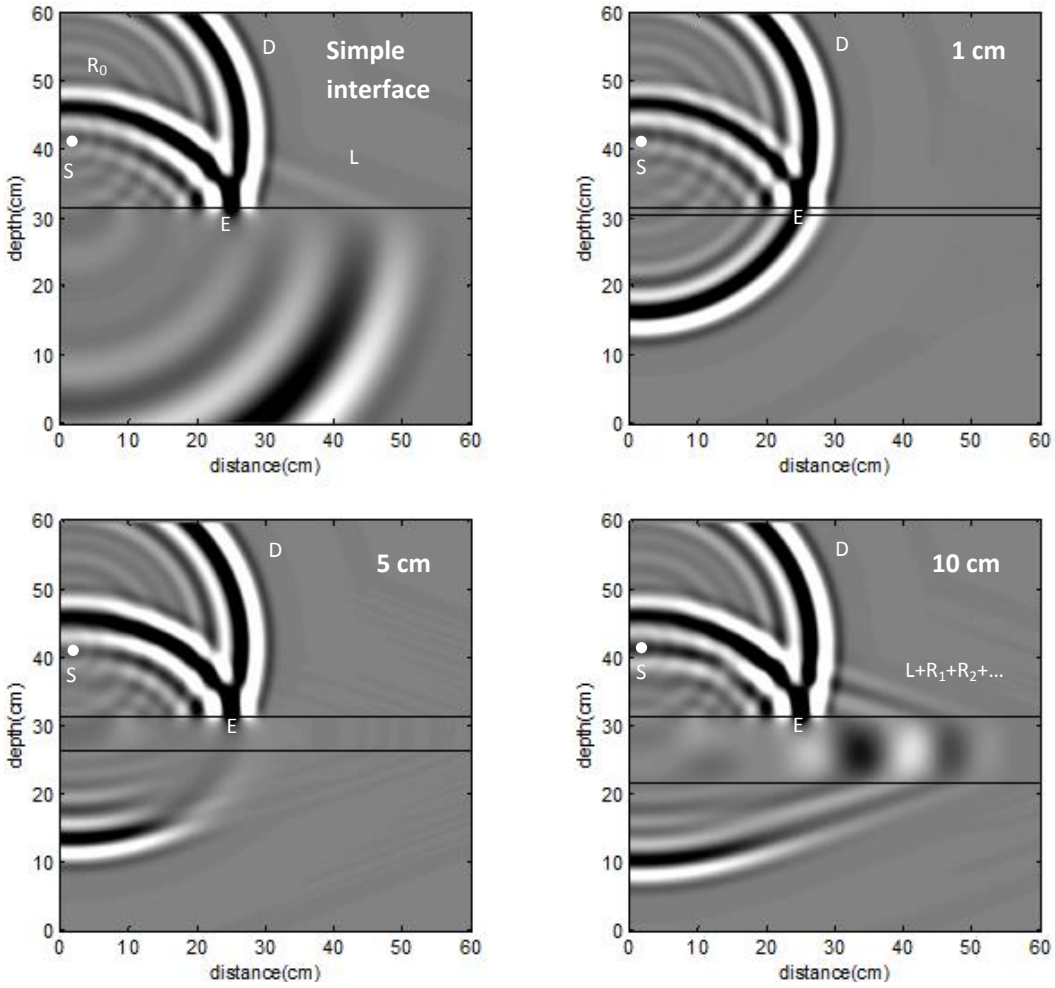

Figure 86 : 2D snapshots of the 2.3 GHz wave propagation from concrete ($\varepsilon'_r = 7.7$) to an air layer of variable thicknesses, and comparison with a simple interface. D, S, L, R_I and E are the direct wave, the source, the lateral wave, the secondary reflections and the evanescent wave, respectively.

On the simple interface, we can observe the direct wave (D), spreading cylindrically away from the source (S). We can also observe the simple reflection (R_0) generated by the interface. The lateral wave (L), moving upward, is generated at the interface by the wave front in the second medium. When the layer is sufficiently thick (10 cm), it travels along with the secondary reflections (R_1,

R_2,…) into the layer. The evanescent wave (E) appears in the snapshot as a fast but progressive decrease of the amplitude in the second medium just below the total reflection point.

When the wave encounters a layer instead of a single interface, the behaviour depends on the layer thickness. When the layer is very thin (1 cm here), no wave front can develop into the layer. This means that no multiple reflection (the waves I1 and I2 in Figure 43) propagates into the layer, and that even the lateral wave is not observed. On the other hand, the bottom of the layer is situated at a depth at which the evanescent wave amplitude has not decreased to zero yet. This wave is then reflected by the interface and propagates to the receivers.

When the layer has an intermediate thickness (5 cm), the evanescent wave is negligible when reaching the bottom of the layer and will not influence the results. But the wave front in the layer, corresponding to the lateral wave and the multiple reflections, is also hardly visible.

Finally, for larger layers (10 cm), the wave front can develop into the layer. The multiples appear simultaneously with the lateral wave and can be clearly observed.

The radargrams obtained for the same simulations can be observed in Figure 87.

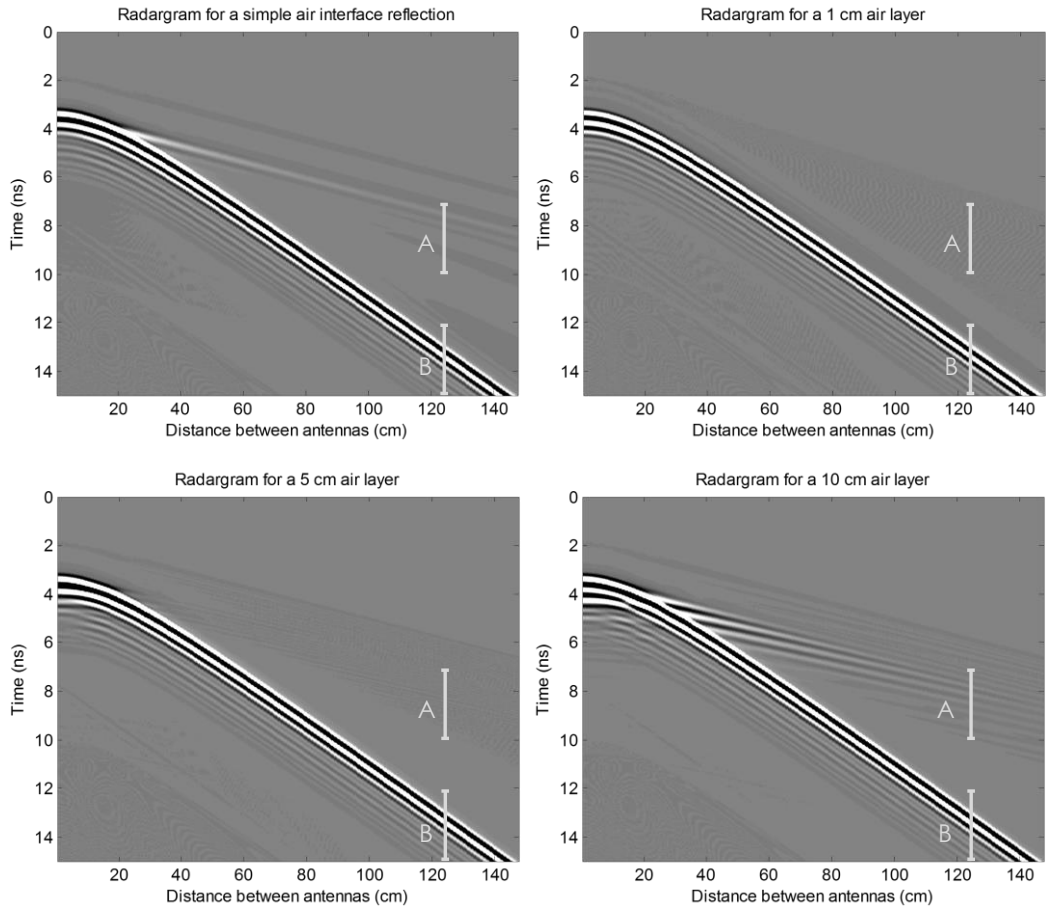

Figure 87 : Numerical CMP radargrams obtained for a single concrete-air interface and for 1, 5 and 10 cm air layers embedded into concrete.

When the receiver is placed sufficiently far from the emitter, the waves arrive in two different time windows, due to the fact that the wave is travelling faster into the layer than into the matrix. In Figure 87, those time windows are represented for a distance emitter-receiver of 125 cm, which was selected in order to have a good separation between the different wavelets.

The first time window (A) corresponds to the arrival of the lateral wave, which is closely followed by the multiple reflections; those waves are travelling almost horizontally into the layer. We observe that their amplitudes are very low for the layers of 1 cm and 5 cm. The lateral wave and the multiple reflections cannot be distinguished in the radargram, except for very thick layers ($> 2\lambda$).

In the second time window (B) of Figure 87, we can observe the simply reflected wave. This wave is closely followed by the evanescent wave, even if it is not evidently visible from the radargram because the evanescent wave amplitude is much lower than the reflected amplitude.

To observe more clearly the measured waves in the time windows of Figure 87, the measured waves in those intervals are plotted for different thicknesses in Figure 88. For a better visibility of the evanescent wave (whose amplitude is very

small compared to the reflected amplitude), the reflection time window (B) is represented after subtraction of the simple reflection on an interface.

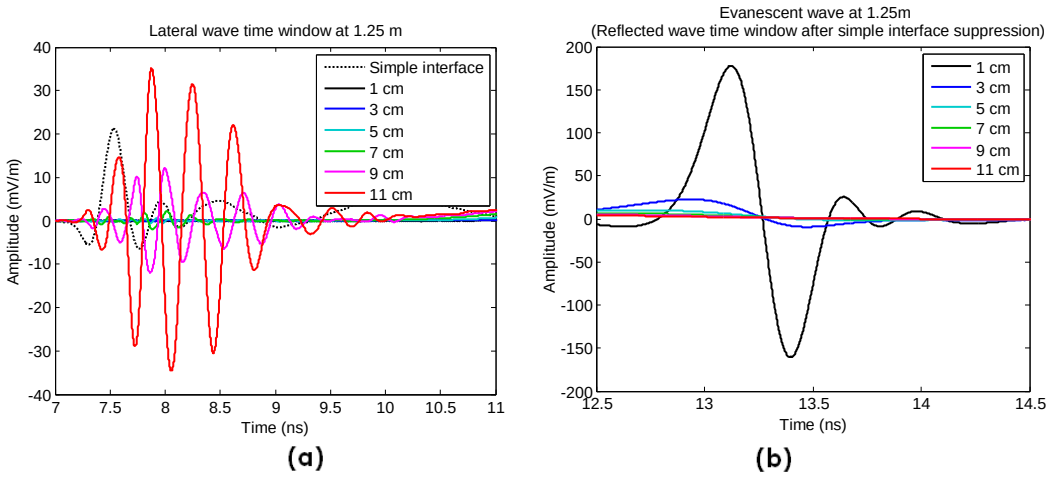

Figure 88 : Traces obtained at 125 cm over an air thin layer of variable thickness embedded into concrete. (a) Lateral wave and multiples; (b) Evanescent wave, obtained by subtracting the reflection on a simple interface from the whole radargram.

When the layer is thin (1 cm, 3 cm and even 5 cm), no reflection is visible at the time at which we should expect lateral wave (Figure 88 (a)). This is coherent with the observation of the snapshots of Figure 86: no wave front can develop into the thinnest air layers. Even for larger layers, we remark that the amplitude of the waves into this time window increases with the layer thickness.

On the opposite, the evanescent wave (Figure 88 (b)) does not appear for layers with a thickness superior to 3 cm. This is due to the fast decay of the evanescent wave amplitude in the second medium (§ 2.1.7.1).

APVO curves were extracted from 2D FDTD simulations realised with the same parameters as for the snapshots of Figure 86. Air layers of thicknesses ranging from 1 to 11 cm were embedded into concrete ($\varepsilon'_{r1} = 7.7$) in ten different models. This thickness range covers the thin layers domain, but also thicknesses approaching the wavelength (~13 cm in air at 2.3 GHz). As explained in § 3.1.2.1, the reflection coefficient was isolated by suppressing the direct wave and comparing the reflected amplitude to the amplitude measured on a perfect reflector. The AVO and PVO curves are displayed in Figure 89.

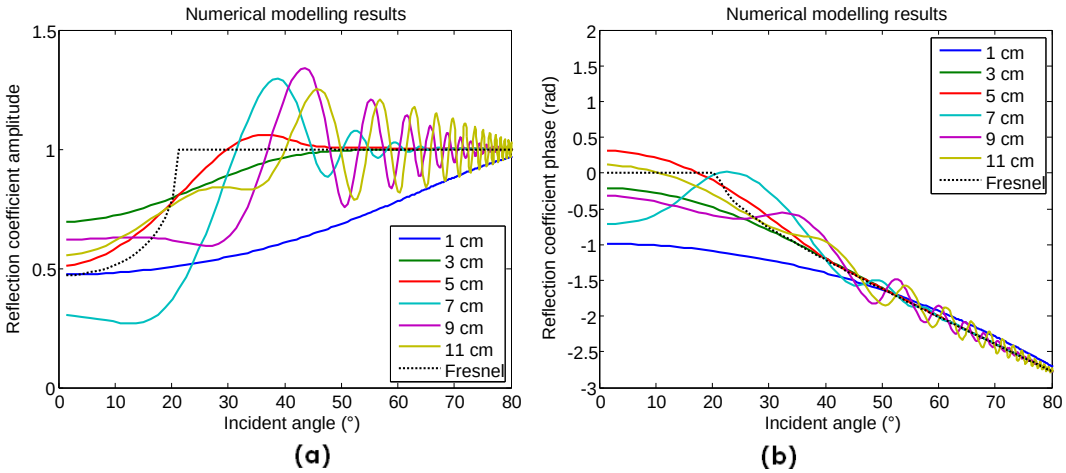

Figure 89 : Amplitude versus offset (a) and phase versus offset (b) curves obtained from 2D FDTD simulations of air thin layers of different thicknesses into concrete.

The curves behaviour depends on the layer thickness: when less than 5 cm, the curve is smooth and the reflection amplitude inferior to 1; over 5 cm, the amplitude oscillates around 1 for the larger offsets. When the thickness is equal to 5 cm, the curve shape seems intermediate, with only one peak visible before attenuation to 1. This thickness dependence seems to be similar in the amplitude curves and in the phase curves.

4.1.2 Comparison of the analytical methods for APVO curves estimation

In § 2.2.2, the complete expression for the APVO curves of a thin layer reflection coefficient was developed. In the case of a normal incidence, or when the wave is plane, the addition of all the multiples can be transformed into a simple expression using the geometric series formula (neglecting only the geometric attenuation within the thin layer). When the incidence angle is not zero, the formulation of the APVO requires further approximation. Two options were then suggested:

- to truncate the series to its n first terms;
- to neglect the angle variation between the different multiples. With this plane wave approximation, the sum can be approximated by a simple geometric series.

In § 2.2.2.3, the two methods were compared, and it appeared that the first one completely neglects the evanescent wave while the second one neglects the reflection multiples. In addition, neither takes into account the spherical reflection and the presence of the lateral wave. Introducing those phenomena into the equations could be a mean to improve the methods.

In this chapter, the objective is to determine which one of the two above methods should be preferred to predict the reflection coefficient of a thin layer, and to see if an equation modification could improve those results. To achieve

this goal, the APVO curves of the reflection coefficients determined by the different methods will be compared with the curves determined by numerical simulations (Figure 89).

The analytical APVO curves are calculated with the same configurations as in the numerical simulations models: thin layers of various thicknesses (1-11 cm) embedded into concrete ($\varepsilon'_{r1} = 7.7$) (§ 4.1.1). Five different methods were tested:

1. Plane wave approximation

   The formula (102) is applied.

2. Exact first terms estimation

   The formula (112) is applied, calculating the first 30 terms.

3. Plane wave approximation with spherical waves formula

   The spherical reflection of the waves (§ 2.1.7.3) only has a large influence on the first reflection R_0. Indeed, the reflections inside the layer occur from a high permittivity medium to a low permittivity medium, and no other critical wave is generated. For this reason, we calculated all the terms of the reflection using the plane wave approximation (102), and then replaced the first reflection by the reflection calculated with the spherical waves formula (72).

4. Exact first terms estimation and spherical waves

   Just as the second method, the global reflection can be calculated by the formula (112), calculating the 30 first terms. Then, from this global reflection coefficient, the Fresnel reflection coefficient from the first reflection (54) is subtracted and replaced by the addition of the spherical reflection coefficient (72).

5. Exact first terms estimation with spherical waves and evanescent waves

   This method combines the replacement of the first reflection by the spherical formula (72) and the addition of the evanescent waves for angles superior to the critical angle.

We must note that none of those methods is susceptible to represent exactly the complex phenomenon of the reflection on a high frequency pulse in the near field. The objective is to estimate the reflected amplitude, not to predict it exactly, which can only be performed with a high precision full waveform modelling approach.

The AVO and PVO curves obtained by those methods for the frequency of 2.3 GHz are respectively represented in Figure 90 and Figure 91, in which they are compared to the curves of Figure 89 obtained by 2D numerical modelling, for the same frequency.

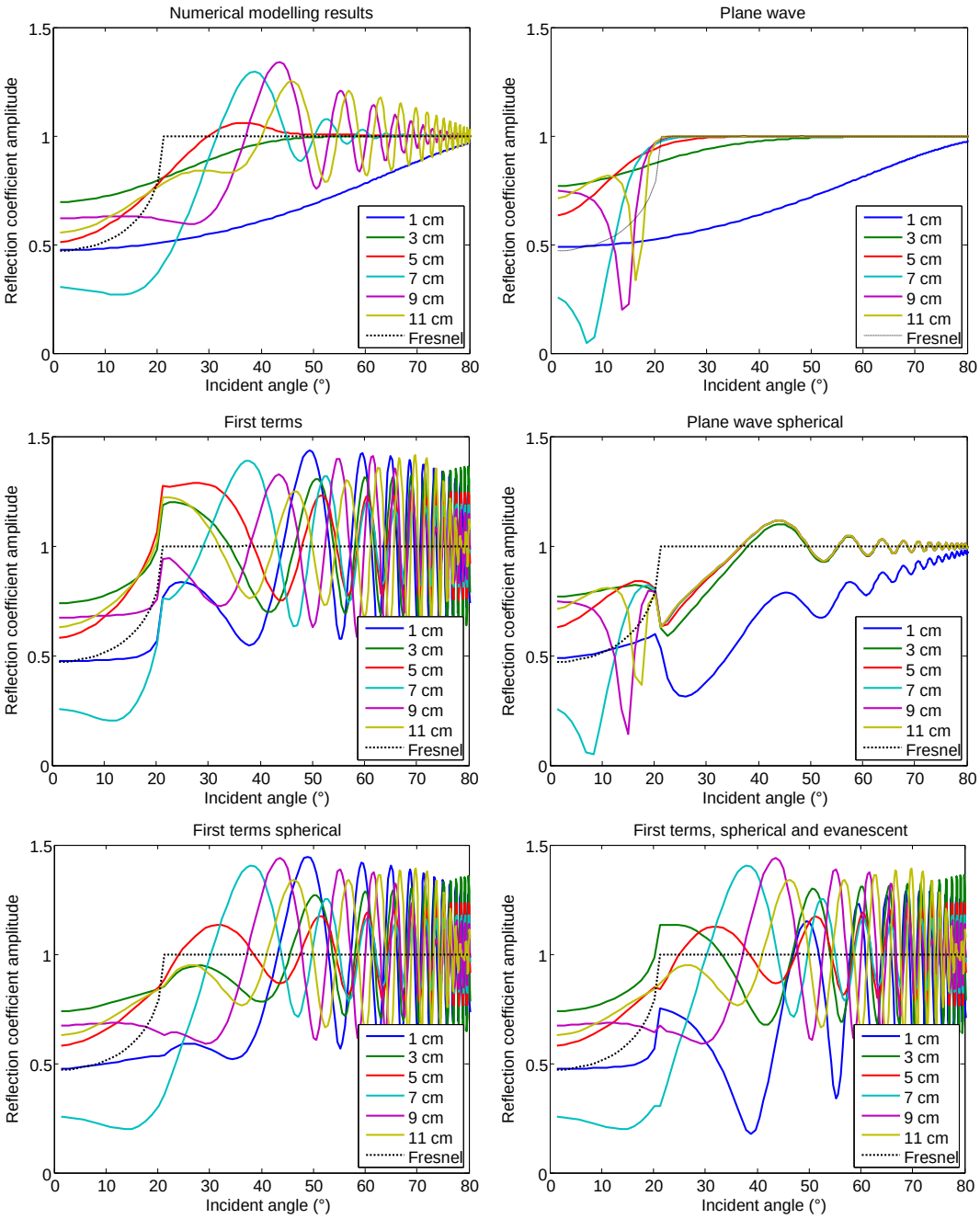

Figure 90 : Amplitude versus offset curves obtained for air thin layers of different thicknesses into concrete. The first diagram is obtained from 2D numerical modelling and the 5 others are analytical approximations obtained with the methods described above.

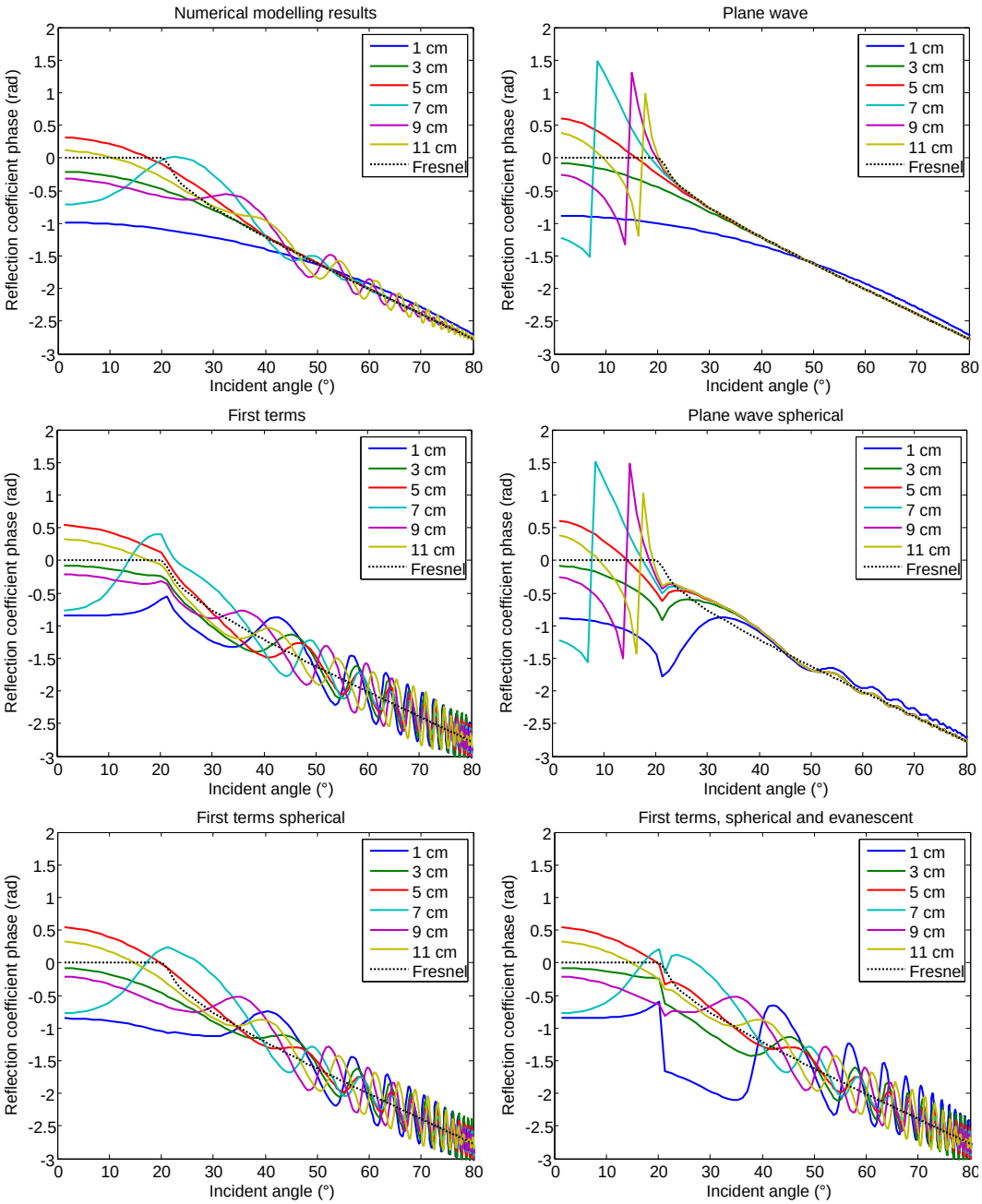

Figure 91 : Phase versus offset curves obtained for air thin layers of different thicknesses into concrete. The first diagram is obtained from numerical modelling and the 5 others are analytical approximations obtained with the methods described above.

From the APVO curves of Figure 90 and Figure 91, we observe that the thinnest layers (1 cm and 3 cm) are very well described by the plane waves approximation, while the thickest layers (7 cm to 11 cm) are better described by the first terms with spherical method. This method predicts well the presence and location of the peaks, but, however, it fails to describe the progressive decrease of the oscillations amplitude (observable on the original radargram).

The methods 3 and 5, introducing evanescent waves into first terms or spherical waves into plane waves approximation, do not improve the basic methods and will thus be abandoned.

The good performance of the plane waves approximation for the description of the reflection on thin layers under 5 cm can be explained by the physical behaviour observed in the snapshots in section 4.1.1: the real multiples of the reflection and the lateral wave were completely invisible into the layer, so the model can totally neglect them. On the opposite, for layers thicker than 5 cm, the evanescent wave amplitude is almost zero and can be neglected (the reflected wave is the same as on a simple interface), while the lateral wave and multiples reflections are present and cause oscillations. For this reason, they are better predicted by the first terms spherical method.

4.1.3 Derivation of a hybrid model for the estimation of APVO curves

In the previous section, we observed that the best analytical method to approach numerical APVO curves depended on the thickness-to-wavelength ratio. For low thicknesses, the plane wave approximations gives good results, while for large thicknesses, the best method is the first term approximation, with introduction of the spherical reflection. In this last case, the method could be improved by the introduction of an attenuation parameter.

To approach the APVO curves in any situations, the forward model should then be hybrid, using one formulation or the other, depending on the thickness-to-wavelength ratio. As a transitional behaviour is observed for intermediate thicknesses, an interpolation method will be selected.

This section will be divided into three parts. Firstly, we will try to determine an analytical formulation for the attenuation of the oscillations. This formulation will be developed for the specific case of air layers. Secondly, the global hybrid model will be implemented and compared to the numerical results. Finally, the same procedure will be applied in order to create a hybrid model to approach the APVO curves obtained from 3D tests.

4.1.3.1 Estimation of the thickness-induced attenuation of the oscillations in the APVO curves

The presence of oscillations in the APVO curves obtained from numerical modelling (Figure 90) is well predicted by the first terms method but, for large offsets, the results do not converge. The equations do not lead to a significant attenuation of the oscillations with the distance while their amplitude rapidly decreases in the curves derived from the numerical tests. Moreover, the attenuation seems to depend on the layer thickness: in the thinner layers, the lateral wave and the multiples are attenuated very rapidly.

To assess those results, we performed a frequency analysis for the radargrams obtained on different thicknesses. For large offsets, the contributions of the lateral/multiples and of the reflected/evanescent waves can be separated. In Figure 92, the radargram is represented for the CMP measured over a simple concrete-air interface. The radargram is cut after total separation of the reflected and the lateral wave. The zone in which the two waves interact is then entirely comprised into the reflected wave radargram.

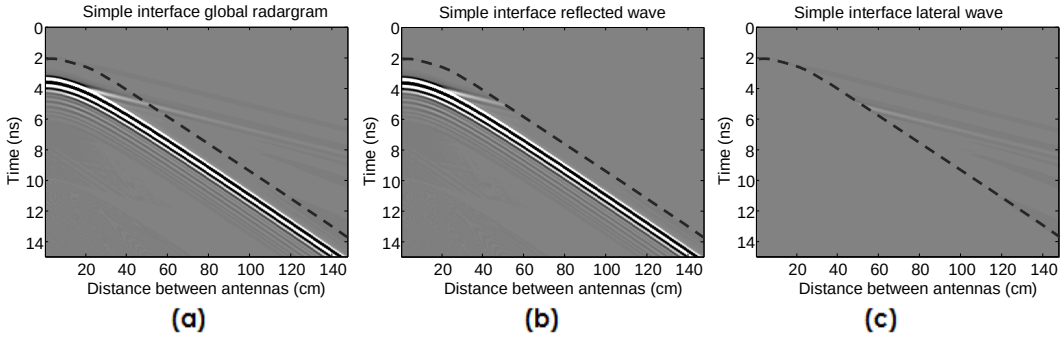

Figure 92 : Radargrams for the detection of a simple interface into concrete. (a) Global radargram; (b) Selection of the reflected wave; (c) Selection of the lateral wave.

By means of this selection, the lateral wave can only be isolated when the antennas are distant of about 60 cm, and we can consider that the corresponding wavelet is completely included in the lateral wave radargram (c) from a distance of about 80 cm. For each offset, a Fourier frequency analysis was carried on. The amplitude determined by this analysis for the three radargrams of Figure 92 are displayed in Figure 93.

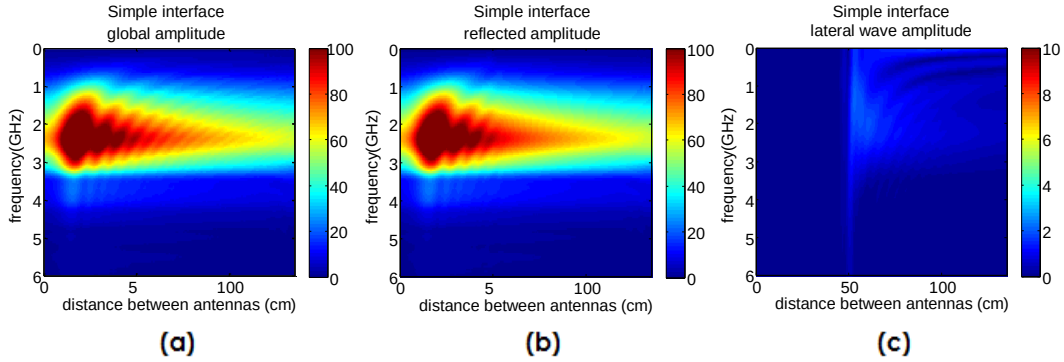

Figure 93 : Frequency-dependant amplitude of the radargrams measured over a simple air interface into concrete (Figure 92). (a) Global radargram; (b) Selection of the reflected wave; (c) Selection of the lateral wave.

In the global radargram (a), the amplitude peak is situated at 2.3 GHz for every antenna offset, but presents oscillations in the frequency domain. When the lateral wave is extracted from the radargram (Figure 93 (b), after 60 cm), the oscillations in the frequency domain disappear, confirming that they are due to the interaction of the reflected wave and the lateral wave.

When only the lateral wave is studied (c), the amplitude is much lower. The amplitude peak is not so clear, presenting also several peaks at lower amplitudes.

We can use this method for checking the theoretical formulas with regard to the amplitude decrease due to geometric attenuation. In 2D, the reflected amplitude is supposed to decrease with the square root of the distance covered by the wave (125). If we multiply by this value each trace of the reflected wave radargram and perform a Fourier analysis, we should then observe a constant amplitude with the distance. This test is performed in Figure 94.

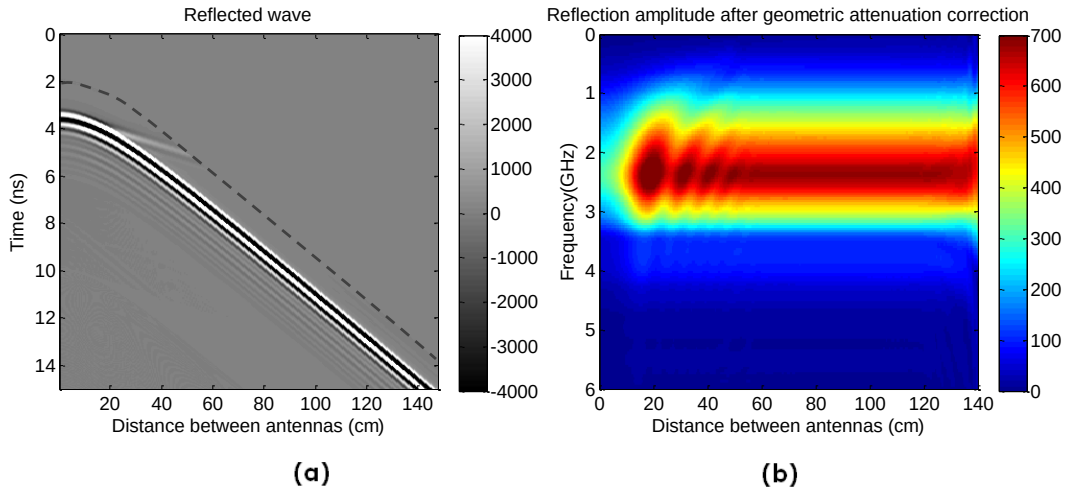

Figure 94 : (a) Radargram and (b) frequency amplitude of the reflection measured over a simple concrete-air interface, after correction of the geometric attenuation.

In Figure 94, we observe that we have a stabilization of the reflected amplitude as soon as the reflected amplitude is completely separated from the lateral wave (around 60 cm). Then, the amplitude is constant until about 125 cm, when the last oscillations of the wavelet begin to disappear out of the time window of the radargram.

The same analysis can be performed with the lateral wave. According to equation (167), the lateral wave amplitude decreases in two dimensions with the 1.5th power of the distance in the layer d_{layer}. The amplitude can thus be corrected by multiplying the measured amplitude by this value:

$$Ampl_{lat,corr} = Ampl_{lat} * d_{layer}^{1.5} \quad (139)$$

The radargrams after this amplitude correction (a) and the amplitude after Fourier analysis (b) are visible in Figure 95.

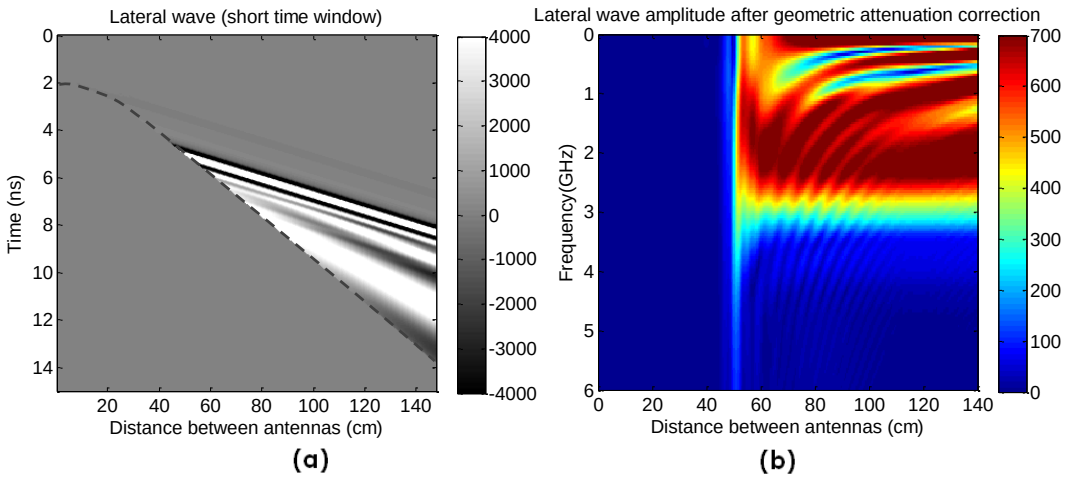

Figure 95 : (a) Radargram and (b) frequency amplitude of the lateral wave measured over a simple concrete-air interface, after correction of the geometric attenuation.

If the frequency amplitude after geometric correction (b) seems more stable with the distance than without correction (Figure 93 (c)), oscillations and low frequency peaks can still be observed. In the radargram (Figure 95 (a)), some oscillations after the wave front of the lateral wave can be observed as well. Those oscillations are not directly part of the lateral wave, and can be cut from the radargram to isolate the lateral wave main wavelet. This analysis has been performed in Figure 96, only differing from Figure 95 by the removal of the triangle under the lateral wave.

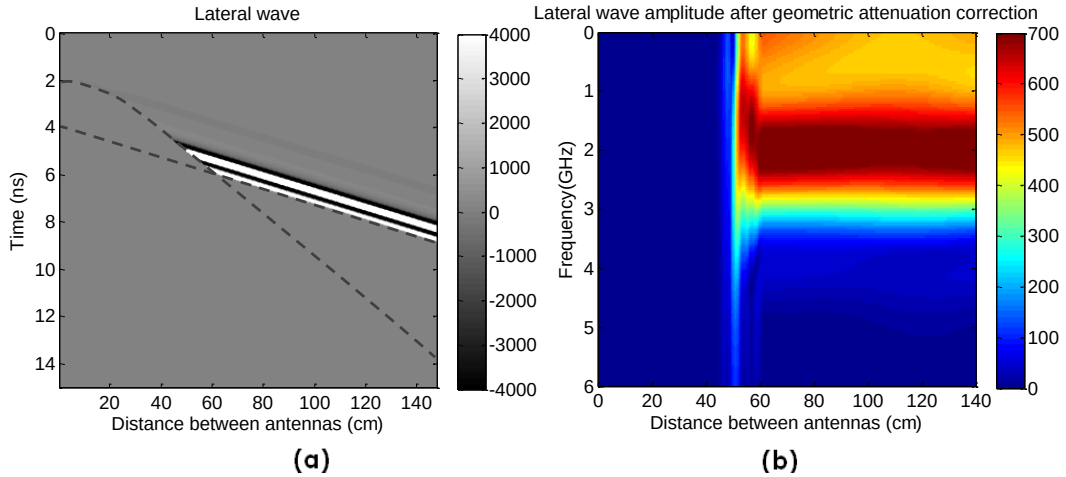

Figure 96 : (a) Radargram and (b) frequency amplitude of the lateral wave principal wavelet measured over a simple concrete-air interface, after correction of the geometric attenuation.

After removal of the secondary oscillations, the frequency amplitude (b) becomes invariant with the distance, confirming the attenuation factor of (139). The oscillations observed in Figure 95 will be present in reality, but are not predicted by the equations. They will thus be a source of error and induce a difference with the simulation results. Fortunately, the geometric attenuation of those waves is strong, so the error should be limited.

If we compare the amplitudes after geometry attenuation correction of the reflected wave (Figure 94 (b)) and the lateral wave (Figure 96 (b)), after separation of the wavelets (at 1 m), we observe that the frequency of the peak is lower for the lateral wave. This is illustrated in Figure 97. This frequency shift of the wave amplitude when propagating laterally was predicted by the lateral wave equation (67), in which appears the frequency-dependant propagation constant k_1.

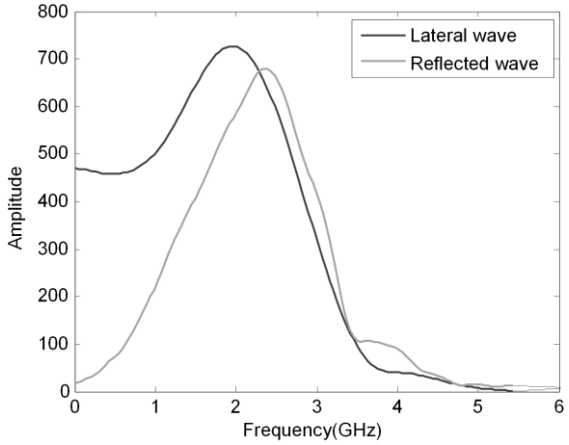

Figure 97 : Geometry-corrected frequency-dependant amplitudes of the lateral and reflected waves, measured for antennas distant of 1 m.

In order to quantify the attenuation of the lateral wave (and the multiple reflections) into thin layers, a similar analysis can be performed. For each thickness (1-11 cm), we performed a Fourier analysis on the complete radargram (Figure 98 (a)), of the reflected wave radargram (Figure 98 (b)) and on the lateral wave radargram (Figure 98 (c)), which will also enclose the multiple reflections into the layer. The results are displayed in Figure 99.

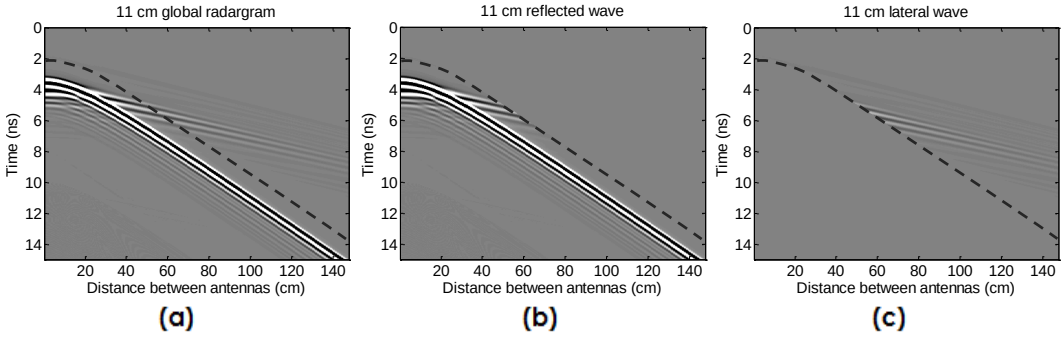

Figure 98 : Radargrams for the detection of a 11 cm thick layer of into concrete. (a) Global radargram; (b) Selection of the reflected wave; (c) Selection of the refracted wave.

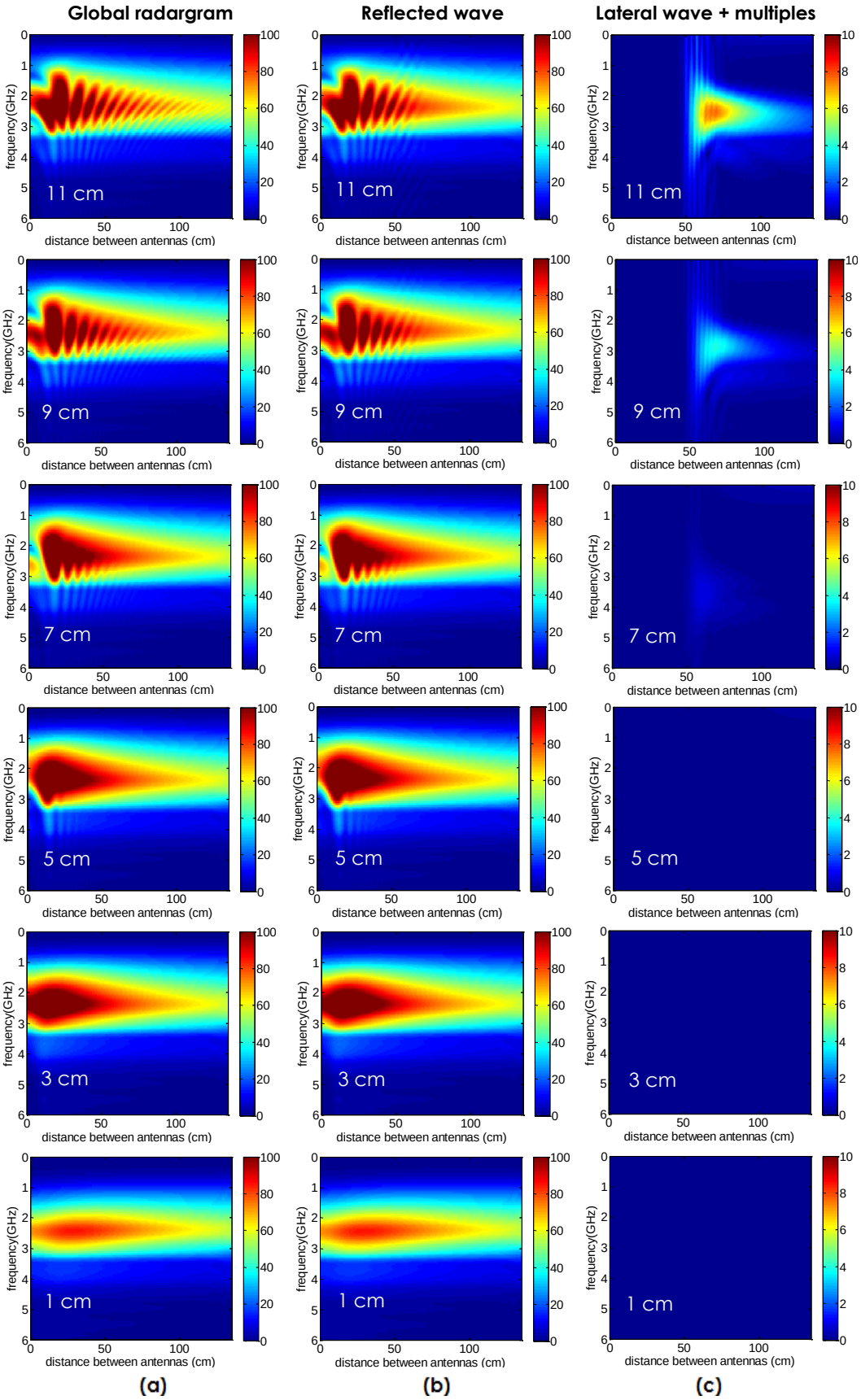

Figure 99 : Frequency-dependant amplitudes for different layer thicknesses: (a) complete radargram, (b) reflected wave and (c) lateral wave and multiples.

We observe that the presence of the oscillations depends on the layer thickness but also on the frequency. In the reflection amplitude diagram for the 5 cm layer, oscillations are present at the frequency of 3 GHz, but not at 2 GHz. In order to visualise the presence of the oscillations for all the frequencies (and not only the frequencies presenting a large amplitude in the selected pulse), we can evaluate the reflection coefficient by using the amplitudes measured with the same configuration on a perfect reflector instead of the air layer. The corresponding radargram (a) and frequency amplitude (b) are displayed in Figure 100.

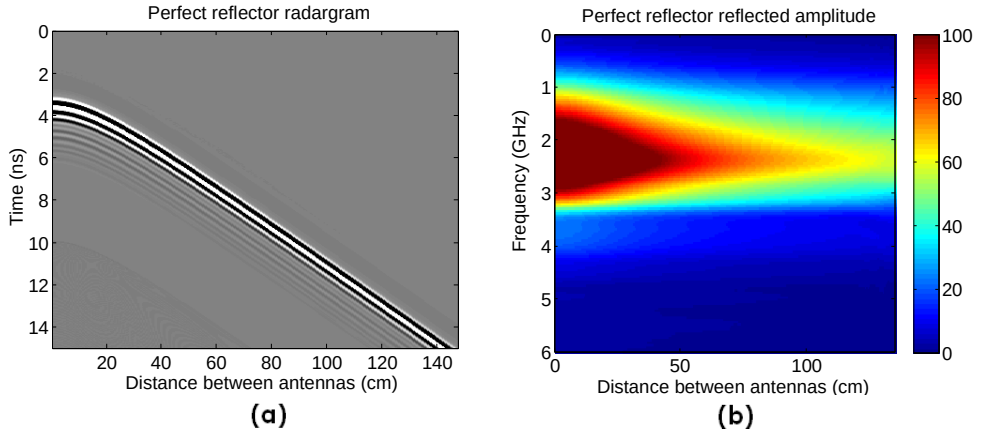

Figure 100 : (a) Radargram and (b) frequency amplitude of wave reflected on a perfect reflector.

To be able to compare the amplitude and the phase of the reflections to numerical equations without having a perfect knowledge of the matrix parameters and of the incident wavelet, it is very interesting to compare the reflected wavelet to a wavelet reflected on a perfect reflector. The reflection coefficient amplitude is obtained by dividing the frequency amplitudes of the global radargrams for all thicknesses (Figure 99 (a)) by the frequency amplitudes of the perfect reflector (Figure 100 (b)). Another advantage of this method is that all the frequencies present in the initial wavelet appear then with an amplitude independent from the initial wavelet. For each layer thickness, the offset and frequency dependant reflection coefficients are presented in Figure 101, along with the reflection coefficient measured on a simple interface.

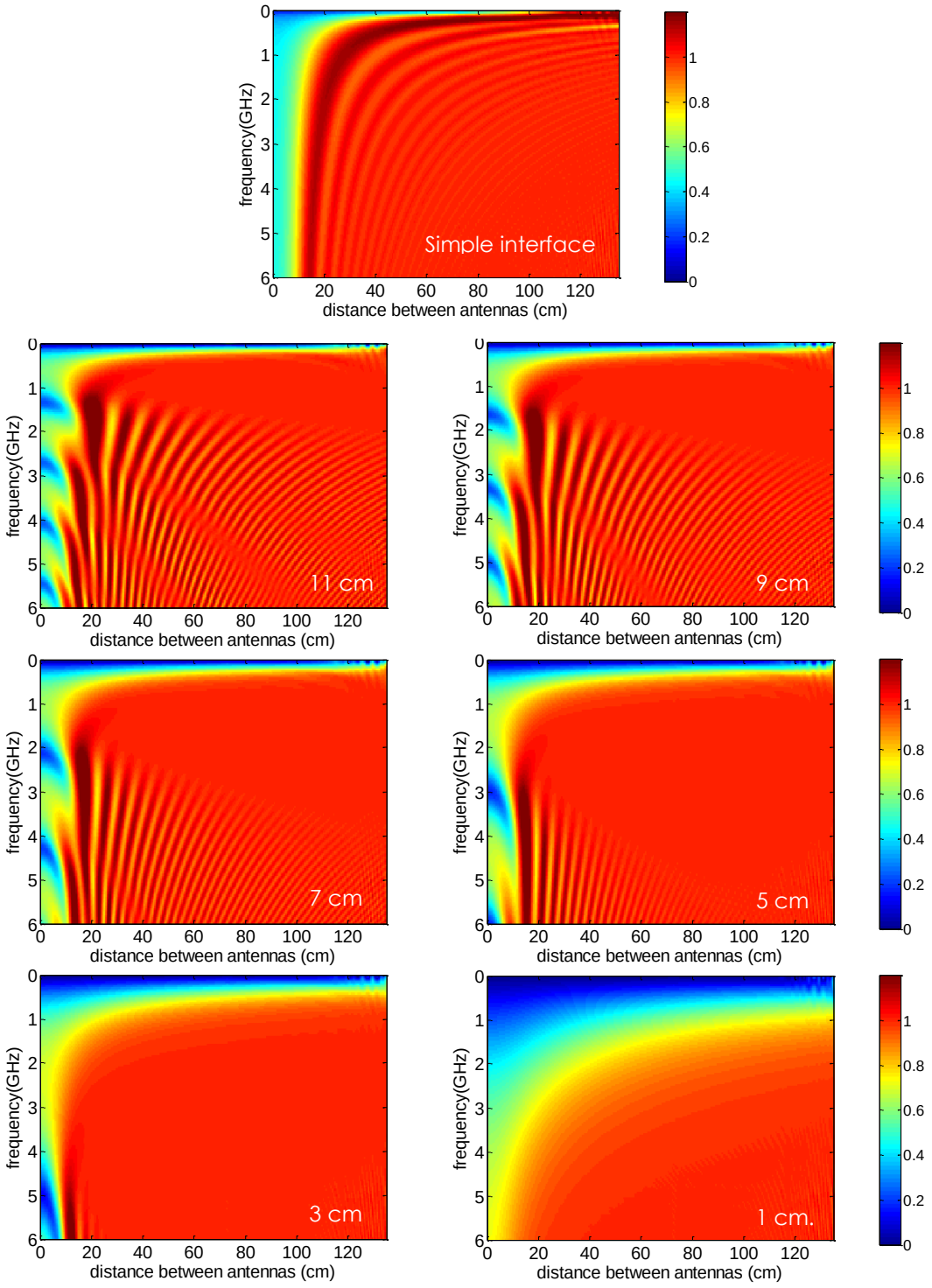

Figure 101 : Reflection coefficients presented as functions of frequency and antennas offsets, for different thicknesses of air layers into concrete ($\varepsilon_r' = 7.7$).

The reflection coefficient behaviour evolves with the frequency as a continuum. Even for a 3 cm layer, for the highest frequencies, oscillations due to the lateral wave and/or the multiples reflected into the layer can be observed. Those waves are not visible after separation of the lateral and reflected wave (Figure 99 (c)), because they are very rapidly attenuated.

The next step of the analysis is to find the law guiding the amplitude decrease of the reflection coefficient oscillations, which corresponds to the amplitude decrease of the wave front into the layer. As a first step, we can represent the reflection coefficient as a function of the dimensionless parameter thickness-to-wavelength ratio (t/λ) (Figure 102). For the 3 cm and 1 cm layers, a wavelength equal to the thickness (when $t/\lambda = 1$) corresponds to frequencies of respectively 10 and 30 GHz. Those frequencies are very scarcely represented in the spectrum of our incident wavelet (Figure 136), which can lead to numerical instabilities.

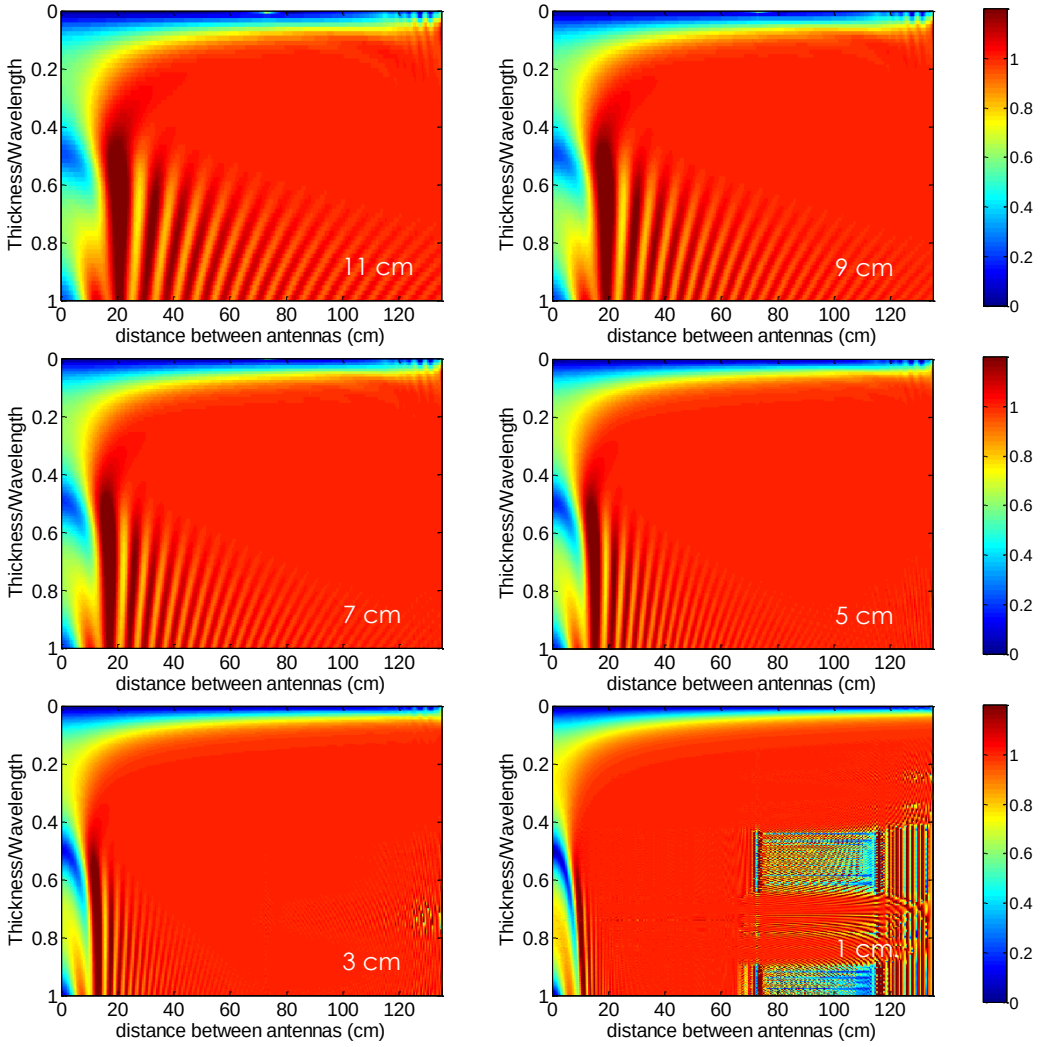

Figure 102 : Reflection coefficients determined as functions of the thickness-to-wavelength ratio and of the antennas offsets for a simple interface and different thicknesses of air layers into concrete.

In Figure 102, we have the confirmation that the layer attenuation is a function of the ratio t/λ. Indeed, thanks to the use of this dimensionless parameter, a general trend appears for all the layer thicknesses: no oscillation is present when the ratio t/λ is inferior to 0.3. For higher t/λ, oscillations are present but decrease with the antennas offset. This decrease appears to be much faster for the thin layers. Consequently, the attenuation into the layer must be a function of the antennas offset, of the thickness t and of the t/λ ratio.

To identify a global trend, we represented, in Figure 103 (a), the reflection coefficients for each layer thickness at the thickness-to-wavelength ratio of 0.7. In order to remove from the graph the numerical instabilities appearing for 1 cm and 3 cm, the reflection coefficients for those thicknesses were set equal to 1 for antennas offsets superior to 60 cm.

In Figure 103 (b), the oscillations are isolated: the amplitude of the reflected wave, equal to 1 after the critical angle, was subtracted from all curves from (a), and the absolute value of the oscillations was considered, in order to take into account the negative interferences as well as the positive ones. They are traced as functions of the distance covered by the wave into the layer, corresponding to L_2 in Figure 33 and simply obtained by subtracting the offset at critical incidence (7.9 cm) from the antenna offsets. The values of all peaks maxima were then reported in order to extract the amplitude envelope (Figure 103 (c)). In this analysis, we only considered the peaks measured for offsets of more than 10 cm.

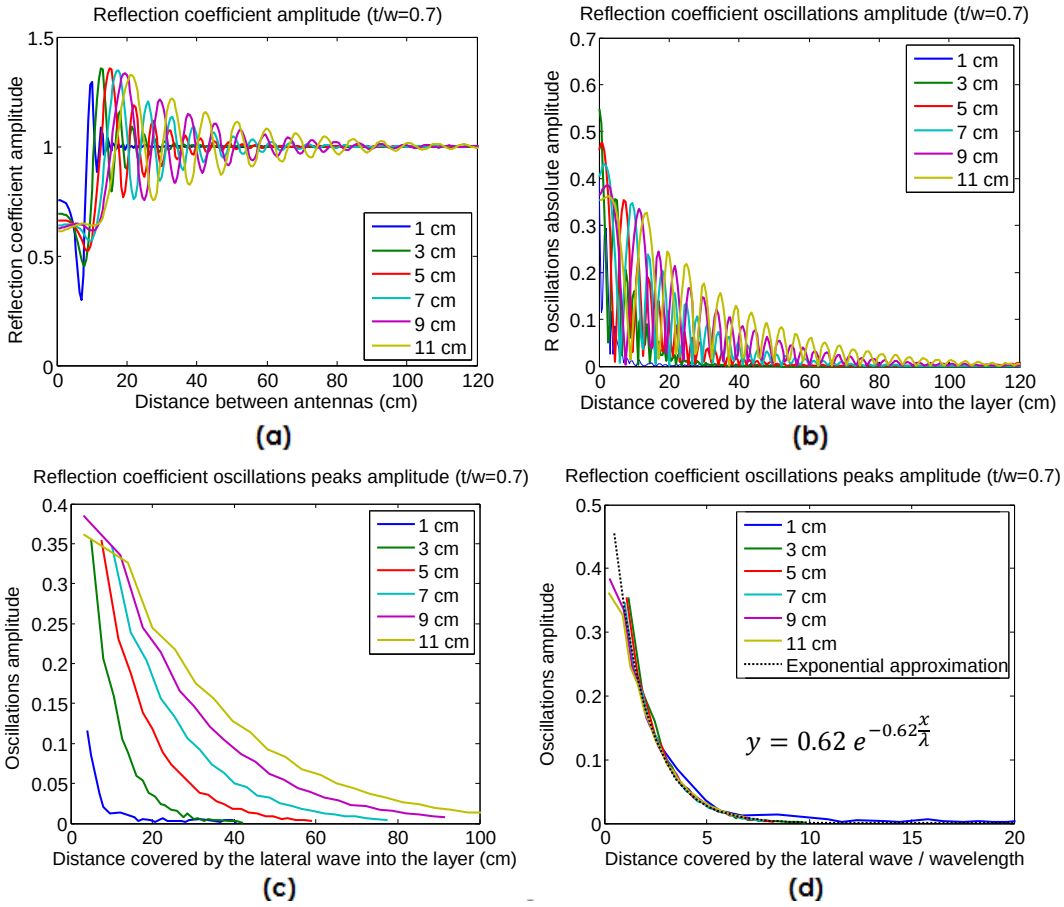

Figure 103 : Estimation of the amplitude of the lateral wave and the multiples traveling into the layer on the basis of the amplitude of their interferences with the perfect post-critical reflection on the first interface, for a thickness-to-wavelength ratio (t/w) of 0.7 and five different thicknesses. (a) Reflection coefficient amplitudes; (b) Absolute amplitude of the interferences; (c) Maximum amplitude of the interferences and (d) Maximum amplitude of the interference, with the horizontal distance normalized with the corresponding wavelength.

But the most interesting result is obtained when dividing the abscissas axis by the wavelength into the layer (Figure 103 (d)). The wavelength is different for every curve, and can be simply obtained by dividing the layer thickness by the studied thickness-to-wavelength ratio (here equal to 0.7). With such normalization, all the curve, even the 1 cm one, are well aligned. Their decrease has an exponential behaviour. If x_{layer} is the horizontal distance into the layer (the difference between the current antennas offset and the offset for a critical incidence), the amplitude of the oscillations for a thickness-to-wavelength ratio of 0.7 ($A_{\frac{t}{\lambda}=0.7}$) can be estimated by:

$$A_{\frac{t}{\lambda}=0.7} = 0.62\, e^{-0.62\frac{x_{layer}}{\lambda}} \tag{140}$$

If the same analysis is performed for different thickness-to-wavelength ratios, the exponential behaviour appears as well, but with different coefficients. The coefficients, estimated with a precision of about 10%, are listed in Table 8. The evolution of the coefficients with the ratio t/λ is also represented in Figure 104.

Table 8 : Coefficients of the normalized amplitude decrease of the waves traveling into the thin layer.

$A_{\frac{t}{\lambda}} = a\, e^{-b\frac{x_{layer}}{\lambda}}$						
t/λ	**0.5**	**0.6**	**0.7**	**0.8**	**0.9**	**1**
a	1.1	0.87	0.62	0.43	0.31	0.24
b	2.5	1.15	0.62	0.37	0.22	0.15

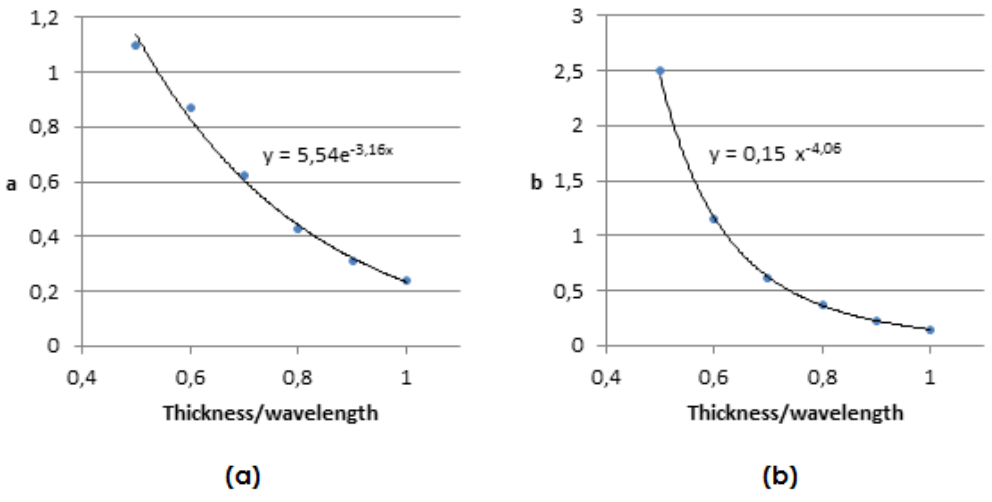

Figure 104 : Representation of the best approximations of the coefficients a (a) and b (b) detailed in Table 8 for the estimation of the amplitude decrease of the waves traveling into the thin layer as functions of the thickness-to-wavelength ratio. The best fit curves are also represented.

We observe that, despite the low precision in the curves parameters estimation, the exponential parameters (Figure 104 (b)) are very well approximated by a power function. The approximation of the amplitude coefficient (a) has a lowest correlation with the data. In particular, the point at $t/\lambda = 0.5$ is not well aligned with the other ones. Nevertheless, using those relationships, we can deduce an equation allowing to estimate the global attenuation of the waves travelling into the layer (lateral and multiples) due to the layer thickness:

$$A\left(\frac{t}{\lambda}\right) = 5.54\, e^{-3.16\frac{t}{\lambda}}\; e^{-0.15\left(\frac{t}{\lambda}\right)^{-4}\frac{x_{layer}}{\lambda}} \tag{141}$$

This equation could be introduced into the first terms spherical model, in order to improve the results from Figure 90, by introducing the layer attenuation into the calculation for incident angles superior to the critical incidence.

But the reflection coefficients calculated by the first terms method already take into account the geometric attenuation of every multiple into the layer. For this reason, the amplitude factor $5.54\, e^{-3.16\, t/\lambda}$ may have to be adapted in order not to take twice the same attenuation into account. The reflection coefficient amplitude and phase obtained with the first terms spherical method, with introduction of the attenuation (141) is represented in Figure 105, in which they are compared to the numerical modelling results.

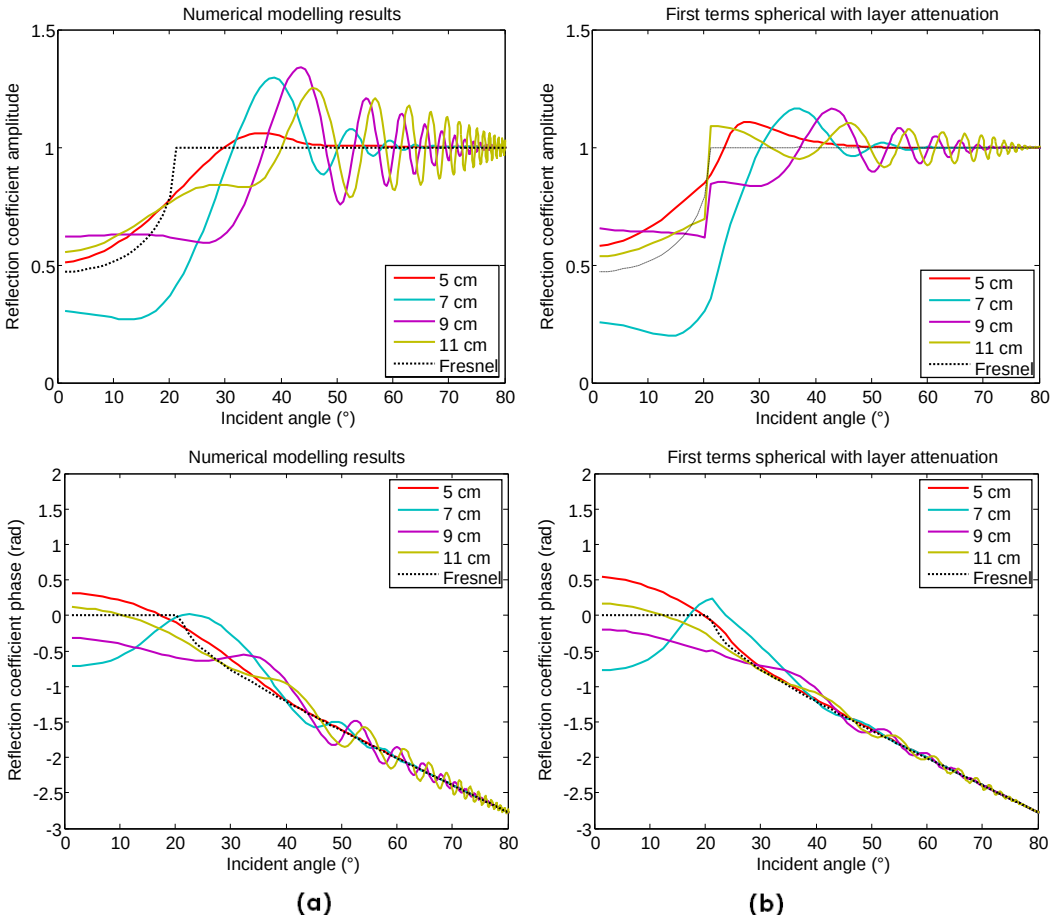

Figure 105 : Amplitude and phase of the reflection obtained with the model using the first terms method, with spherical equation and introduction of the attenuation (141) induced by the layer thickness. The curves (b) are compared to the APVO curves obtained by numerical simulations (a).

As expected, the oscillations amplitude is too attenuated. A discontinuity of the amplitudes at the critical angle can also be observed, due to the fact that the attenuation term, as proposed in (141), is not continuous at this point. It is equal to one for lower incidence (the distance into the layer is equal to zero), but is only equal to 1 for higher incidence when $t/\lambda = 0.54$.

This is not incompatible with the observations made from numerical tests. Indeed, in the graphs representing the oscillations amplitudes as functions of the distance into the layer (Figure 103 (b)), the exponential amplitude decrease could not be observed starting from the critical angle. From the observation of similar graphs for different t/λ ratios, the distance from which this attenuation could be observed seems to be comparable to the layer thickness.

The attenuation is then equal to 1 at the critical distance and can be described by the attenuation function (141) when the distance between the antennas is equal to the sum of the critical distance and the layer thickness. Between those points, we decided to use a sinusoidal (between 0 and pi/2) interpolation, in order to have a smooth variation at the limits (null derivative).

The other issue of the attenuation function (141), identified in Figure 105, is the fact that the geometric attenuation is taken into account while it was already considered in the spherical equation. To solve this problem, we decided to improve the amplitude coefficients of the attenuation function. Their global formulation $c\,e^{-d\,t/\lambda}$ was kept and we determined the optimum values of c and d to minimize the error between the analytical curves and the curves obtained from numerical simulations. The curves for thicknesses of 1 cm and 3 cm were excluded from the optimization, as they are mostly influenced by the evanescent wave which does not appear in the calculations. The error estimation was performed for values of c ranging from 1 to 25 and values of d ranging from 0 to 5. Results are represented in Figure 106.

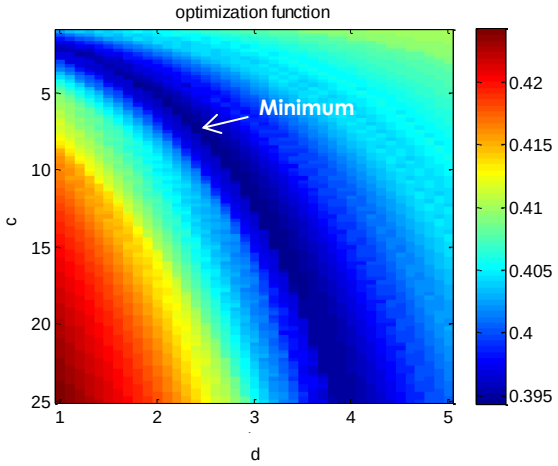

Figure 106 : Optimization function for the coefficient c and d of the amplitude function of the first terms with spherical formula. The theoretical reflection coefficient curves obtained for 5, 7, 9 and 11 cm with this formula are compared to the reflection coefficients measured in 2D numerical simulations.

It appeared that the minimum was obtained for $c = 7.5$ and $d = 2.4$. There is a high correlation between the optimum values of the coefficients, with a low difference in the error of the different optimum values. The attenuation function to apply to the lateral wave and the multiples is then given by (142):

$$A\left(\frac{t}{\lambda}\right) = 7.5\; e^{-2.4\,\frac{t}{\lambda}}\; e^{-0.15\left(\frac{t}{\lambda}\right)^{-4}\,\frac{x_{layer}}{\lambda}} \qquad (142)$$

The corresponding curves are compared to the 2D numerical modelling results in Figure 107.

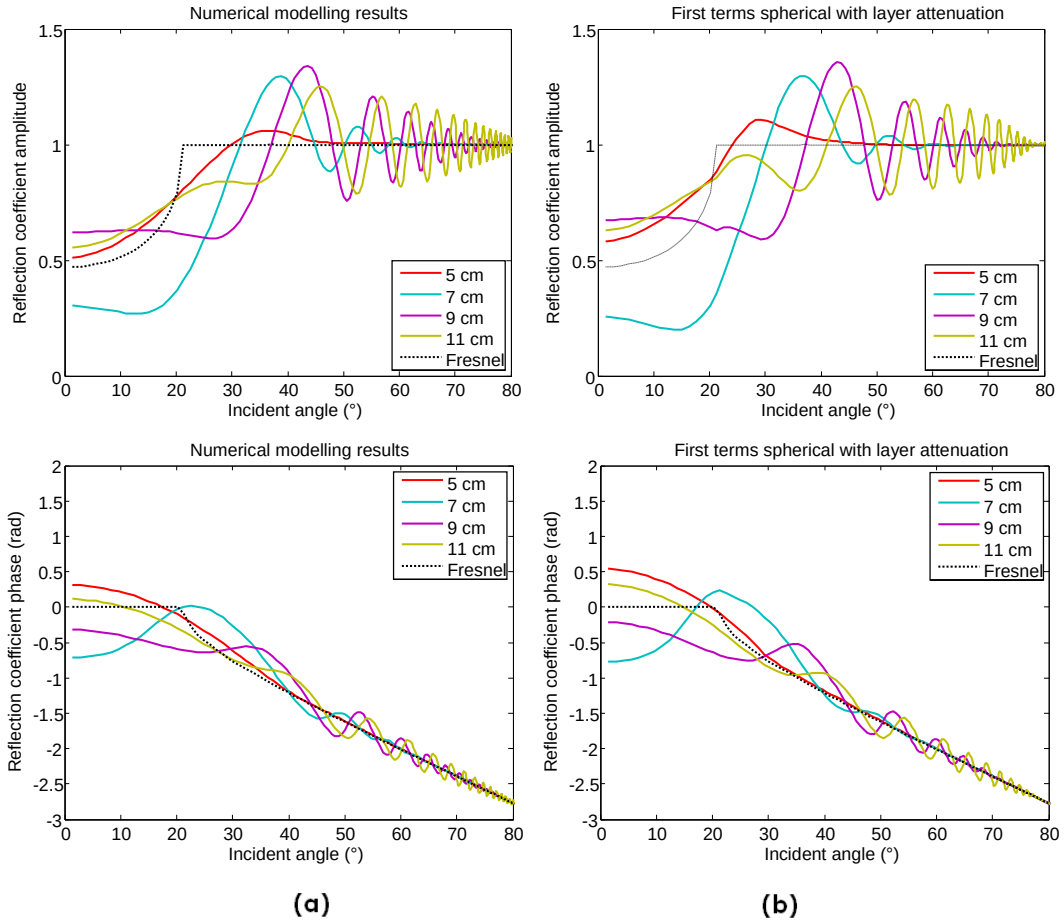

Figure 107 : Amplitude and phase of the reflection obtained with the model using the first terms method, with spherical equation and introduction of attenuation induced by layer thickness. The attenuation function is interpolated between 1 at the critical distance and equation (142) when the distance into the layer is equal to the thickness. The curves (b) are compared to the APVO curves obtained by numerical simulations (a).

The correspondence between APVO curves obtained by the improved method (Figure 107 (b)) and the curves derived from numerical tests (Figure 107 (a)) is excellent for the thicker layers. It will be used to estimate the APVO curves for those layers into the hybrid model that will be developed in the next chapter.

4.1.3.2 Generation and validation of the hybrid model

As the different models are efficient in different situations, we can build a hybrid model that would give good results for every thickness. In this model:

- for thin layers (under 0.3 λ), or for layers presenting a higher permittivity than the matrix, the plane waves approximation is used;

- for thick layers (above 0.5 λ), the first terms methods with spherical reflection is used, with the introduction of the thickness-dependent attenuation function (142);

- for the intermediate layers (0.3 λ - 0.5 λ), the reflection coefficient is calculated by a linear interpolation between the two previous methods.

The three thickness-to-wavelength zones for the reflection coefficient are represented in Figure 108 for the case of a 9 cm layer.

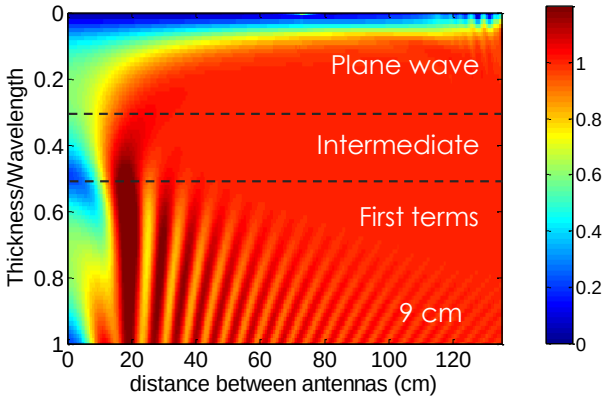

Figure 108 : Representation of the three zones of the hybrid model reflection coefficient.

In Figure 109, the APVO curves obtained by this hybrid method are compared to the curves derived from numerical tests.

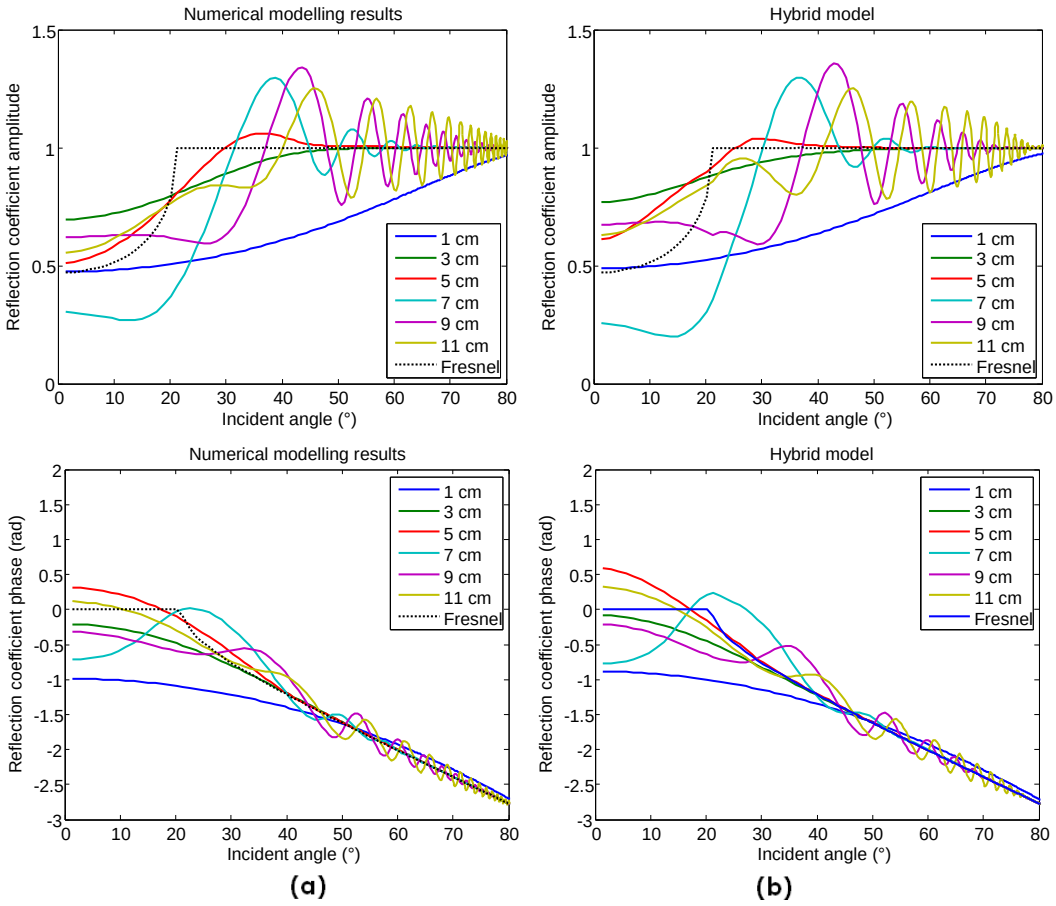

Figure 109 : Amplitude and phase obtained with the hybrid model compared to the APVO curves obtained by numerical simulations. (a) Curves derived from numerical simulations; (b) Analytical hybrid model.

All the curves are relatively well represented, even if the representation of the layers of intermediate thicknesses is less accurate.

As all the phenomena occurring in the reflection of a near-field spherical wave into a thin layer cannot be taken into account by a simple ray method, this method is an approximation; it can however be used to estimate the reflection coefficient of a wave for any thickness. If the user is sure to investigate a layer thinner than 0.3λ, the plane wave model remains an effective alternative, as it will display the same curves, but with a slightly shorter calculation time.

The codes of the different Matlab functions involved in the calculation of the hybrid model are detailed in Appendix 7. These equations have been developed after observation of the reflections on air layers. For other materials, the numerical values may need to be adapted.

4.1.3.3 Hybrid model in three dimensions

The model developed in the previous paragraph can be directly applied to 3D data. The only difference in the analytical calculation is then the 3D evaluation of

the spherical reflection coefficient (72) instead of the 2D. The results are displayed in Figure 110.

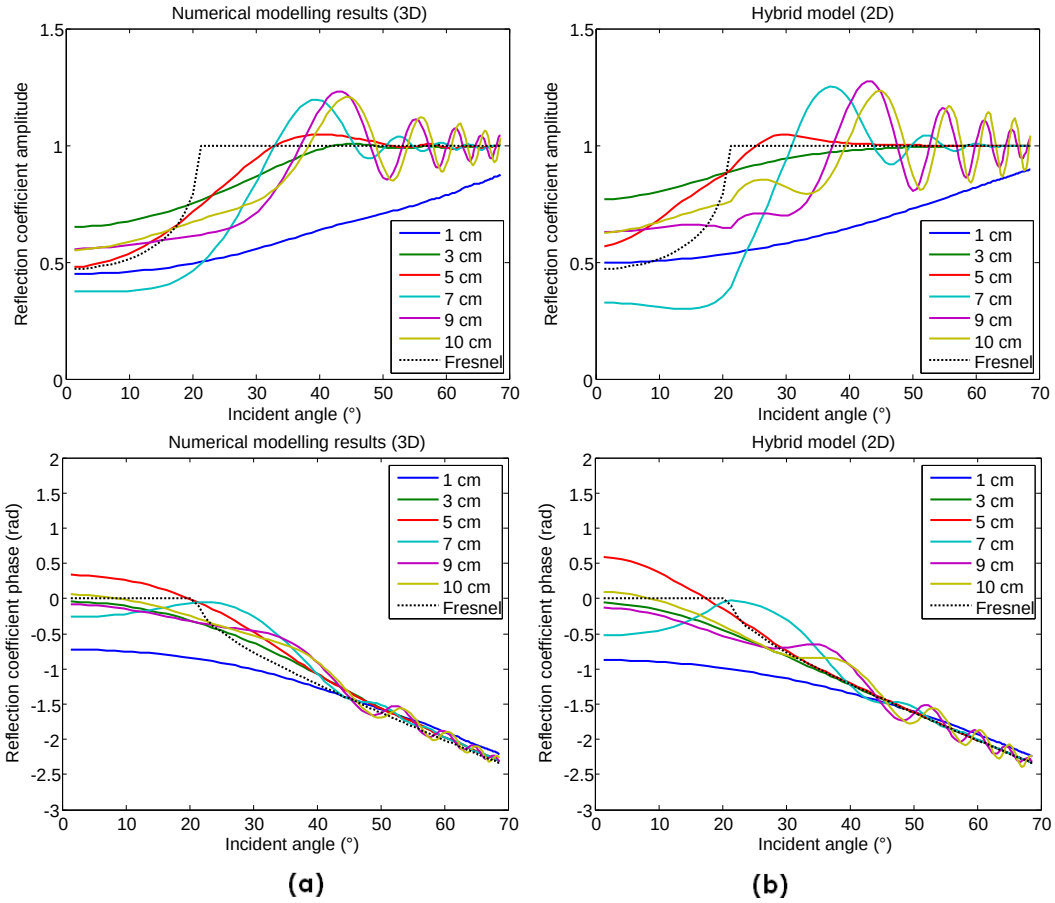

Figure 110 : Comparison of the APVO curves (a) measured from 3D numerical modelling and (b) estimated with the hybrid model determined from 2D measurements in § 4.1.3.2.

The correspondence is acceptable, but the interferences amplitude is overestimated by the model. As the 2D attenuation equation (142) was derived from numerical 2D simulations, we can try to derive similarly a 3D attenuation equation.

The disadvantage of 3D simulations is that the model size has to be reduced and the spatial step increased in order to maintain the required memory under the maximum allocation. This also leads to a lower number of frequencies evaluated by the Fourier analysis and thus to a lower resolution. The incident wavelet was changed to a Ricker wavelet, whose shorter duration allows a faster separation. Finally, due to the increase of spatial step, layers with thicknesses of 11 cm could not be observed in our 3D model, because they interfered with the PML layers (see § 2.3.4). Therefore, they will be replaced in the analysis by 10 cm layers.

To have an idea of the difference of the refracted wave behaviour in 3D, compared to the 2D, we can trace the equivalent of Figure 88 (a) for the 3D model and its equivalent in 2D.

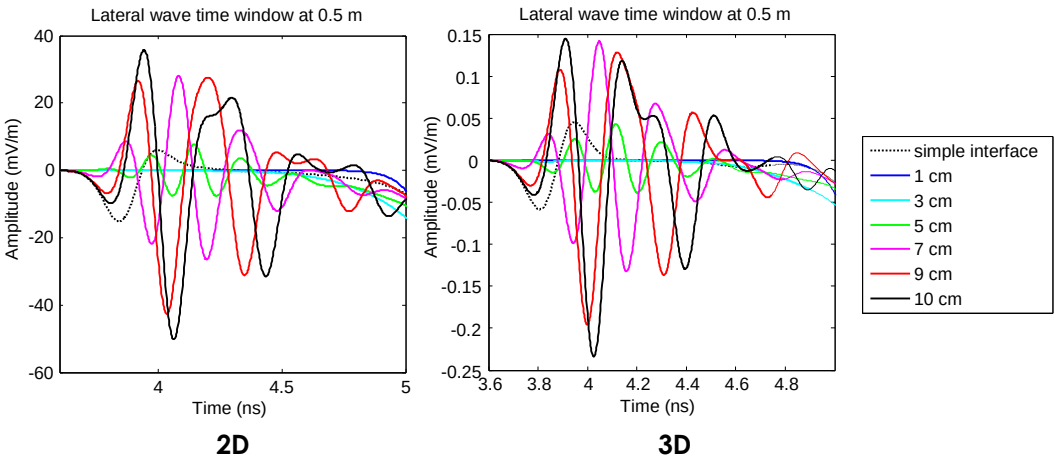

Figure 111 : Critical wave and multiples estimated from 2D and 3D modelling for a 50 cm antennas offset on air layers of different thicknesses, and comparison with a simple interface reflection.

As in 2D, the refracted wave amplitude is almost zero for thicknesses lower than 7 cm. Similarly to the Figure 101 in 2D, the frequency reflection coefficient can be drawn for each thickness and compared to the reflection coefficient for a simple interface.

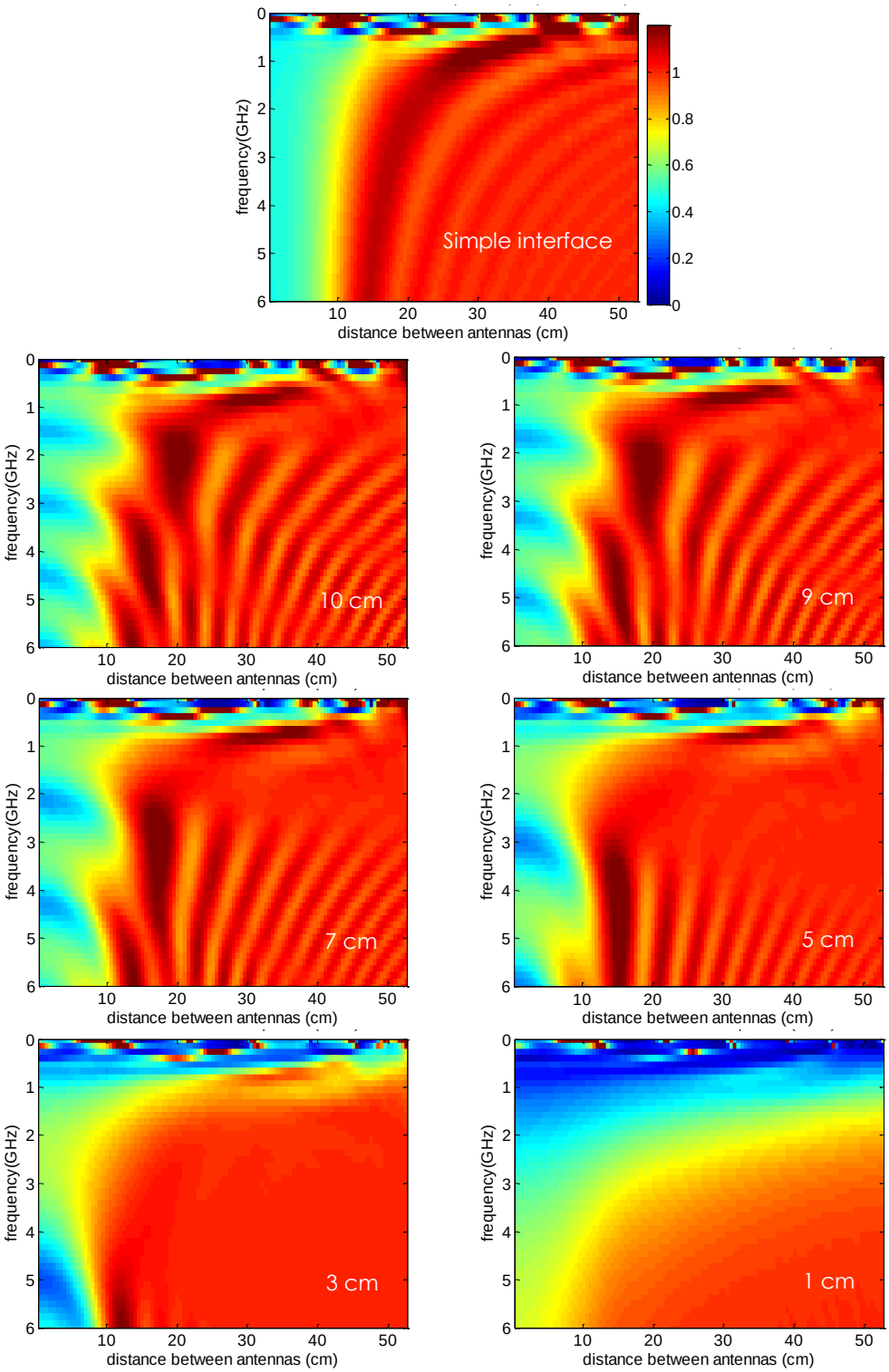

Figure 112 : Reflection coefficient determined from 3D modelling in function of the frequency and of the antennas offsets for different thicknesses of air layers into concrete.

Due to the smaller model dimensions and larger step, the precision in the graphs is lower than in two dimensions. In particular, instabilities are observed for low frequencies (until $t/\lambda = 0.2$ for the thickness of 10 cm).

But we can also observe another phenomenon that was not visible in 2D: the lateral wave seems to influence the results for every t/λ at frequencies around 1 GHz. To assess this difference between 2D and 3D tests, the reflection coefficients for the 10 cm layer are traced in Figure 113, both in 3D and 2D (with the same parameters).

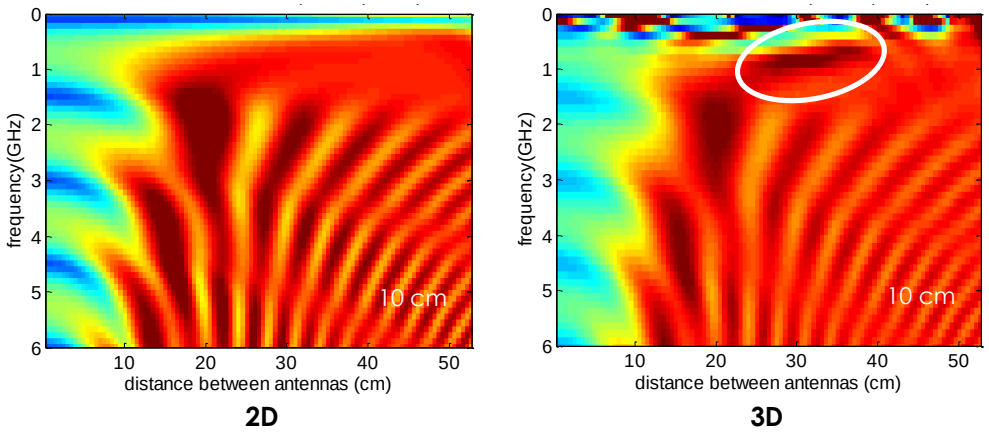

Figure 113 : Comparison between the reflection coefficients for the simple interface and for the 10 cm layer, both in 2D and 3D. The white circle designates the low-frequency peak detected in 3D.

While all simulations parameters are identical in both cases, the lateral wave is present in 3D while it was not in 2D. The maximum of the peak is situated at low frequencies (~1 GHz) and may influence the APVO curves that would be estimated for those frequencies in 3D.

The graphs of Figure 113 can be retraced using the thickness-to-wavelength ratio instead of the frequency as the y axis. Results are represented in Figure 114.

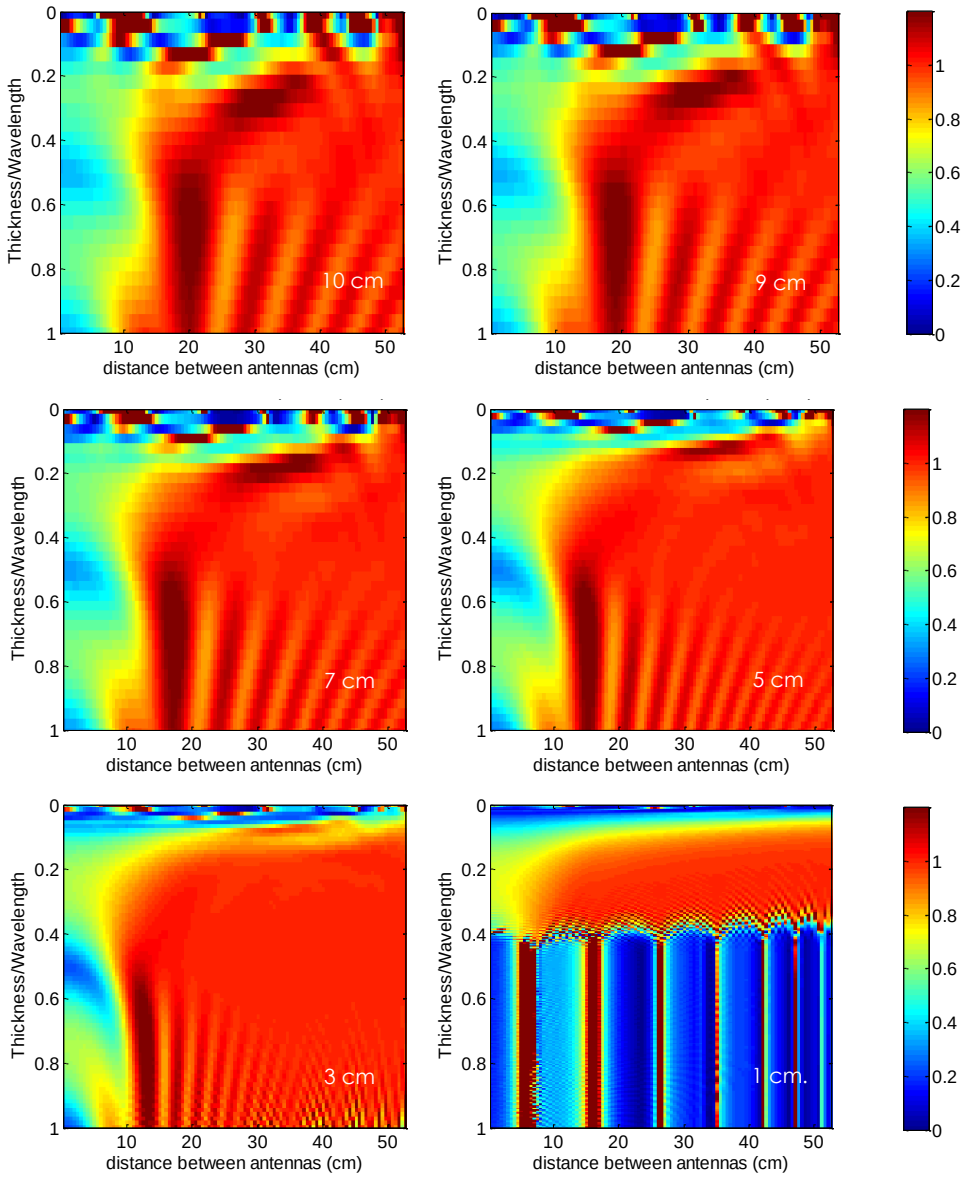

Figure 114 : Reflection coefficient measured from 3D modelling for different thicknesses of air layers into concrete, as a function of the thickness-to-wavelength ratio.

Due to the smaller model dimensions, the reflection coefficient for 1 cm thickness cannot be evaluated for t/λ superior to 0.3; moreover, some numerical instabilities appear for the thickness of 3 cm when $t/\lambda > 0.7$. The same analysis as in 2D can be performed to estimate the attenuation curve for a given thickness-to-wavelength ratio (as in Figure 103 (d)). The example for $t/\lambda = 0.7$ is given in Figure 115.

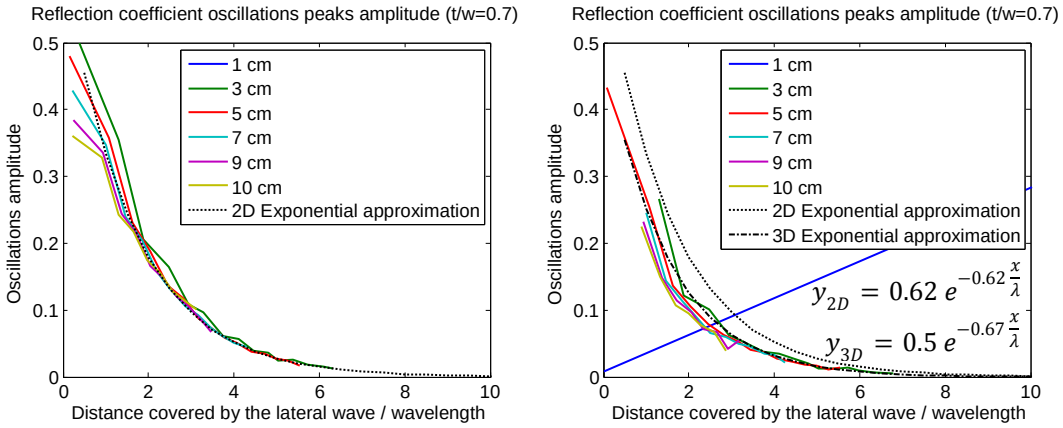

Figure 115 : Maximum amplitude of the interferences, as a function of the horizontal distance normalized with the corresponding wavelength. The 2D attenuation equation does not describe accurately the attenuation measured in 3D. A similar equation in 3D is then introduced.

The 2D attenuation equation (142) developed in the previous chapter fits perfectly the 2D amplitude measurements of Figure 115, even if the modelling has been performed with a greater spatial step to match the 3D model (1 mm instead of 0.625 mm). This confirms that the attenuation is not produced by numerical artefacts.

On the other hand, the amplitudes of the oscillations observed in 3D are lower than estimated by the 2D equation. The superposition of the different curves after normalization appears less clearly than in 2D; the results will consequently suffer from more imprecision, but the parameters describing the 3D attenuation curves can be estimated for different t/λ. They are listed in Table 9 and displayed in Figure 116. The results obtained by modelling a 1 cm curve had to be removed from the calculation because of the noise predominance for that thickness (see Figure 114). The results obtained for $t/\lambda = 0.5$ had to be removed as well, because of the lack of points for the attenuation, and because of secondary oscillations, probably due to the presence of the lateral wave that could be observed for the larger layer thicknesses.

Table 9 : Coefficient of the normalized amplitude decrease of the waves traveling into the thin layer in 3D

$\frac{A_t}{\lambda} = a\, e^{-b\frac{x_{layer}}{\lambda}}$					
t/λ	**0.6**	**0.7**	**0.8**	**0.9**	**1**
a	0.6	0.5	0.31	0.25	0.2
b	1.1	0.67	0.44	0.27	0.22

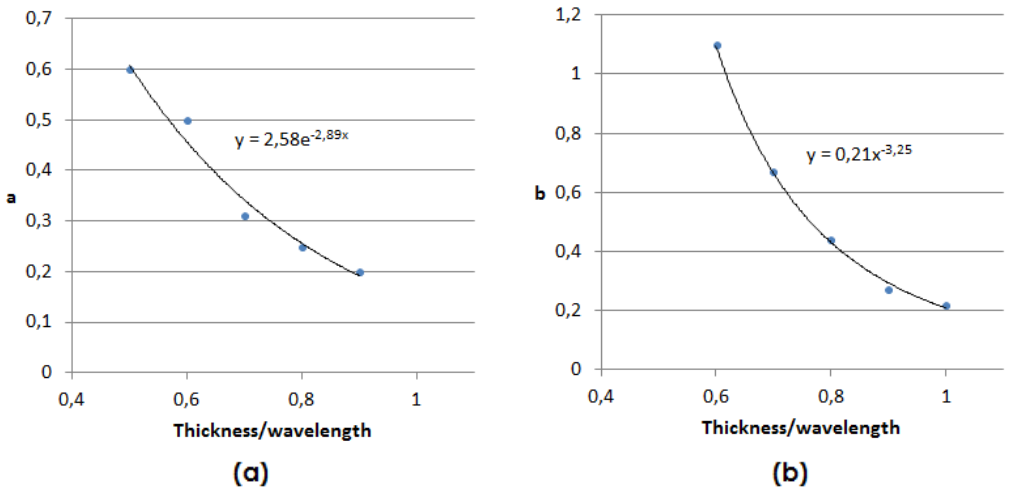

Figure 116 : Representation of the best approximations of the coefficients a (a) and b (b) detailed in Table 8 for the estimation of the amplitude decrease of the waves traveling into the thin layer as a function of the thickness-to-wavelength in 3D. The best fit curves are also represented.

The amplitude of the interferences observed from numerical modelling in three dimensions can then be approached by the formula:

$$A\left(\frac{t}{\lambda}\right) = 2.58\, e^{-2.89\frac{t}{\lambda}}\; e^{-0.21\left(\frac{t}{\lambda}\right)^{-3.25}\frac{x_{layer}}{\lambda}} \tag{143}$$

As in two dimensions, the amplitude coefficient $2.58\, e^{-2.89\frac{t}{\lambda}}$ will be inaccurate for describing the attenuation of the theoretical equation, because those equations already take into account some sources of attenuation. As in two dimensions, the parameters will have to be optimized. The attenuation equation will thus have the form:

$$A\left(\frac{t}{\lambda}\right) = c\, e^{-d\frac{t}{\lambda}}\; e^{-0.21\left(\frac{t}{\lambda}\right)^{-3.25}\frac{x_{layer}}{\lambda}} \tag{144}$$

The optimization function of the distance independent coefficients c and d is displayed in Figure 117.

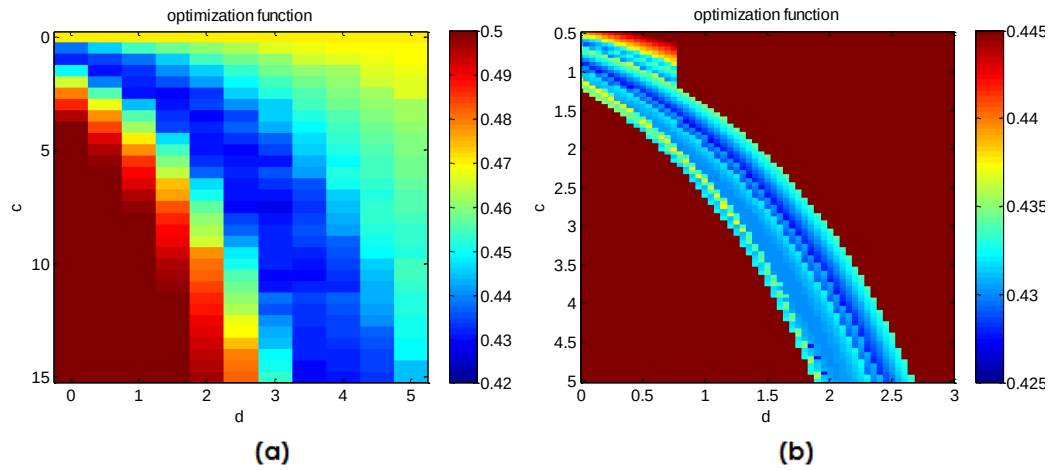

Figure 117 : Optimization function for the attenuation parameters in 3D. (a) First estimation; (b) refined analysis, with calculation of the optimum only in the minimum neighbourhood.

In a first step (Figure 117 (a)), the space of parameters was poorly sampled in order to determine an optimum zone. As in the 2D case, we observed a high correlation between the two parameters: all the optima are situated along the curve $c = e^{0.75d}$. Using this property, we refined the parameters estimation into that domain (Figure 117 (b)). This method allowed to drastically reduce the computational time. The overall minimum was obtained for $c = 1.65$ and $d = 0.85$. The overall attenuation function is then equal to:

$$A\left(\frac{t}{\lambda}\right) = 1.65\, e^{-0.85\frac{t}{\lambda}}\; e^{-0.21\left(\frac{t}{\lambda}\right)^{-3.25}\;\frac{x_{layer}}{\lambda}} \qquad (145)$$

As in the 2D case, this attenuation function was limited to 1 and only applied to the multiples and the critical wave for distances in the layer superior to the layer thickness. For distances into the layer inferior to the layer thickness, the same sinusoidal approximation as in two dimensions was applied.

As in two dimensions, the plane waves spherical model, improved with the attenuation function (145), was introduced into a hybrid model, in combination with the plane waves method. The same limits and interpolations methods as in 2D were kept (Figure 108). The comparison between numerical modelling results and results obtained with the 3D hybrid model are presented in Figure 118.

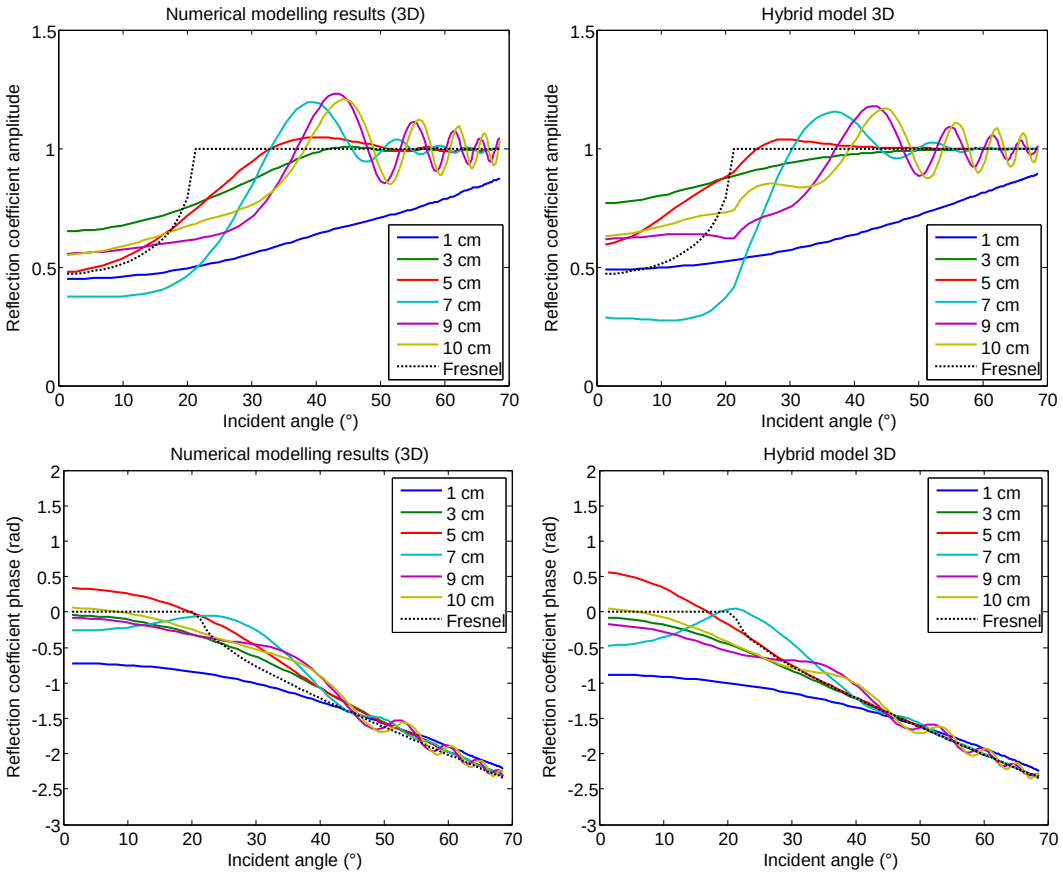

Figure 118 : Comparison of the APVO curves measured from 3D numerical modelling and estimated with the hybrid model determined from 3D measurements.

The correspondence is slightly less good than in two dimensions. One of the reasons of this difference is the presence of the lateral wave, which does not disappear for thin layers as in 2D; on the opposite, it seems to keep a significant amplitude for the low frequencies (see Figure 113). This is visible on the curves of Figure 118. The first peaks of 9 cm and 10 cm are a bit underestimated by the model, the first peak for the 7 cm curve appears later in the modelling. It is more visible for the 5 cm curve, whose peak of maximum amplitude appears much later than in the prediction (and also than in the 2D model). The 3 cm curve displays a small peak as well, followed by low amplitude oscillations. Even the 1 cm curve presents a slight upward inflection for the angle of 40° due to the lateral wave.

As an alternative to this 3D hybrid model, we tested a substitute model in which the attenuation function is not applied to the lateral wave but only to the multiple reflections. This model, described in Appendix 6, did not reveal to improve the results, which proves that the lateral wave is submitted to attenuation as well. A mean of improving the results could then be the development of a 3D hybrid model with a specific attenuation term for the lateral wave. This attenuated lateral wave should be introduced for layers with a low thickness-to wavength ratio as well.

4.2 Comparison of the analytical APVO curves to experimental measurements

The analytical APVO curves developed in § 4.1 allow estimating the reflection coefficient of a thin layer embedded into a matrix. But the fact that the antennas are not embedded into the first medium but placed at the concrete surface will induce the presence of additional phenomena:

- multiple reflections between the surface and the thin layers will appear;
- lateral waves will travel along the surface, after and before reflecting on the thin layer with a critical incidence;
- the radiation pattern of the wave in the semi-infinite medium is not circular anymore and will influence the results (§ 3.2.5.1).

In this chapter, we study -numerically and experimentally- the influence of these phenomena on the APVO radargrams. Our goal is to determine to which extent they can affect the precision in the parameters determination and which method could be developed in the future to limit or take into account their influence.

4.2.1 Influence of the multiple reflections

The presence of the reflection multiples (the waves reflecting alternately on the interface or the thin layer and on the surface, see wave e in Figure 24) is the most visible effect of the surface testing on the radargram. To illustrate its influence, the numerical radargrams and the reflection coefficient frequency amplitude (obtained with a method similar to that of § 4.1.3.1) are compared in Figure 119, for surface and embedded testing. The medium properties are selected for corresponding to the experimental setup that will be tested later: $\varepsilon'_{r1} = 8.3$, $\sigma = 0.01\ S/m$, $t = 1.2\ cm$ and $h = 10\ cm$.

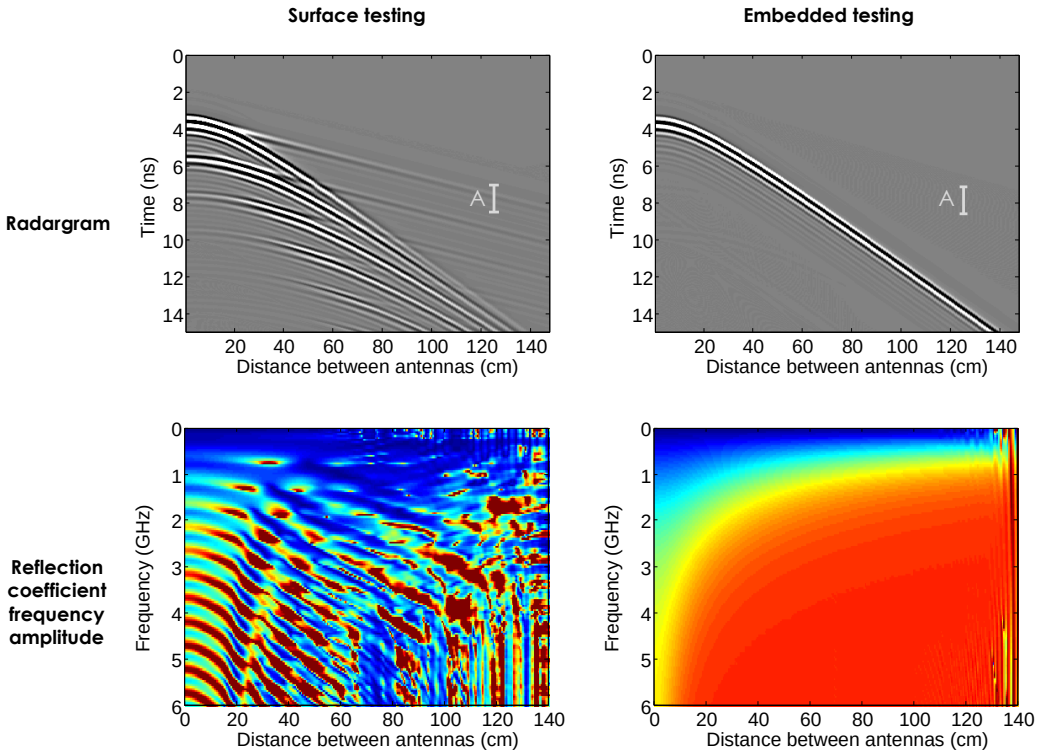

Figure 119 : Comparison of the FDTD radargrams and the corresponding frequency amplitude of the reflection coefficient, for surface and embedded numerical testing of a 1.2 cm air layer embedded into concrete.

Due to the presence of the multiple reflections between the surface and the layer, the reflection coefficient frequency changes drastically. To be able to exploit it when the measurement is performed from the surface, it will be necessary to cut the radargram before the occurrence of the first multiples of the reflection and of the lateral wave. In Figure 120, the shortened radargram and the corresponding reflection coefficient amplitudes are displayed for the same configuration as in Figure 119, in the case of surface testing.

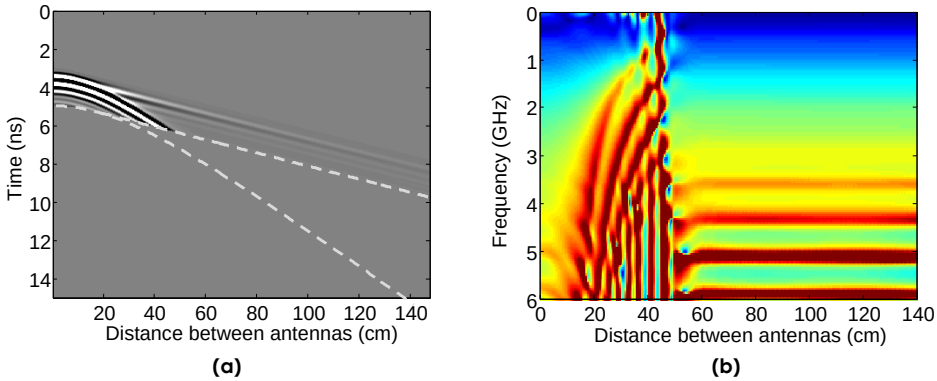

Figure 120 : (a) FDTD Radargram and (b) frequency amplitude of the reflection coefficient for a 1.2 cm air layer embedded into concrete measured by surface testing, after isolation of the first reflection.

The time filtering of radargram (Figure 120 (a)) allows the reflection coefficient for the small offsets to get closer to the reflection coefficient for an embedded layer

(Figure 119, bottom right). The correspondence is however not perfect: the time filtering of the radargram also suppresses the end of the first reflection wavelet, which slightly disturbs the frequency amplitude. In addition, some important oscillations, due to the interaction with the different surface-lateral waves, are visible in the frequency amplitude. The influence of these waves will be detailed in the next paragraph.

4.2.2 Influence of the surface-lateral waves

In addition to the presence of the multiple reflections, another important difference between the radargrams obtained through surface and embedded testing on the 1.2 cm layer is the presence of a reflection appearing in the time window of the lateral wave for surface testing (A interval in Figure 119). For embedded testing, no reflection is visible in this time window because the layer is so thin that the lateral wave (c in Figure 121) is totally attenuated (see § 4.1.1). But for surface testing (Figure 121), additional surface-lateral waves travelling along the surface before or after reflecting on the layer with a critical incidence are present as well (waves d and e).

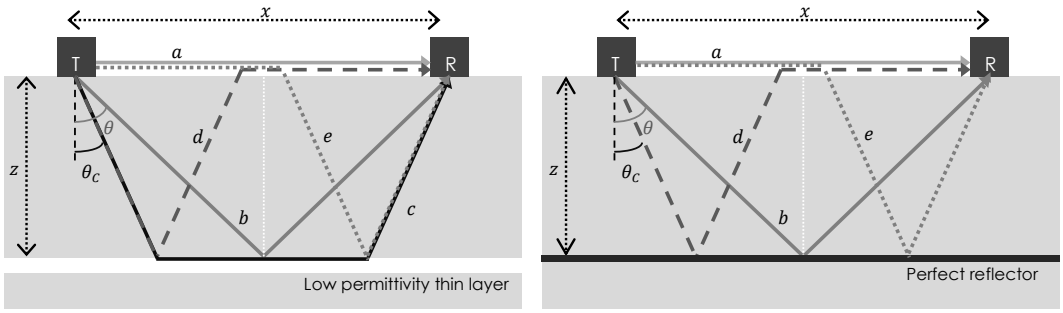

Figure 121 : Representation of the different waves travelling between the antennas for a post-critical incidence, on a low permittivity thin layer and on a perfect reflector.

For assessing the presence of the wave e in Figure 121, travelling along the surface before reflecting on the layer, we performed a simulation without any reflector. In this simulation, the receiver antenna is buried into the concrete at different lateral positions (Figure 122 (a)), but at a constant depth (z) equal to 30 cm. The resulting radargram is displayed in Figure 122 (b).

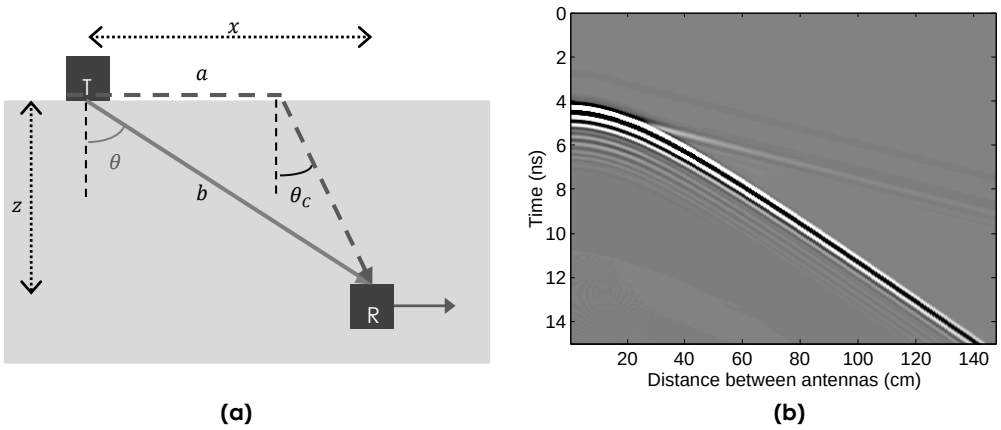

Figure 122 : FDTD test performed to assess the presence of a surface-lateral wave: (a) test configuration and (b) resulting radargram.

A wave travelling at the speed of light is present in the radargram of Figure 122. The path of this wave is without any doubt the path e in Figure 121. The amplitude is not important, but sufficient to influence the CMP radargrams, especially when the reflection coefficient on the buried interface or layer is important.

Consequently, the amplitude observed in the lateral wave time window (interval A in Figure 119) corresponds to the interaction of the waves c, d and e in Figure 121. In the case of a perfect reflector or of an interface with a high permittivity material, only the waves d and e are present (Figure 121 (b)), because no lateral wave can travel in the second medium.

The "reflection coefficient" of these lateral and surface-lateral waves is obtained by comparing the amplitudes on a thin layer and on a metallic reflector (see § 3.1.2). This calculation has already been performed in Figure 120 (b) for the large offsets. Indeed, the time filtering of the radargram leads to a quick isolation of the lateral wave. We observe that the amplitude of the reflection coefficient is frequency dependant (with the presence of sharp peaks), but is not much influenced by the offset. This means that the attenuation of the surface-lateral wave is similar in the cases of the thin layer and of the metallic reflector.

In Figure 123, the amplitudes in the lateral wave time window (A in Figure 119) are drawn for the 1.2 cm air layer, but also for a perfect reflector and a simple concrete-air interface. The amplitudes obtained in a similar configuration with embedded antennas are drawn as well.

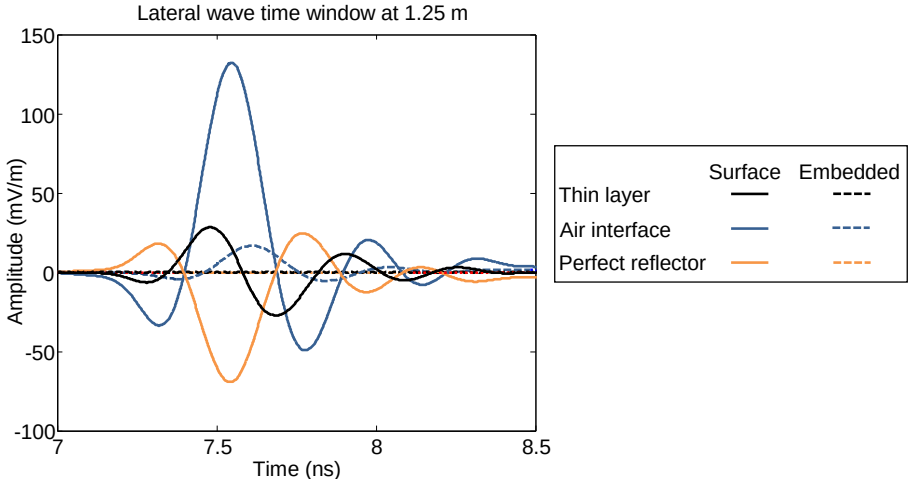

Figure 123 : Amplitudes measured in the lateral wave time window over a 1.2 cm air layer, a perfect reflector and a simple air interface, for surface and embedded numerical testing.

The lateral wave obtained on an air interface with surface testing appears earlier than for embedded testing. This could be due to the presence of a fast thin air layer between the antennas and the surface (of 2.5 mm). The amplitude for surface testing is also much higher, but the general shape of the wavelet is similar. The wavelets measured with surface testing on air and on metal also present a similar shape, but with opposite phases. The shape of the wavelet measured on the thin layer is similar to the derivative of the air interface reflection.

This suggests that some information could be extracted from the phase and amplitude of the "lateral waves": for achieving this, the mathematical expressions of the different events should be determined, similarly to the expression of the lateral wave (67).

4.2.3 Influence of the radiation pattern

To precisely take into account the radiation pattern is very important for a deep analysis of the APVO curves. Indeed, the different waves measured simultaneously propagate initially with different angles (Figure 121). They have thus a different initial amplitude that should be taken into account when calculating the analytical formulation of their sum (see § 3.2.5.1).

From the numerical test of Figure 122, in which the receiver antenna is embedded into concrete, we can also estimate the combined influence of the radiation pattern and the wave *e* of Figure 121. In Figure 124, the wave measured by the embedded antennas is compared to a wave that would be only affected by the intrinsic and geometric attenuations. The relative amplitudes are obtained by respect to the amplitude at a vertical incidence.

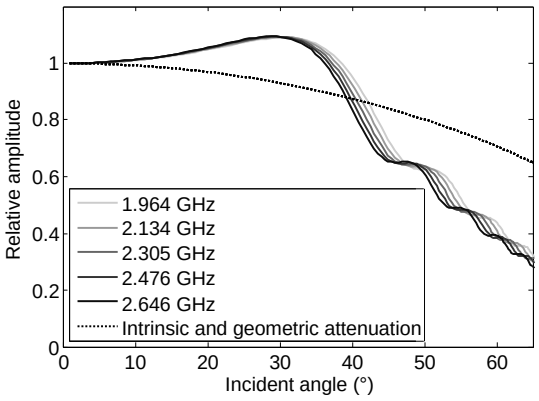

Figure 124 : Amplitude transmitted to an antenna buried into concrete as a function of the incident angle.

We observe some oscillations in the measured amplitude, due to the interaction between the reflected wave and the wave *e*. As those waves appear almost simultaneously for incident angles inferior to 40°, it is not possible to separate their influence for the small angles. This explains why the numerically determined radiation patterns in the literature sometimes present some oscillations [58].

Nevertheless, if we disregard the oscillations due to the surface-lateral wave, the effect of the radiation pattern is important as well: the amplitude decreases much faster than a wave that would be just affected from the intrinsic and geometric attenuation.

The radiation pattern precise determination is likely to be one of the most difficult challenge for the future improvement of our thin layers determination method. Indeed, it depends on the material properties, on the distance with the antennas, on the frequency and on the antennas themselves (§ 3.2.5). With the method developed in this thesis to estimate the reflection coefficient using the comparison with a perfect reflection (§ 3.1.2.1), the problem is probably less acute. Nevertheless, if we want to extend the present method to the cases in which a perfect reflector cannot be buried at the same depth as the thin layer, we will have to base the analysis on the relative amplitude and phase change compared to a vertical incidence. In this configuration, the specific inclination of each offset will have to be taken into account with a good precision.

4.2.4 Comparison of APVO curves obtained through surface and embedded testing

In the previous sections (§§ 4.2.1-4.2.3), the different phenomena appearing in surface testing and that are not present in embedded testing have been described. In this section, the feasibility of the determination of thin layers from their measured APVO curves using the equations derived in § 4.1.3, despite all those phenomena, is investigated. We want to determine if the analysis could lead to a rough estimation of the parameters, and if this concordance could be improved by considering a reduced section of the curves.

For this analysis, we first consider the APVO curves obtained numerically on an air interface embedded at a depth of 10 cm into concrete ($\varepsilon'_{r1} = 8.3$). The curves obtained by surface and embedded testing are compared in Figure 125.

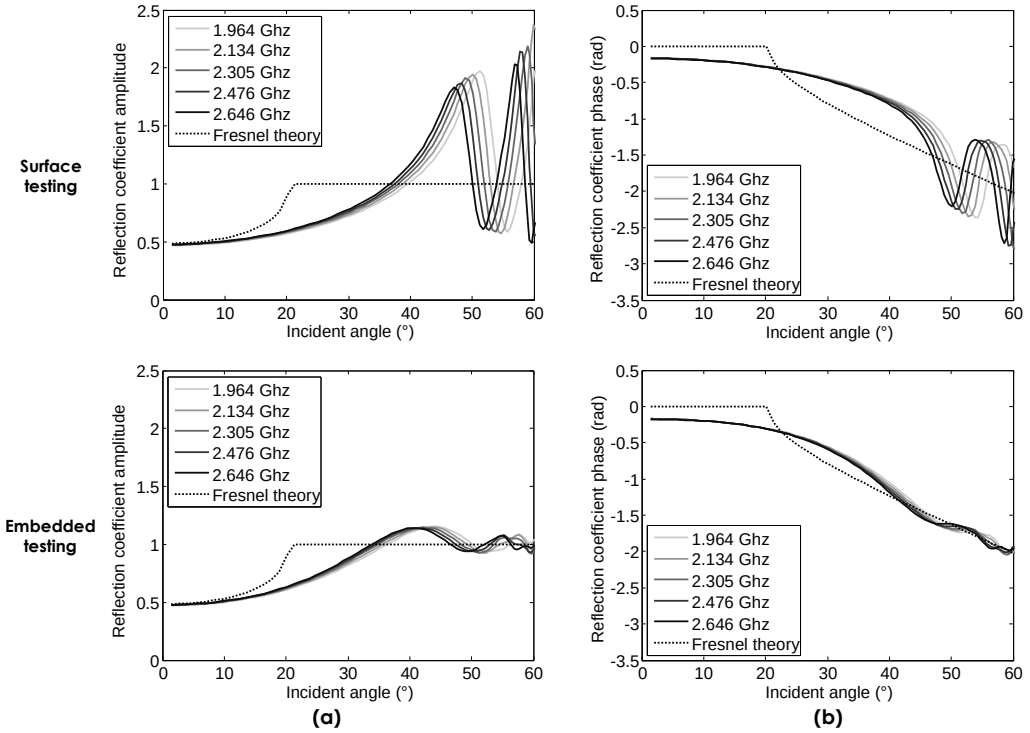

Figure 125 : (a) Amplitude and (b) phase versus offset curves obtained numerically on an air interface embedded at a depth of 10 cm into concrete ($\varepsilon'_{r1} = 8.3$): comparison of the results for surface and embedded testing.

The curves are very similar for the small incidences (up to the critical angle). For higher incidences, the amplitude of the oscillations observed for surface testing are much more important than for embedded testing (up to a factor 10). To be able to approach the first curves by expressions describing the second ones, we should limit the analysis to the small offsets. For the considered geometry and frequencies, an analysis limited to the first 40° could possibly lead to an acceptable estimation of the parameters.

In Figure 126, the APVO curves obtained by experimental measurements for the same configuration are represented. In order to limit the oscillations due to the measurement noise, the signals are treated with a mobile mean filter before representation.

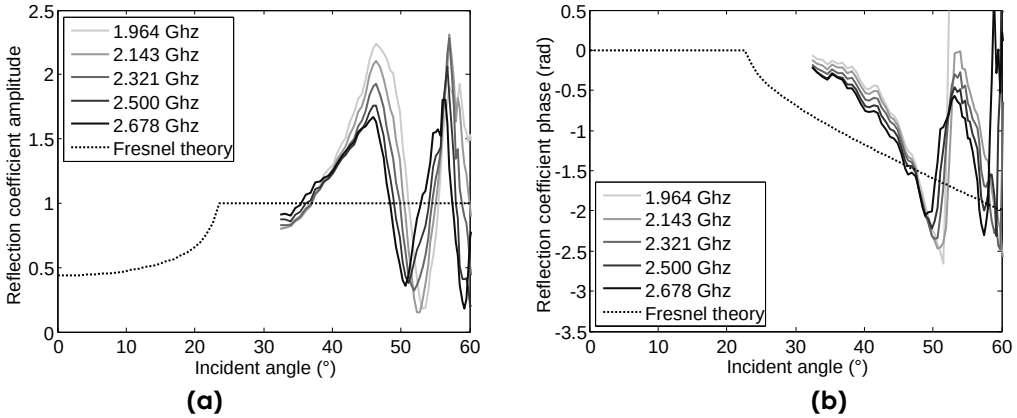

Figure 126 : (a) Amplitude and (b) phase versus offset curves obtained experimentally on an air interface embedded at a depth of 10 cm into concrete ($\varepsilon'_{r1} = 8.3$).

The concordance with the numerical predictions (Figure 125) is relatively good. This means that numerical simulations are able to approach experimental data, even if they are performed in 2D, and do not consider any antenna shielding or material dispersion. However, only the angles superior to 32° are available in experimental data. This is due to the fact that the smallest antennas offset for CMP is 13 cm (Figure 45). If we limit the analysis to the first 40°, this will strongly limit the exploitable angle range (32°-40° instead of 0°-40°). Moreover, by comparison to smaller incidence angles, this part of the signal is more affected by surface effects and by noise, due to the longer ray path.

The most interesting part of the curves are thus unavailable because of the antennas dimensions. A mean that could improve the feasibility of parameters determination using the APVO curves, even without equations improvement, would be to modify the geometry of one antenna so that the angle at the initial position is decreased. A simple inversion of the antennas position into one of the two shielded boxes (Figure 45) would reduce the initial offset from 13 to 9 cm. The initial angle would then be 24°, which would double the total angle range to be investigated.

The same analysis can be performed for the reflection on thin layers. In Figure 127, the APVO curves for surface and embedded testing are compared for a 1.2 cm air layer embedded into concrete.

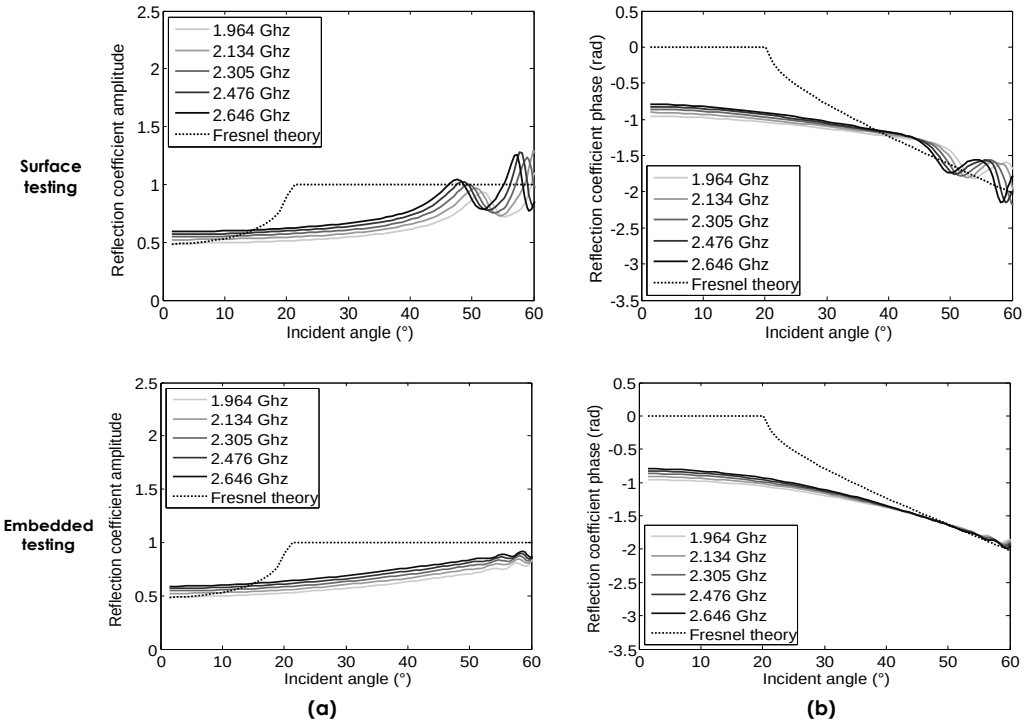

Figure 127 : (a) Amplitude and (b) phase versus offset curves obtained numerically on a 1.2 cm air layer embedded at a depth of 10 cm into concrete ($\varepsilon'_{r1} = 8.3$): comparison of the results for surface and embedded testing.

The oscillations in surface testing have a smaller amplitude, which increases slightly the angle range in which the different curves could be compared. The experimental APVO curves for the same 1.2 cm air layer are drawn in Figure 128.

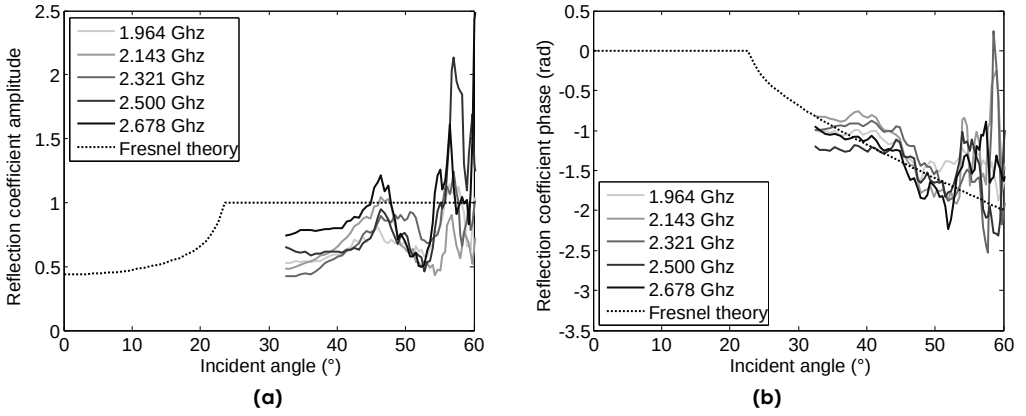

Figure 128 : (a) Amplitude and (b) phase versus offset curves obtained experimentally on a 1.2 cm air layer embedded at a depth of 10 cm into concrete ($\varepsilon'_{r1} = 8.3$).

The real curves are affected by an important noise, even after the use of the mobile mean filter. Nevertheless, the global shape of the curves in the interval 32°-42° is not drastically different from their equivalents in the embedded testing (Figure 127). A parameters determination using those curves may then be attempted, but the precision of the results is not expected to be very high.

As an alternative to the determination of the parameters using the whole curves, we will also consider the possibility to test only one offset. Indeed, this method would allow using the static measurements, in which the offset is 4 cm and the surface-lateral waves are not present. Such tests will be performed in §§ 5.1 and 5.2.

4.3 Conclusions

We developed a 2D and 3D hybrid model able to estimate the reflection coefficient of a thin layer for any thickness-to-wavelength ratio. This model uses the most appropriate of the methods described in § 2.2.2 depending on the layer properties. For the very thin layers ($t/\lambda < 0.3$), the reflection coefficient is calculated using the plane wave approximation. On the opposite, for thick layers ($t/\lambda > 0.5$), it is calculated using the first terms method, with introduction of the spherical waves formula for the first reflection and of an attenuation term for the propagation into the layer. This term was derived from FDTD simulations performed on air layers. The reflection coefficient for intermediate layers is calculated through an interpolation between the results of the two methods.

This hybrid method allows calculating the APVO curves of the reflection coefficient, taking into account the lateral wave. But when the tests are performed from the surface, additional phenomena will develop and influence the measured amplitude: the multiple reflections, the surface-lateral waves and the radiation pattern.

The effect of the multiple reflections on the measured reflection coefficient is important, but it can be limited through a time-filtering of the radargram. The large oscillations caused by the surface-lateral wave only affect the large offsets, so a limitation of the offset range can reduce its influence. The radiation pattern has a limited influence on the amplitudes as long as the reflection coefficient is determined by using a perfect reflection comparison.

With these restrictions, the analytical APVO curves for the reflection coefficient should then be able to approach measured APVO curves, but only after time filtering and limiting the considered range. The main difficulty is then the important initial offset, preventing the measurement for the smallest angles, which were the most promising for the parameters determination. A first method for improving the layer determination method for surface measurements would then be a modification of the antenna geometry, in order to reduce the CMP initial offset.

Another method would consist in an analytical characterization of the behaviour of the surface-lateral waves, similar to the lateral wave equations developed in § 2.1.7.2. After consequent mathematical developments, this would allow to use a wider offset range for the layer characterization. In particular, the very specific frequency content of the lateral and surface-lateral waves could be used to

determine the layer properties. This method could allow to exploit the part of the APVO curves measured with larger offsets.

If the APVO curves cannot be approached analytically for the considered angle range, another solution would be to estimate them through FDTD simulations. This method is much slower, but we have shown in this chapter that the numerical data were able to predict with a good accuracy the experimental measurements, even if they do not take into account some factors as the antennas shielding or the concrete dispersive properties.

As an alternative to the analysis of APVO curves, the layer determination can also be based on static measurements. Indeed, the monostatic offset (4 cm) is sufficiently small to prevent the apparition of the surface effects. For this reason, in addition to the APVO curves, we will also attempt in the next chapters to characterize the layers using static measurements.

Chapter 5: Numerical and experimental thin layers characterization

This fifth and last chapter is dedicated to the determination of thin layers, using the results of 2D simulations and measured datasets. We will compare the results to different analytical curves studied in the previous chapter, in order to see if this comparison can lead to a reliable estimation of the layer parameters.

In § 4.2.4, it was suggested that the layer parameters could be advantageously determined from static measurements instead of CMPs. Indeed, with this method, the antennas offset is sufficiently small to avoid the post-critical surface effects, which could compensate for the lower information content. This method will be investigated in the two first sections of this chapter. The simplest method (§ 5.1) is based on the evaluation of the peak-to-peak amplitude in static measurements. The signal treatment is then limited to a minimum and the equations can be simplified due to the small incident angles.

The analysis of static measurements can also be refined by the use of a spectral analysis of the wavelet (§ 5.2). This method is supposed to increase the concordance with the analytical formulation and to maximize the possibilities for the layer determination. We will determine the best analytical formulation in function of the parameters, as well as the influence of surface measurements.

Finally, we will try to use the CMP curves for the layers determination. We have shown in § 4.2 that this method would be subject to uncertainties due to the post critical incidence, but that an analysis of only the smallest angles of the CMP was still susceptible to give a fair estimation of the parameters. This will be tested on a set of experimental CMPs in § 5.3.

5.1 Static measurements with peak-to-peak analysis

This method is the most basic for the thin layers analysis. It is based on the study of a single trace: it can be applied to various points of a profile if the layer has a variable thickness with the location. As suggested by its name, the peak-to-peak amplitude is the difference between the maximum value of the reflected wavelet and its minimum value. In addition to the tests on the thin layer, tests were performed on a perfect reflector. The direct wave was measured as well, in order to isolate the reflection event (Figure 129).

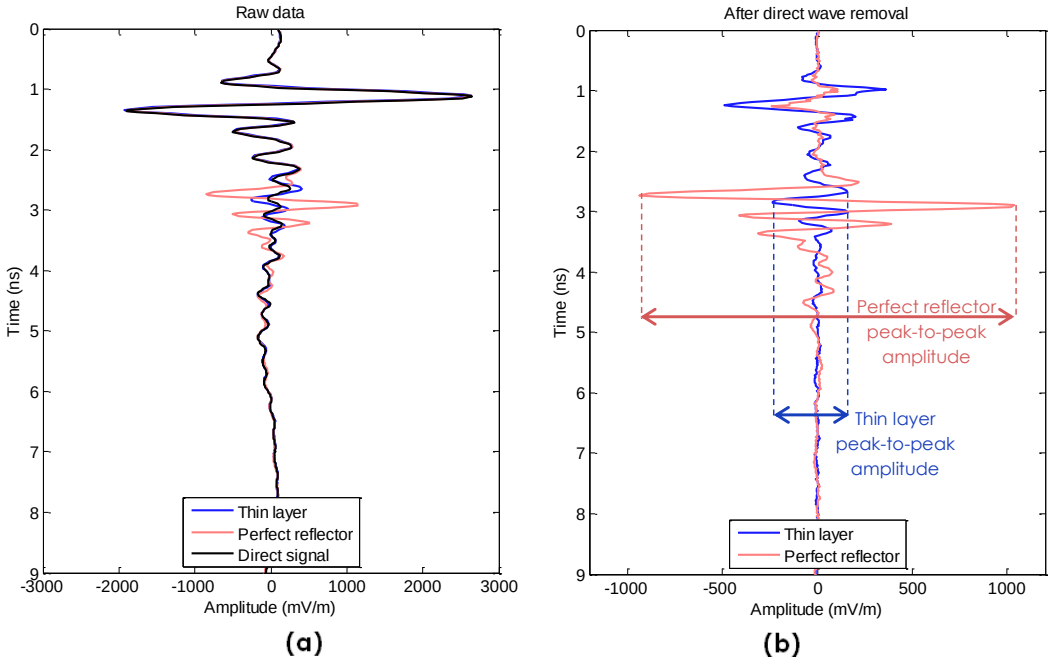

Figure 129 : Experimental peak-to-peak amplitude evaluation over a 0.5 cm air layer embedded at a depth of 10 cm into concrete: (a) Raw data; (b) After direct wave subtraction.

In the methods based on the peak-to-peak amplitude, the phase variation of the reflection is not considered. All the frequency components of the wave are also supposed to travel at the same speed and to be attenuated with the same factors. The dispersion of the properties with the frequency (§ 2.1.6) is thus neglected, but this approximation is valid for dry concrete at frequencies ranging from 0.5 to 3 GHz [44].

In this chapter, the objective is to determine the limits of this simple method for the determination of thin layers. In order to achieve this, we will determine numerically and experimentally the peak-to-peak reflection coefficient on different interfaces and thin layers. We will then compare the results to the reflection coefficient predicted by the different analytical expressions developed in § 4.1.

5.1.1 Estimation of the peak-to-peak reflection coefficient through 2D simulations

Two different sets of simulations were run in GprMax 2D. In the first set, the incident wave was a continuous sine, in order to match the analytical results and estimate the influence of the geometric attenuation into the layer, which is not taken into account by the geometric series equations (102). Then, in the second set, we introduced a realistic pulse (Figure 53) to predict experimental results. Those results were published in [116, 117].

5.1.1.1 Numerical evaluation of the thin layers reflection coefficient for a sine wave

The first simulations, performed with a continuous sinusoidal incident wave (2.3 GHz), were carried out for a layer placed at a depth of 10 cm into concrete and for a quasi-vertical incidence (antenna separation of 0.5 cm), both for an air layer ($\varepsilon'_{r1}/\varepsilon'_{r2} = 10$) and a saturated layer ($\varepsilon'_{r1}/\varepsilon'_{r2} = 0.25$). The reflection coefficient was obtained from numerical simulations by comparing the maximum peak-to-peak amplitude (after suppression of the direct wave) to the amplitude of a wave reflected on a perfect reflector at the same depth (§ 3.1.2.1).

Figure 130 enables us to compare the numerical results obtained for the layers of both materials to analytical equations for the static detection of thin layers: the plane wave approximation (102) and the first terms estimation (112). The two methods are expected to give the same results for a vertical incidence, except that the plane wave approximation does not take into account the geometric attenuation into the thin layer (which is different for each ray, depending on the number of reflections).

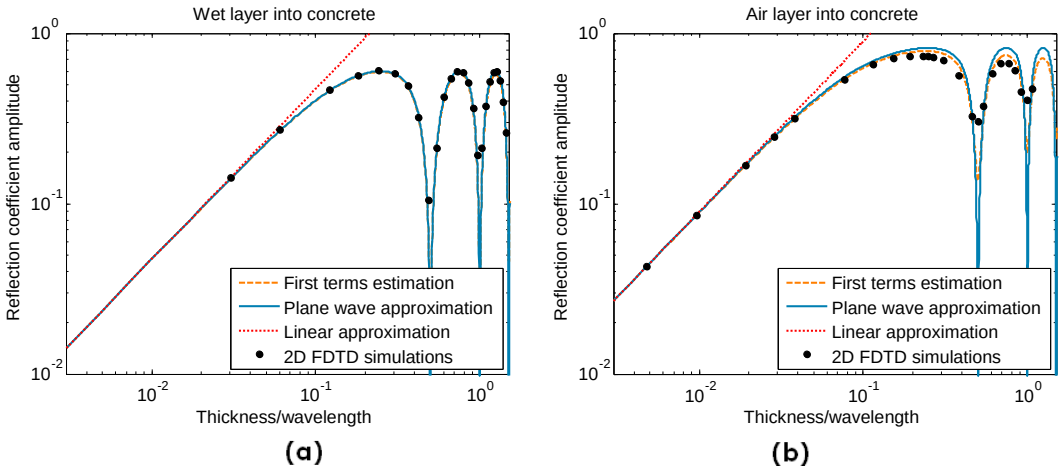

Figure 130 : Reflection coefficient amplitude of a thin (a) air and (b) saturated layer (ε'_{r2}=40) into concrete as a function of the thickness-to-wavelength ratio, and comparison with the theoretical estimations.

In Figure 130 (a), we observe that the concordance between numerical results and analytical predictions is excellent for the saturated layer ($\varepsilon'_{r2} = 40$). The large

permittivity of the thin layer induces a very small wavelength so that, for a given thickness-to-wavelength ratio, the layer thickness is small, which limits the geometric attenuation.

When the layer material is air (Figure 130 (b)), the layers are thicker and the oscillations of the amplitude are decreased by the geometric attenuation into the layer. This attenuation is different for each reflection multiple; the complete destructive interferences, producing a reflection coefficient equal to zero, is not observable. The geometric attenuation is supposed to be predicted by the first terms estimation method, but the attenuation observed in the numerical results is even stronger.

Nevertheless, in both cases, the amplitude of the reflection coefficient generated by very thin layers ($t < \lambda/20$) can be approximated by the linear approximation (86) that was proposed in § 2.2.1.

Those results were obtained for a vertical incidence but, when static tests are performed experimentally, the antennas offset of 4 cm is not always negligible regarding the depth of the thin layer. For example, when the layer is situated 10 cm below the surface, the incidence angle is equal to 11.3°. The difference between the different analytical methods can then become more visible.

To observe the influence of a small but non negligible incident angle (11.3°), we performed the same simulations as in Figure 130, changing only this parameter. The results are compared to the analytical results obtained with the methods of plane wave approximation, first terms estimation, and also the first terms estimation with spherical wave reflection. This last method was added, because it was shown in section 4.1.2 that it generates the best results for thick layers (the different methods accuracy can be estimated from Figure 90, considering only the incident angle of 11,3°). The results are displayed in Figure 131.

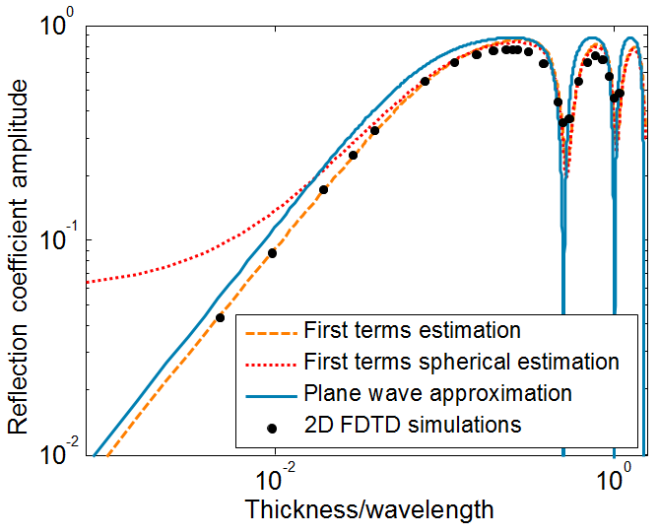

Figure 131 : Reflection coefficient amplitude of a thin air layer into concrete (ε'_{r1}=10) as a function of the thickness-to-wavelength ratio, and comparison with the theoretical estimations, for an incident angle of 11.3°.

In Figure 131, we observe that the plane wave approximation overestimates the reflection coefficients for all the thicknesses, while the firsts terms estimation predicts very well the reflection coefficient for the thinner layer and gives a good estimation for thicker layers. The linear approximation presented in Figure 130 is not represented on this graph. Nevertheless, it is based on the plane wave approximation, so it introduces a similar significant error when the angle is not negligible.

The introduction of the spherical equation into the first terms estimations does not improve the results: the prediction is only slightly better for the thicker layers, but it is totally incoherent for the very thin layers. It is due to the fact that the spherical equation is introduced quite abruptly as a replacement of the first reflection of the series. This approximation is valid for thick layers but leads to significant errors for very thin layers.

5.1.1.2 Numerical evaluation of the peak-to-peak reflection coefficient for realistic conditions

In the previous section, it was shown that the reflection amplitude of radar waves into a thin layer can be predicted by analytical expressions, and that the first terms estimation method was preferable when the incident angle could not be neglected. But this analysis differs from real GPR measurements in two points. First, the most frequent incident signal for GPR is a short electromagnetic pulse and not a continuous sine. Then, the antennas are placed on the surface and not into the concrete: this will induce surface-related effects (see § 4.2). In this section, we will test the influence of those parameters on the measured peak-to-peak reflection coefficient.

First, we introduced into our simulation the realistic incident pulse described in § 3.1.4.1. The results are displayed in Figure 132 for the case of the air layer. On the same diagram, we have redrawn as well the analytical prediction obtained with the first terms method and the numerical results that were obtained for a sine wave (Figure 131).

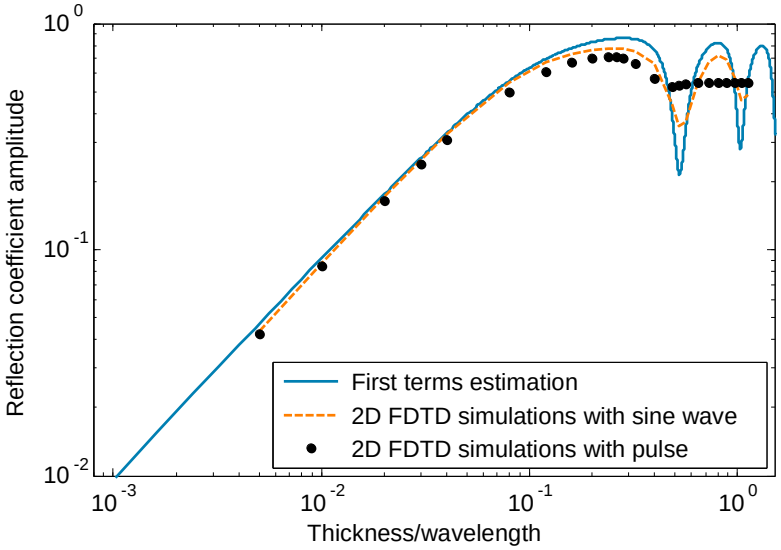

Figure 132 : Reflection coefficient for an air thin layer embedded at a depth of 10 cm into concrete (ε'_{r1}=10), depending on the thickness-to-wavelength ratio. The theoretical estimation for a sine wave is compared to the modelled results obtained with a continuous sine wave and with a realistic short pulse.

The reflection coefficient of the realistic pulse stabilizes for the large thickness-to wavelength ratios, because the two wavelets get separated from each other (see Figure 38). Nevertheless, for the very thin layers, the reflection coefficients measured with a pulse are almost identical to the reflection coefficients measured with a sine wave. For those very thin layers, the first terms estimation method can predict very well the reflection coefficient. We estimate the limit to λ/11, which corresponds to an air thickness of a bit more than 1 cm into a wet concrete ($\varepsilon'_{r1} = 10$).

For layers with a larger thickness, the thickness cannot be estimated by this analytical method. The FDTD simulations with realistic wavelet are then of a particular interest, because they allow a direct comparison to the experimental measurements.

After introducing a realistic wavelet, we introduced another important factor: the surface effects. As explained in § 3.1.2.1, the surface effects are supposed to be suppressed when dividing the amplitude measured on the thin layer by the amplitude measured on a perfect reflector, because they are identical in both cases. Before comparing the analytical expressions to the experimental data, we have to prove, at least for numerical simulations, that this assessment was correct. To achieve this goal, we performed the same simulations as in Figure 132, but with the radar placed on the concrete surface (ε'_{r1} = 7.7) instead of being embedded into concrete. The results are visible in Figure 133.

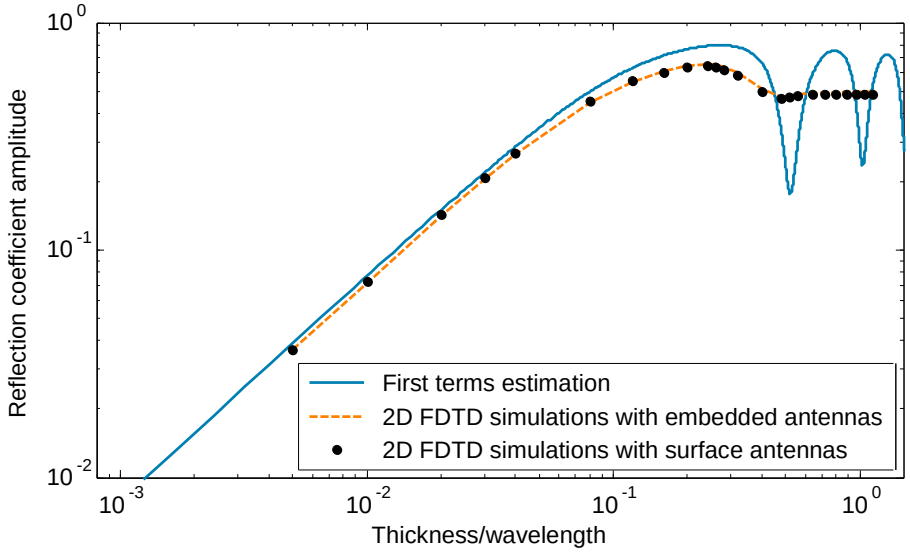

Figure 133 : Reflection coefficient for an air thin layer embedded at a depth of 10 cm into concrete (ε'_{r1}=7.7), as a function of the thickness-to-wavelength ratio. The theoretical estimation (with first terms estimation) for a sine wave is compared to the modelled results obtained with a realistic short pulse, for an embedded and surface testing.

The presence of the surface does not influence the measure of the reflection coefficient. This validates our experimental procedure (§ 3.1.2) for the determination of the reflection coefficient in static tests.

5.1.2 Comparison of the numerical and experimental peak-to-peak reflection coefficients

The experimental study was performed with the procedure described in § 3.1.2.2, on two 10 cm thick concrete slabs enclosing an air layer. The concrete dielectric permittivity was deduced from measurements on the slab: with a surface reflection test (Figure 51 (b)), we measured an air-concrete reflection coefficient R_{12} of 0.47, corresponding to a permittivity $\varepsilon'_{r1} = 7.7$. (134). This permittivity was confirmed by the analysis of the reflection time (§ 113).

This permittivity was introduced into the FDTD model. The simulation was realised in realistic conditions (with surface testing and a realistic pulse) (§ 5.1.1.2) in order to obtain the best concordance between the experimental and numerical results. The reflection coefficients obtained by these methods are traced in Figure 134, in which they are compared to the curve obtained by the analytical method of the first terms estimations (§ 2.2.2.2).

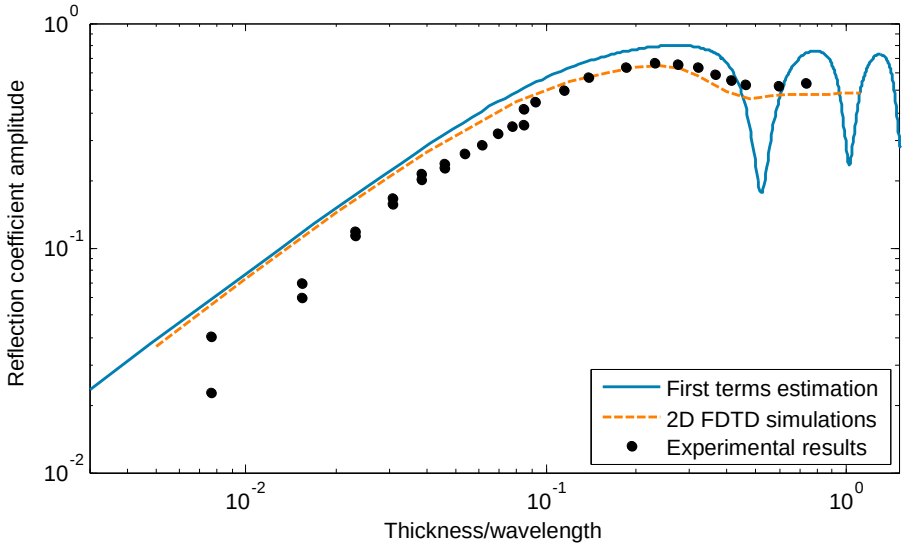

Figure 134 : Comparison between the peak-to-peak amplitudes measured by experimental measurements, estimated by 2D FDTD numerical simulations and calculated through analytical expressions.

With these tests, we show that layers with a thickness as thin as 1 mm, which corresponds to a thickness inferior to λ/100, can be visible with GPR. The concordance between experimental and numerical results is relatively good, and proves the efficiency of numerical modelling to predict the global results.

Nevertheless, discrepancies are observed, especially for the very thin layers. This difference is probably due to the lower signal-to-noise ratio, and maybe to the fact that the slabs were smooth but not polished, limiting the precision of the determination of the direct wave. As an illustration of the noise that can affect the measurements, it is visible on the graph that the measurements were performed in two different sets (with $t/\lambda \leq 0.085$ and $t/\lambda \geq 0.085$), resulting on an amplitude gap on the graph. Realised at an interval of only a few days, the measured amplitudes are visibly higher for the second set.

Because of this relatively important noise affecting the results, it will be very difficult to directly use the linear dependence of the reflection coefficient on the thickness-to-wavelength ratio to estimate the thickness of the layer. This difficulty adds up to the other drawbacks inherent to the method. First, the amplitude has to be compared to the amplitude on a perfect reflector, which is not always possible in reality. Second, the layer thickness and its permittivity cannot be determined simultaneously, as they both influence the thickness-to-wavelength ratio. This last limitation will be overpassed in the next section, through the spectral analysis of the reflected wavelet.

5.2 Static measurements with frequency analysis

In the previous chapter, it was shown that the peak-to-peak reflection coefficient obtained on thin layers was dependant on the thickness-to-wavelength ratio and could be evaluated by analytical estimations or numerical simulations. In addition to the relatively low precision of the predictions and to the important noise that was observed, the main problem of that method is that, for each measurement, only one point is determined: this means that it will be impossible to estimate the layer thickness if the dielectric permittivity is unknown and vice-versa.

A solution to this problem is to use all the frequency components present into the incident wavelet. Indeed, the pulse created by the GPR covers a range of different frequencies, approximately up to twice the nominal frequency of the antenna (see § 3.2.1.2). With this method, different points of the reflection coefficient amplitude and phase versus thickness-to-wavelength ratio can be obtained from a single static measurement. A similar approach was considered by Gregoire [56] and Jeannin [57]. They showed that it was possible to determine the layer parameters using the reflection spectral content, and that the simultaneous analysis of the amplitude and the phase increased the thickness range that could be characterized.

As an example, we can model the presence of a 1 cm saturated layer ($\varepsilon_r' = 40$) embedded into concrete ($\varepsilon_r' = 7.7$) at a depth of 10 cm (Figure 135 (a)). After direct wave removal (Figure 135 (b)) and application of a fast Fourier transform (FFT), we can compare the frequency spectrum of the reflection on the thin layer to the spectrum of the reflection obtained on a perfect reflector (Figure 136).

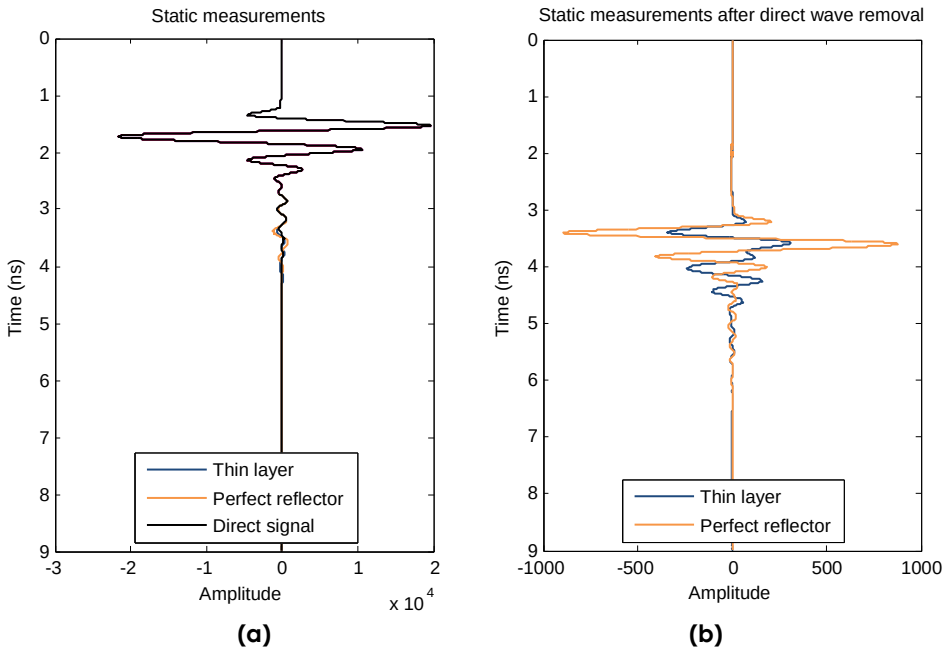

Figure 135 : FDTD simulations of static measurements over a 1 cm wet layer embedded at a depth of 10 cm into concrete: (a) initial data; (b) after direct wave subtraction.

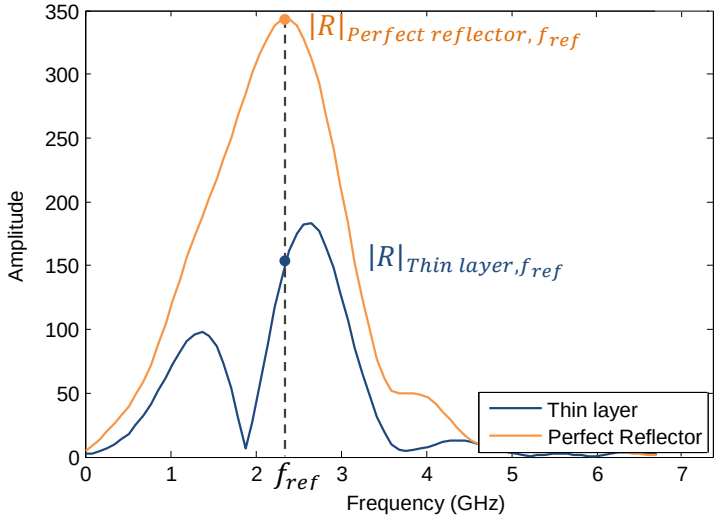

Figure 136 : Frequency spectra of the signals shown in Figure 135 (b) for a thin layer and a perfect reflector.

Those spectra, that can be obtained from numerical simulations or from actual measurements, can be compared to analytical curves generated for different parameters sets with the methods described in § 4.1.2. Minimizing the difference between the curves can lead to an estimation of the actual layer parameters.

In this chapter, the method is first validated by comparing the measurements obtained with only one frequency for various thicknesses to the analytical curves (§ 5.2.1). It is then applied to numerical measurements performed on thin layers (§ 5.2.2) in order to evaluate the precision of the parameters estimation. The same methodology is finally used for the analysis of experimental measurements (§ 5.2.3).

5.2.1 Comparison of numerical and experimental data to the analytical predictions

In this section, we performed numerical simulations and experimental measurements on thin layers of various thicknesses embedded into concrete. In the amplitude and phase spectra of these measurements, we will only consider a single reference frequency: the frequency f_{ref} of the maximum amplitude for the metallic reflection. The amplitude and phase at this frequency are extracted from each measurement, for the perfect reflector and the thin layers (Figure 136).

The same frequency is also used for the determination of the theoretical curves, to which the results will be compared. Those curves are calculated with the analytical methods which revealed to be the most promising in § 4.1.2:

- the plane waves approximation (§ 2.2.2.1);
- the first terms estimation, which uses only the 30 first terms of the sum, but takes into account the geometric attenuation (§ 2.2.2.2);

- the hybrid model, developped in § 4.1.3.2, which uses the plane wave approximation for the thinnest layers and a model derived from the first terms estimation for the thicker layers.

This last analytical method will only be used when the layer permittivity is lower than the matrix permittivity (it was shown in Figure 60 that it did not bring any improvement otherwise). The goal is to determine which method could be the most adapted for the analysis of real datasets.

5.2.1.1 Modelling of a saturated thin layer into concrete

The first analysis is performed on a saturated layer ($\varepsilon'_r = 40$) of variable thickness embedded into concrete ($\varepsilon'_r = 7.7$). The layer is located at a depth of 10 cm and the antennas are separated by 4 cm in order to correspond to the experimental setup of monostatic tests. They are also compared to the raw peak-to-peak measurements.

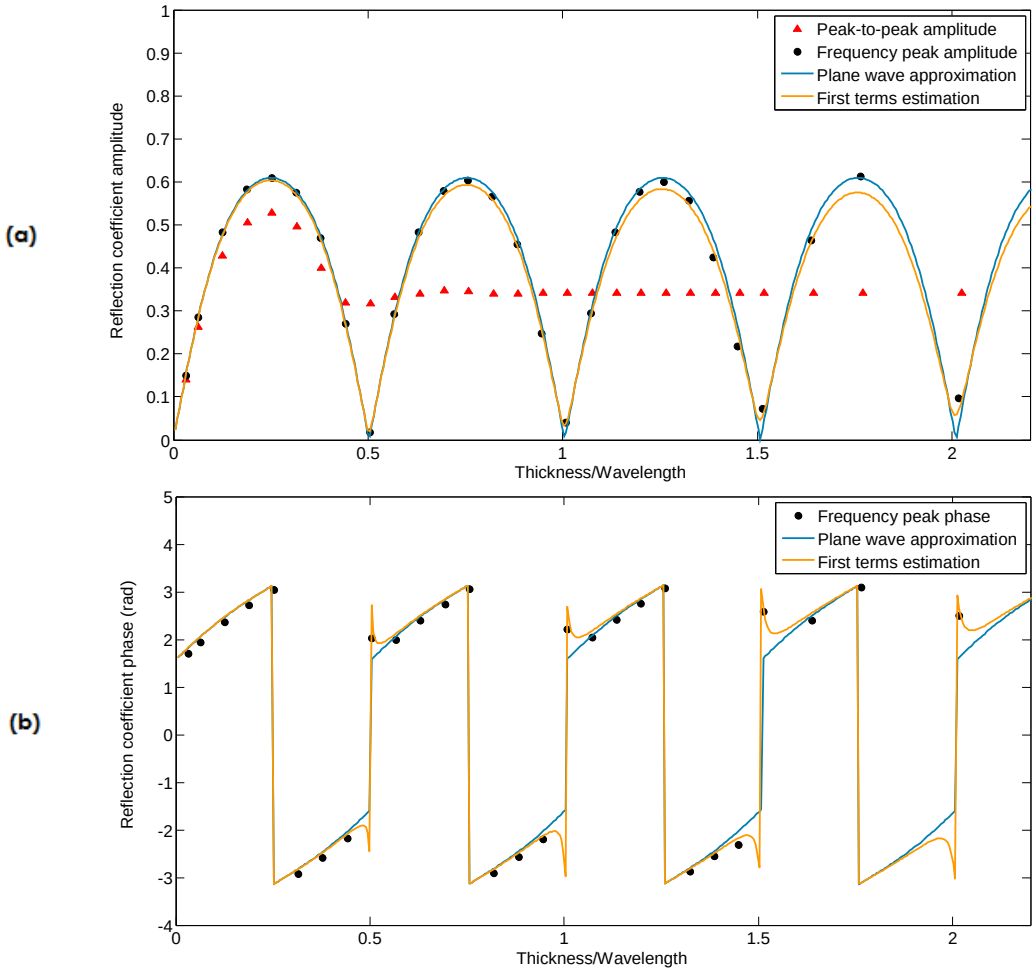

Figure 137 : (a) Amplitude and (b) phase of wet thin layers reflection coefficients, depending on the thickness-to-wavelength ratio. Comparison of numerical test results with peak-to-peak and frequency spectrum analyses and analytical curves.

Firstly, we observe that the frequency analysis of the reflected pulse allows obtaining amplitude and phase curves following very well the theoretical predictions. Indeed, the separation of the wavelets does not limit anymore the maximum thickness-to-wavelength ratio that can be studied. Those results are very similar to the data obtained with a continuous sine wave (Figure 130 (a)).

The FDTD amplitudes are better predicted by the plane wave approximation than by the first terms estimation. This is surprising, as the first terms estimation is supposed to take into account the geometric attenuation into the layer. Nevertheless, the first terms estimation method gives a better prediction of the phase changes, especially for discontinuities observable when t/λ is a multiple of 0.5.

5.2.1.2 Modelling of a thin air layer embedded into concrete

A similar analysis was then performed with an air layer of variable thickness into concrete ($\varepsilon'_r = 7.7$). Because the layer permittivity is lower than the matrix permittivity, the hybrid model will be compared to the results as well. To simplify the graph, the peak-to-peak amplitude will not be represented anymore. The results are presented in Figure 138.

(a)

(b)

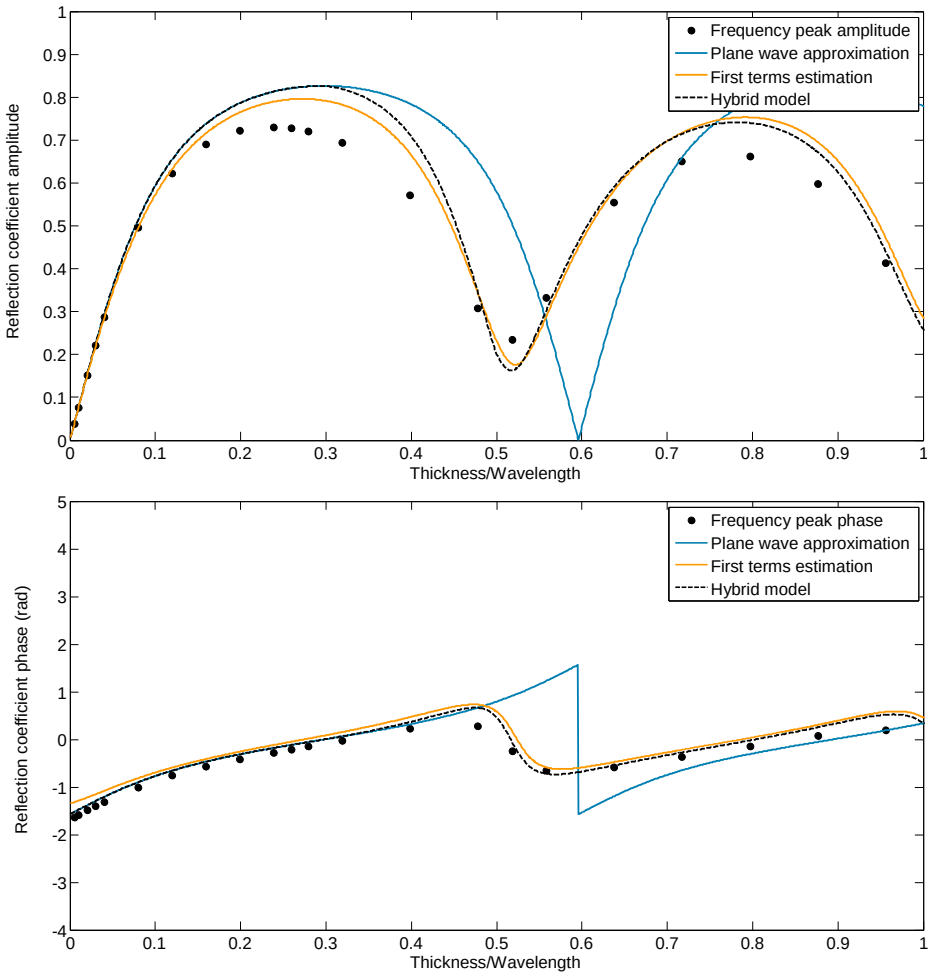

Figure 138 : (a) Amplitude and (b) phase of air thin layers reflection coefficients, depending on the thickness-to-wavelength ratio. Comparison of numerical test results and analytical curves.

If we compare the analytical predictions to the numerical results, we observe that the hybrid method gives the best prediction of the curves amplitude. Indeed, it uses the plane wave approximation for the very thin layers, and then a variation of the first terms methods which is far more accurate for large t/λ. The modifications applied to the first terms methods in the hybrid model (see § 4.1.3) seem to improve slightly the amplitude and phase prediction, especially for the thicker layers.

On the contrary to the observations made for an embedded wet layer in § 5.2.1.1, the geometric attenuation (visible in the graph as a decrease of the peaks amplitude) is very strong. This is due to the fact that the wavelength in air is relatively large (~13 cm), which means that the geometric attenuation into the layer plays a real role in the amplitude attenuation. Even for the first terms estimation and the hybrid methods, taking into account the geometric attenuation, the peaks amplitudes are always 10% overestimated by the analytical formulas.

5.2.1.3 Validity of the method for larger offsets and surface measurements

Before applying this method to the determination of the parameters of embedded layers, for numerical or experimental datasets, we want to estimate the influence of two additional factors: the surface testing and the post-critical incidence. Those parameters, especially when they are combined, are susceptible to decrease the precision of the method (§ 4.2).

In a first step, we modelled the same air thin layers into concrete as in the previous paragraph, but with an initial offset of 13 cm instead of 4 cm. This offset corresponds to the initial offset of CMP tests and the incident angle is equal to 33°, which is superior to the critical angle (21°). The results are visible in Figure 139.

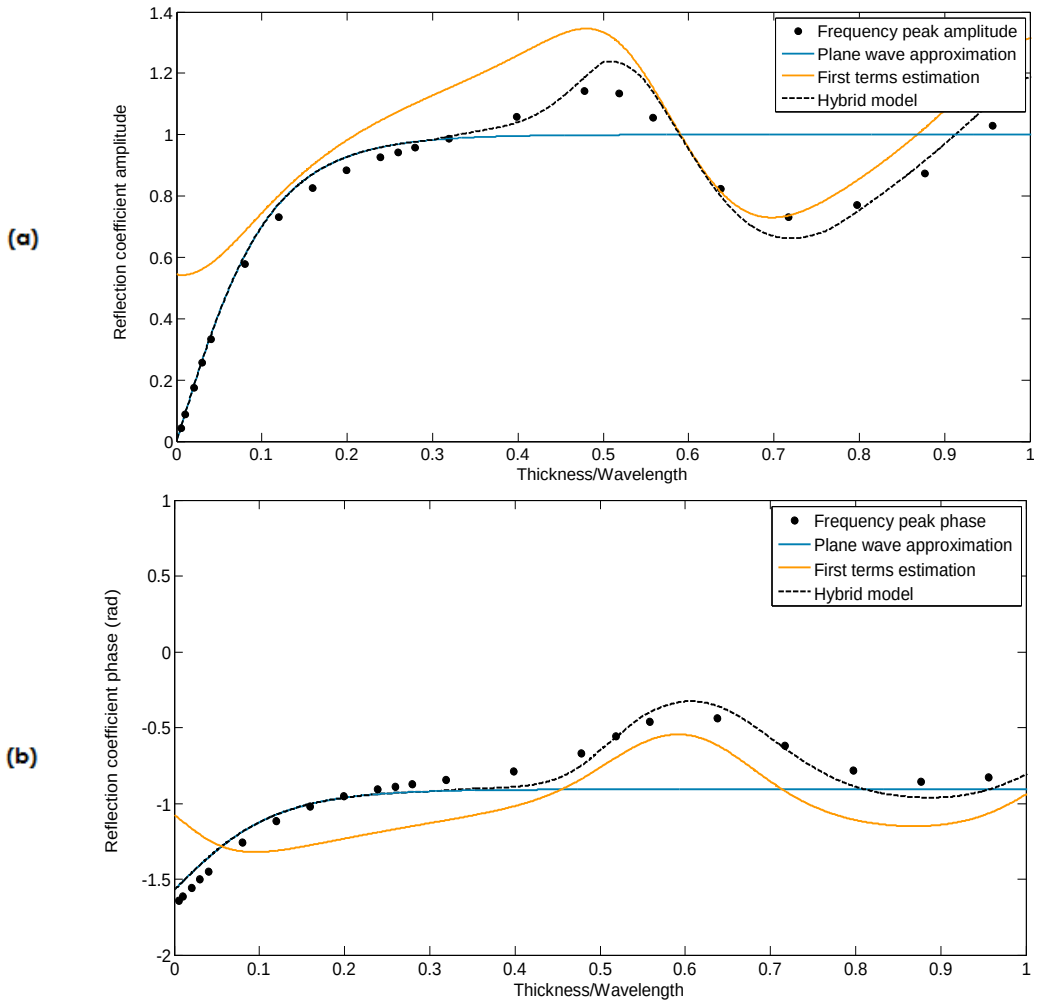

Figure 139 : (a) Amplitude and (b) phase of air thin layers reflection coefficients, depending on the thickness-to-wavelength ratio, for a post-critical incidence. Comparison of numerical test results and analytical curves.

The evolution of the amplitude with a post-critical incidence is very different from for a small incidence (Figure 138). In this case, the hybrid model reveals to be far more accurate than the two other approximations.

The issue of the surface testing has been studied on CMP radargrams in § 4.2.1, in which it was concluded that the part of the radargram after the first reflection had to be removed. Under this condition, the presence of the surface should not have an important influence on the APVO curves for the small offsets. For static measurements, we chose to set the limit to 5 lobes after the midpoint between the main maximum and the main minimum of the reflection on the metallic plate. The time truncation and its influence on the frequency spectrum are represented in Figure 140.

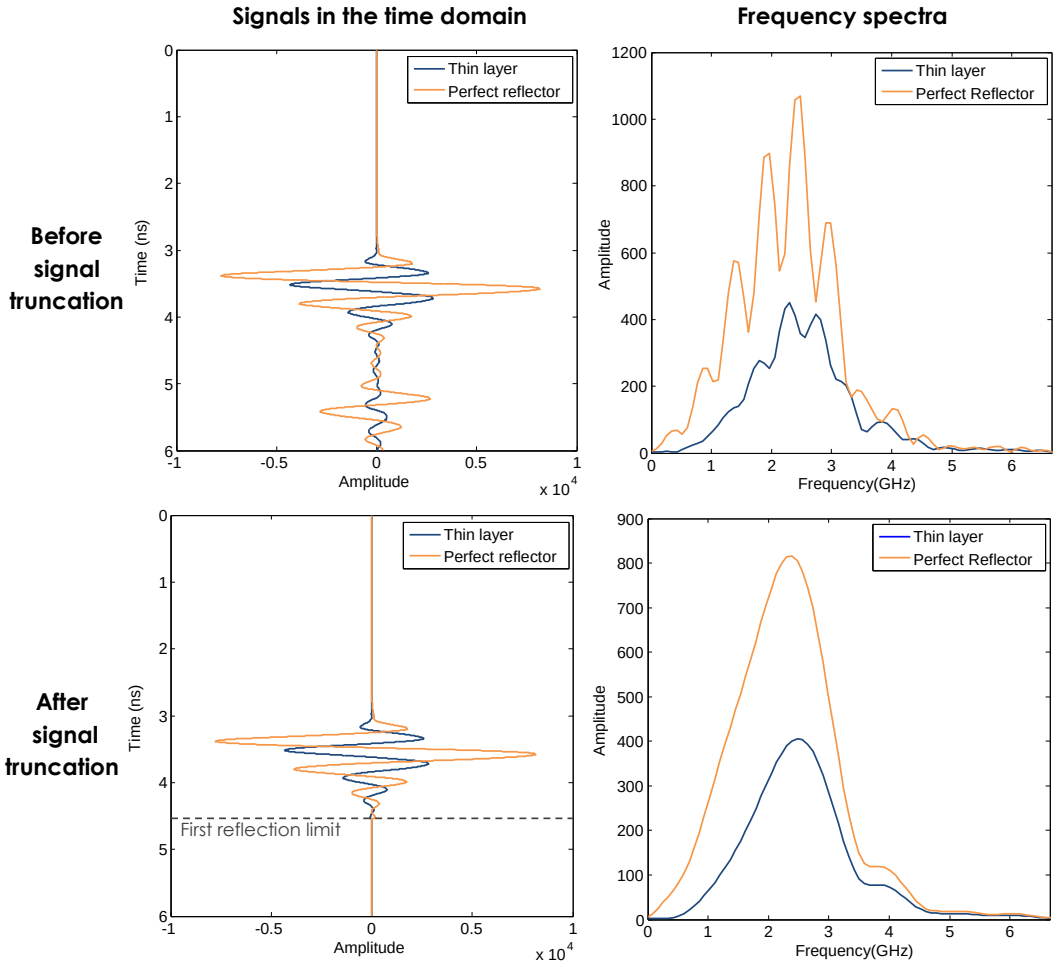

Figure 140 : Influence of the signal time truncation on the frequency spectrum for signals measured from the surface. The radargram has been obtained from FDTD simulations over a 1 cm air layer embedded into concrete.

In Figure 140, the benefit of the time signal truncation on the frequency spectrum is evident. Without this filtering, the spectra present interference lobes from the different reflections that will influence the apparent reflection coefficient. After this signal truncation, the results obtained for a low incident angle do not change if the results are obtained with surface measurements (Figure 141) instead of embedded antennas (Figure 138).

(a)

(b)

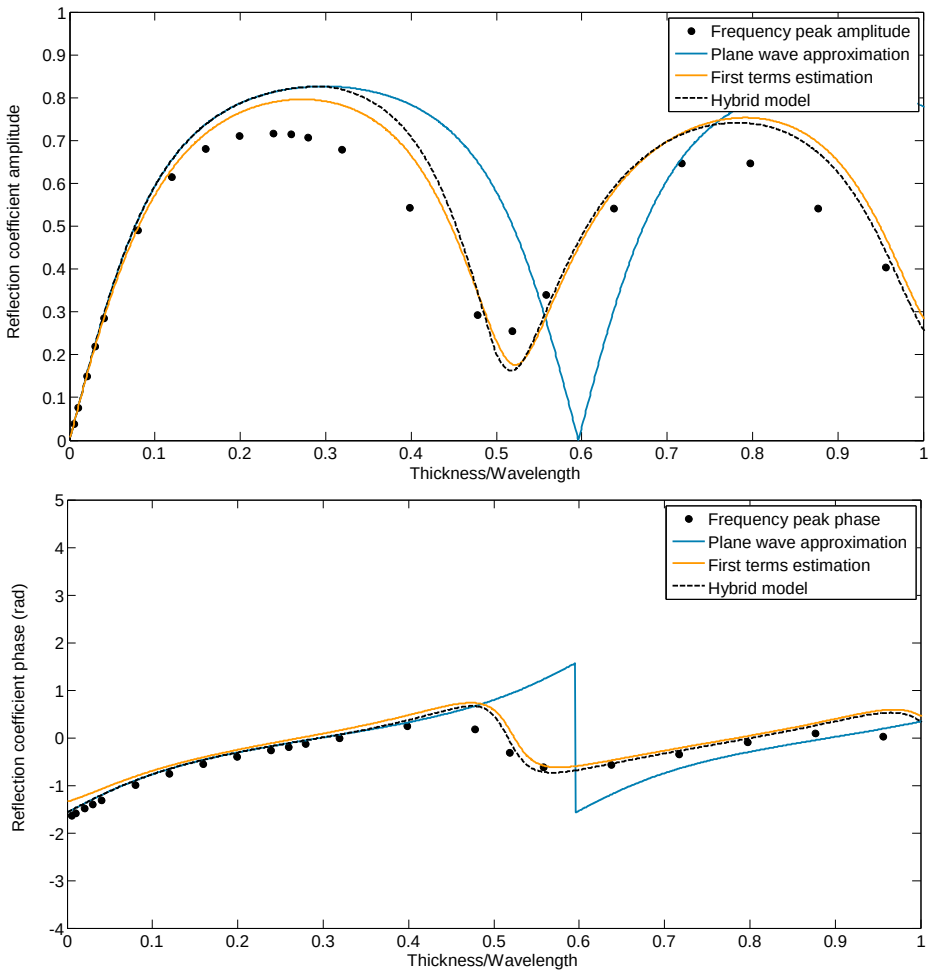

Figure 141 : (a) Amplitude and (b) phase of air thin layers reflection coefficients, depending on the thickness-to-wavelength ratio, for a surface measurement and truncated signal. Comparison of numerical test results and analytical curves.

When the measurement is performed from the surface with a post-critical angle, the signal has to be truncated as well to remove the second reflections. But the surface-lateral wave (§ 4.2.2) will also influence the results and will not be removable from the radargram. They appear both for thin layers and for the perfect reflector.

The results obtained in this situation for an offset of 13 cm are compared to the analytical curves obtained for the embedded layers in Figure 142.

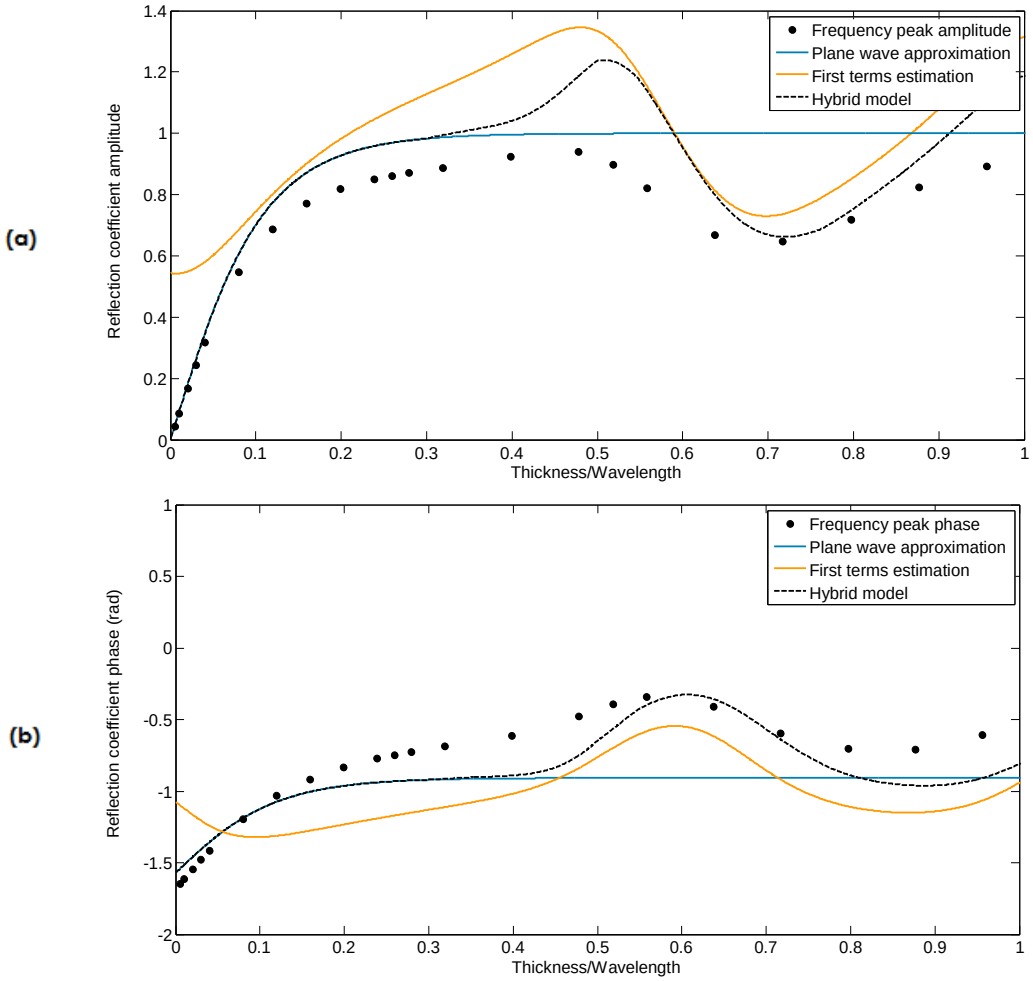

Figure 142 : (a) Amplitude and (b) phase of air thin layers reflection coefficients, depending on the thickness-to-wavelength ratio, for a post-critical incidence: comparison of numerical test results and analytical curves.

As expected, the results are affected by the presence of the surface. Only the very thin layers (t/λ<0.1) are still well predicted by the analytical curves. As a consequence, for large incident angles and layers with a thickness superior to $\lambda/10$, the estimation of the parameters using the analytical expressions is not expected to give reliable results. This will be tested on numerical results in § 5.2.2.3 and on experimental results in § 5.2.3.2.

5.2.1.4 Comparison of the analytical curves to experimental results

The previous section proved with numerical results that the analytical expressions could be used to predict the evolution of the amplitude and phase of the reflection coefficient as a function of the thickness-to-wavelength ratio. In particular, the hybrid model developed in § 4.1.3 revealed to give the most accurate prediction in almost all the configurations.

In this section, the objective is to extend those conclusions to experimental measurements. Instead of numerical simulations, we will use the experimental dataset already studied in § 5.1.2 (in which only the peak-to-peak amplitude was

extracted). Those experimental tests were performed statically over air layers of various thicknesses, ranging from 1 mm to 9.6 cm. The 3D hybrid equations, developed in § 4.1.3.3, will be used instead of the 2D model.

A difference between numerical and experimental results is the presence of noise. An important source of noise is the insufficient stabilization of the signal (see § 3.2.2) between the measurements of direct wave, wave on metal and wave on thin layer. The noise is generally described by the signal-to-noise ratio (see § 3.2.3). It will be stronger in the parts of the signal presenting the largest amplitude: the strong reflections and the direct wave. The amplitude of the noise remaining after suppression of the direct wave is thus important.

An easy solution to reduce the noise related to the direct wave is to filter this part of the radargram in the time domain, just as the radargram was filtered after the first reflection in Figure 140. In Figure 143, the frequency amplitudes of the wavelet are represented, before (a) and after (b) suppression of the amplitudes before the first reflection.

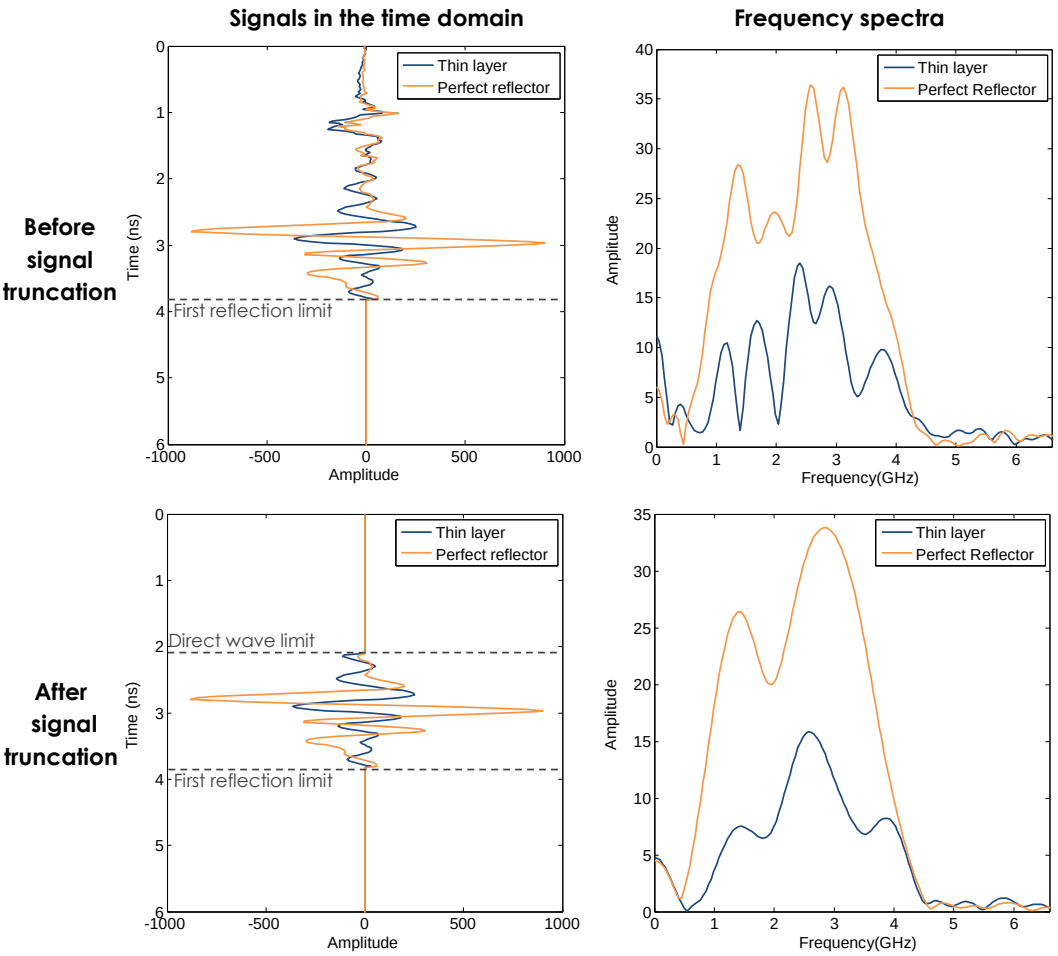

Figure 143 : Influence of the signal time truncation on the frequency spectrum for signals measured from the surface. The radargram has been obtained from experimental tests over a 1 cm air layer embedded into concrete.

Figure 143 confirms that the removal of the second reflection is not sufficient to obtain a smooth frequency spectrum. Even after the direct wave removal, the signal noise in this part of the radargram considerably influences the frequency spectrum. When this part of the signal is set equal to zero, the spectrum is much smoother, even if two peaks are visible for the perfect reflector. We also remark that the frequency of the transmitted peak can be very different from the nominal frequency of 2.3 GHz, which had been confirmed by direct air signals (§ 3.2.1.2). After propagation into concrete, the frequeny peak of the measured reflection can rise up to 3 GHz. In our developements, it is this real, measured, peak frequency that has been used, instead of the nominal frequency.

In Figure 144, the amplitude (a) and phase (b) of the experimental measurements are compared to the values obtained with the different analytical formulations

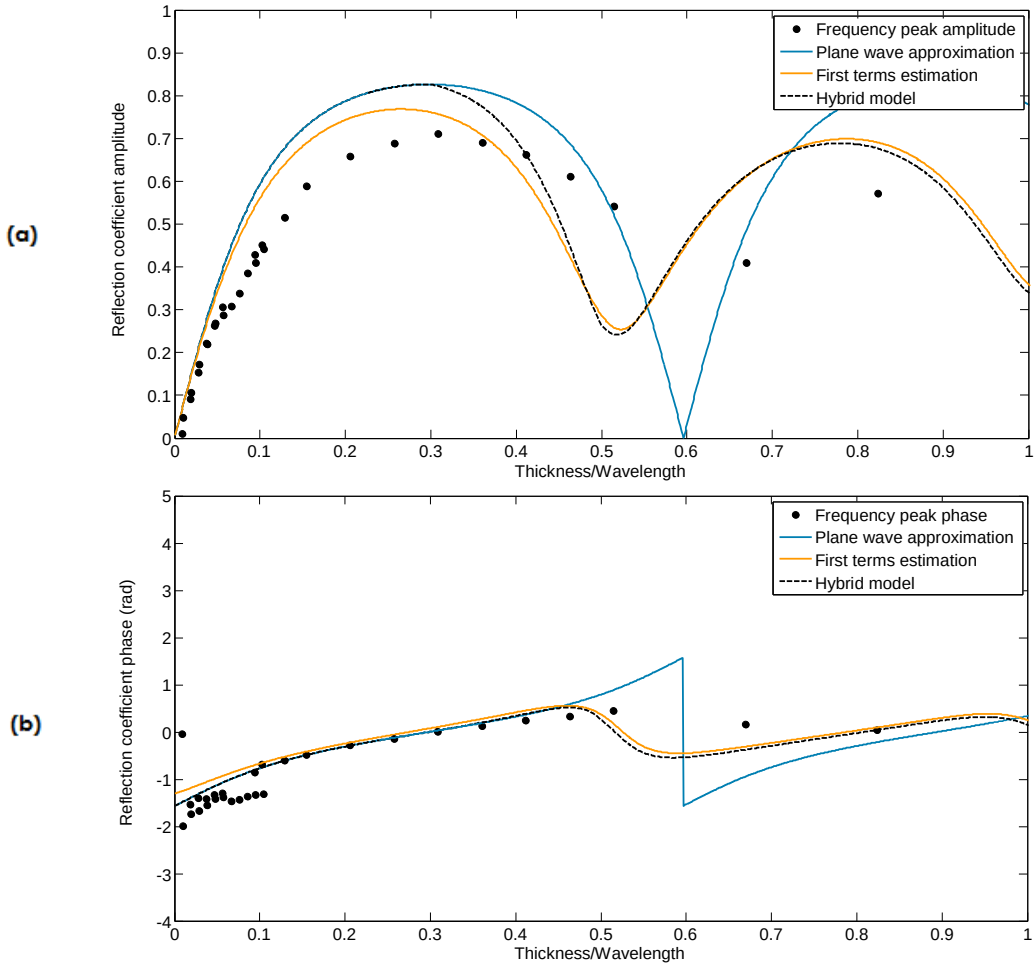

Figure 144 : (a) Amplitude and (b) phase of air thin layers reflection coefficients, depending on the thickness-to-wavelength ratio: comparison of experimental measurements and analytical curves.

The experimental results are in an acceptable concordance with the numerical predictions. The amplitude seems better predicted for the very thin layers, while the phase prediction for these layers is poorer. The amplitude peaks are overestimated by the analytical curves, but correspond relatively well to the

amplitudes of the numerical curves that were presented in Figure 141 for the same configuration. The main difference is that the curves seem to be submitted to an expansion to the right direction, which would correspond to an overestimation of the t/λ ratio.

5.2.2 Application to the determination of thin layers properties from numerical static measurements

In the previous chapter, we have compared the analytical curves to the reflection coefficient amplitude and phase at a reference frequency estimated for different layer thicknesses. In this chapter, we will try to use the concordance with the analytical curves to determine the layers properties from numerical radargrams. Instead of extracting the amplitude and phase for a reference frequency (Figure 136), we will extract a set of points, obtained with a set of frequencies well represented into the spectrum. The range of thickness-to-wavelength ratios that will be usable for this analysis will depend on the frequency content of the wavelet and on the wavelength into the layer.

We want to use the analytical curves to determine the layer properties. In this section, we will first describe this method using the simple case of a thin saturated layer embedded into concrete. We will then test the method on different numerical models of increasing complexity: air layers with embedded antennas, but also air layers with surface antennas and post-critical incidence.

5.2.2.1 Determination of wet layers into concrete

The layer determination method will be detailed on the example illustrated in Figure 135: a 1 cm wet layer ($\varepsilon_r' = 40$) embedded into concrete ($\varepsilon_r' = 7.7$) at a depth of 10 cm (Figure 135 (a)). After suppression of the direct wave (Figure 135 (b)), the frequency spectrum of the reflection is calculated (Figure 136) for the thin layer and the direct wave. The amplitudes ratio gives the reflection coefficient of the thin layer and the phase shift can be evaluated as well. The results are displayed in Figure 145.

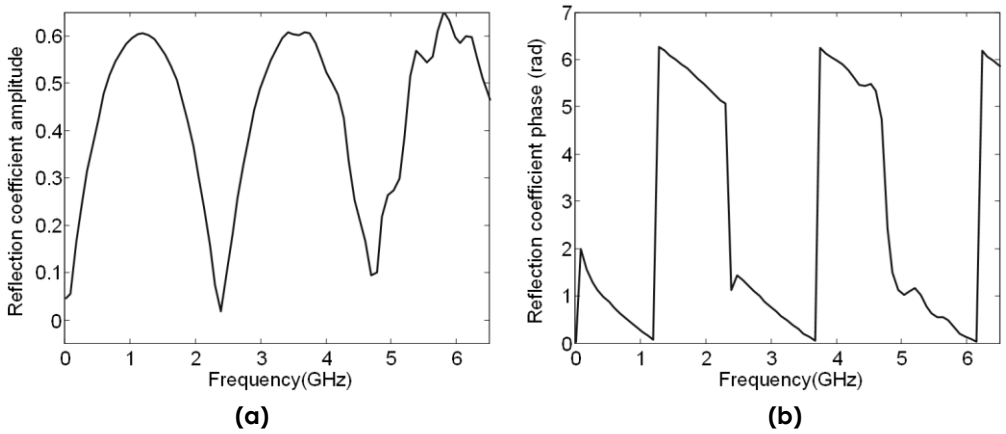

Figure 145 : (a) Frequency dependant amplitude obtained through the FDTD simulation of a 1 cm wet layer into concrete; (b) Phase difference obtained on the thin layer compared to the perfect reflector.

Those curves look similar to the theoretical curves that have been drawn in the previous chapter. Given the large number of frequencies resulting from the FFT analysis and the limited frequency content of the wavelet, the whole curves will not be considered to determine the layers properties, but only the values for a set of representative frequencies. This will reduce the computation time for the parameters determination and limit the noise due to insufficient amplitude.

In the example of Figure 146, we select the frequencies ranging from 0.5 to 3.5, which do not seem to be affected by any noise. If we set the frequency interval to 0.25 GHz, 13 different frequencies will be considered. In Figure 146, the values of the amplitude and phase of the reflection coefficient for those frequencies are compared to the analytical curve for the real parameters. This curve is obtained by the plane wave method, as we consider a high permittivity layer (see § 4.1.3.2).

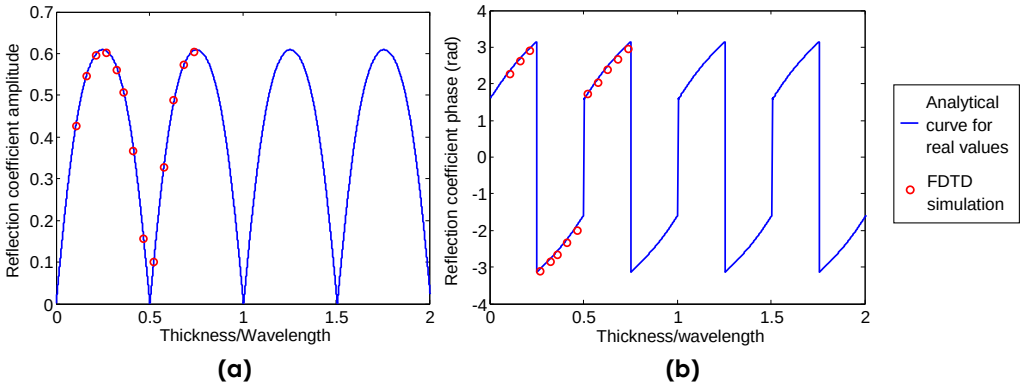

Figure 146 : Comparison between the reflection coefficient amplitude (a) and phase (b) curves obtained from a static measurement and values obtained from analytical curve (plane wave approximation), for a 1 cm wet thin layer.

The correspondence is very good and only limited by the frequency content of the wavelet. The next step of the analysis consists in comparing the experimental or numerical curves (whose initial parameters are supposed to be unknown) to

analytical curves determined for different sets of parameters. The estimated layer parameters are the parameters giving the minimum difference between theoretical curve and the experimental or numerical data. In this process, different steps have to be selected:

- the determination of the parameters sets (range and interval);
- the forward model, used to determine the theoretical curves;
- the method to estimate the error of each theoretical curve regarding the experimental results;
- the weighting associated to the different parameters.

In this work, the parameters to be determined are the layer thickness and its dielectric permittivity. We would like to determine the thickness with a precision of 1 mm and the relative permittivity with a unitary precision. The dielectric permittivity values range from 1 to 81 (see Table 1). If we assume that the layer thickness falls in the interval 1 mm to 10 cm, the number of possibilities to investigate is equal to 8100. Given the low number of parameters (2) to retrieve and the low CPU cost of a forward model (about 0.1 second on a 2.5 GHz 4-core processor), we will investigate the whole parameter space.

In situations where the number of parameters or the required precision on their values are higher, or where the forward model requires more CPU time, search algorithms should be used such as the neighbourhood algorithm [118, 119]. This approach would allow us to consider a limited number of parameter sets, iteratively selected to refine the zones of interest in the parameters space.

As a forward model, we will compare the results obtained with the plane wave approximation and the hybrid model (see § 4.1).

The error is calculated with a L2 norm (minimization of the sum of the squared errors). For each $d - \varepsilon'_{r2}$ combination, the squared errors are calculated for both the amplitude curve and the phase curve. Before being summed up to obtain a global optimum, the two errors have to be weighted, because the reflection coefficient amplitude is falls in the range 0 to 1, while the phase values range from $-\pi$ to π. For this reason, the phase error will be divided by 2π before to be summed up with the amplitude error to obtain the global error.

$$Global\ error = Amplitude\ error + \frac{Phase\ error}{2\pi} \tag{146}$$

Another method that could have been used for the inversion of the complex reflection coefficient is to invert the amplitude first, then fix it and invert for the phase (see [120]). In Figure 147, the amplitude (a), the phase (b) and their weighted sum (c) are represented, for the simulation performed on the 1 cm wet layer. The real parameters are marked by small white crosses.

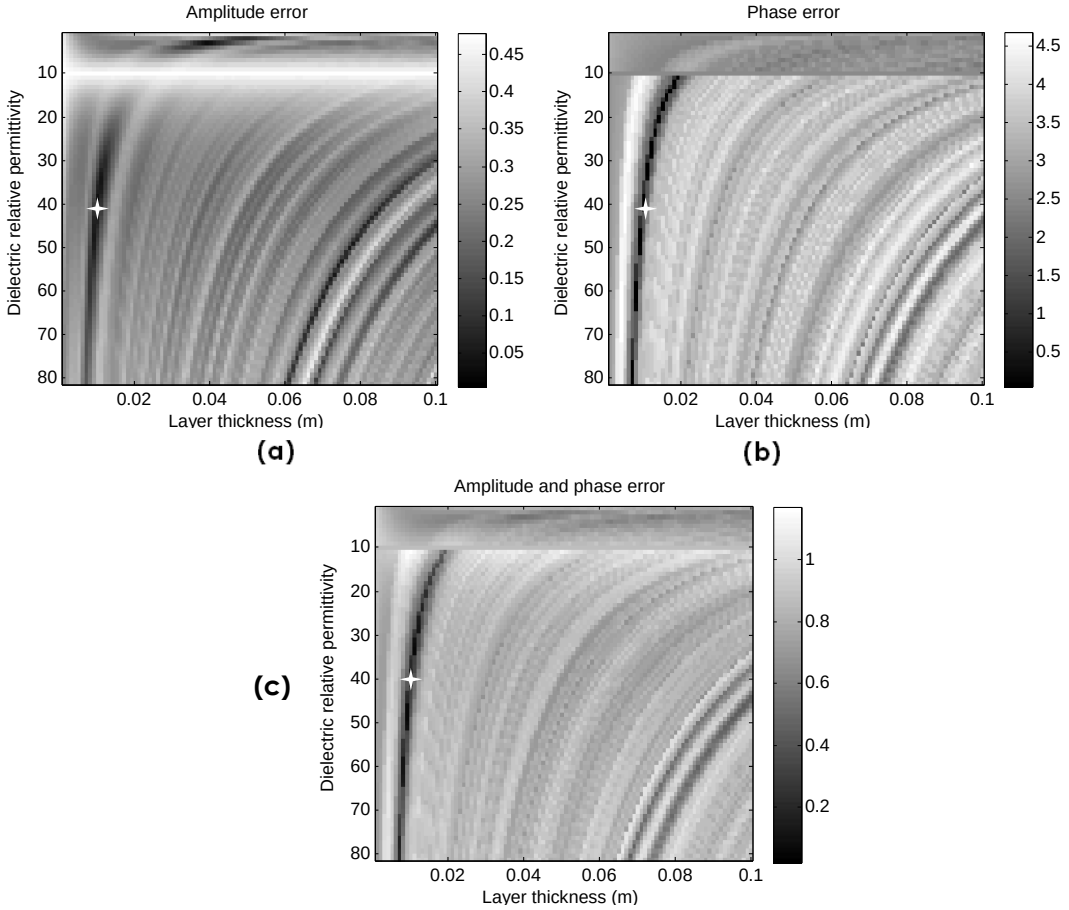

Figure 147 : Mean error between the reflection coefficient numerically estimated on a 1 cm saturated layer into concrete and forward calculations using plane wave: (a) amplitude, (b) phase and (c) weighted sum of the amplitude and phase.

The minimum of the weighted residuals designates, for dielectric permittivity and thickness, $\varepsilon'_{r2} = 40$ and $d = 1\,cm$, which are the real parameters of the layer. We observe a disruption of the error values when the permittivity is equal to 10, which corresponds to the value of the matrix permittivity. Both the amplitude and phase present characteristics that could have corrupted the results. The amplitude presents a local minimum for $\varepsilon'_{r2} = 3$, while the minimum appears as a line in the phase error function, which could easily lead to a strong error on the permittivity. Summing up the amplitude and phase creates a minimum in a reduced zone, without any significant other minimum. The comparison between the numerical values and the curves obtained from real and from estimated parameters are presented in Figure 148.

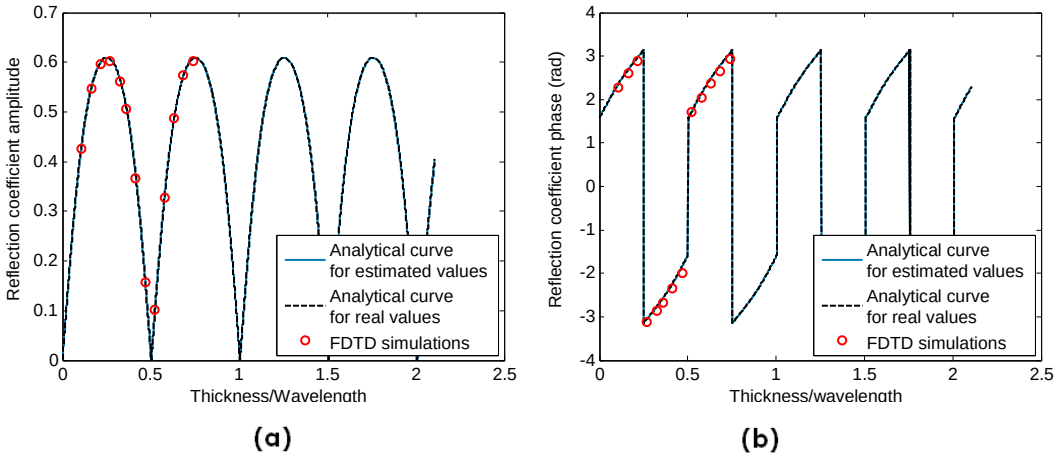

Figure 148: (a) Amplitude and (b) phase comparison of the points obtained from the analysis of the radargram for representative frequencies to the theoretical curves calculated for the real value (which are merged as the parameters are perfectly determined).

In this very simple case, the correspondence is perfect, because the layer parameters are well determined by the method. In Table 10, the parameters are determined for wet layers of different thicknesses using the plane wave method and the hybrid model.

Table 10 : Parameters of the minimum of the error function for the determination of a wet layer ($\varepsilon'_{r2} = 40$) into concrete ($\varepsilon'_{r1} = 10$).

	Plane wave	Hybrid model
$d = 2.5\ mm$	$d = 2\ mm$ $\varepsilon'_{r2} = 47$	$d = 2\ mm$ $\varepsilon'_{r2} = 47$
$d = 5mm$	$d = 5\ mm$ $\varepsilon'_{r2} = 37$	$d = 5\ mm$ $\varepsilon'_{r2} = 37$
$d = 1cm$	$d = 1\ cm$ $\varepsilon'_{r2} = 40$	$d = 1\ cm$ $\varepsilon'_{r2} = 40$
$d = 2\ cm$	$d = 2.1\ cm$ $\varepsilon'_{r2} = 36$	$d = 2.1\ cm$ $\varepsilon'_{r2} = 36$
$d = 5\ cm$	$d = 4.8\ cm$ $\varepsilon'_{r2} = 43$	$d = 4.8\ cm$ $\varepsilon'_{r2} = 43$

The error is inferior to 10% in every case, except for the thinnest layer. The hybrid model gives the same results as the plane wave method, due to the fact that the hybrid model uses the plane wave approximation for high permittivity layers. A detailed analysis shows that the main source of error is the phase determination. To improve the results for the thinnest layers, it would be useful to use an incident pulse containing higher frequencies in order to extend the thickness-to-wavelength range (Figure 149 (a)).

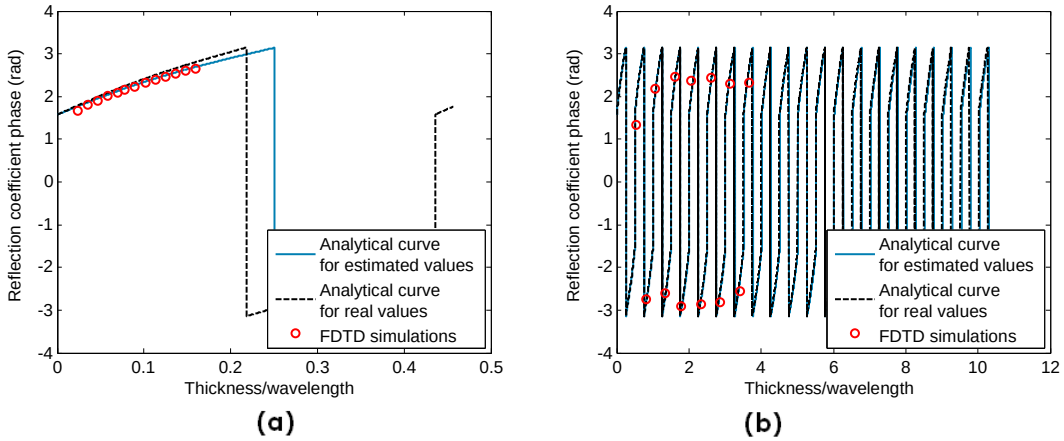

Figure 149 : Phase comparison of the points obtained from the analysis of the radargram for representative frequencies to the theoretical curves calculated for the real value.
(a) t=2.5 mm: the precision is limited by the limited range of t/λ values;
(b) t=5 cm: the precision is limited by the samples down sampling.

For the thickest layers, this range is more than sufficient, but relatively down sampled (Figure 149 (b)). In this case, a good method for decreasing the error would be to consider more points in the frequency range. Of course, if one of the parameters d or ε'_{r2} is known, the errors are dramatically reduced.

5.2.2.2 Determination of air layers into concrete

The same analysis is performed, replacing the wet layer by a 1 cm air layer, with the same reference frequencies. The estimated amplitude and phase are compared to the different analytical curves in Figure 150. The investigated frequencies still range from 0.5 to 3.5 GHz. Because the geometric attenuation is important in the case of air layers (Figure 138), we will also compare the results to the analytical curve obtained with the first terms estimation method.

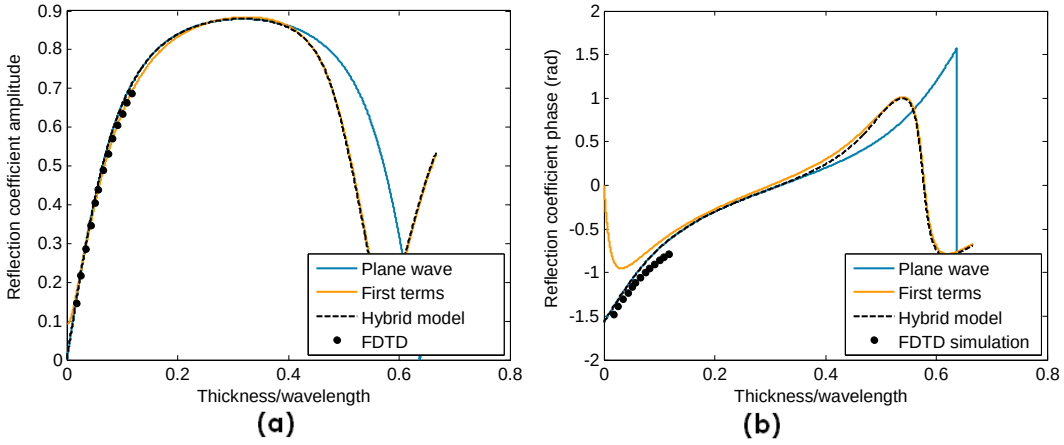

Figure 150 : Comparison between the reflection coefficient (a) amplitude and (b) phase curves obtained from a static numerical simulation and the theoretical curves, for a 1 cm air layer into concrete.

The correspondence is less exact than in the case of a wet layer (Figure 146). Because the wavelength in air is larger, the thickness-to-wavelength ratios that can be observed with the same pulse are smaller. For this reason, only a small portion of the curve can be traced, which may lead to the same problem as for very thin wet layers (Figure 149 (a)) and reduce the precision of the method. Because the thickness is small, the hybrid model is equal to the plane wave model, which will be preferred due to its faster computation. The first terms method slightly improves the results for the amplitude but is completely wrong for the phase: it will not be considered.

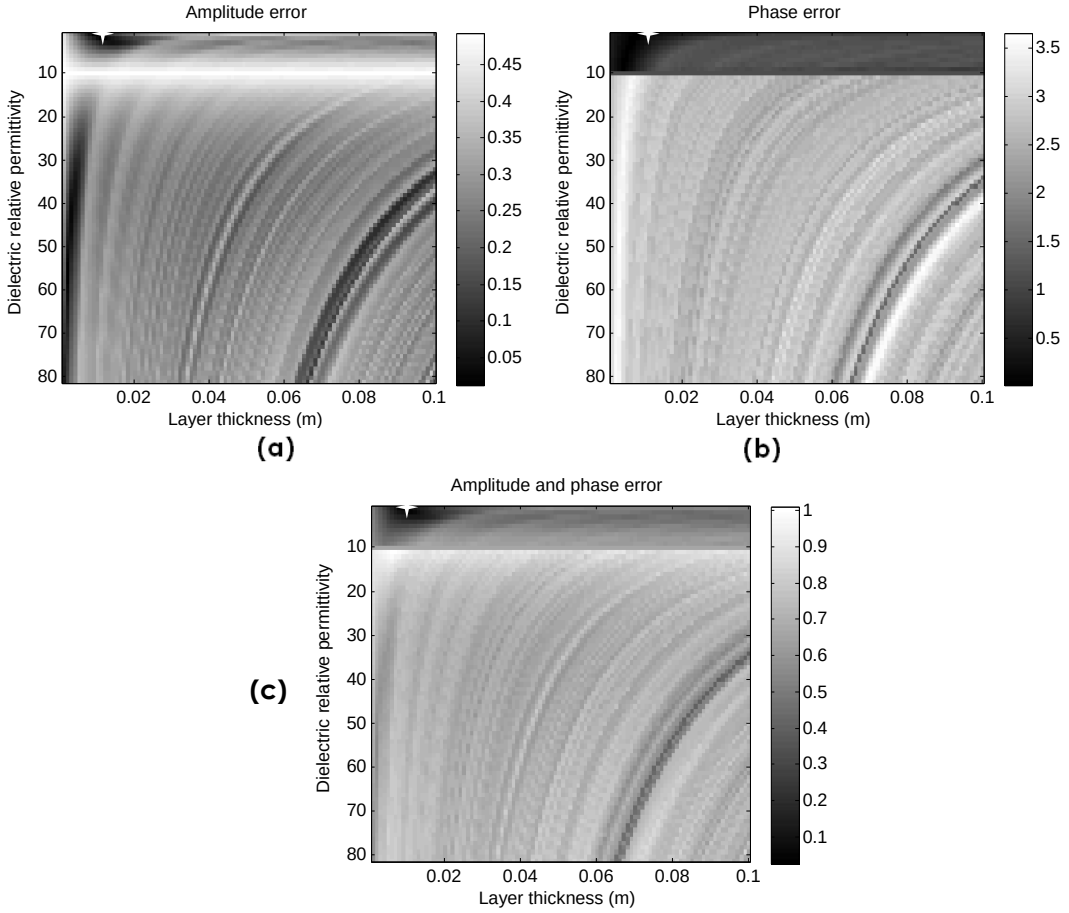

Figure 151 : Mean error between the reflection coefficient numerically estimated on a 1 cm air layer into concrete and forward calculations using plane wave: (a) amplitude; (b) phase and (c) weighted sum of the amplitude and phase.

From the last graph, the minimum of the error function is obtained for $\varepsilon'_{r2} = 1$ and $d = 0.9\,cm$. The thickness is slightly underestimated but the results are good. If only the amplitude error is considered, the best fit is obtained for another local minimum: $\varepsilon'_{r2} = 56$ and $d = 0.2\,cm$. The phase error minimum is less precise (d=0.8 mm instead of 0.9 mm), but the phase error for the permittivities superior to the matrix permittivity is so large that it allows eliminating many local minima. This confirms the necessity to combine both data.

In Figure 152, the amplitude and phase of the reflection obtained from the numerical tests are compared to the theoretical curves calculated for the real

value (d=1 cm) and for the estimated value (d=0.9 cm). We observe that the curve for the estimated values is closer to the numerical values than the curves calculated with their actual parameters. To improve the parameters determination process, the only method would then be to improve the forward model or use an incident signal with higher frequencies.

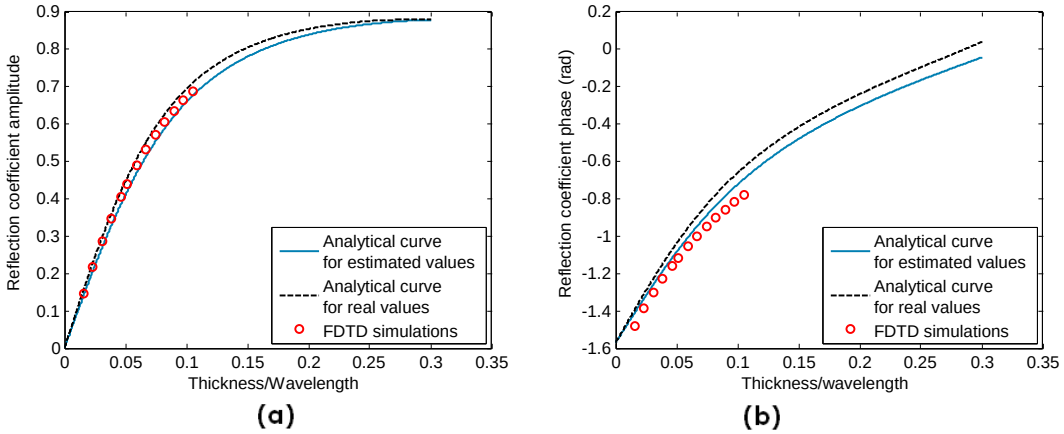

Figure 152: (a) Amplitude and (b) phase comparison of the points obtained from the analysis of the FDTD radargram for representative frequencies to the theoretical curves calculated for the real value (d=1 cm) and for the estimated values (d=0.9 cm).

The case of thicker layers is of particular interest when low permittivity materials are considered. Indeed, the hybrid model differs then from the plane wave approximation. In Figure 153, the amplitude and phase of the reflection obtained in the FDTD tests are compared to the curves obtained with the different analytical methods (plane wave approximation, first terms method and hybrid model) for the case of a 5 cm air layer.

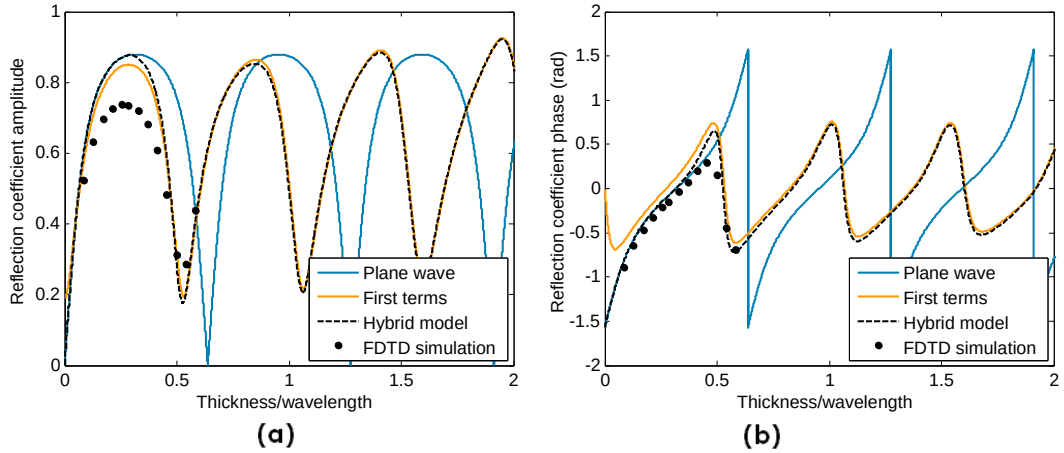

Figure 153 : Comparison between the reflection coefficient (a) amplitude and (b) phase curves obtained from a static numerical simulation and analytical values, for a 5 cm air layer.

We observe that the plane wave approximation is very poor in this case: the best parameter estimation will deduce a thickness of 3,8 cm for a permittivity of 2, while the best fit using the hybrid model predicts correctly the permittivity of 1 and

estimates the thickness to 5.1 cm. In such cases, the use of the hybrid model, despite its increased computation time, is therefore recommended. The results for both methods and different thicknesses are summarized in Table 11.

Table 11 : Parameters of the minimum of the error function for the determination of an air layer ($\varepsilon'_{r2} = 1$) into concrete ($\varepsilon'_{r1} = 10$).

	Plane wave	Hybrid model
$d = 2.5\ mm$	$d = 2.5\ mm$ $\varepsilon'_{r2} = 1$	$d = 2.5\ mm$ $\varepsilon'_{r2} = 1$
$d = 5\ mm$	$d = 5\ mm$ $\varepsilon'_{r2} = 1$	$d = 5\ mm$ $\varepsilon'_{r2} = 1$
$d = 1\ cm$	$d = 0.9\ cm$ $\varepsilon'_{r2} = 1$	$d = 0.9\ cm$ $\varepsilon'_{r2} = 1$
$d = 2\ cm$	$d = 1.7\ cm$ $\varepsilon'_{r2} = 1$	$d = 1.7\ cm$ $\varepsilon'_{r2} = 1$
$d = 5\ cm$	$d = 3.8\ cm$ $\varepsilon'_{r2} = 2$	$d = 5.1\ cm$ $\varepsilon'_{r2} = 1$
$d = 10\ cm$	$d = 7.7\ mm$ $\varepsilon'_{r2} = 2$	$d = 10.0\ cm$ $\varepsilon'_{r2} = 1$

These values confirm the interest to use the hybrid method for the thick layers. Even if the prediction of the curves is poorer than for the wet layers, the errors in the parameters estimations are not greater.

5.2.2.3 Influence of the post-critical incidence and surface tests

The influence of the post-critical incidence will be tested in the problematic case that has been determined in § 5.2.1.3: with the test performed from the surface. To illustrate the results, we select the intermediate layer thickness of 2 cm, and an antennas offset of 13 cm. The numerical reflection amplitude and phase are compared to the analytical curves in Figure 154.

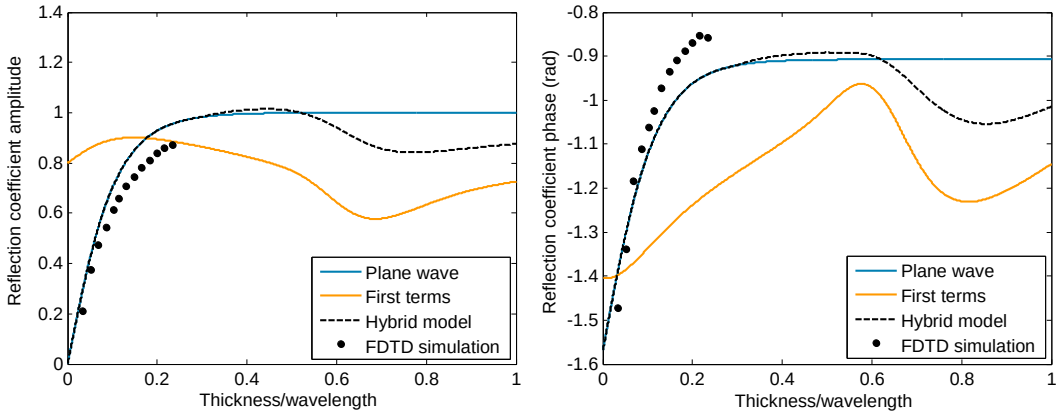

Figure 154 : Comparison between the reflection coefficient (a) amplitude and (b) phase curves obtained from a static numerical simulation and analytical values, for a 2 cm air layer and a post-critical incidence.

We observe that the concordance is not so bad: at least for $t/\lambda < 0.1$, the points seem to follow the plane wave approximation. The same curve is traced for the 5 cm layer in Figure 155.

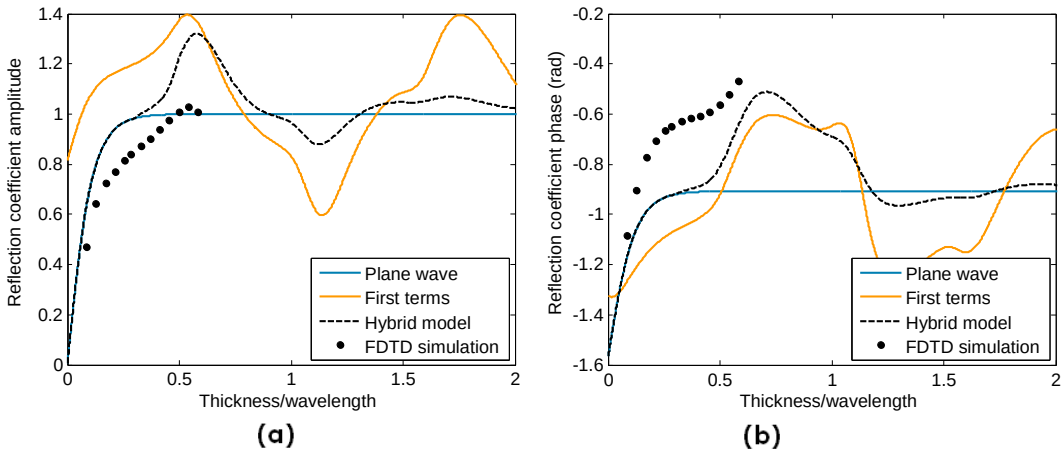

Figure 155 : Comparison between the reflection coefficient (a) amplitude and (b) phase curves obtained from a static numerical simulation and analytical values, for a 5 cm air layer and a post-critical incidence.

The numerical results still seem acceptable for $t/\lambda < 0.1$, even if the amplitude is underestimated and the phases overestimated. Only the shape of the curve roughly corresponds to the hybrid approximation. This is due to the presence of the surface-lateral wave (§ 4.2.2), which is not taken into account by any of our models. The best parameters for different thicknesses and both methods are detailed in Table 12.

Table 12 : Parameters of the minimum of the error function for the determination of an air layer $(\varepsilon'_{r2} = 1)$ into concrete $(\varepsilon'_{r1} = 7.7)$ with a post-critical incidence.

	Plane wave	Hybrid model
$d = 2.5\ mm$	$d = 2.5\ mm$ $\varepsilon'_{r2} = 1$	$d = 2.5\ mm$ $\varepsilon'_{r2} = 1$
$d = 5\ mm$	$d = 5\ mm$ $\varepsilon'_{r2} = 1$	$d = 5\ mm$ $\varepsilon'_{r2} = 1$
$d = 1\ cm$	$d = 0.9\ cm$ $\varepsilon'_{r2} = 1$	$d = 0.9\ cm$ $\varepsilon'_{r2} = 1$
$d = 2\ cm$	$d = 1.9\ cm$ $\varepsilon'_{r2} = 2$	$d = 1.9\ cm$ $\varepsilon'_{r2} = 2$
$d = 5\ cm$	$d = 3.8\ cm$ $\varepsilon'_{r2} = 2$	$d = 3.2\ cm$ $\varepsilon'_{r2} = 2$
$d = 10\ cm$	$d = 3.3\ cm$ $\varepsilon'_{r2} = 2$	$d = 6.9\ cm$ $\varepsilon'_{r2} = 2$

As we could expect from the observation of Figure 154 and Figure 155, the parameters prediction for a post-critical incidence is not reliable, except when an important number of the considered t/λ are inferior to 0.1. In the particular case of this incident wavelet and air layer, the maximum thickness that can be determined is about 2 cm. For larger thicknesses, the use of monostatic tests (with a small incident angle) should be privileged.

5.2.3 Experimental determination of thin layers

In this section, the procedure tested in the previous chapter on numerical datasets to span the parameter space and determine the layer properties is applied on experimental measurements. Considering the experimental frequency spectrum (Figure 143), the investigated frequencies will range from 1 to 3 GHz.

In a first step, we will test the layers using monostatic tests. From §§ 5.2.1.3 and 5.2.1.4, we know that they should not be affected by surface-lateral waves, due to the small offset, but that the results may appear shifted to the right, which can lead to a lack of precision.

Then, some bistatic tests will be performed. For the small thickness-to-wavelength ratios, obtained with very thin layers, the results presented in § 5.2.2.3 seemed to indicate that the models remained valid, despite the post-critical incidence.

Finally, the method will be applied to the determination of a bitumen layer, first embedded into a matrix of concrete and then suspended into air.

5.2.3.1 Monostatic test on air thin layer

Before applying the method described in § 5.2.2.1 for determining the parameters of a layer from experimental static measurements, we compare the experimental points to the theoretical curves in Figure 156. The measurements are performed on a thin air layer of 6 mm embedded into a concrete whose permittivity is estimated to $\varepsilon'_r = 7.7$. The test is monostatic ($x_0 = 4\ cm$). For a 6 mm layer, we expect the plane wave method (equal to the hybrid model) to predict the reflection coefficient relatively well.

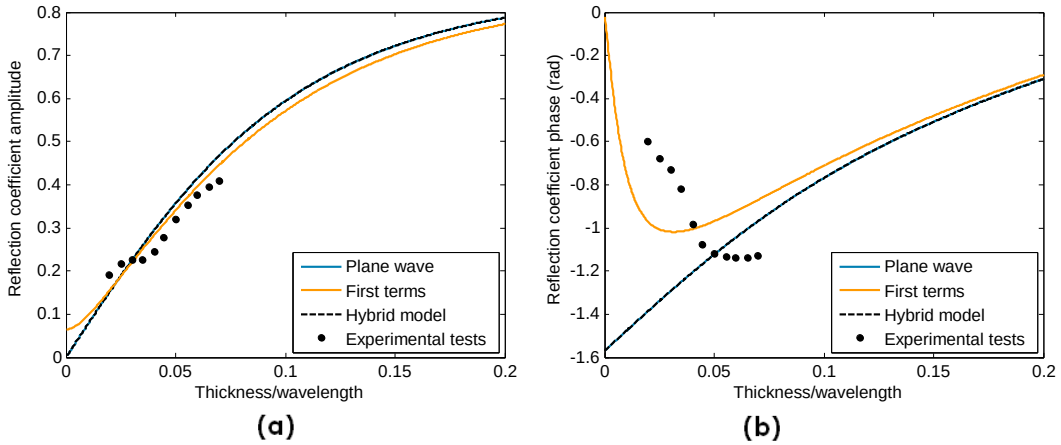

Figure 156 : (a) Amplitude and (b) phase comparison of the points obtained from the analysis of the experimental radargram on a 6 mm air layer for representative frequencies (1-3.5 GHz) to the theoretical curves calculated for the real values.

The amplitudes of the experimental reflection coefficients correspond relatively well to the analytical curves, but their values are slightly inferior. This could lead to an underestimation of the layer thickness or to an underestimation of the permittivity contrast. This underestimation of the amplitude had been predicted by the numerical tests (Figure 147).

The concordance for the phase is much poorer. We observe a strong decrease of the reflection coefficient phase, which is not predicted by the plane waves method. A decrease was predicted by the first terms method, but the location and value of the minimum are poorly predicted. This decrease was not observed at all in the numerical tests, which followed accurately the plane wave approximation. These observations are valid for most of the tests performed for layers inferior to 1 cm.

For thicker layers, the behaviour is different. The case of a 6 cm air layer is represented in Figure 157.

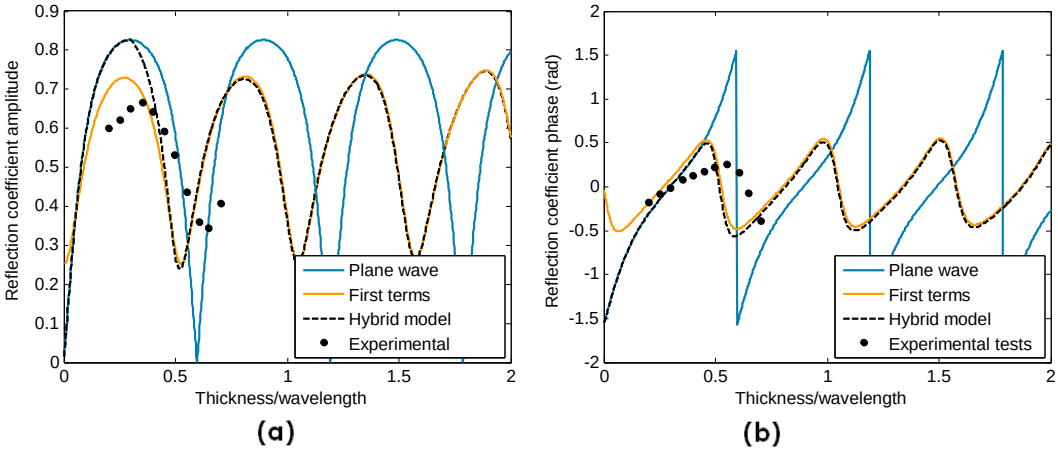

Figure 157 : (a) Amplitude and (b) phase comparison of the points obtained from the analysis of the experimental radargram on a 6 cm air layer for representative frequencies (1-3.5 GHz) to the theoretical curves calculated for the real values.

The same behaviour is observed as when only the amplitude peak was considered (Figure 144): the curve of the experimental points seems stretched to the right. Nevertheless, the amplitude of the peaks is relatively well predicted by the first terms (and hybrid) methods, even if slightly overestimated. We conclude that the model that will produce the best thickness prediction for all thicknesses is the first terms approximation.

The errors functions obtained by this method for the layer of 6 mm are displayed in Figure 158.

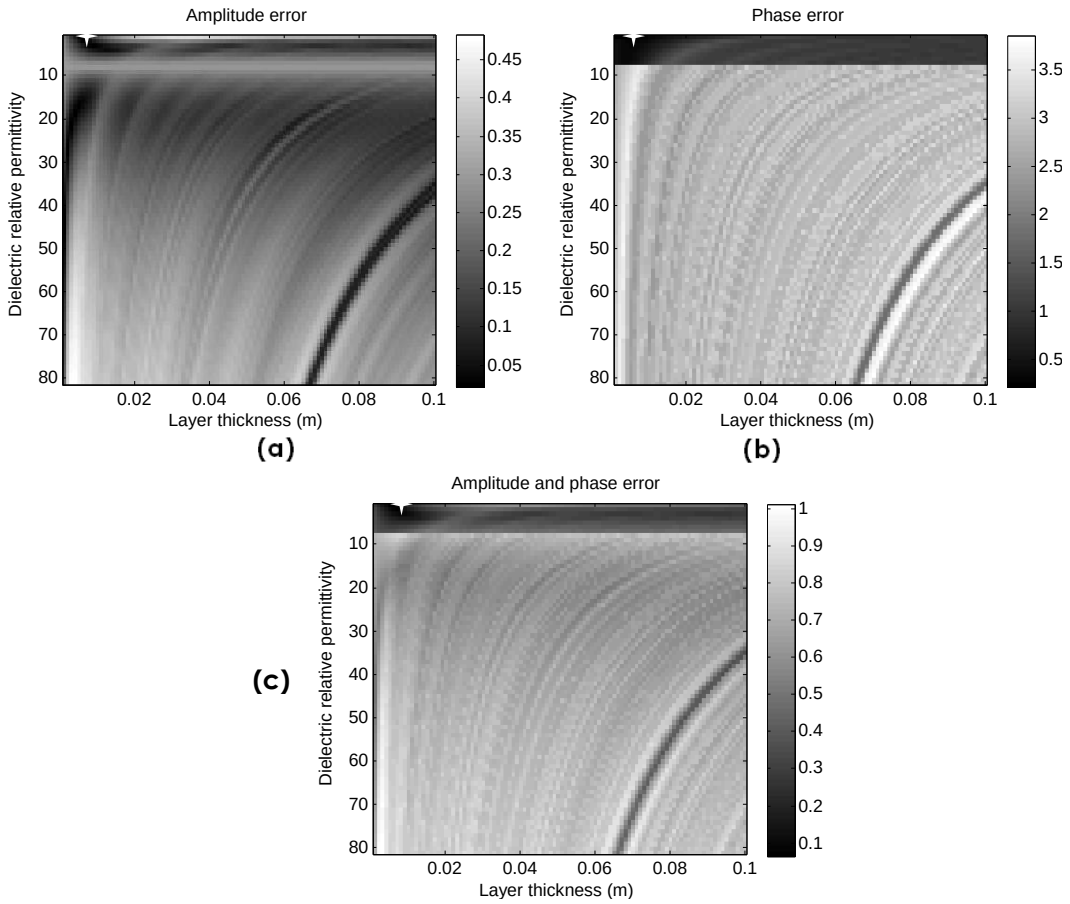

Figure 158 : Mean error between the reflection coefficient experimentally estimated on a 6 mm air layer into concrete and forward calculations using plane wave: (a) amplitude; (b) phase and (c) weighted amplitude and phase sum.

The minimum of the global error function (Figure 158 (c))corresponds to the actual parameters of the layer ($d = 6\ mm$ and $\varepsilon'_{r2} = 1$). This is not the case for the separate error functions: the minimum for the amplitude appears for $d = 9\ mm$ and $\varepsilon'_{r2} = 3$, while the minimum for the phase is obtained for $d = 4\ mm$ and $\varepsilon'_{r2} = 1$.

If the same analysis is performed on the 6 cm layer curve, the best parameters calculated by the same method are $d = 5.1\ cm$ and $\varepsilon'_{r2} = 1$. The corresponding curves are compared to the measurements in Figure 159.

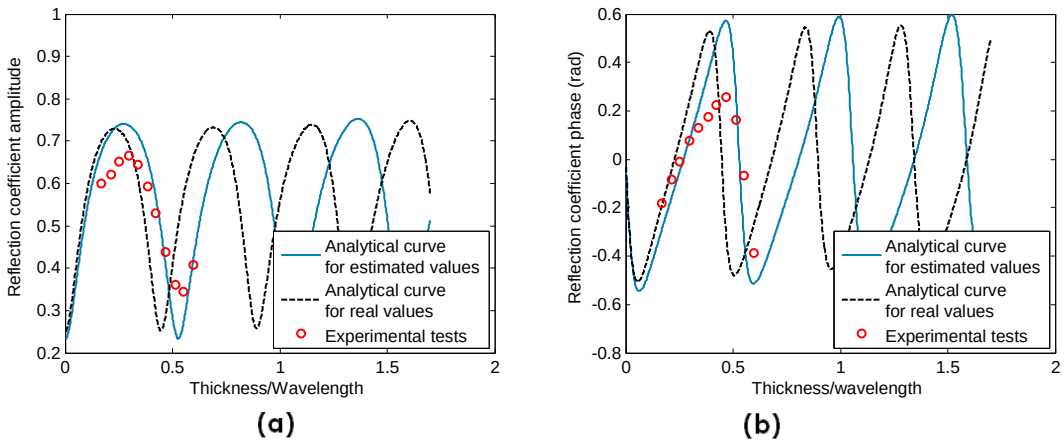

Figure 159 : Comparison between the reflection coefficient (a) amplitude and (b) phase curves obtained from a static experimental measurement and analytical values, for a 6 cm air layer.

The same method was applied to 23 air layers with thicknesses ranging from 1 mm to 9.6 cm. The best parameters determined in each case are summarized in Figure 160.

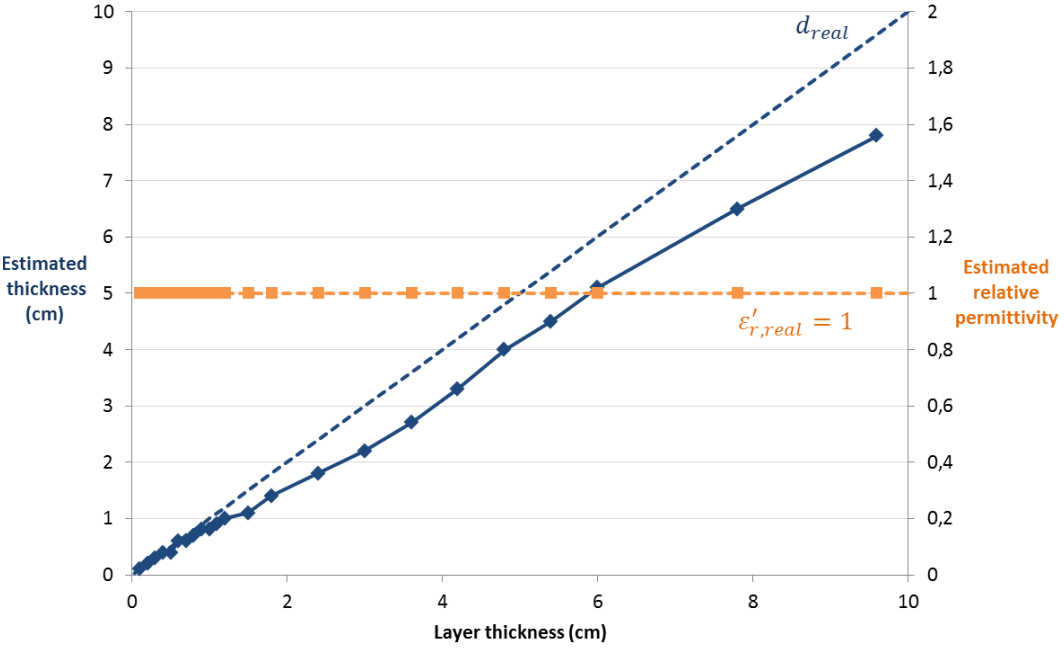

Figure 160 : Experimental estimation of layer thickness and permittivity determined by minimization of the global error function.

The thickness is underestimated of about 20%, except for the very thin layers which are well determined. The unitary permittivity is perfectly determined in each case. The underestimation of the thickness is partly due to the underestimation of the amplitudes, which had already been observed in the numerical tests, and partly to the shift of the values to larger t/λ, only visible for the experimental measurements.

5.2.3.2 Bistatic measurements (with post-critical incidence)

In § 5.2.2.3, it was shown that the tests with post-critical incidence could be predicted by the plane wave approximation if the thickness was inferior to a tenth of the wavelength. With the frequency of our antenna, this will be the case for thicknesses inferior to 1 cm. We only consider here initial offsets of 13 cm, corresponding to the offset of the initial measurement of a CMP. This measurement can be performed simultaneously to the monostatic measurement performed with one antenna. This is the case in the example of Figure 161, which corresponds to the bistatic measurement performed on a 6 mm air layer and has been measured simultaneously to the monostatic test displayed in Figure 156.

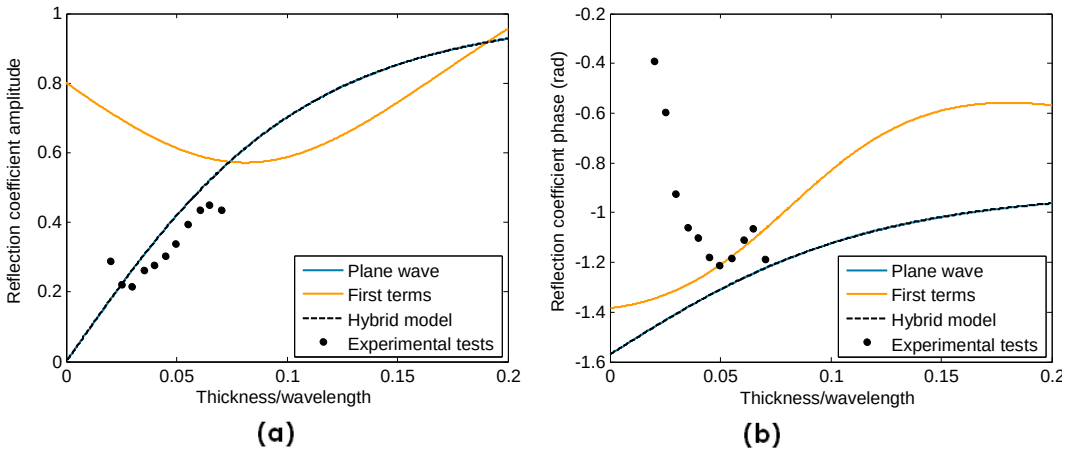

Figure 161 : (a) Amplitude and (b) phase comparison of the points obtained from the analysis of the experimental bistatic radargram on a 6 mm air layer for representative frequencies (1-3.5 GHz) to the theoretical curves calculated for the real values.

The amplitude of the measured reflection coefficients corresponds quite well to the analytical curve obtained with the plane wave approximation for the same values. This behaviour had been predicted correctly by the numerical test in § 5.2.2.3. On the opposite, the fitting is poor for the phase, especially for the plane wave approximation but also for the first terms model. Indeed, the initial phase decrease that had been observed for the monostatic tests in the previous chapter is still present. It was not predicted at all by the equations, which will reduce the properties determination accuracy.

To improve the accuracy of the parameters determinations, it would be interesting to take mainly the amplitude into account, with the plane wave approximation. But it was observed in Figure 151 that it is necessary to combine the amplitude and the phase information to eliminate the local minima that can appear in the amplitude error function. So the phase error will be taken into account, but it will be calculated regarding the first terms method, and its weighting factor in the global function will be divided by two. With this improved process, the error functions are calculated. The amplitude, phase and global error for the 6 mm example are represented in Figure 162.

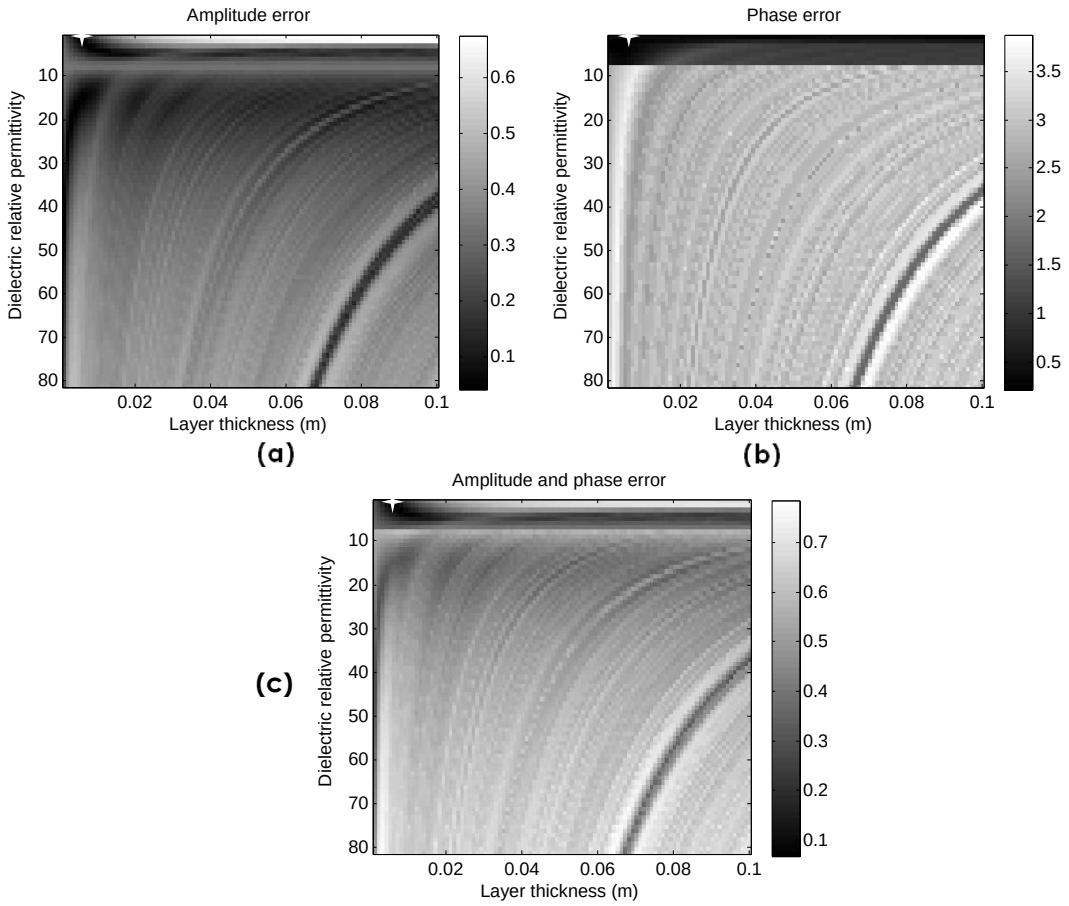

Figure 162 : Mean error between the reflection coefficient estimated from measurements on a 6 mm air layer into concrete and forward calculations using plane wave for the amplitude and first terms for the phase. (a) Amplitude; (b) phase and (c) weighted sum of the amplitude and phase.

The minimum is observed for $d = 6\,mm$ and $\varepsilon'_{r2} = 2$. The estimated curves are compared to the experimental curves in Figure 163.

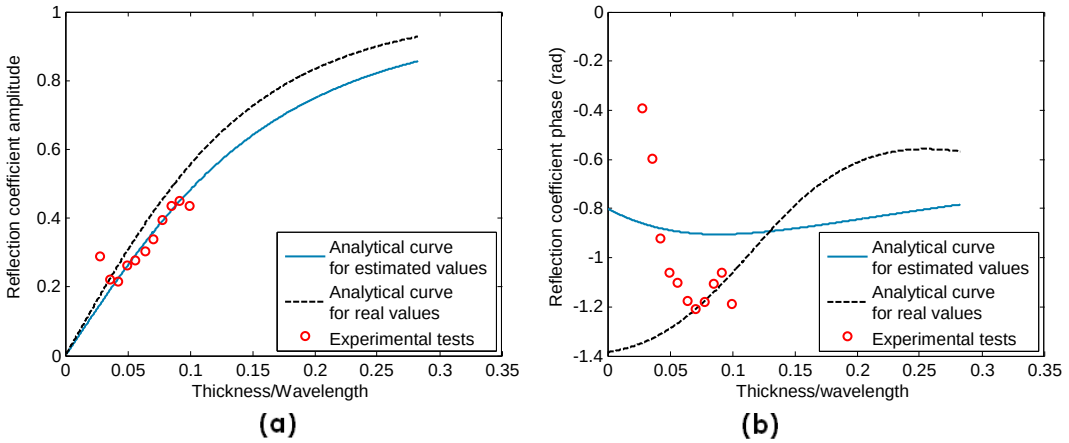

Figure 163 : (a) Amplitude and (b) phase comparison of the points obtained from the analysis of the radargram for representative frequencies (1-3.5 GHz) to the theoretical curves calculated for the real values.

The same test has been performed for thicknesses ranging from 1 to 9 mm. With those thicknesses, the investigated range of t/λ remains inferior to the limit of 0.1 which had been fixed as a validity limit from the numerical tests (§ 5.2.2.3). The estimated parameters are represented in Figure 164.

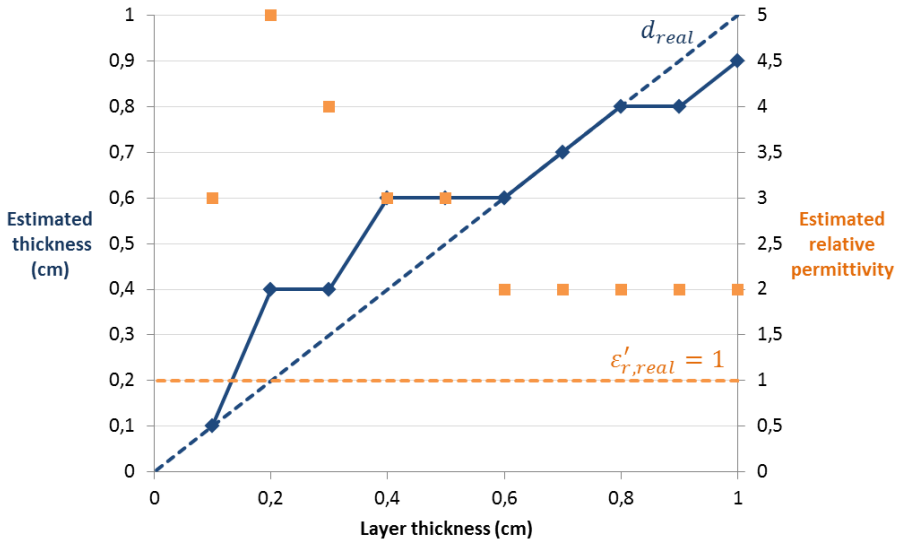

Figure 164 : Experimental estimation of layer thickness and permittivity determined by minimization of the global error function for a bistatic measurement.

We observe that the layer thickness is relatively well determined, even if the error is higher than for monostatic measurements. But the permittivity is overestimated in each case, and even reaches 5 for the 2 mm layer. As a conclusion, we can say that the use of bistatic mono-offset measurements for the determination of thin layers is relatively worthless with the method displayed here: the precision was higher for monostatic measurements.

5.2.3.3 Application to the determination of a bituminous thin layer

In order to test the method on a thin layer made of another material than air, we tested a bitumen thin layer in two different configurations. First, the bitumen was embedded into concrete, using the same smooth concrete slabs as in the previous paragraphs. In a second configuration, the test was performed on the layer directly, using the air as the matrix material. In both configurations, we will try to estimate the bitumen permittivity and thickness from the radargrams and we will compare these values to the known properties of the material: the measured thickness of the layer is equal to 4.5 mm and the relative permittivity of bitumen does not vary much and is generally comprised between 2.6 and 2.8 [73].

Bitumen embedded into concrete

To perform this test, the bitumen layer was placed between two smooth concrete slabs, whose permittivity had been estimated to $\varepsilon'_{r1} = 8.3$ (§ 3.3.2). In accordance with the observations of § 5.2.1.1, we performed the measurement statically and compared the results with the curve obtained with the first terms method. The

error functions of the reflection coefficient amplitude, phase, and of the weighted function of amplitude and phase are represented in Figure 165.

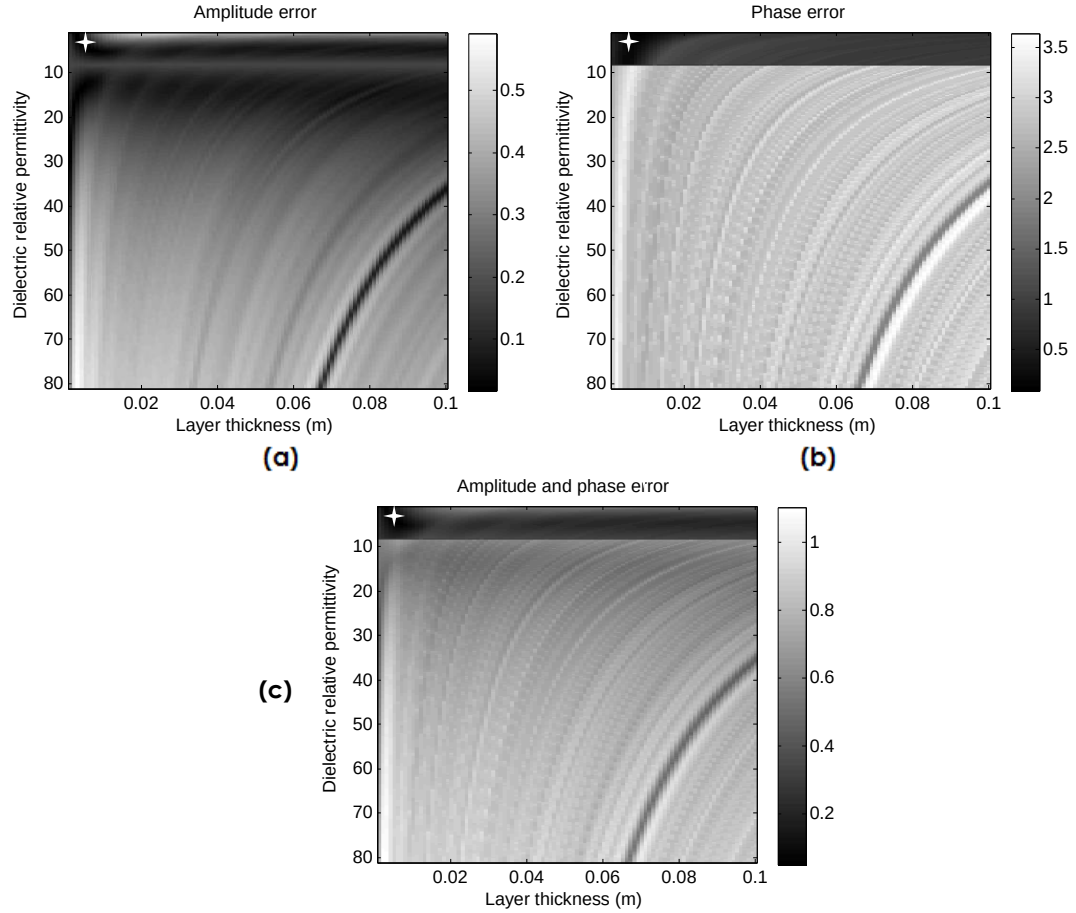

Figure 165 : Error function of the reflection coefficient on a bitumen layer into concrete for different thicknesses and permittivity intervals:
(a) amplitude, (b) phase and (c) global error function.

The optimum is found for the permittivity $\varepsilon_{r2} = 4.6$ and thickness $d = 5.6\,mm$. The relative error with the expected values ($\varepsilon_{r2} = 2.7$ and $d = 4.5\,mm$) is not negligible, especially for the permittivity. The amplitude and phase versus thickness-to-wavelength, for the estimated values, for the real values, and for the experimental points are represented in Figure 166.

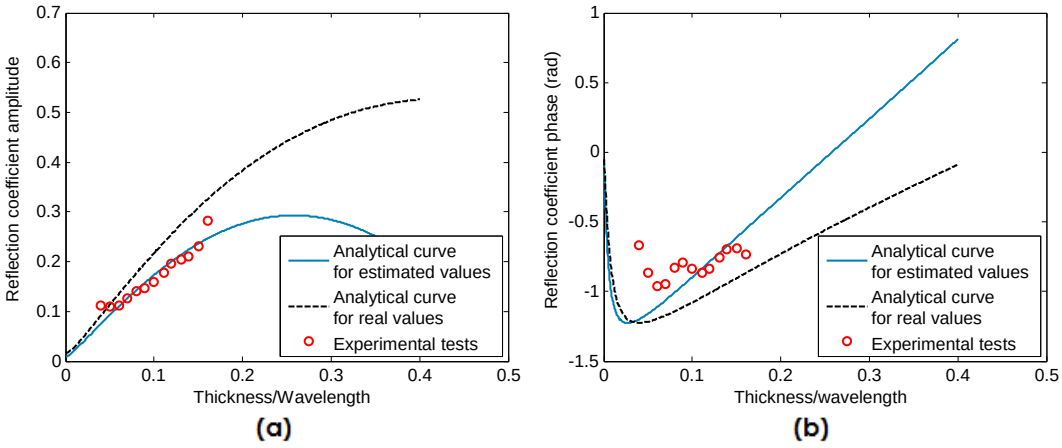

Figure 166 : (a) Amplitude and (b) phase of the reflection coefficient for the bitumen layer embedded into concrete. Comparison of the experimental values used for the error function calculation to the theoretical curves for the estimated parameters.

The amplitude and phase curves obtained from experimental measurements do not present the expected smoothness, and their position is relatively far from the expected curves. This explains the lack of precision for parameters determination.

If the thickness is known and the optimisation only concerns the permittivity, the error function is minimum for a permittivity of $\varepsilon'_{r2} = 3.9$. The permittivity is thus overestimated even when the thickness is precisely known. This lack of accuracy can be due to the fact that the bitumen presents a lower contrast with the matrix than the air layer.

Bitumen embedded into air

In the second configuration, the bitumen layer was placed in front of the immobile antenna, at a distance of about 20 cm. The test configuration is similar to the surface reflection test depicted in Figure 51 (b) (p 78). The measurement on the perfect reflector was performed first, with an aluminium sheet taped on the bitumen. This foil was carefully removed for the second test, without moving the bitumen. In Figure 167, the radar traces are represented, before (a) and after (b) direct wave removal and after selection of the first reflection (c).

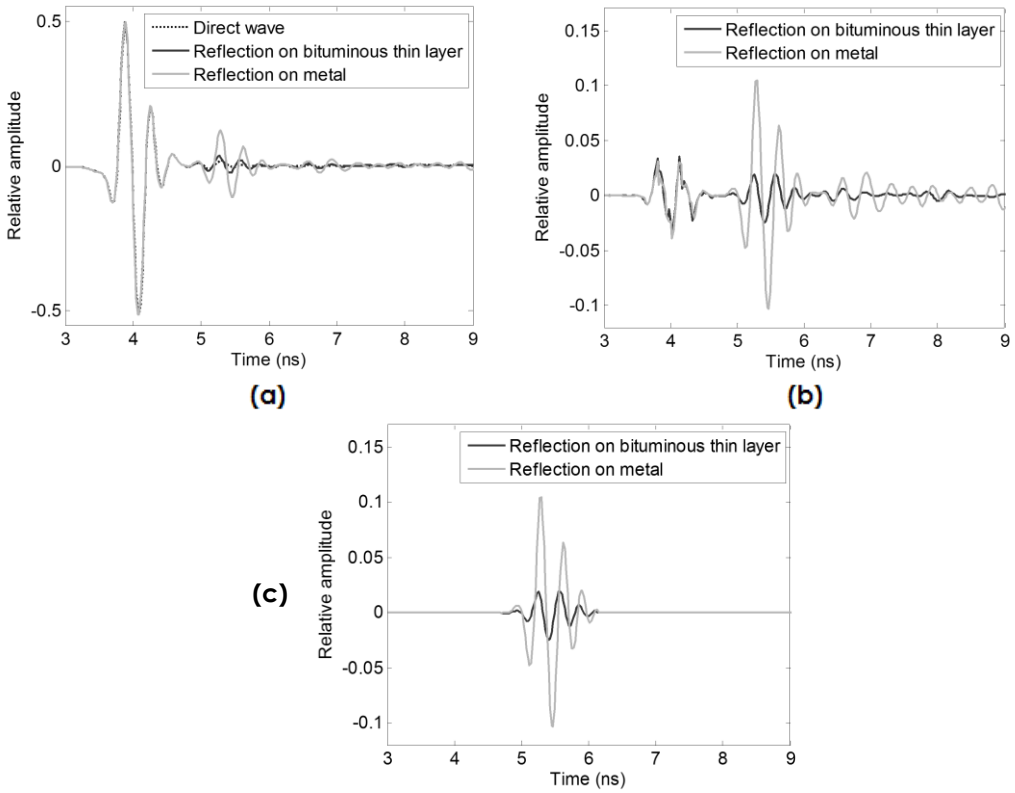

Figure 167 : Radar traces measured on the bitumen embedded in air. (a) Raw traces; (b) after direct wave removal and (c) after isolation of the reflection.

We observe in Figure 167 (b) that, despite the respect of a long warming up time (§ 3.2.2) and the fact that the wave propagates in a totally homogeneous medium (air), the suppression of the direct wave is not perfect. Just as when the test was performed on concrete (§ 5.2.1.4), the remaining direct wave amplitude should be suppressed, as well as the signal after the reflection. This is only possible if the antenna is placed sufficiently far from the target, which was the case here (Figure 167 (c)). Using the method presented in § 5.2.3.1, the error function is calculated for thicknesses ranging from 0.1 to 10 cm and relative permittivities ranging from 1 to 80. 11 frequencies, comprised in the interval 2-4 GHz are considered in the analysis. The results are displayed in Figure 168.

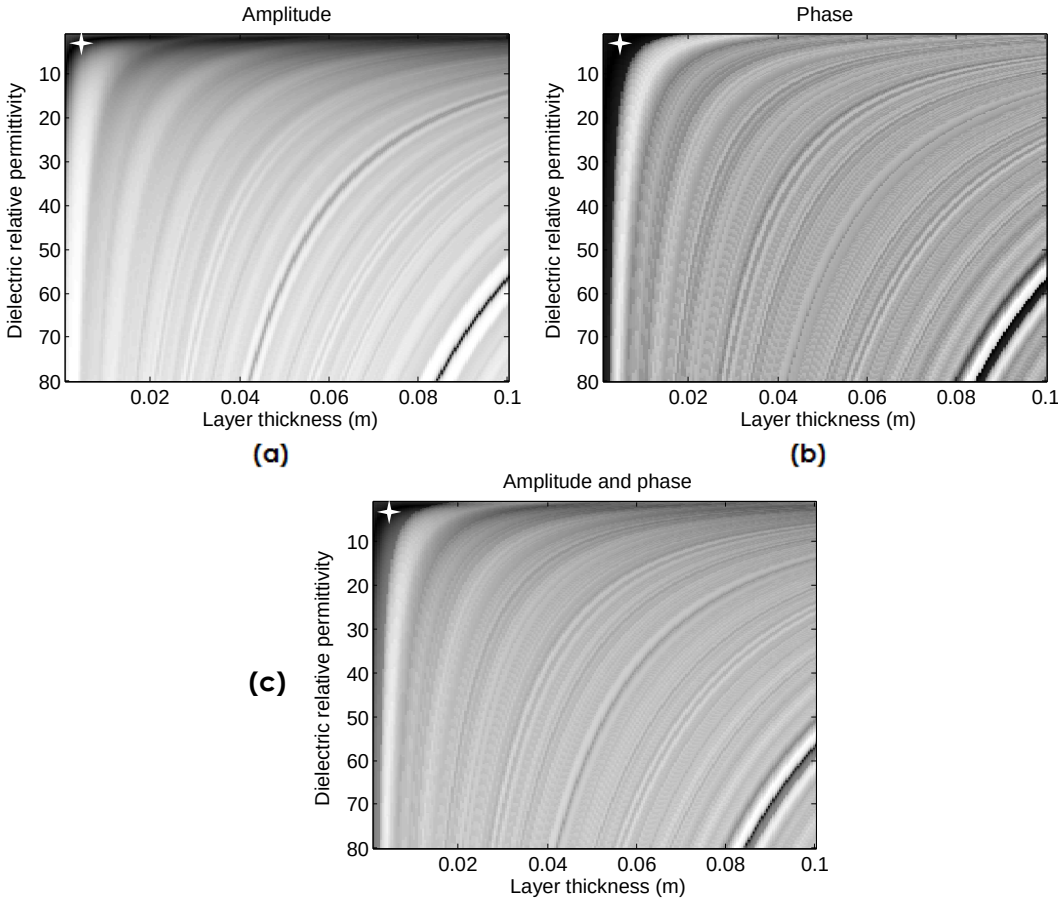

Figure 168 : Error function of the reflection coefficient for different thickness and permittivity intervals: (a) amplitude, (b) phase and (c) global function.

The optimum of the global function is obtained for $d = 6\,mm$ and $\varepsilon_{r2} = 2.3$. The thickness is higher than the nominal value (4.5 mm) while the permittivity is lower (2.7). Those values are situated in the zone of small error function. In Figure 169, we compared the points used to estimate the error function to the theoretical curves of amplitude and phase of the reflection coefficient, both for the estimated parameters and for the expected parameters.

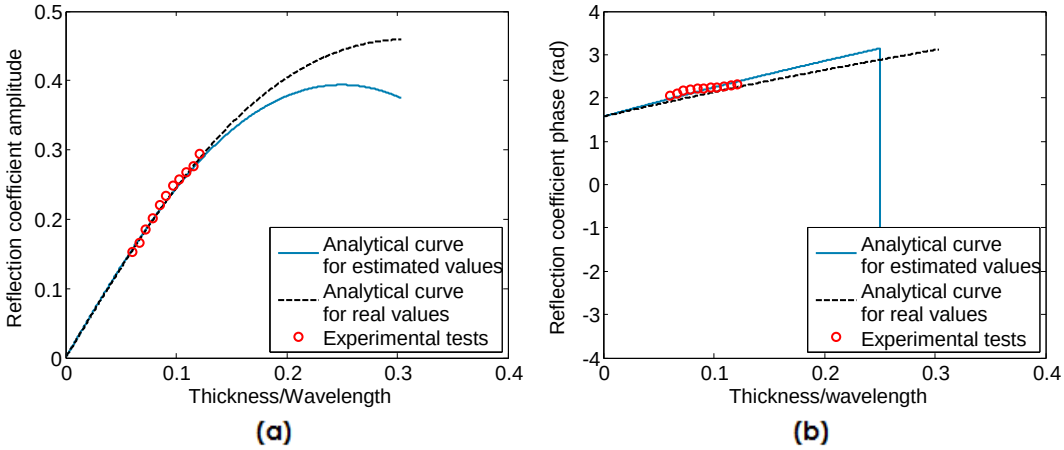

Figure 169 : (a) Amplitude and (b) phase of the reflection coefficient for the bitumen layer. Comparison of the experimental values to the theoretical curves calculated for the real and estimated parameters.

Observing the results comparison of Figure 169, we understand the lack of precision on the permittivity and thickness estimation. Indeed, in the considered frequency interval, both curves of estimated and expected values give an acceptable estimation for the considered points. To increase the precision of the measurement, a wider thickness/wavelength variation interval could be used. This would be the case for materials presenting a higher permittivity or could be obtained by the use of an antenna presenting a broader frequency range.

If the layer thickness is known, which is the case here because the bitumen layer thickness has been measured in the laboratory and is equal to 0.45 cm, the same analysis can be performed with the permittivity as the only variable, whose precision can be increased to 0.1. The error functions of the amplitude, the phase and the combined parameters of the reflection coefficient are displayed in Figure 170.

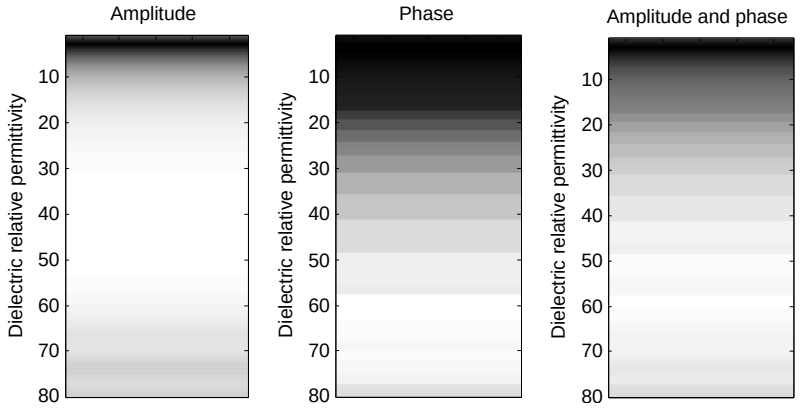

Figure 170 : Error functions for the amplitude, the phase and their combination in the bitumen permittivity determination when the thickness is known.

The optimum peak for the amplitude is relatively sharp and equal to $\varepsilon_r = 2.7$. For the phase, the optimum is less sharp and equal to 3.7. In the combination of both parameters, the sharp peak present in the amplitude is predominant, giving a

global optimum equal to $\varepsilon'_r = 2.7$. This is exactly the value predicted by the literature ($\varepsilon'_r \in [2.6 - 2.8]$[73]).

This method, in which the thin layer is embedded into an air matrix, gives better results than when the thin layers were embedded into concrete. This was expected, because the layer has then automatically a larger permittivity than the matrix. In addition, the direct wave can be measured with a high precision and is only affected by the antenna time drift. For all these reasons, this method could be an advantageous alternative to all the permittivity determination tests of § 3.3.1 (surface reflection amplitude, bottom reflection time,…) when the two surfaces of the material to be tested are free.

5.3 APVO curves parameters determination

In this section, we attempt to determine the layer parameters on the basis of numerical and experimental APVO curves. In a first step, we will analyse numerical curves obtained with surface testing. This will allow checking the assumptions of § 4.2 on the limitation of the angle range for the parameters determination. Then, we will try to determine the parameters of air thin layers of various thicknesses on the basis of experimental CMPs.

5.3.1 Numerical APVO curves

The first test consists in determining the parameters of a 1.2 cm air layer, on the basis of the same numerical test as displayed in Figure 127. The radargram has been cut to isolate the first reflection (Figure 120) and the angle range considered in the analysis is 0°-42°. Five frequencies are considered, ranging from 1.7 to 2.9 GHz. The error functions of the amplitude, the phase and their weighted sum, determined with the method presented in § 5.2.2.1 are represented in Figure 171, in which the real values are represented by a white cross.

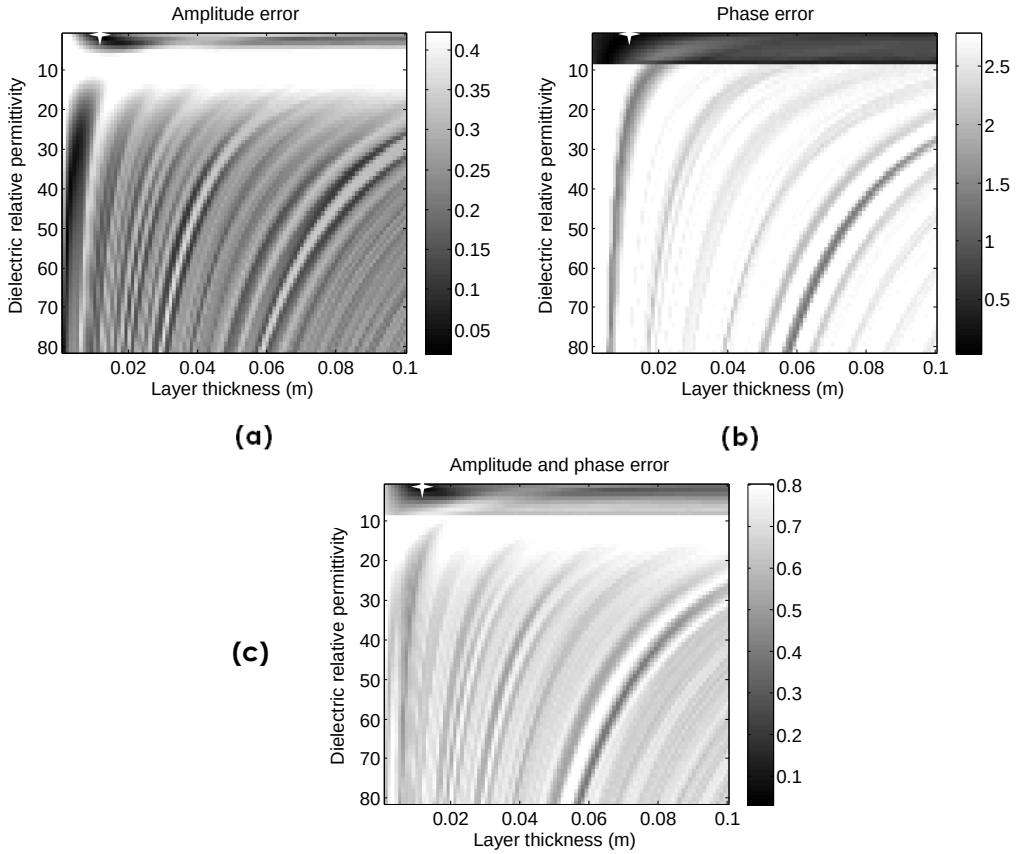

Figure 171 : Mean error between the reflection coefficient numerically estimated on a 1.2 cm air layer into concrete and forward calculations using the hybrid model: (a) amplitude; (b) phase and (c) weighted sum of the amplitude and phase.

The minimum of the error function is obtained for the parameters $d = 1.1\ cm$ and $\varepsilon'_{r1} = 1$. These estimated parameters are very close to the real parameters, despite the fact that the numerical tests are performed from the surface. The position of the maximum is mainly determined by the amplitude error (Figure 171 (a)), but the phase error (Figure 171 (b)) allows eliminating the local minimum appearing in the amplitude error for high permittivities and low thicknesses.

If the same analysis is performed on the angle range 32°-42°, the optimum is obtained for $d = 1.3\ cm$ and $\varepsilon'_{r1} = 2$. Those parameters are not exact but still give a fair approximation of the layer parameters.

5.3.2 Experimental APVO curves

The same analysis as in the previous paragraph is performed on experimental APVO curves measured on the same configuration: $d = 1.2\ cm$ and $\varepsilon'_{r1} = 1$. The considered angles interval ranges from 32°, the minimum angle measureable for this configuration with our antenna, to 42°, the maximum value for which the influence of the surface-lateral wave remains limited (see § 4.2.4). The error functions are drawn in Figure 172.

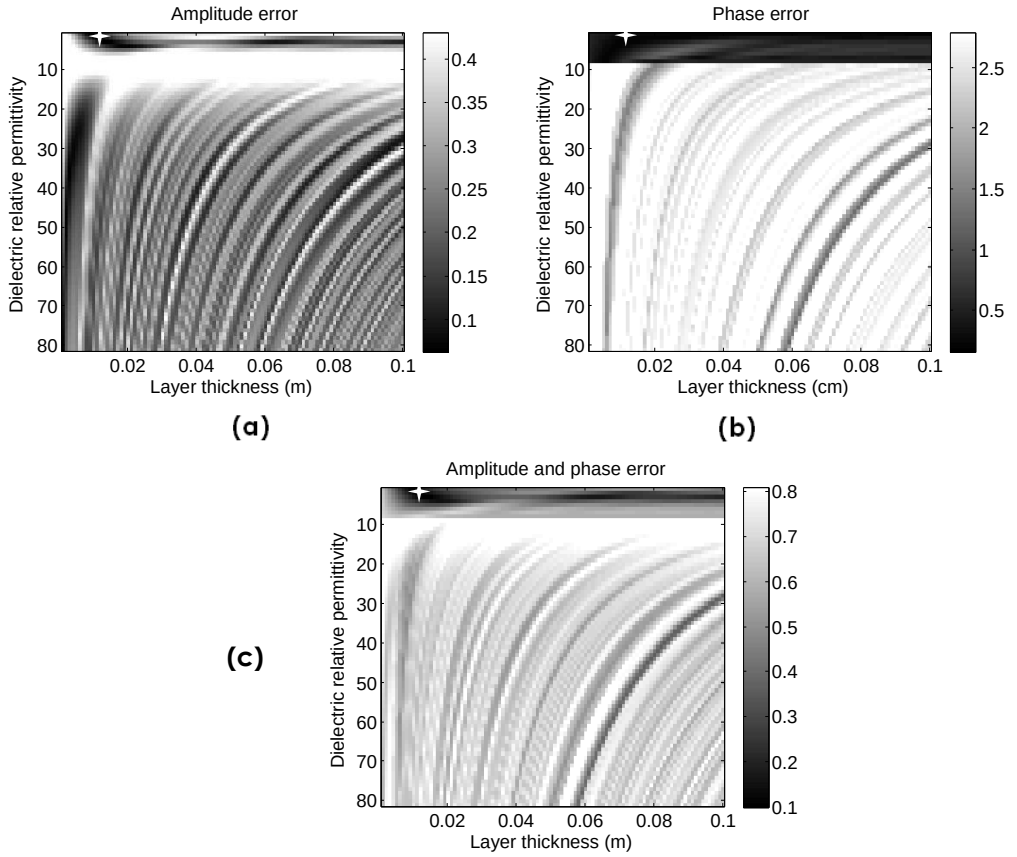

Figure 172 : Mean error between the reflection coefficient numerically estimated on a 1.2 cm air layer into concrete and forward calculations using the hybrid model: (a) amplitude; (b) phase and (c) weighted sum of the amplitude and phase.

The optimum value is obtained for $d = 1.4\ mm$ and $\varepsilon'_{r2} = 3$. This value is farther from the real values than the best parameters obtained from numerical curves, due to the important noise. We note that the minimum zone near the optimum value is an oblique line: If the permittivity is overestimated, it is likely that the layer thickness will be overestimated as well. On the opposite, if the value of one of the parameters is known, the error on the other parameter will be reduced. A difference with the error functions obtained for the numerical curves is the presence of a local minimum for thicker layers ($d = 5 - 10\ cm$) with a permittivity of 3-4.

The APVO curves estimated with the hybrid method for these estimated parameters are compared in Figure 173 to the experimental curves and to the curves calculated with the real parameters.

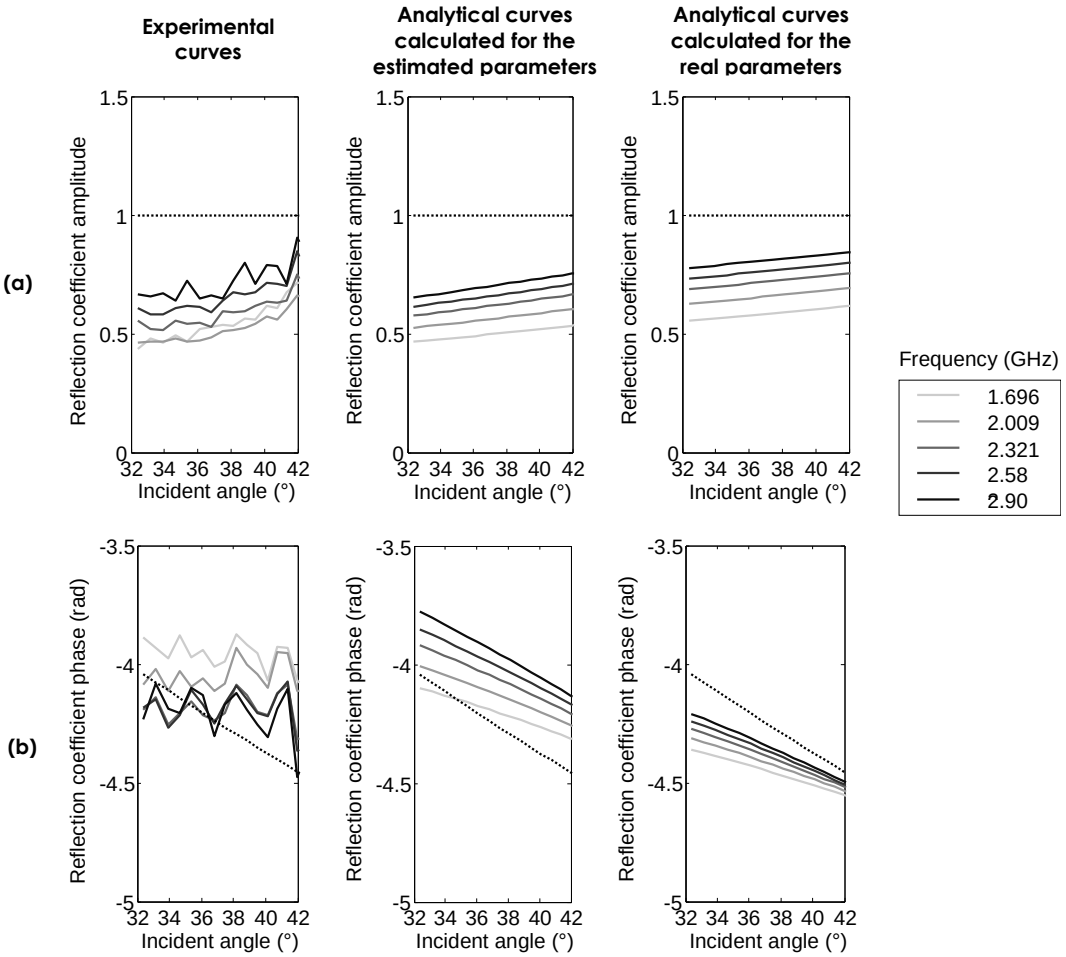

Figure 173 : (a) Amplitude and (b) phase comparison of the reflection coefficient experimentally measured on a 1.2 cm air layer embedded into concrete to the APVO curves calculated with the hybrid method for the estimated parameters and for the real values.

In Figure 173, we observe that the amplitude of the curves calculated with the estimated values corresponds slightly more to the experimental curves than the ones calculated with the real parameters. This concordance is more evident again for the phase curves. The higher values observed for the phase are probably due to the surface-lateral waves and were predicted by the simulations (Figure 127 (b)).

Finally, the same test was performed on air thin layers with amplitudes ranging from 1 mm to 1.8 cm. The estimated parameters are compared to the actual values in Figure 174.

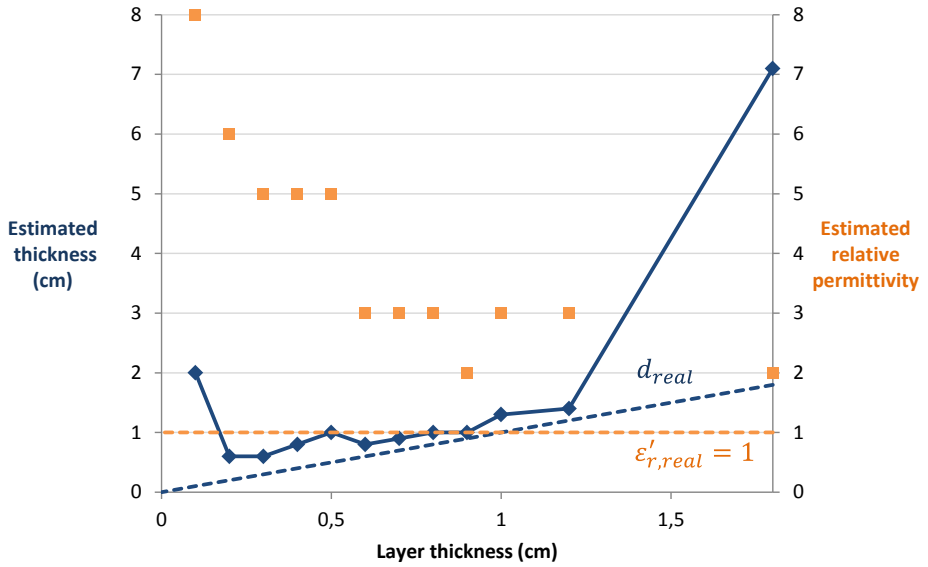

Figure 174 : Experimental estimation of layer thickness and permittivity determined by minimization of the global error function for a CMP measurement.

In Figure 14, we observe that both the permittivity and the thickness are systematically overestimated by the method. The results are acceptable between 2 mm and 1.2 cm: the global trend of the thickness increase is visible. In this range, the thickness error is inferior to 4 mm and the permittivity error is inferior to 5. The worst results are obtained for the 1 mm layer, probably due to the excessive noise, and for the 1.8 cm layer, for which the global optimum is obtained for the local minimum that was observed in Figure 172 (c).

As expected, due to the numerous factors that are not taken into account in our analysis (§ 4.2), the parameters estimation using the APVO curves is not as efficient as the method using the static measurements. Nevertheless, the method is promising, and a diminution of the dimensions of the antennas or the introduction of the surface-lateral waves into the hybrid model are likely to increase the method accuracy and robustness.

5.4 Conclusions

The peak-to-peak amplitude of a radar pulse reflected on a thin layer is linearly influenced by the layer amplitude. But the concordance with the analytical curves is reduced due to the peak separation. Moreover, as long as only one value (the peak-to-peak amplitude) is extracted from each measurement, the method is insufficient to determine simultaneously the thickness and the permittivity of the layer, but it can help determining one parameter if the other one is known.

A spectral analysis of static measurements allows a simultaneous determination. With this method, all the frequencies present in the pulse can be exploited, and

the phase information can be used in addition to the amplitude information. The validity of the method was demonstrated on numerical tests. In particular, when the layer thickness is important, the hybrid model revealed to give a better parameters estimation than the plane wave method.

The method was then tested experimentally to determine thin air layers of different thicknesses embedded into concrete. The concordance between the experimental points (especially the phase) and the curves was far poorer than for the numerical data. This may be due to the dispersive properties of concrete, which are not accounted for in the simulations nor in the equations. Nevertheless, the parameters determination was possible with a precision of 20% on the thickness, and the permittivity was perfectly determined. The same test was performed on a thin bitumen layer instead of air. Probably due to the lower permittivity contrast, the precision in parameters determination was lower than for the air layers.

The static determination method can also be adapted to measure layers "embedded" into air. A test performed on a bitumen layer gave promising results. The precision was good, and could clearly be improved by using a wider range of thickness-to-wavelength ratios. This method is directly applicable to any layer whose both faces are in contact with air. In this case, it may be an interesting alternative to all the methods presented in § 3.3 for the permittivity determination.

Without surprise, the layer determination using CMP measurements performed at the surface has a relatively low precision. The phenomena induced by the surface testing with large offset (§ 4.2) decrease the parameters estimation precision, even when a limited angle range is considered. Without improvements, this method should not be preferred to the frequency analysis of static measurement, despite the fact that each measurements contains more information.

Conclusions and perspectives

The aim of this thesis was to investigate the possibilities of determining the properties of thin layers embedded into concrete with a commercial GPR antenna.

In the first chapter, we presented the general context of the bridge testing with GPR. We described the different pathologies that could affect concrete structures and the different non-destructives methods that can be used to detect the problems. Finally, we showed that the GPR is particularly suitable to detect layers, and we described different existing strategies for the layers determination.

In the second chapter, we presented the physical bases of the GPR waves propagation, with an emphasis on the phenomenon of wave reflection on simple interfaces and on thin layers. In this last case, we noticed that the plane wave approximation, frequently used for the thin layers characterization, could be invalid in some cases, namely when the layer is in the near field or has a low permittivity.

The third chapter was dedicated to the analysis of the radar incident signal. We determined different test configurations and a method to extract the reflection coefficient from numerical and experimental data. We also determined procedures to optimize the experimental acquisition, the signal treatment and the properties determination of the surface material.

The fourth chapter tackled the problem of the analytical estimation of the reflection coefficient APVO curves. First, the analytical methods detailed in the second chapter were confronted to the offset-dependent reflection coefficients obtained from FDTD simulations. We determined a hybrid model in 2D and 3D, allowing to approach satisfactorily the reflection coefficient amplitude and

phase by using the best method depending on the layer thickness-to-wavelength ratio. This model is valid for antennas embedded into the matrix. When the measurement is performed from the surface, additional phenomena influence the curves. By comparing the APVO curves, obtained by the model, to realistic numerical and experimental curves, we determined a signal treatment procedure for limiting the influence of those phenomena and discussed different strategies for future improvements of the method.

In the fifth and last chapter, we attempted to characterize embedded thin layers using the analytical curves described in the previous chapter. A simple method to suppress the influence of the different refracted waves consists in performing static measurements, with an angle inferior to the critical incidence. First, we performed a very simple analysis of the data, extracting only the peak-to-peak amplitude. This method showed a very good concordance with the numerical results, and a relatively good concordance with the analytical curves, for the very thin layers. But it is very limited in terms of parameters determination. To be able to simultaneously determine the thickness and the permittivity of the layer, it is necessary to perform a spectral analysis of the wave, so that all the frequency content of the pulse can be exploited. This method revealed to give good results, with a permittivity perfectly detected and an error on the thickness inferior to 20%.

Finally, we investigated the possibility to determine the layers parameters using the CMP measurements. As expected, the presence of the surface effects, in combination with the measurement noise, decreased the parameters estimation precision. Nevertheless, for most tests, the parameters could be estimated with a limited error, which is encouraging for the future developments of the method.

The methods presented in this work aim at determining the reflection coefficient of a simple interface or a thin layer. By consequence, they can only be applied practically in cases where this parameter can be isolated in the measurement. This is the case in two situations:

- When a measurement on a metallic reflector placed at the same position as the layer is possible. This reflector can be placed into the structure during its building, in the perspective of future testing, but can difficultly be introduced at the required depth for the auscultation of existing structures. On the opposite, this is always possible and relatively easy when the layer to determine is embedded into air.

- When all the other parameters influencing the measured amplitude are known or can be estimated (included the permittivity and conductivity of the first medium and the corresponding radiation pattern of the antenna). This may be easier to achieve when the antennas are situated in the far field.

The comparison of the experimental APVO curves with analytical curves leads to a fair parameters estimation for air thin layers embedded into concrete, after a fast computation. In addition to this main contribution, the thesis also gives a comprehensive description of the different phenomena affecting the thin layers detection as well as of the complexity of the signals for this type of measurements

with contact antennas and near-field measurements. Indeed, the interaction of the reflection curve with the lateral and the surface-lateral wave, the multiple reflections, the time drift of the antenna or the near-field radiation pattern are phenomena that strongly influence the measured data and impair the direct application of simple APVO curves inversion methods.

Different solutions were proposed along the different chapters to improve the proposed analytical solution. Three methods seem particularly promising to increase the precision of the estimation of the APVO curves in the case of near-field concrete testing.

The first one is the evaluation of the surface-lateral wave, whose amplitude revealed to be important and which is present for almost all the angle range that can be investigated in CMPs. The second path of improvement consists in taking into account the antenna radiation pattern in the equations. The analytical formulation of this radiation diagram may depend on many parameters, including the distance to the antenna for measurements performed in the near-field, but this analysis will be necessary in order to be able to compare rigorously the post-critical reflections on the thin layers and on the perfect reflector. Finally, a phenomenon that has been neglected but may have an influence on the results is the dispersive behaviour of concrete. This frequency dependence of the properties may be taken into account by the determination of the Jonscher parameters. In this case, the layer conductivity will be determined by the method, in addition to its permittivity.

Additional developments could also be implemented in the model, so that it could be used in more situations. First, the equations developed for a layer embedded into a matrix, could be developed for the cases where the materials above and under the layer are different. If the permittivity of the second layer is superior to the matrix permittivity, this should not pose any problem, but it will add an additional parameter to determine (ε'_{r3}). On the opposite, if the second medium has a lower permittivity, a lateral wave is susceptible to propagate at the interface, which will considerably complicate the equations.

The second method development that we recommend would be to compare the measurements for each offset to the first trace in the same APVO curve. With this method, the parameters estimation could be performed in many more cases, because it frees the layer determination from the necessity of a comparison with a perfect reflection. This method requires a good estimation of all the factors influencing the amplitude, and especially the radiation pattern and the surface conductivity.

A last method development would consist in performing CMPs in the TM mode, in addition to the TE mode. The energy transmitted in this mode is much lower, but the evolution of the reflection coefficient is much more variable with the incident angle. For this reason, measurements performed in the transverse magnetic mode are likely to allow improving the current measurements precision.

The introduction of all these parameters into the equations will increase the computational time. But the introduction of an inversion method, allowing to test only selected values instead of spanning the whole parameter space is likely to reduce drastically the computation time.

After being implemented with all these improvements, it is likely that the analytical model will be able to determine the layer properties with a very good precision from experimental measurements. Nevertheless, under a few conditions, the method proposed in this work can be applied unaltered for an estimation of the layer properties. Due to its fast computation, this analytical approach can also be used as a first step of a more sophisticated method. Indeed, it could be part of the data pre-treatment phase of a more comprehensive method, like modelling or full waveform inversion. The investigated parameters would then be roughly estimated by comparison to the analytical curves, in order to reduce the space of parameters to investigate with the high precision method.

The applicability of this method on real structures, in the framework of a nondestructive inspection campaign, will depend on the field conditions. It is expected that a thin layer embedded into a structure presenting a large humidity gradient, high chloride infiltrations or a dense surface reinforcement will not be possible to characterize. Nevertheless, in good field conditions, the method presented in this thesis can contribute to the quantitative characterization of layered structures. For instance, it can help to the determination of the composition of a road or bridge pavement or to the estimation of the thickness of an insulation layer inside a wall or a soil.

References

1. OECD, *Infrastructure to 2030 : telecom, land transport, water and electricity*. 2006. OECD Publishing.
2. Hammad, A., Yan, J. and Mostofi, B. *Recent development of bridge management systems in Canada*. in *Annual Conference and Exhibition of the Transportation Association of Canada: Transportation-An Economic Enabler (Les Transports: Un Levier Economique)*. 2007.
3. Herrmann, A.W. *ASCE 2013 Report Card for Americas Infrastructure*. in *IABSE Symposium Report*. 2013. International Association for Bridge and Structural Engineering.
4. Caby, V. and Piessevaux, E. *Gestion et classification des ouvrages d'art* in *Congrès belge de la route*. 2009. Gand.
5. Daerden, M., *La gestion des ouvrages d'art en Région wallonne*, Parlement Wallon. 2007.
6. Fédération Inter-Environnement Wallonie, *Réseau routier de Wallonie, Document de réflexion*. 2010: Namur. p. 6.
7. Cour des comptes, *L'entretien des routes et autoroutes en Wallonie – Programmation, financement et contrôle de la qualité des travaux*. 2012: Bruxelles.
8. Mommer, P., Dondonne, E. and Demars, P., *Degradation des dalles de tablier de ponts en Région Wallonne. Etude d'une pathologie complexe.* Revue scientifique des ISILF, 2004(18).
9. Gilles, P. and Dondonne, E. *Le phénomène de pourrissement des dalles de tablier de ponts*. in *Congrès belge de la Route*. 2009. Gent.
10. Gilles, P. and Toussaint, P., *Les besoins en CND d'un gestionnaire d'ouvrages d'art*, in *Diagnobéton*. 2007: Aix en provence.
11. Lataste, J.-F. *Contrôle non destructif des ouvrages d'art : un point de vue français sur l'organisation, les besoins et les développements en cours*. in *Progression de la recherche québécoise sur les ouvrages d'art*. 2012. Québec.

12. Gagné, R., *GCI 714 - Durabilité et réparations du béton*. [Notes de cours] 2009 [cited 2009, 10 février]; Available from: http://www.civil.usherbrooke.ca/cours/gci714/.

13. Carino, N.J., *Nondestructive Test Methods to Evaluate Concrete Structures*, in *Sixth CANMET/ACI International Conference on Durability of Concrete*. 2003: Thessaloniki.

14. Raupach, M., *Concrete repair according to the new European Standard EN 1504*, in *Concrete Repair, Rehabilitation and Retrofitting*, M. Alexander, et al., Editors. 2006, Taylor & Francis Group: Cap Town. p. 6-8.

15. Emmons, P.H. and Emmons, B.W., eds. *Concrete repair and maintenance illustrated : problem analysis, repair strategy, techniques*. 1993, R.S. Means Co.: Kingston, MA. 295.

16. Mays, G.C., Lees, T.P., Baker, A.F., Tabor, L.J. and Keer, J.G., *Durability of Concrete Structures*, ed. G. Mays. 1992, London. E & FN Spon. 270.

17. INDOT, *Certified Technician Program Training Manual for Bridge Construction and Deck Repair*. 2007 2008 [cited 2009, 16 march]; Available from: http://www.in.gov/indot/3092.htm.

18. Demars, P., Gilles, P., Dondonne, E., Lefebvre, G., Darimont, A., Lorenzi, G., Henriet, G. and Marion, A.-M. *The degradation of the bridge decks slabs in Belgium mainly involves alkali-aggregate reactions*. in *ICAAR*. 2008. Trondheim, Norway.

19. Courard, L., Van der Wielen, A. and Darimont, A., *From defects to causes: pathology of concrete and investigation methods.* Startegjia Izvedbe Sanacij Objektov, 2010.

20. Pigeon, M., *La durabilité au gel du béton.* Materials and Structures, 1989. **22**(1): p. 3-14.

21. Lacroix, R. and Calgaro, J.A. *Pathologie et évaluation des ponts existants*. Techniques de l'ingénieur, 1999.

22. Gilles, P., *Investigation et réparation des ouvrages atteints de pourrissement de dalles de tablier de ponts*, in *Diagno-béton*. 2004: Montréal.

23. Courard, L., Garbacz, A. and Piotrowski, T., *Some theoretical and practical considerations about surface preparation of concrete and adhesion of repair systems*, in *16. Slovenski kilikvij o betonih*. 2009: Ljubljana.

24. Courard, L. and Bissonnette, B., *Quality assurance in repairing industrial floors: parameters and recommendations.* Moznot Pocenitive Izvajanja Betonarskih Del, 2011.

25. Maierhofer, C., Reinhardt, H.W. and Dobmann, G., *Non-Destructive Evaluation of Reinforced Concrete Structures: Non Destructive Testing Methods*. 2010. CRC Press.

26. International Atomic Energy Agency, *Guidebook on non-destructive testing of concrete structures*. 2002: Vienna. p. 242.

27. Courard, L., Garbacz, A. and Wolff, L., *Chapter 4: Evaluation and quality assessment*, in *RILEM TC 184-IFE "Industrial Floors"*, P. Seidler, Editor. 2006, Rilem publications: Bagneux. p. 59-89.

28. Taffe, A., Feistkorn, S. and Kind, T. *Modern NDT-CE methods*. in *International Conference on Concrete Repair, Rehabillitation and Retrofitting*. 2012. Cape Town.

29. Sabt-Blanquet, C., *Les ondes électromagnétiques*, in *Synophysique*. 2006.

30. Centre de recherches routières, *Code de bonne pratique pour la conception, la mise en œuvre et l'entretien des complexes étanchéité-revêtement de ponts à tablier en béton (R83/12)*. 2011. p. 326.

31. *Detection by infrared thermography of the heat signature of diseases and defects in concrete structures of civil engineering*. [cited 2013, December 20]; Available from: http://www.reseaulieu.be/fr/licensing-opportunities/detection-infrared-thermography-heat-signature-diseases-and-defects-concrete.

32. Rhazi, J., *NDT in civil engineering: the case of concrete bridge decks.* CSNDT JOURNAL, 2000. **21**(5): p. 18-25.

33. Developing Innovative Systems for Reinforced Masonry Walls (DISWall), *Review on the NDTs for inspecting masonry walls* 2006, Universidade do Minho, Università de Padova.

34. Andrade, C. and Alonso, C., *Test methods for on-site corrosion rate measurement of steel reinforcement in concrete by means of the polarization resistance method.* Materials and Structures, 2004. **37**(9): p. 623-643.

35. Sadowski, Ł., *New non-destructive method for linear polarisation resistance corrosion rate measurement.* Archives of Civil and Mechanical Engineering, 2010. **10**(2): p. 109-116.

36. Sansalone, M. and Street, W.B., *The Impact Echo Method*. 1998 [cited 2009, 10 May]; Available from: http://www.ndt.net/article/0298/streett/streett.htm.

37. Blitz, J. and Simpson, G., *Ultrasonic methods of non-destructive testing*. Vol. 2. 1996. Springer.

38. Sansalone, M.J. and Street, W.B., *Impact-echo. Nondestructive evaluation of concrete and masonry*. 1997, Jersey Shore. Bulbrier Press.

39. Bungey, J.H., *Sub-surface radar testing of concrete: a review.* Construction and Building materials, 2004. **18**(1): p. 1-8.

40. Al-Qadi, I.L. and Lahouar, S., *Measuring layer thicknesses with GPR - Theory to practice.* Construction and Building materials, 2005. **19**(10): p. 763-772.

41. Hugenschmidt, J. and Loser, R., *Detection of chlorides and moisture in concrete structures with ground penetrating radar.* Materials and Structures/Materiaux et Constructions, 2008. **41**(4): p. 785-792.

42. Balayssac, J.P., Kringkaï, V., Sbartaï, M., Klysz, G., Laurens, S. and Arliguie, G., *Contribution au développement du radar pour la caractérisation non destructive du béton*, in *25e rencontres de l'AUGC*. 2007, LMDC: Bordeaux.

43. Dérobert, X., Iaquinta, J., Klysz, G. and Balayssac, J.-P., *Use of capacitive and GPR techniques for the non-destructive evaluation of cover concrete.* NDT & E International, 2008. **41**(1): p. 44-52.

44. Viriyametanont, K., *Reconnaissance physique et géométrique d'éléments en béton armé par radar et RNA*. LMDC. Ph.D. Thesis. 2008, INSA: Toulouse.

45. Hugenschmidt, J., *Geophysics and non-destructive testing for transport infrastructure, with special emphasis on ground penetrating radar*. 2010, Diss., Eidgenössische Technische Hochschule ETH Zürich, Nr. 19225, 2010.

46. Saarenketo, T. and Scullion, T., *Road evaluation with ground penetrating radar.* Journal of Applied Geophysics, 2000. **43**(2–4): p. 119-138.

47. Loizos, A. and Plati, C., *Accuracy of pavement thicknesses estimation using different ground penetrating radar analysis approaches.* NDT & E International, 2007. **40**(2): p. 147-157.

48. Pérez-Gracia, V., García García, F. and Rodriguez Abad, I., *GPR evaluation of the damage found in the reinforced concrete base of a block of flats: A case study.* NDT & E International, 2008. **41**(5): p. 341-353.

49. SPW, *Le cahier des charges-type RW 99*. 2004: Namur.

50. Courard, L., *Maintenance, entretien et réparation des constructions en béton*. Notes de cours, ed. CdC. 2008.

51. Rayleigh, J.W.S., *The Theory of Sound (2nd edn), Vol. 2*. 1945. Dover Publications, New York.

52. Widess, M.B., *How thin is a thin bed?* Geophysics, 1973. **38**: p. 1176-1176.

53. Cai, J. and McMechan, G., *Ray-based synthesis of bistatic ground-penetrating radar profiles.* Geophysics, 1995. **60**(1): p. 87-96.

54. Annan, A.P., *Ground-Penetrating Radar*, in *Near-Surface Geophysics Part 1: Concepts and Fundamentals*, D.K. Butler, Editor. 2005, Society of Exploration Geophysicists. p. 357 - 438.

55. Bradford, J.H. and Deeds, J.C., *Ground-penetrating radar theory and application of thin-bed offset-dependent reflectivity.* Geophysics, 2006. **71**: p. K47-K57.

56. Grégoire, C. and Hollender, F., *Discontinuity characterization by the inversion of the spectral content of ground-penetrating radar (GPR) reflections - Application of the Jonscher model.* Geophysics, 2004. **69**(6): p. 1414-1424.

57. Jeannin, M., *Etude des processus d'instabilités des versants rocheux par prospection géophysique-Apport du radar géologique*. Ph.D. Thesis. 2005, Université Joseph-Fourier-Grenoble I.

58. Deparis, J. and Garambois, S., *On the use of dispersive APVO GPR curves for thin-bed properties estimation: Theory and application to fracture characterization.* Geophysics, 2009. **74**(1): p. J1-J12.

59. Deparis, J., *Etude des éboulements rocheux par méthodes géophysiques*. Ph.D. Thesis. 2007, Université Joseph-Fourier-Grenoble I.

60. Lambot, S., Slob, E.C., van den Bosch, I., Stockbroeckx, B. and Vanclooster, M., *Modeling of ground-penetrating radar for accurate characterization of subsurface electric properties.* Geoscience and Remote Sensing, IEEE Transactions on, 2004. **42**(11): p. 2555-2568.

61. Kalogeropoulos, A., Van der Kruk, J., Hugenschmidt, J., Busch, S. and Merz, K., *Chlorides and moisture assessment in concrete by GPR full waveform inversion.* Near Surface Geophysics, 2011. **9**(3): p. 277-285.

62. Patriarca, C., Lambot, S., Mahmoudzadeh, M., Minet, J. and Slob, E., *Reconstruction of sub-wavelength fractures and physical properties of*

masonry media using full-waveform inversion of proximal penetrating radar. Journal of Applied Geophysics, 2011. **74**(1): p. 26-37.

63. Busch, S., van der Kruk, J., Bikowski, J. and Vereecken, H., *Quantitative conductivity and permittivity estimation using full-waveform inversion of on-ground GPR data.* Geophysics, 2012. **77**(6): p. H79-H91.

64. Lambot, S., Tran, A.P. and André, F. *Near-field modeling of radar antennas for wave propagation in layered media: when models represent reality*. in *14th International Conference on Ground Penetrating Radar (GPR)*. 2012. IEEE.

65. Reynolds, J.M., *An Introdution to Applied and Environnemental Geophysics*. 1997, Chichester. Jonh Wiley & Sons.

66. Martín, R.G., *Electromagnetic field theory for physicists and engineers: Fundamentals and applications*. [Electronic course] 2010 [cited 2012, 20/08]; Available from: http://maxwell.ugr.es/rgomez/.

67. Strange, A.D., *Robust thin layer coal thickness estimation using ground penetrating radar*. School of Enineering Systems. Ph.D. Thesis. 2007, Queensland University of Technology.

68. Soutsos, M.N., Bungey, J.H., Millard, S.G., Shaw, M.R. and Patterson, A., *Dielectric properties of concrete and their influence on radar testing.* NDT & E International, 2001. **34**(6): p. 419-425.

69. Bourdi, T., Rhazi, J.E., Boone, F. and Ballivy, G., *Application of Jonscher model for the characterization of the dielectric permittivity of concrete.* Journal of Physics D-Applied Physics, 2008. **41**(20).

70. Annan, A.P., *Electromagnetic principles of Ground Penetrating Radar*, in *Ground penetrating radar theory and applications*, H.M. Jol, Editor. 2009, Elsevier. p. 1-38.

71. Knight, R., *Ground penetrating radar for environmental applications.* Annual Review of Earth and Planetary Sciences, 2001. **29**(1): p. 229-255.

72. Bennett, S., Jones, O.C., Sené, M. and Phillips, G.F., *Electricity and Magnetism*. 2009 [cited 2009, May 10]; National Physical Laboratory. Available from: http://www.kayelaby.npl.co.uk/general_physics/#2_6.

73. Saarenketo, T., *Measuring electromagnetic properties of asphalt for pavement quality control and defect mapping*. 2001, Roadscanners.

74. Read, J. and Whiteoak, D., *The Shell bitumen handbook*. 2003. Thomas Telford.

75. Giannopoulos, A., *Modelling ground penetrating radar by GprMax.* Construction and Building materials, 2005. **19**(10): p. 755-762.

76. Annan, A., *Ground penetrating radar workshop notes.* Sensors and Software Inc., Mississauga, Ontario, 2001.

77. Irving, J.D. and Knight, R.J., *Removal of wavelet dispersion from ground-penetrating radar data.* Geophysics, 2003. **68**(3): p. 960-970.

78. Shevgaonkar, R., *Electromagnetic waves*. 2005. Tata McGraw-Hill Education.

79. Chapman, C., *Basic wave propagation*, in *Fundamentals of seismic wave propagation*. 2004, Cambridge University Press.

80. de Fornel, F., *Evanescent waves: from Newtonian optics to atomic optics*. Vol. 73. 2001. Springer.

81. White, J.C., *Development and application of the phase-screen seismic modelling code*. 2009, Durham University.

82. Červený, V. and Hron, F., *Reflection coefficients for spherical waves.* Studia Geophysica et Geodaetica, 1961. **5**(2): p. 122-132.

83. Brekhovskikh, L.M. and Beyer, R.T., *Waves in layered media*. Vol. 4. 1960. Academic press New York.

84. Pérez-Gracia, V., González-Drigo, R. and Di Capua, D., *Horizontal resolution in a non-destructive shallow GPR survey: An experimental evaluation.* NDT & E International, 2008. **41**(8): p. 611-620.

85. Van der Wielen, A., Courard, L. and Nguyen, F., *Static Detection of Thin Layers into Concrete with Ground Penetrating Radar.* Restoration of Buildings and Monuments = Bauinstandsetzen und Baudenkmalpflege, 2012. **18**(3/4): p. 247-254.

86. van der Kruk, J., Streich, R. and Green, A.G., *Properties of surface waveguides derived from separate and joint inversion of dispersive TE and TM GPR data.* Geophysics, 2006. **71**(1): p. K19-K29.

87. Taflove, A. and Hagness, S.C., *Computational electrodynamics : the finite-difference time-domain method*. Third ed. 2005. Norwood : Artech House, Inc. 1006.

88. Pernet, S., Ferrieres, X. and Cohen, G. *An original finite element method to solve Maxwell's equations in time domain*. in *Proceedings of EMC Zurich*. 2003.

89. Yee, K., *Numerical solution of initial boundary value problems involving Maxwell's equations in isotropic media.* IEEE Transactions on Antennas and Propagation, 1966. **14**(3): p. 302-307.

90. Courant, R., Friedrichs, K. and Lewy, H., *On the partial difference equations of mathematical physics.* IBM Journal of Research and Development, 1967. **11**(2): p. 215-234.

91. Mur, G., *Absorbing boundary conditions for the finite-difference approximation of the time-domain electromagnetic-field equations.* IEEE Transactions on Electromagnetic Compatibility, 1981(4): p. 377-382.

92. Berenger, J.P., *A perfectly matched layer for the absorption of electromagnetic waves.* Journal of computational physics, 1994. **114**(2): p. 185-200.

93. Modave, A., *Absorbing Layers for Wave-Like Time-Dependent Problems. Design, Discretization and Optimization*. Ph.D. Thesis. 2013, ULg.

94. Giannopoulos, A., *GprMax 2D/3D: User's Manual*. 2005.

95. ASTM, *Standard test method for evaluating asphalt-covered concrete bridge decks using ground penetrating radar*. 2005.

96. Daniels, D.J., *Ground penetrating radar, 2nd Edition, Volume 1*. 2004, London. Institution of electrical engineers.

97. O'Haver, T., *An introduction to signal processing with applications in Chemical Analysis*. [Illustrated essay] 2012 9 july 2012 [cited 2012, 16 july]; Available from: http://terpconnect.umd.edu/~toh/spectrum/TOC.html.

98. Rangel, D., Carreón, D., Cerca, M. and Méndez, E., *Valuation of ground penetrating radar for the record of structures in fluvio lacustrine soils.* Journal of Applied Research and Technology, 2002. **1**(01): p. 85-93.

99. Smith, J.O., *Physical Audio Signal Processing*. 2010. W3K Publishing.

100. Belli, K., Rappaport, C.M., Zhan, H. and Wadia-Fascetti, S., *Effectiveness of 2-D and 2.5-D FDTD Ground-Penetrating Radar Modeling for Bridge-Deck Deterioration Evaluated by 3-D FDTD.* IEEE Transactions on Geoscience and Remote Sensing, 2009. **47**(11): p. 3656-3663.

101. Rial, F., Lorenzo, H., Pereira, M. and Armesto, J., *Waveform Analysis of UWB GPR Antennas.* Sensors, 2009. **9**(3): p. 1454-1470.

102. *Electronic warfare and radar systems engineering handbook*, N.A.W. Center and N.A.S. Command, Editors. 1999. p. 299.

103. Grimm, R.E., Heggy, E., Clifford, S., Dinwiddie, C., McGinnis, R. and Farrell, D., *Absorption and scattering in ground-penetrating radar: Analysis of the Bishop Tuff.* Journal of Geophysical Research: Planets (1991–2012), 2006. **111**(E6).

104. Millard, S.G., Shaari, A. and Bungey, J.H., *Field pattern characteristics of GPR antennas.* NDT & E International, 2002. **35**(7): p. 473-482.

105. Radzevicius, S.J. and Daniels, J.J., *Ground penetrating radar polarization and scattering from cylinders.* Journal of Applied Geophysics, 2000. **45**(2): p. 111-125.

106. Engheta, N., Papas, C. and Elachi, C., *Radiation patterns of interfacial dipole antennas.* Radio Science, 1982. **17**(6): p. 1557-1566.

107. Smith, G., *Directive properties of antennas for transmission into a material half-space.* IEEE Transactions on Antennas and Propagation, 1984. **32**(3): p. 232-246.

108. Jiao, Y.R., McMechan, G.A. and Pettinelli, E., *In situ 2-D and 3-D measurements of radiation patterns of half-wave dipole GPR antennas.* Journal of Applied Geophysics, 2000. **43**(1): p. 69-89.

109. Radzevicius, S.J., Chen, C.C., Peters, L. and Daniels, J.J., *Near-field dipole radiation dynamics through FDTD modeling.* Journal of Applied Geophysics, 2003. **52**(2-3): p. 75-91.

110. Valle, S., Zanzi, L., Sgheiz, M., Lenzi, G. and Friborg, J., *Ground penetrating radar antennas: theoretical and experimental directivity functions.* Ieee Transactions on Geoscience and Remote Sensing, 2001. **39**(4): p. 749-758.

111. Lampe, B., *Finite-Difference Time-Domain Modeling of Ground-Penetrating Radar Antenna Systems*. Doctor of Natural Sciences. 2003, Swiss Federal Institute of Technology: Zurich. 162.

112. Huisman, J., Hubbard, S., Redman, J. and Annan, A., *Measuring Soil Water Content with Ground Penetrating Radar A Review.* Vadose Zone Journal, 2003. **2**(4): p. 476-491.

113. Klysz, G., Balayssac, J.P. and Ferrières, X., *Evaluation of dielectric properties of concrete by a numerical FDTD model of a GPR coupled antenna--Parametric study.* NDT & E International, 2008. **41**(8): p. 621-631.

114. Van der Wielen, A., *Non-destructive methods for the detection of delaminations in concrete bridge decks*. ArGEnCo. Master thesis. 2009, University of Liege: Liege. 109.

115. Ferrieres, X., Klysz, G., Mazet, P. and Balayssac, J.P., *Evaluation of the concrete electromagnetics properties by using radar measurements in a context of building sustainability*. Computer Physics Communications, 2009. **180**(8): p. 1277-1281.

116. Van der Wielen, A., Nguyen, F. and Courard, L. *Utilisation du GPR pour la détection des discontinuités dans les tabliers de ponts*. in *11e édition des Journées Scientifiques du (RF)2B*. 2010. Quebec.

117. Van der Wielen, A., Courard, L. and Nguyen, F. *GPR Limits for Thin Layers in Concrete Detection: Numerical and Experimental Evaluation*. The Electromagnetics Academy.

118. Sambridge, M., *Geophysical inversion with a neighbourhood algorithm—II. Appraising the ensemble*. Geophysical Journal International, 1999. **138**(3): p. 727-746.

119. Sambridge, M., *Geophysical inversion with a neighbourhood algorithm—I. Searching a parameter space*. Geophysical Journal International, 1999. **138**(2): p. 479-494.

120. Kemna, A., *Tomographic inversion of complex resistivity*. Ruhr-Universität Bochum, 2000.

121. Debye, P.J.W., *Polar molecules*. 1929. Dover New York.

122. Cassidy, N.J. and Harry, M.J., *Chapter 2 - Electrical and Magnetic Properties of Rocks, Soils and Fluids*, in *Ground Penetrating Radar Theory and Applications*. 2009, Elsevier: Amsterdam. p. 41-72.

123. Cole, K.S. and Cole, R.H., *Dispersion and absorption in dielectrics I. Alternating current characteristics*. The Journal of Chemical Physics, 1941. **9**(4): p. 341-351.

124. Jonscher, A.K., *The universal dielectric response*. Nature, 1977. **267**: p. 673-679.

125. Bano, M., *Modelling of GPR waves for lossy media obeying a complex power law of frequency for dielectric permittivity*. Geophysical Prospecting, 2004. **52**(1): p. 11-26.

126. Chahine, K., Ihamouten, A., Baltazart, V., Villain, G. and Dérobert, X. *On the variants of Jonscher's model for the electromagnetic characterization of concrete*. in *13th International Conference on Ground Penetrating Radar*. 2010.

127. Hollender, F. and Tillard, S., *Modeling ground-penetrating radar wave propagation and reflection with the Jonscher parameterization*. Geophysics, 1998. **63**(6): p. 1933-1942.

Appendices

Appendix 1. *Theoretical equations of the characteristic waves in CMPs*

The equation of all the waves appearing in the radargram obtained with the CMP acquisition mode (Figure 175) can be calculated.

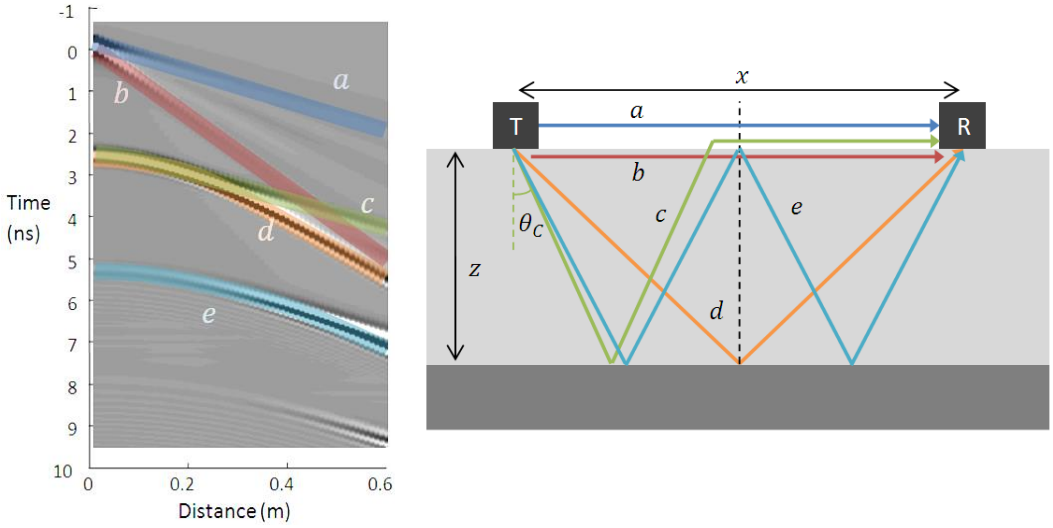

Figure 175 : Typical radargram obtained with CMP.

The equations of the time of arrival of the waves a and b, which are respectively the direct wave in the air and in the material, have already been developed in § 2.1.3.2 :

$$t_a = t_0 + \frac{x}{c} \tag{147}$$

$$t_b = t_0 + \frac{x}{v} \tag{148}$$

Wave c, the critically refracted wave, travels into the ground with an incident angle equal to θ_c, the critical angle, which is the incident angle corresponding to an horizontal path into the air. At every interface, refraction laws stipulate that we have:

$$\frac{1}{v_1} sin\,\theta_1 = \frac{1}{v_2} sin\,\theta_2 \tag{149}$$

In this case, material 1 is concrete and material 2 is air, thus if $\theta_1 = \theta_c$, θ_2 should be equal to 90°. It gives us the value of θ_c:

$$\frac{sin\,\theta_c}{v} = \frac{sin\,90°}{c} = \frac{1}{c} \tag{150}$$

$$\theta_c = arcsin\frac{v}{c} \tag{151}$$

If the offset is equal to $2z\tan\theta_c$, the critically refracted wave is coincident with the first reflected wave d. If the offset x is superior to this value, the time of travel of the wave is equal to the constant time of travel through the concrete plus the time of travel in the air:

$$t_c = t_0 + \frac{2z}{v\,cos\,\theta_c} + \frac{x - 2z\,tan\,\theta_c}{c} \tag{152}$$

First reflected wave d is a function of the offset and the speed into the material. Its time of arrival is:

$$t_d = t_0 + 2\frac{\sqrt{z^2 + \frac{x^2}{4}}}{v} \tag{153}$$

Finally, second reflected wave e has exactly the same parameters than the first reflected wave. Its measurement time is

$$t_e = t_0 + 4\frac{\sqrt{z^2 + \frac{x^2}{16}}}{v} \tag{154}$$

Of course, an infinite number of reflection multiples on the first interface can be represented in the same way. Anyway, because of the attenuation, the number of visible multiples is quite limited.

Appendix 2. *Mathematical models for the estimation of the frequency-dependent permittivity*

As explained in § 2.1.6, the dielectric properties of a material are frequency dependent. Under some conditions (in the GPR plateau), this dependence may be neglected. But when this is not possible, different mathematical models have been elaborated to take into account the evolution of the properties with the frequency.

Debye model

Debye model [121] is valid for materials such as water, that present a variation between a low frequency permittivity and a high frequency permittivity, as well as a relaxation time.

$$\varepsilon'(\omega) = \varepsilon_\infty + \frac{\varepsilon_S - \varepsilon_\infty}{1 + \omega^2\tau^2} \tag{155}$$

$$\varepsilon''(\omega) = (\varepsilon_S - \varepsilon_\infty)\frac{\omega\tau}{1 + \omega^2\tau^2} \tag{156}$$

In (155) and (156), ε_S is the static, or very low frequency permittivity, corresponding to a good alignment between the electromagnetic field and the dipolar molecules. On the opposite, ε_∞ is the optical, or very high frequency, permittivity: it corresponds to a point at which the dipoles cannot align on the field, which changes at a high frequency. Instead, they are agitated, creating high heat dissipation. The permittivity relaxation time τ corresponds to the time necessary for the dipoles to align on the field. When the excitation period is equal to τ, the dipoles are almost always on phase opposition to the field and the imaginary component is maximum.

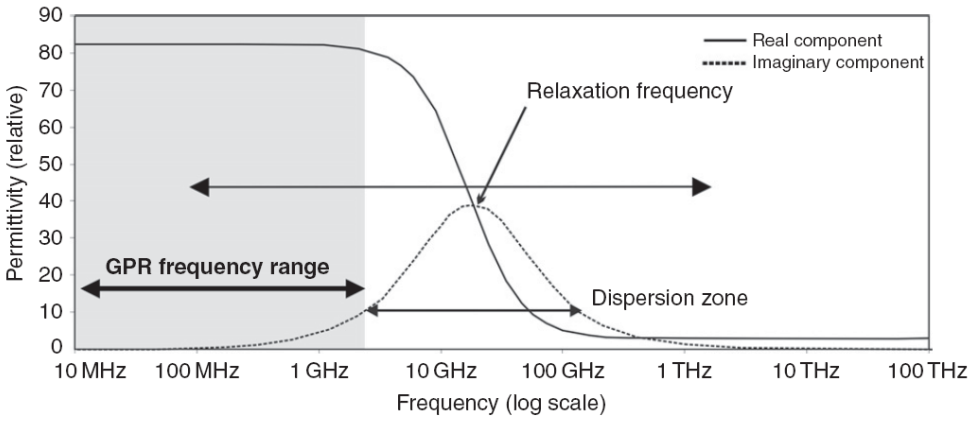

Figure 176 : Permittivity spectrum of free, pure water at room temperature illustrating the single Debye relaxation mechanism at approximately 19 GHz [122].

Cole-Cole model

The Debye formula is very well describing the behaviour of free polar molecules, but often fails to describe the behaviour of mixed materials, in which different materials can have different relaxation times, and molecular collisions can modify the global response. Cole and Cole [123] improved the Debye formula by incorporating an experimental broadening factor α. The complex dielectric permittivity is then equal to:

$$\varepsilon(\omega) = \varepsilon_\infty + \frac{\varepsilon_S - \varepsilon_\infty}{1 + (j\omega\tau)^{1-\alpha}} \tag{157}$$

Studies showed that for typical underground materials, α is comprised between 0 (the Cole-Cole formula is then equal to the Debye relationship) and 0.7 [122] .

Jonscher model

The Debye and Cole-Cole models cannot describe phenomena as the charge carrier relaxation phenomenon; they give unsatisfactory results to describe the high frequency part of dipolar relaxation [56]. Jonscher [124] introduced a more global model which uses the exponential dependence of the imaginary and real parts of the dielectric permittivity for large frequencies, with the exponent ω^{n-1} [125]. In his theory, the complex dielectric permittivity is given as a function of the dielectric susceptibility $\chi_e = \varepsilon_r - 1$.

$$\varepsilon_e(\omega) = \varepsilon_\infty + \varepsilon_0\chi_e(\omega) - \frac{i\sigma_{dc}}{\omega} \tag{158}$$

In equation (158):

- $\varepsilon_\infty(\mathrm{F\,m^{-1}})$ is the limiting high-frequency value of the real part of the effective permittivity. It is constant and real and describes the

mechanisms of polarization that rapidly respond to the application of an electric field;

- σ_{dc} is dc (direct current) conductivity (real and constant);

- χ_e is the sum of various susceptibilities related to polarizations responding more slowly. It is expressed by the relationship called the Jonscher universal dielectric response.

$$\chi_e(\omega) = \chi_r \left(\frac{\omega}{\omega_r}\right)^{n-1} \left[1 - i\cot\left(\frac{n\pi}{2}\right)\right] \quad (159)$$

In (159):

- n is an empirical parameter without dimension that characterizes the change in amplitude as a function of frequency. It varies from 0 for materials with high dielectric loss to 1 for material without dielectric losses;

- χ_r is the real part of the susceptibility at the reference frequency;

- ω_r is a reference frequency, arbitrarily chosen.

The complete Jonscher formulation counts four unknowns: ε_∞, σ_{dc}, n and χ_r. The efficiency of this model for the concrete has been assessed in different papers, for different water contents and aggregate sizes. Different simplification assumptions can be used to reduce the number of unknowns or to reduce the computation time in simulations [125, 126].

A classic way to reduce the number of unknown for high frequency tests is simply to neglect the ratio σ_{dc}/ω, which decreases with the frequency [69, 126, 127]. Then, the effective dielectric permittivity can be written:

$$\varepsilon_e(\omega) = \varepsilon_\infty + \varepsilon_0\chi_r \left(\frac{\omega}{\omega_r}\right)^{n-1} \left[1 - i\cot\left(\frac{n\pi}{2}\right)\right] \quad (160)$$

The complete Jonscher formulation and different approximations with two and three unknowns were compared by Chahine [126] for different concretes and water contents. They showed that the complete formulation (158) gave the best results, but that the three unknowns approximation (160) was quite close to the experimental results in most cases.

Appendix 3. *Reflection coefficients in the TM mode*

In the transverse magnetic mode, the reflection coefficient for magnetic waves is given by:

$$R_{TM} = \frac{Z_1 \cos\theta_1 - Z_2 \cos\theta_2}{Z_1 \cos\theta_1 + Z_2 \cos\theta_2} \tag{161}$$

In this equations, Z_1 and Z_2 are the respective impedances of the two layers and θ_1 and θ_2 are the respective inclinations of the wave. If the medium is lossless, this equation can be expressed in function of the dielectric permittivities of the media ε'_{r1} and ε'_{r2}, using (46):

$$R_{TM} = \frac{\sqrt{\varepsilon'_{r2}} \cos\theta_1 - \sqrt{\varepsilon'_{r1}} \cos\theta_2}{\sqrt{\varepsilon'_{r2}} \cos\theta_1 + \sqrt{\varepsilon'_{r1}} \cos\theta_2} \tag{162}$$

$$R_{TM,\perp} = \frac{\sqrt{\varepsilon'_{r2}} - \sqrt{\varepsilon'_{r1}}}{\sqrt{\varepsilon'_{r2}} + \sqrt{\varepsilon'_{r1}}} = -R_{TE,\perp} \tag{163}$$

For a perpendicular incidence, the reflection coefficient will be the opposite of the TE reflection coefficient. When the incident angle grows, the behaviour is different from the TE because there is an incident angle (called the Brewster's angle) for which the reflection coefficient is null. For superior angles, the reflection coefficient keeps decreasing to -1.

Using the relationships (52) and (53), equation (162) becomes:

$$
\begin{aligned}
R_{TM} &= \frac{\sqrt{\varepsilon'_{r2}}\cos\theta_1 - \sqrt{\varepsilon'_{r1}}\cos\theta_2}{\sqrt{\varepsilon'_{r2}}\cos\theta_1 + \sqrt{\varepsilon'_{r1}}\cos\theta_2} \\
&= \frac{\cos\theta_1 - \frac{\sqrt{\varepsilon'_{r1}}}{\sqrt{\varepsilon'_{r2}}}\cos\theta_2}{\cos\theta_1 + \frac{\sqrt{\varepsilon'_{r2}}}{\sqrt{\varepsilon'_{r1}}}\cos\theta_2} \\
&= \frac{\cos\theta_1 - \frac{\sqrt{\varepsilon'_{r1}}}{\sqrt{\varepsilon'_{r2}}}\sqrt{1 - \frac{\varepsilon'_{r1}}{\varepsilon'_{r2}}\sin^2\theta_1}}{\cos\theta_1 + \frac{\sqrt{\varepsilon'_{r1}}}{\sqrt{\varepsilon'_{r2}}}\sqrt{1 - \frac{\varepsilon'_{r1}}{\varepsilon'_{r2}}\sin^2\theta_1}} \\
&= \frac{\cos\theta_1 - \sqrt{\frac{\varepsilon'_{r1}}{\varepsilon'_{r2}}\left(1 - \frac{\varepsilon'_{r1}}{\varepsilon'_{r2}}\sin^2\theta_1\right)}}{\cos\theta_1 + \sqrt{\frac{\varepsilon'_{r1}}{\varepsilon'_{r2}}\left(1 - \frac{\varepsilon'_{r1}}{\varepsilon'_{r2}}\sin^2\theta_1\right)}}
\end{aligned}
\tag{164}
$$

In some specific acquisition configurations, it is useful to estimate the reflection coefficient of the electric field in the TM plane, or the magnetic field in the TE plane. They are simply linked by the relationship [54]:

$$
R_{TM}^{E} = -R_{TM}^{H} \tag{165}
$$

Appendix 4. *Adaptation of the lateral wave equations for 2D propagation*

The main difference between 2D and 3D propagation is the geometric spreading. While 3D waves amplitudes decrease proportionally to the distance, 2D waves decrease with the square root of the distance, and are then less attenuated (§ 2.1.7.3).

The reflection coefficient (to the restrictive meaning of the term), is not affected by this attenuation difference: the same proportion of the energy is reflected at the interface, even if this energy is higher in 2D case. For this reason, equations (59)-(66) remain valid in two dimensions.

The difference appears when we consider the lateral wave. Indeed, the wave reaches the interface has a different amplitude. Then it will attenuate less into the layer, due to the fact that in 2D, lateral waves travel along a 1D interface and are not submitted to circular spreading into the interface plane. Then, it will interact with a reflected wave less attenuated as well. In every case, the 3D attenuation factor $1/x$ will have to be replaced by a 2D attenuation factor $1/\sqrt{x}$, which corresponds to multiply each equation by $\sqrt{x}$.

For incident angles superior to the critical angle, the field of the lateral wave (67) becomes then:

$$E_{lat,3D} = \frac{2in}{k_1(1-n^2)\sqrt{x}\ {L_2}^{3/2}}\ e^{i(k_1 L_{cr}+k_2 L_2)}\ F(\eta) \tag{166}$$

$$\begin{aligned} E_{lat,2D} &= \sqrt{L_{1,crit}}\ \frac{2in}{k_1(1-n^2)\sqrt{x_{crit}}\ {L_2}^{3/2}}\ e^{i(k_1 L_{cr}+k_2 L_2)}\ F(\eta) \\ &= \frac{2i\sqrt{n}}{k_1(1-n^2)\ {L_2}^{3/2}}\ e^{i(k_1 L_{cr}+k_2 L_2)}\ F(\eta) \end{aligned} \tag{167}$$

This attenuation in $1/L_2^{3/2}$ has been confirmed by numerical simulations. Indeed, when the measured amplitude is multiplied by $L_2^{3/2}$ for each offset, the frequency amplitude obtained after Fourier analysis is then constant with the offset (see Figure 94). The factors $\sqrt{x_{crit}}$ and $\sqrt{L_{1,crit}}$ appear to take into account the change of geometrical spreading into the matrix. η and $F(\eta)$ are supposed to be similar in 2D than in 3D. Equations of § 2.1.7.3 will then be used.

The pseudo-reflection coefficient of the lateral wave has to be changed as well, as the propagation term of the reflected wave is now $e^{i\,k_1 L_1}/\sqrt{L_1}$.

$$R_{lateral} = E_{lat}\frac{\sqrt{L_1}}{e^{i\,k_1 L_1}} \tag{168}$$

We obtain then the apparent reflection coefficient for the spherical waves:

$$\begin{aligned} R_{global} &= R_{lateral} + R_{spherical} \\ &= \frac{2i\sqrt{n}}{k_1(1-n^2)\ {L_2}^{3/2}}\ e^{i(k_1 L_{cr}+k_2 L_2)}\ F(\eta)\frac{\sqrt{L_1}}{e^{i\,k_1 L_1}} \\ &\quad + R_1 + R_2\sqrt{1-sin^2\,\theta_1}\sqrt{n^2-sin^2\,\theta_1}\,\mu(\beta) \end{aligned} \tag{169}$$

The angle-dependent amplitude and phase of the global reflection coefficient obtained with this formula with $\varepsilon'_{r_1} = 7.7$, $\varepsilon'_{r_2} = 1$ and $h = 10\,cm$ for different frequencies are represented in Figure 35(a). Those curves can be compared to reflection coefficient measured through 2D numerical modeling for the same configuration, represented in Figure 35 (b).

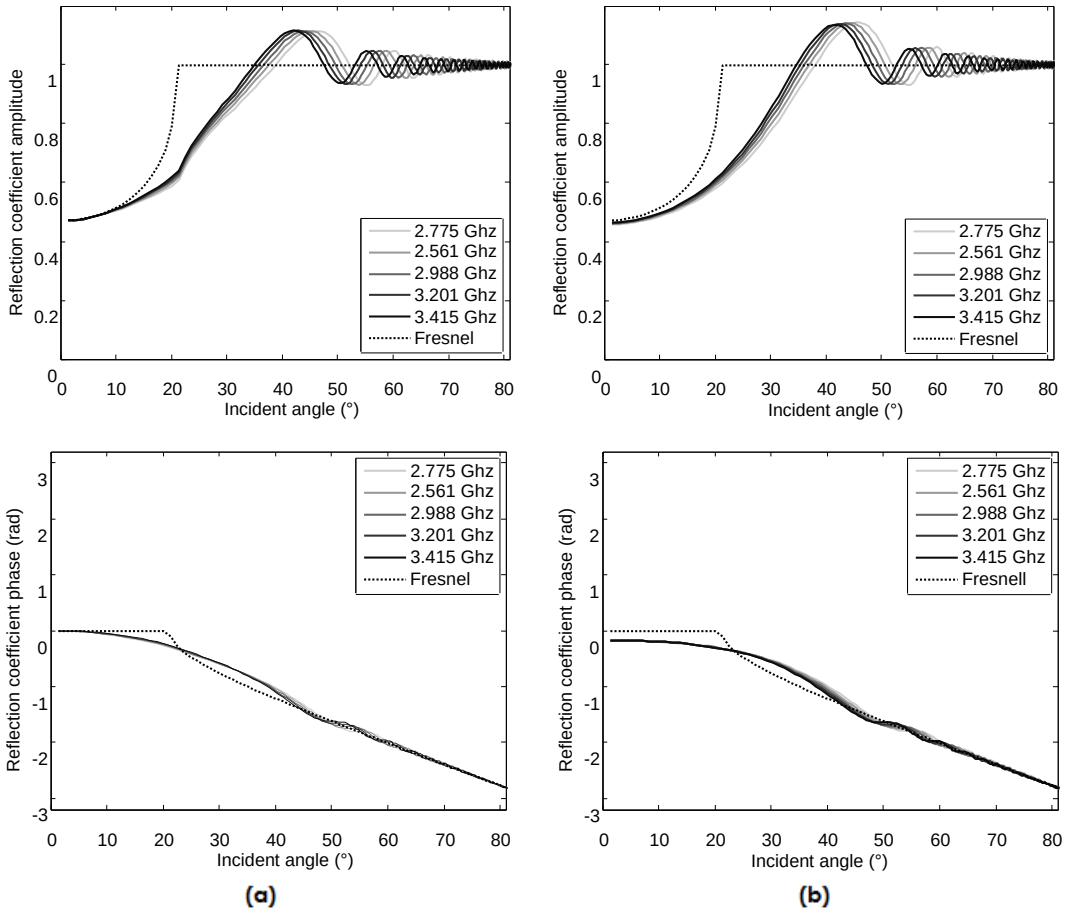

Figure 177 : Amplitude and phase of the global reflection coefficients with $\varepsilon'_{r_1} = 7.7$, $\varepsilon'_{r_2} = 1$ and $h = 10\,cm$; (a) obtained with the modified formulas taking into account the spherical waves reflection and the lateral; (b) measured through the analysis of numerical 2D simulations.

Appendix 5. *Signal performance compliance*

Different tests can be performed on the signal in order to insure the signal quality. We evaluated the system performances in different configurations, with a procedure inspired from the ASTM D 6087 – 05 standard, concerning the evaluation of asphalt-covered bridge decks [95] with horn antennas. Moreover, we also studied the influence of different acquisition factors and methods on the test results.

Long-time stability test

The test consists in measuring every minute the reflection of the radar placed in the air on a metal plate. According to the standard [95], we should have:

$$\frac{A_{max} - A_{ref}}{A_{ref}} < 3\% \tag{170}$$

In (170), A_{ref} is the amplitude at the reference warming up time and A_{max} is the maximum amplitude observed for longer times.

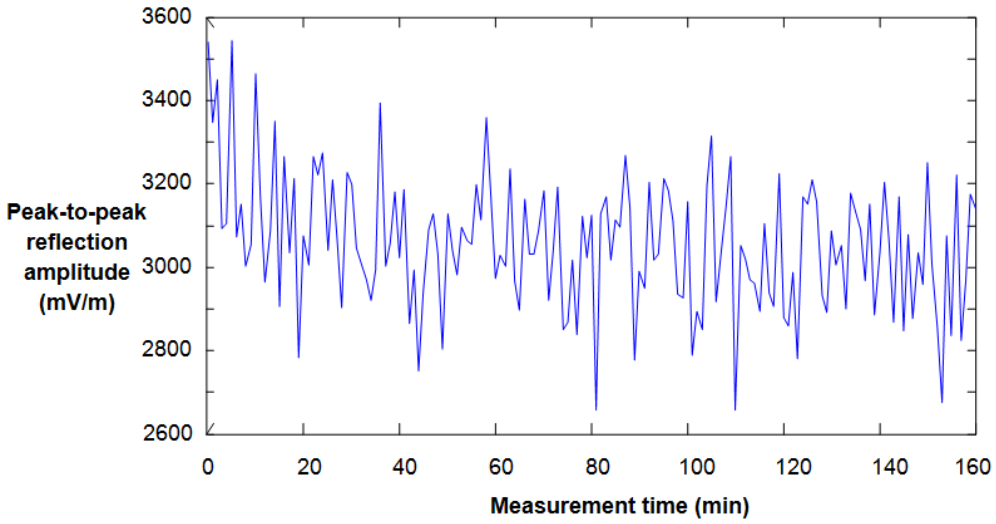

Figure 178 : Evolution of the peak-to-peak amplitude reflected on a metallic plate with a stack of 1.

In Figure 178, we can observe that the amplitude is slightly decreasing; however, the most important observation is probably related to the important variation with time of the signal. This variation is up to 20% of the amplitude, even after a long warming up time.

The same test was performed again, with an automatic stack of 8 (Figure 179)

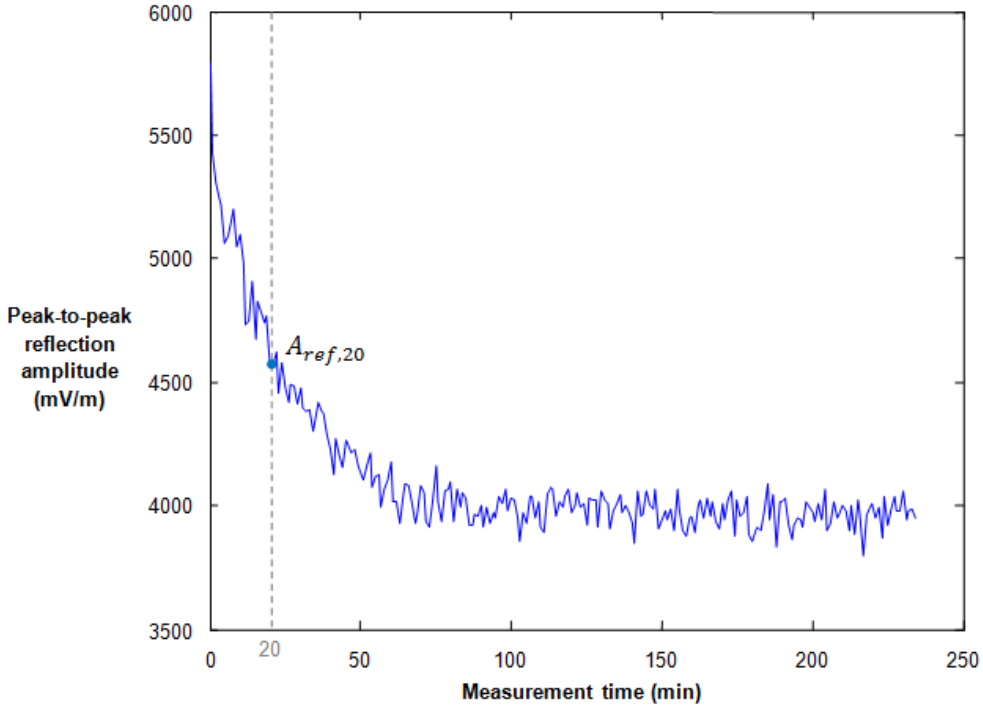

Figure 179 : Evolution of the peak-to-peak amplitude reflected on a metallic plate with a stack of 8.

If we rigorously follow the standard, the stability criteria is respected with the stack of 8, even for a warming up time of 20 minutes since

$$\frac{A_{max} - A_{ref20}}{A_{ref20}} = 1\% \tag{171}$$

But this is only the case because the reflected amplitude is decreasing, while the standard seems to expect an increase. If we perform a similar analysis for a signal that decreases with the time, we obtain

$$\frac{A_{ref20} - A_{min}}{A_{ref20}} = 15.8\% \gg 3\% \tag{172}$$

If we respect a warming up time of 80 minutes, we find

$$\frac{A_{ref80} - A_{min}}{A_{ref80}} = 5{,}5\% > 3\% \tag{173}$$

To respect rigorously the standard, the warming up time should be superior to 80 minutes, or the stack higher than 8.

The same test was performed with a stacking of 16 and more than 6 hours of measurements.

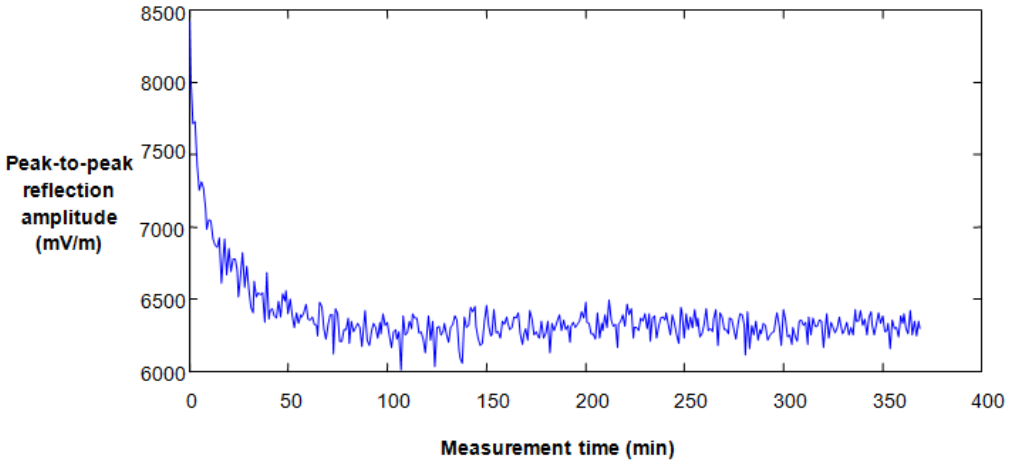

Figure 180 : Evolution of the peak-to-peak amplitude reflected on a metallic plate with a stack of 16.

We observe in Figure 180 that, since the metallic plate was placed closer to the antenna, the reflected amplitude is higher than in the previous tests. Unfortunately, the stability criterion is still not respected, because the variations are still up to 20%.

The long-time stability criterion of the standard is not fulfilled by our antenna, even by increasing the stacks number. We conclude that the long-time stability of our antenna signal is poorer that the stability that can be reached with horn antennas (for which the standard was initially written).

Signal stability test

The signal stability control, according to the standard, consists in 100 measurements performed over a metallic plate with the maximum acquisition rate. We should then have

$$\frac{A_{max} - A_{min}}{A_{avg}} < 0.001 \tag{174}$$

The test was performed and we found

$$\frac{A_{max} - A_{min}}{A_{avg}} = 0.2533 \tag{175}$$

We see that it is impossible to fit to the standard requirement; the signal of the radar is too unstable. To decrease this variability, one can use the signal stacking method, but the number of stacks necessary to fit to the standard is very large as long as the noise proportionally decreases to the inverse of the root mean of the stack number (see § 3.2.3.1).

Appendix 6. *Alternative 3D hybrid model*

As an alternative to the 3D hybrid model developed in § 4.1.3.3, we developed an second model in which the attenuation function is not applied to the lateral wave but only on the multiples. The only attenuation for the lateral wave is then its attenuation described by (67), unrelated to the layer thickness. The parameters of the attenuation equation (144) had to be optimized to this new configuration. The best fit was obtained for $c = 5.5$ and $d = 3$. The results are shown in Figure 181.

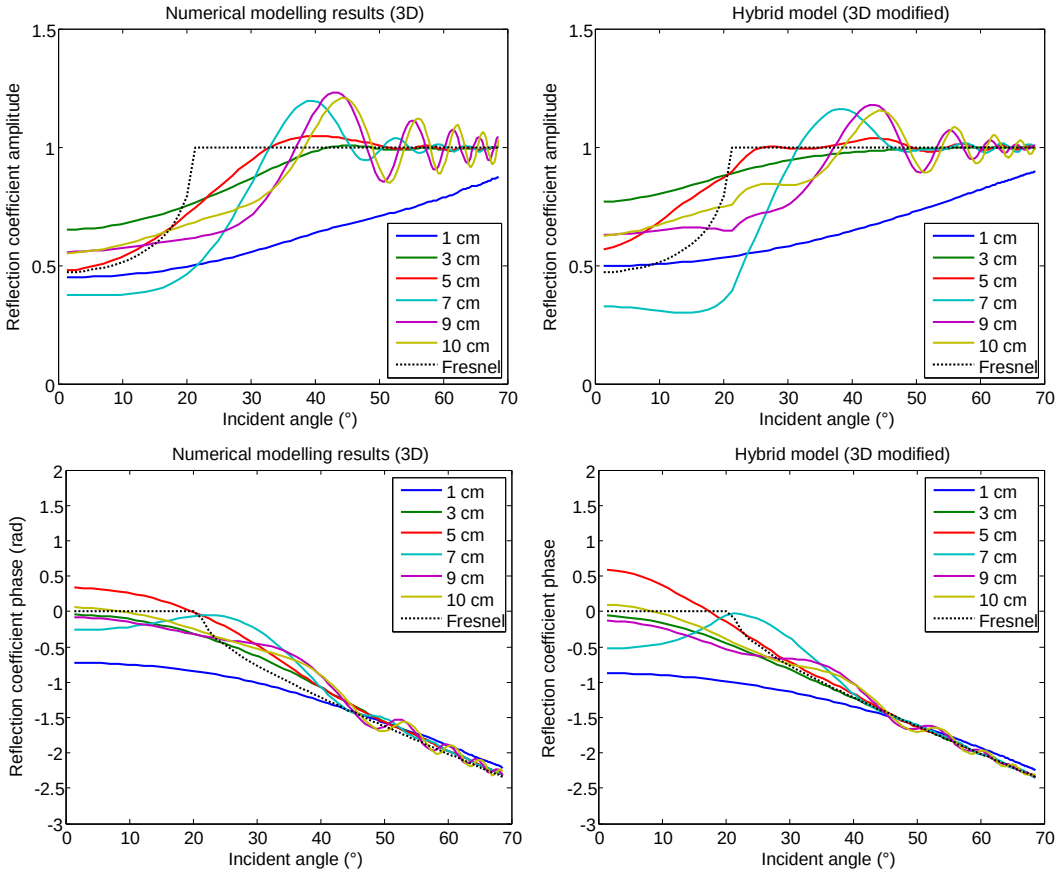

Figure 181 : Comparison of the APVO curves measured from 3D numerical modelling and estimated with the hybrid model determined from 3D measurements, without applying attenuation function to the lateral wave.

The value of the error function calculated on the thicker curves (7-11 cm) is equal to 0.4186 without applying attenuation to the lateral wave (Figure 181) while it was equal to 0.4273 with the first model (Figure 118). But no improvement is really visible on the curves. For example, the position of the first peak of the 7 cm curve is improved, but for larger incidences, the oscillations are completely attenuated because the lateral wave is in phase opposition with the multiples. This does not appear in the numerical modelling results, suggesting that the lateral wave is present but still undergoes attenuation due to the layer thickness.

Appendix 7. *Codes of the main Matlab functions*

In this appendix, the hybrid function used for the determination of APVO curves is detailed. All the sub-functions used in this routine (written in italic and bold) will be detailed as well.

```
function [AVO,PVO]=APVO_Hybrid(e_r1,e_r2,sig_1,sig_2,h,d,x,nk,freq,nbdim,fig)

% This function evaluates the AVO and PVO curves with the hybrid method.
% e_r1 and e_r2 are the respective relative dielectric permittivities of the
matrix
% and of the layer,
% sig_1 and sig_2 are their respective conductivities.
% h is the layer depth, d the layer thickness, x the antennas offsets (in m)
% nk is the number of terms of the series truncation,
% freq is the array of considered frequencies (in Hz),
% nbdim is the number of dimensions of the problem (2 or 3) and
% fig is 0 or 1, depending if figures should be displayed.

v_c=0.3/sqrt(e_r2);% speed into the layer
valtheta=atan(x/2/h); %Range of incident angles

for k=1:length(x)% Loop on the different positions

    xk=x(k); % Local offset value

    for l=1:length(freq)

        freqk=freq(l);
        lambda_c=(v_c/(freqk/10^9));% wavelength into the matrix

        if d<0.3*lambda_c
            Rcompl=R_tl_plane(e_r1,e_r2,sig_1,sig_2,h,d,xk,freqk);

        elseif d>0.5*lambda_c
            Rcompl=R_tl_cerv_att(e_r1,e_r2,sig_1,sig_2,h,d,xk,nk,freqk,nbdim);

        else % interpolation between both methods

Rcompl_cerv=R_tl_cerv_att(e_r1,e_r2,sig_1,sig_2,h,d,xk,nk,freqk,nbdim);
       Rcompl_ev=R_tl_plane(e_r1,e_r2,sig_1,sig_2,h,d,xk,freqk);
Rcompl=Rcompl_cerv*(d-0.3*lambda_c)/(0.2*lambda_c)+Rcompl_ev*(0.5*lambda_c-
d)/(0.2*lambda_c);
        end

        phase(k,l)=angle(Rcompl);
        R(k,l)=abs(Rcompl);

    end
end

AVO=R;
PVO=phase;

if fig==1
    equation_str = (num2str((freq*10^-9)',4));

    figure
    plot(valtheta/pi*180,R)
            ylabel('Reflection coefficient amplitude')
            xlabel('Incident angle (°)')
            title('Hybrid model')
            hl=legend(equation_str,'Location', 'EastOutside');
```

```
            vl = get(hl,'title');
            set(vl,'string','Frequency (GHz)');

    figure
    plot(valtheta/pi*180,phase)
            ylabel('Reflection coefficient phase (rad)')
            xlabel('Incident angle (°)')
            title('Hybrid model')
            hl=legend(equation_str,'Location', 'EastOutside');
            vl = get(hl,'title');
            set(vl,'string','Frequency (GHz)');
end
```

```
function Rcompl=R_tl_cerv_att(e_r1,e_r2,sig_1,sig_2,h,d,x,nk,freq,nbdim)

% This function evaluates the AVO and PVO curves with the first terms method with
spherical waves and layer attenuation.
% e_r1 and e_r2 are the respective relative dielectric permittivities of the
matrix
% and of the layer,
% sig_1 and sig_2 are their respective conductivities.
% h is the layer depth, d the layer thickness, x the antennas offset (in m)
% nk is the number of terms of the series truncation,
% freq is the frequency (in Hz),
% nbdim is the number of dimensions of the problem (2 or 3) and

r=sqrt(e_r1)/sqrt(e_r2);%speed ratio
v_m=0.3/sqrt(e_r1);% speed into the matrix
v_c=0.3/sqrt(e_r2);% speed into the layer
lambda_c=(v_c/(freq/10^9));% wavelength into the matrix
dOnLambda=d/lambda_c;% Thickness-to-wavelength ratio

%Determination of the geometric attenuation coefficient
if nbdim==2
    att_coeff=0.5;
else
    att_coeff=1;
end

%Calculation of the intrinsic attenuation coefficient
att_m=sig_1*sqrt(4*pi()*10^(-5))/(2*sqrt(e_r1*8.854187*10^-10));
att_c=sig_2*sqrt(4*pi()*10^(-5))/(2*sqrt(e_r2*8.854187*10^-10));

theta_crit=asin(v_m/v_c); %Critical angle
x_crit=2*h*tan(theta_crit); %Critical distance

% Determination of the incidence angles of every multiple
[alpha]=Find_alpha(e_r1,e_r2,h,d,x,nk);
% Calculation of Fresnel reflection coefficient for each multiple
Rsimple=(cos(alpha)-sqrt(e_r2/e_r1-(sin(alpha).^2))./(cos(alpha)+sqrt(e_r2/e_r1-
(sin(alpha)).^2));
% Distance of each multiple into the matrix
x_m=ones(size(alpha)).*2*h./cos(alpha);
% Distance of each multiple into the layer
x_c=(0:2:2*nk).*d./cos(asin(r*sin(alpha)));
% Calculation of the reflection coefficient of each multiple
R_loc=-(1-Rsimple.^2).*Rsimple.^(-1:2:2*nk-1);
% The first reflection coefficient is replaced by a calculation by the spherical
equation
[R_loc(1),R_refl,~]=
R_cerveny_refl_lat(e_r1,e_r2,sig_1,sig_2,h,2*h*tan(alpha(1)),freq,nbdim);
x_tot=x_m+x_c; % Total path of the wave
t_tot=x_m/v_m+x_c/v_c; % Total travelling time of the wave
% geometric attenuation for each multiple
geom=x_tot(1)^att_coeff./x_tot.^att_coeff;
% Intrinsic attenuation for each multiple
att=exp(x_m*att_m).*exp(x_c*att_c);
x_peak=x_crit+d;

%Calculation of the attenuation function
```

```
if nbdim==2
    attd=min(7.5*exp(-2.4*dOnLambda)*exp(-0.15*dOnLambda.^-4*(x-
x_crit)/lambda_c),1);
else
    attd=min(1.65*exp(-0.85*dOnLambda)*exp(-0.21*dOnLambda.^-3.25*(x-
x_crit)/lambda_c),1);
end

%The attenuation function is applied progressively between the critical
%distance and the peak distance

if x<x_crit
   attd=1;
elseif x<x_peak
   attd=attd*sin(pi/2*(x-x_crit)/(x_peak-x_crit))+1*(1-sin(pi/2*(x-
x_crit)/(x_peak-x_crit)));
end

%Calculation of the propagation of every multiple
prop=exp(1i*2*pi().*freq.*t_tot*10^-9)./exp(1i*2*pi()*freq*t_tot(1)*10^-9);
glob=R_loc.*att.*geom.*prop;

%Summation of the considered multiples
Rcompl=sum(glob)*attd+R_refl.*(1-attd);
```

```
function Rcompl=R_tl_plane(e_r1,e_r2,sig_1,sig_2,h,d,x,freq)

% This function evaluates the AVO and PVO curves with the plane wave
approximation.
% e_r1 and e_r2 are the respective relative dielectric permittivities of the
matrix
% and of the layer,
% sig_1 and sig_2 are their respective conductivities.
% h is the layer depth, d the layer thickness, x the antennas offsets (in m)
% nk is the number of terms of the series truncation,
% freq is the array of considered frequencies (in Hz),
% nbdim is the number of dimensions of the problem (2 or 3) and
% fig is 0 or 1, depending if figures should be displayed.

r=sqrt(e_r1)/sqrt(e_r2);%speed ratio
v_c=0.3/sqrt(e_r2);% speed into the layer
lambda_c=(v_c/(freq/10^9));% wavelength into the matrix
dOnLambda=d/lambda_c;

%Calculation of the intrinsic attenuation coefficient
att_m=sig_1*sqrt(4*pi()*10^(-5))/(2*sqrt(e_r1*8.854187*10^-10));
att_c=sig_2*sqrt(4*pi()*10^(-5))/(2*sqrt(e_r2*8.854187*10^-10));

%Incident angle
alpha=atan(x/2/h);
%Fresnel reflection coefficient
Rsimple=(cos(alpha)-sqrt(e_r2/e_r1-(sin(alpha).^2)))./(cos(alpha)+sqrt(e_r2/e_r1-
(sin(alpha)).^2));% Calculation of Fresnel reflection coefficient for each
multiple
%Angle into the layer
phi=asin(r*sin(alpha));
%Path change into the matrix and the layer
dx_m=-2*d*r*(sin(alpha(1)))^2/sqrt(1-r^2*(sin(alpha(1)))^2);
dx_l=2*d/sqrt(1-r^2*(sin(alpha(1)))^2);
%Intrinsic attenuation term
att_term=exp(-att_c*dx_l+att_m*dx_m);
%Phase shift term
beta_1=exp(1i*4*pi()*dOnLambda*cos(phi));
%Global formula
Rcompl=Rsimple*(1-beta_1*att_term)/(1-Rsimple^2*beta_1*att_term);
```

```
function [alpha]=Find_alpha(er_1,er_2,h,d,x,nk)

%This function evaluates the reflection angles of the multiples when a
%wave reflects into a thin layer. The parameters are er_1 and er_2 the
%relative dielectric permittivities of the matrix and the layer,
%h, the depth of the layer, d its thickness and x the antennas offset (all
%in m). nk is the number of multiples that will be considered.

r=sqrt(er_1)/sqrt(er_2);
alpharef=atan(x/2/h);
alpha(1)=alpharef;

for j=1:nk

    A=-r^2*h^2-r^2*j^2*d^2-x^2/4*r^2;
    B=h^2+r^2*j^2*d^2+x^2/4+x^2/4*r^2;
    C=-x^2/4;
    D=-2*r*j*d*h;
    E=r^2;
    F=(-1-r^2);

    p=[(A^2-D^2*E),0,(2*A*B-D^2*F),0,(B^2+2*A*C-D^2),0,(2*B*C),0,C^2];
    rac=asin(roots(p));

    alpha(j+1)=0;
    for i=1:size(rac,1);
        if rac(i)>0 & imag(rac(i))==0 &rac(i)<alpharef;
            alpha(j+1)=rac(i);
        end
    end

end
```

```
function [R,R_refl,R_lat]
       =R_cerveny_refl_lat(er_1,er_2,sig_1,sig_2,h,x,freq,nbdim)

% This function evaluates the reflection coefficient R from Cerveny equations.
% It also gives its decomposition into reflected amplitude (R_refl) and
% amplitude of the lateral wave (R_lat)
% e_r1 and e_r2 are the respective relative dielectric permittivities of the
matrix
% and of the layer,
% sig_1 and sig_2 are their respective conductivities.
% h is the layer depth, d the layer thickness, x the antennas offsets (in m)
% freq is the  considered frequencies (in Hz)

v1=0.3/sqrt(er_1);
v2=0.3/sqrt(er_2);

epsilon0=8.854187*10^-10;
mu0=4*pi()*10^-5;

n=sqrt(er_2/er_1);
alpha_1=sig_1/100*sqrt(mu0)/(2*sqrt(er_1*epsilon0));

k1=2*pi()*freq/(v1*10^9)+1i*alpha_1;

theta=atan(x/2/h);

theta_crit=asin(v1/v2);
x_crit=2*h*tan(theta_crit);
```

```
A0=(cos(theta)-sqrt(n^2-(sin(theta))^2))/(cos(theta)+sqrt(n^2-(sin(theta))^2));

%%%%%%Situation before critical point%%%%%%%%%%%%%%%%%%%%%%
beta=sqrt(k1*x./(2.*(sin(theta)).^3)).*(sqrt(1-n^2)-sqrt(1-(sin(theta)).^2));
A2=-2./((1-(sin(theta).^2))-(n^2-(sin(theta)).^2));


g=@(xk) exp(-xk.^2).*sqrt(xk-beta.*exp(1i*pi()/4));
L=integral(g,-Inf,Inf);
mu1=L./(sqrt(pi())*sqrt(-beta.*exp(1i*pi()/4)));

%%%%%%Beyond the critical point %%%%%%%%%%%%%%%%%%%%%%%%%%%%
L=x-2*h*n./(sqrt(1-n^2));
eta=((k1.*n*(1-n^2))./(2*x)).^0.5.*L;
A1=((1-(sin(theta)).^2)+(n^2-(sin(theta)).^2))./((1-(sin(theta)).^2)-(n^2-
(sin(theta)).^2));


f = @(xk) exp(-xk.^2-sqrt(2).*eta.*xk.*(1+1i)).*(xk).^0.5;
Q = integral(f,0,Inf);
mu2=Q.*(2*eta).^1.5.*(exp(1i*pi()/4)).^1.5./gamma(3/2);


R=2*h./cos(theta);
if nbdim==2;
    dim_corr=R.^-0.5.*(x_crit./sin(theta_crit)).^0.5.*x.^0.5./x_crit.^0.5;
else
    dim_corr=1;
end


R_refl=A0+sqrt(1-(sin(theta)).^2).*sqrt(n^2-(sin(theta)).^2).*A2.*(mu1-1);
R_lat=0;


if x>=x_crit
    R_lat=2*n*mu2*x^0.5/(k1*sin(theta)*(1-
n^2)*(L)^1.5)*dim_corr*exp(1i*k1*(x*n+(2*h*sqrt(1-n^2)-R))+1i*pi()/2);
    R_refl=A1+1i*A2*(1-(sin(theta))^2)^0.5*((sin(theta))^2-n^2)^0.5*mu1;
end


R=R_refl+R_lat;
```